Vibration and Thermal Stress Analyses of Functionally Graded Materials

Analyses met betrekking tot vibraties en thermische belasting
van functionelegradiëntmaterialen

Behnam Sobhaniaragh

Promotoren: prof. dr. ir. M. Abdel Wahab, prof. dr. ir. M. H. Yas
Proefschrift ingediend tot het behalen van de graad van
Doctor in de Ingenieurswetenschappen: Werktuigkunde-Elektrotechniek

Vakgroep Mechanische Constructie en Productie
Voorzitter: prof. dr. ir. P. De Baets
Faculteit Ingenieurswetenschappen en Architectuur
Academiejaar 2013 - 2014

UNIVERSITEIT
GENT

ISBN 978-90-8578-712-9
NUR 978, 950
Wettelijk depot: D/2014/10.500/58

Promoters:

Prof. dr. ir. Magd Abdel Wahab

Prof. dr. ir. Mohammad Hossein Yas

Examination Committee:

Prof. dr. ir. Rik Van de Walle (Chair)

Prof. dr. ir. Magd Abdel Wahab

Prof. dr. ir. Mohammad Hossein Yas

Prof. dr. ir. Patrick De Baets

Prof. dr. ir. Guido De Roeck

Prof. dr. ir. Wim De Waele

Prof. dr. ir. Patricia Verleysen

Prof. dr. ir. Mia Loccufier

Research Institute

Ghent University
Faculty of Engineering and Architecture
Department of Mechanical Construction and Production
Laboratory Soete
Technologiepark 903
B-9052 Zwijnaarde
Belgium

Tel: +32 9 331 0477

Cell: +32 478 638575

Email: Behnam.Sobhaniaragh@UGent.be, behnamsobhani@yahoo.com

http://www.soetelaboratory.ugent.be

Dedicated to my parents

Acknowledgement

I would like to take this opportunity to thank all those who have been involved with this thesis and my publications directly or indirectly and who helped me to successfully complete this work. First and foremost, I would like to really thank my supervisor Prof. Magd Abdel Wahab for his strong support, patience, and encouragement during my research period at Ghent University, Laboratory Soete.

My sincere thanks and appreciation to Prof. Mohammad Hossein Yas, distinguished professor in Razi University, for the opportunity to work for him and for his outstanding help, support, guidance, and valuable discussions during the last six years.

Special thanks are reserved for all examination committee members, particularly for Prof. Wim De Waele and Prof. Mia Loccufier for their useful comments and considerations.

I would like to express my gratitude several colleagues beyond Ghent University who in one way or another contributed in my research. I would like to express my sincere appreciation to:

- Prof. Saeed Jafari Mehrabadi in Islamic Azad University of Arak for supervision and his excellent contributions in various research projects.
- My best friends and colleagues: Hadi Hedayati from Isfahan University of Technology, Ehsan Borzabadi Farahani from Razi University, Mohammad Hedayati from Kashan Univesrsity, and Amir Nasrollah Barati from Islamic Azad University of Aligoudarz who were abundantly helpful and offered invaluable assistance, support and guidance.

I would like to thank friends and colleagues that made enjoyable time at laboratory Soete: Yue Tongyan, Reza Hojjati Talemi, Hanan Al Ali, Phuc Phung Van, Xin Chen, Zamaan Sadeghi, Abdelwaheb Ferjaoui, Jacob Sukumaran, Diego Belato Rosado, Saosometh Chhith, Gusztav Fekete, Yeczain Perez, Vanessa Rodriguez, Stijn Hertele, Jan De Pauw, Timothy Galle, Nahuel Micone, Koen Van

Minnebruggen, Wouter Ost, Tony Lefevre, Rudi Denys, Wim De Waele, Georgette D'Hondt, Chris Bonne, Rudy Desmet, and Jonathan Vancoillie.

I would also thank to my friends Behnam Bahrami, Ehsan Yadollahi, Arash Farnam, Soroosh Naghdy for all the enjoyed moments, trips and weekends.

Most of all, I would like to give my deepest gratitude to my family, my dear parents Mohammadali and Azam, my brother Babak, my sister Samira, without my family's unending encouragement, support, and love this work would have not been done. I am deeply grateful to Gholamreza Farhoomand and Pegah Taghvai for their great support. I also would like to thank my lovely nieces, Parmis and Sania for gifting so much laughter.

Summary

In recent years, astonishing advances in science and technology have motivated researchers to develop new class of structural materials with improved properties. Functionally graded materials (FGMs) are new generation of composite materials consisting of two or more constituent phases with a continuously variable distribution. The concept of FGMs can be used to take advantage of certain desirable features of each constituent phases and tailor the distribution of material properties so that the desired responses to given mechanical and thermal loadings are achieved or natural frequencies are modified to a required manner. In order to take the full benefit of exceptional properties of FGMs in new product development, fundamental studies on the mechanics of such materials must be carried out along with research on their processing.

Taking theoretical numerically modelling and analysis of FGMs into account, the main objective of this thesis is to study thermo-mechanical responses and free vibration of plates and shells composed of FGM composites. To this end, methodology used in this thesis is organized as follows.

Firstly, theoretical formulations for free vibration, static and thermal analyses of FGMs are developed based on 3-D elasticity theory and 2-D plate theories. The main approach in formulations based on 3-D elasticity theory is to combine the equilibrium equations with the stress-strain and strain-displacement relations to derive the governing equations in term of the displacement components. This approach is called Navier method. In case of 2-D theories, the displacements are expanded in terms of thickness and transverse displacement is independent of the transverse coordinate. This causes coupled governing equations to be independent of transverse displacement. For the first time, thermo-elastic governing equations for a 2-D FGM panel based on third-order-shear deformation theory are derived.

Secondly, for modelisation of variation of volume fraction or fiber orientation, classic form of power-law distribution is introduced. Then, as one of the contributions of this thesis, 1-D and 2-D generalized power-law distributions are presented. By using generalized power-law distribution, it is possible to study the effects of the various kinds of material profiles including symmetric, asymmetric, sigmoidal and classic on mechanical behaviour of FGM structures. To compute effective material properties of composites, rule of mixture and Mori-Tanaka method are used. In case of nanocomposites, Eshelby-Mori-Tanaka method is employed to determine the effective material properties of composites reinforced by various type of carbon nanotubes dispersion.

Thirdly, owing to the complexity of governing equations with variable coefficients initiated from non-homogeneity, it is very rigorous to obtain the exact solutions. Due to non-linear variation of material properties, seeking a powerful numerical method is highly desirable. In this thesis, generalized differential quadrature method (GDQM) is adopted to solve coupled governing differential equations. The 1-D and 2-D GDQM are applied to various problems consisting of thermal, vibration, and static analyses of FGMs. By solving free vibration, static, and thermal problems and by comparing the results with those of other methodologies, accuracy, convergency and efficiency of the methodology are asserted. Less computational efforts of the proposed approach for FGMs problems with respect to other available methods have been found.
According to contributions of the thesis into FGMs, significant motivations and findings can be categorized into three parts as follows: 1) 1-D FG fiber-reinforced composites, 2) 2-D FGM composites, and 3) FG carbon nanotubes-reinforced composites.

1. 1-D FG fiber-reinforced composites

The fiber-reinforced laminated composites possess some major problems, such as failure owing to delamination and other effects in the material formation, and also effects of transverse shear deformation because of the low ratio of transverse shear modulus to axial modulus. Interlaminar stresses in laminated composites comprising the normal and transverse shear stresses are profound effects on the delamination phenomena. To overcome those drawbacks, motivated by FG metal-ceramic materials, researchers have extended the gradient idea into the design of fiber-reinforced composites. By using the concept of FGMs, fiber-reinforced composites can be tailored to meet various in-plane stiffness or strength requirements. Increasing interest towards using the idea of FGM in fiber-reinforced composites, in recent years some literature has been allocated to the study of mechanical responses of FG fiber-reinforced composites. A critical review on the literature shows that available

studies on the 1-D FG fiber-reinforced composites are still very few to number, and more research is notably needed. Inspired by this idea, stress, deformation, thermoelastic, and vibration problems of 1-D FG fiber-reinforced plates and shells are studied. For the first time, natural frequencies, static and thermal stresses of FG fiber orientation and volume fraction fiber-reinforced composites panels have been compared with discretely laminated composites. Additionally, effects of continuously grading fiber orientation face sheets on free vibration of sandwich panels with FG core have been studied. An effort has been made to investigate impacts of Winkler and shearing layer elastic parameters on the natural frequencies FG fiber-reinforced plates resting on elastic foundation.

2. 2-D FGM composites

In most available literature regarding FGMs, the material properties were assumed to have a smooth variation only in one direction. Conventional FGM may not be so effective in design problems inasmuch as all outer/inner surface of the body have the same composition distribution. Furthermore, tailoring of materials profile in two directions can be more effective to modify the response of the structure to a required manner by selecting suitable different parameters of power-law distribution. Motivated by the main idea of 2-D dependent material properties, bending, thermal and free vibration problems of 2-D FGM composites are studied. To this end, 2-D generalized power-law distribution is proposed for modelisation of material properties in two directions. It has been inferred that the 2-D generalized power-law distribution proposed for volume fractions of 2-D FGM composites gives designers a powerful tool for flexible design of structures under multi-functional requirements. Results indicated the advantages of using panels with graded volume fractions in two directions to a more flexible design than the conventional 1-D FGM composites.

3. FG carbon nanotubes-reinforced composites

In the modelling of carbon nanotube-reinforced composites the concept of FGMs might be incorporated to effectively make use of the carbon nanotubes (CNTs). In the present thesis, for the first time, effects of CNT agglomeration and various graded CNTs volume fractions on the free vibration characteristics of CNT-reinforced composites are studied. Eshelby-Mori-Tanaka approach and extended rule of mixture are employed to calculate the effective elastic moduli of composites reinforced by CNTs. In addition, the interesting results for mechanical buckling of an FG nanocomposite rectangular plate reinforced by aligned CNTs subjected to uniaxial and biaxial in-plane loadings have been presented. It is concluded that CNTs distributed close to top and bottom are more efficient than those distributed nearby the mid-plane of the plate.

Samenvatting

In de laatste jaren heeft onmiskenbare vooruitgang in wetenschap en technologie onderzoekers gemotiveerd om een nieuwe klasse van structurele materialen met betere eigenschappen te ontwikkelen. Functionele Gradiënt Materialen (FGMs) zijn een nieuwe generatie van composietmaterialen die uit twee of meer fasen met een continu veranderlijke distributie bestaan. Het concept FGMs kan worden gebruikt om uit bepaalde positieve eigenschappen van elke constituent voordeel te halen. Door een geschikte fasering is de distributie van materiële eigenschappen dusdanig dat optimale reacties op bepaalde mechanische en thermische belastingen worden bereikt of dat eigenfrequenties op gewenste wijze worden verandere. Om het volledige voordeel van de uitzonderlijke eigenschappen van FGMs in nieuwe productontwikkeling te bekomen, moeten fundamentele studies over de mechanica van dergelijke materialen samen met onderzoek in verband met hun productie worden uitgevoerd.

Theoretische numerieke modellering en analyse van FGMs, is de belangrijkste doelstelling van deze thesis waarin thermo-mechanische reacties en vrije trilling van platen en schalen, die uit FGM worden samengesteld, worden bestudeerd. Daartoe wordt de methodologie die in deze thesis wordt gebruikt, georganiseerd als volgt.

Ten eerste worden de theoretische formuleringen voor vrije trillingen, statische en thermische analyses van FGMs ontwikkeld gebaseerd op 3-D elasticiteitstheorie en 2-D plaattheorieën. De belangrijkste aanpak voor de formuleringen die op 3-D elasticiteitstheorie gebaseerd zijn, is de evenwichtsvergelijkingen met spanning-rek en rek-verplaatsing relaties te combineren om de vergelijkingen in functie van de verplaatsingscomponenten af te leiden. Deze benadering is beter gekend als de vergelijkingen van ‘Navier’. In het geval van 2-D theorieën worden de verplaatsingen uitgebreid in functie van dikte en de transversale verplaatsing is onafhankelijk van de transversale coördinaat. Dit veroorzaakt dat de gekoppelde vergelijkingen van transversale verplaatsing onafhankelijk zijn. Voor het eerst

worden thermo-elastische vergelijkingen voor een 2-D paneel uit FGM op basis van de theorie van de 'Third-order Shear Deformation Theory (TSDT)' afgeleid.

Ten tweede, wordt voor de modellering van de variatie van volumefractie of vezeloriëntatie de klassieke vorm van gegeneraliseerde machtsfunctie-distributie geïntroduceerd. Dan, als één van de bijdragen van deze thesis, worden 1-D en 2-D machtsfunctie-distributies voorgesteld. Door de gegeneraliseerde machtsfunctie-distributie te gebruiken is het mogelijk om de gevolgen van diverse soorten graderingsprofielen (symmetrisch, asymmetrisch, sigmavormig en klassiek) op het mechanisch gedrag van FGM componenten te bestuderen. Om efficiënte materiële eigenschappen van samenstellingen te verwerken, worden de mengregel en de methode van Mori-Tanaka gebruikt. In het geval van nano-composieten is de methode Eshelby-Mori-Tanaka aangewend om de materiële eigenschappen te bepalen van composieten die door diverse types van koolstof-nanobuizen worden versterkt.

Ten derde, ten gevolge van de complexiteit van de vergelijkingen met veranderlijke coëfficiënten ten gevolge van niet-homogeniteit, is het zeer moeilijk om nauwkeurige oplossingen te verkrijgen. Wegens niet-lineaire variaties van materiële eigenschappen, is het hoogst wenselijk om naar een krachtige numerieke methode te streven. In deze thesis wordt de methode 'Generalized Differential Quadrature Method (GDQM)' aangewend om de gekoppelde differentiële vergelijkingen op te lossen. 1-D en 2-D GDQM worden toegepast op diverse problemen m.b.t. thermische, statische en trillingsanalyses van FGMs. Door vrije trilling, statische en thermische problemen op te lossen en door de resultaten te vergelijken met die van andere methodologieën, worden nauwkeurigheid, convergentie en efficiëntie van de methodologie aangetoond. De voorgestelde benadering voor problemen van FGMs leidt tot verminderde computertijd in vergelijking met andere beschikbare methodes zijn gevonden.

De bijdragen van de thesis op gebied van FGMs kunnen in drie delen worden gecategoriseerd als volgt: 1) 1-D FG vezelversterkte composieten, 2) 2-D FGM composieten en 3) koolstof nanobuis-versterkte FG composieten.

1. 1-D FG vezelversterkte composieten

De vezelversterkte gelamineerde composieten vertonen sommige belangrijke problemen, zoals schade ten gevolge van delaminatie, en ook gevolgen van transversale afschuiving wegens de lage verhouding van de transversale schuifmodulus tot de axiale modulus. Interlaminaire spanningen in gelamineerde composieten, die zowel uit normaalspanningen als transversale schuifspanningen bestaan, zijn gevolgen van de delaminatie fenomenen. Om die nadelen te

overwinnen, die door FG metaal-keramische materialen worden gemotiveerd, hebben onderzoekers het gradiëntidee in het ontwerp van vezelversterkte composieten uitgebreid. Door het concept FGMs te hanteren, kunnen vezelversterkte composieten worden gemaakt die aan diverse stijfheid- of sterktevereisten voldoen. De stijgende belangstelling naar het gebruiken van het idee van FGM in vezelversterkte composieten heeft de laatste jaren geleid tot heel wat literatuur omtrent de studie van mechanische reacties van FG vezelversterkte composieten. Een kritische beoordeling van de literatuur toont aan dat de beschikbare studies over de FG vezelversterkte composieten nog zeer beperkt is en dat meer onderzoek nodig is. Hierdoor geïnspireerd worden de spanning, de vervorming, de thermo-elastische en trillingsproblemen van FG vezelversterkte platen en schalen bestudeerd. Voor het eerst zijn de eigenfrequenties, de statische en thermische spanningen van composieten panelen met gradiënten in vezeloriëntatie en in volumefractie vergeleken met discreet gelamineerde composieten panelen. Bovendien zijn de gevolgen van continu variërende vezeloriëntatie voor de vrije trilling van sandwichpanelen met FG kern bestudeerd. Een inspanning is geleverd om effecten te onderzoeken van de elastische Winkler parameters op de eigenfrequenties van FG vezelversterkte platen die op de elastische fundering rusten.

2. 2-D FGM composieten

In de meeste beschikbare literatuur betreffende FGMs werd verondersteld dat de materiële eigenschappen een variatie in slechts één richting vertonen. Conventionele FGM zijn minder efficiënt voor ontwerpproblemen aangezien zowel de buiten- als de binnenoppervlakte van het lichaam de zelfde samenstellingsdistributie hebben. Voorts kan het maken van materiaaldistributies in twee richtingen efficiënter zijn om de reactie te wijzigen van de structuur op een vereiste manier. Dit door geschikte parameters van de machtsfunctie-distributie te selecteren. Gemotiveerd door het belangrijkste idee van 2-D afhankelijke materiële eigenschappen, worden de mechanische, thermische en vrije trillingsproblemen van 2-D composieten FGM bestudeerd. Daartoe wordt een 2-D algemene machtsfunctie-distributie voorgesteld voor het modelleren van materiële eigenschappen in twee richtingen. Men heeft geconcludeerd dat de 2-D algemene machtsfunctie-distributie, die voor volumefracties is voorgesteld, aan ontwerpers een krachtig hulpmiddel voor flexibel ontwerp van structuren onder multifunctionele vereisten beschikbaar stelt. De resultaten wezen op de voordelen om panelen met gegradeerde volumefracties in twee richtingen tijdens ontwerp te gebruiken, beter dan de conventionele samenstellingen 1-D FGM.

3. Koolstof nanobuis-versterkte FG composieten

Voor een effectieve modellering van koolstof nanobuis-versterkte (CNT) compsoieten wordt het concept FGMs geïmplementeerd. In deze thesis worden voor het eerst de gevolgen van agglomeratie CNT en diverse gradiënt volumefracties CNTs op het vrije trillingsgedrag van CNT-versterkte composieten bestudeerd. De benadering Eshelby-Mori-Tanaka en de uitgebreide mengregel zijn aangewend om de efficiënte elastische modulus van composieten die door CNTs worden versterkt te berekenen. Bovendien worden interessante resultaten voor het knikken van een FG nano-composiet rechthoekige plaat, die door gerichte CNTs wordt versterkt, onder de actie van éénassige en tweeassige belastingen voorgesteld. Men besluit dat CNTs dicht bij de bovenkant en de bodem efficiënter zijn dan dichtbij het midden van de plaat.

Contents

Symbols

Upper case

C_{ijkl}	Fourth-order elasticity tensor
U_0	Strain energy density function
C_{ij} $(i, j = 1, 2, 3, 4, 5, 6)$	Elastic stiffness elements
E_1, E_2, E_3	Young's (extension) modulus in the 1-, 2-, and 3-directions
G_{23}, G_{13}, G_{12}	Shear modulus in the 2-3, 3-1, and 1-2 planes of fiber-reinforced composites
E	Young's (extension) modulus of isotropic materials
G	Shear modulus of isotropic materials
B_i	Body force
S, C, F	Simply support, Clamped support and Free support, respectively
R	Mid-radius of panel
T	Change in temperature of a material
T_o	Temperature load
N_{ij}, M_{ij} $(ij = xx, yy, xy)$	Resultant forces and moments
Q_i $(i = x, y)$	Transverse shear forces

K_e, P_e	Kinetic energy, elastic potential energy
N_x , N_y	Mechanical plane forces
$\overline{V}$	Overall potential energy
Ω	Work done by the external forces
Z_m	Mid-radius of panel in third-order shear deformation theory
U, V, W	Displacement components of an arbitrary point within the shell domain in third-order shear deformation theory
P	Temperature-dependent material property
N_{ij}, M_{ij}, P_{ij} $(ij = xx, x\theta, \theta\theta)$	Conventional Stress resultants
Q_{ij}, R_{ij}, P_{ij} $(ij = xz, \theta z)$	Higher order Stress resultants
V_i , V_o	Volume fractions of two different orthotropic materials
V_{CN}^{*}	Whole volume fraction of nanotubes in nanocomposite
P_f	Effective material properties
V_f , V_m	Fiber and matrix volume fractions
V_c	Volume fraction of particulate phase
K_m , G_m	Bulk modulus and shear modulus of matrix phase
K_c , G_c	Bulk modulus and shear modulus of particulate phase
K	Effective local bulk modulus
$E_{\|\|}, E_{\perp}$	Elastic modulus parallel and normal to nanotubes
$V_r^{inclusion}, V_r^{m}$	Volumes of nanotubes dispersed in the inclusions and in the matrix, respectively

V_r	Total volume of the nanotubes in the representative volume element
K_{in} , K_{out}	Effective bulk modulus of inclusions and matrix, respectively
G_{in} , G_{out}	Effective shear modulus of inclusions and matrix, respectively
N, M	Number of grid points in radial and axial directions, respectively
$[S_{db}],[S_{dd}],[S_{bb}],[S_{bd}]$	Stiffness matrices
$[M]$	Mass matrix
$\{\hat{T}\}$	Thermal load vector
$\{U_d\}$	Domain degrees of freedom vector
$\{U_b\}$	Boundary degrees of freedom vector
$\{F_{Tb}\}$, $\{F_{Td}\}$	Thermal vectors
N_x	Number of grid points in axial direction
S	Mid-radius to thickness ratio
$\overline{\mathrm{T}}$	Non-dimensional temperature field
K_w	Non-dimensional Winkler elastic coefficient
K_g	Non-dimensional shear layer elastic coefficient
D_m	Flexural rigidity of plate
N_r , N_z	Number of grid points in the radial and thickness directions of annular sectoral plate
K_s	Non-dimensional shearing layer elastic coefficient of annular sectorial plate

Lower case

$\nabla \mathbf{u}$	Displacement gradient matrix
(x_1, x_2, x_3)	Principal material coordinates
a_i	Acceleration of a particle
r , θ , z	Radial, circumferential and axial coordinates in cylindrical coordinate system
(u_0, v_0, w_0)	Displacement components along the (x, y, z) coordinate directions of a point at mid-surface
(u_r, u_θ, u_z)	Radial, circumferential and axial displacement components, respectively
h	Thickness of structure
r_i , r_o	Inner and outer radius of panel
h_c , h_f	Thickness of the core and the face sheets
$u_r^{\,k}$, $u_\theta^{\,k}$, $u_z^{\,k}$	Displacement components in radial, circumferential and axial directions of *k*th layer
k_w	Winkler elastic coefficient of rectangular plate
k_g	Shear layer elastic coefficient of rectangular plate
(u, v, w)	Displacement components along the *x*, *y* and *z* axes, respectively
$\overline{r_i}, \overline{r_o}$	Inner and outer radius of annular sectorial plate
k_s	Shearing layer elastic coefficient of annular sectorial plate
q_θ, q_r, q_z	Components of the heat flux vector
k_i	Thermal conductivity
k'	Transverse shear correction coefficient

$(\overline{u},\overline{v},\overline{w})$	Displacement components along the *z*, θ and *x* axes, respectively, based on TSDT
p	Power law index for volume fraction profile
q	Power law index for fiber orientation profile
m_f	Mass fraction of nanotubes
a,b,c,d	Parameters of generalized power-law distribution for fiber orientation variation profile
s	Sigmoidal exponent
k, l, m, n, p	Hill's elastic moduli
k_r, m_r, n_r, l_r	Hill's elastic moduli for the reinforcing phase
m	Circumferential wave number
t	Time variable
c_{ij}, d_{ij}	First order weighting coefficients in radial and axial directions, respectively
$c_{ij}^{(2)}, d_{ij}^{(2)}$	Second order weighting coefficients in radial and axial directions, respectively
$\{q\}$	Mechanical load vector
q_0	Heat flux
h_a	Heat-transfer coefficient of ambient air
q	Static load
$\overline{u}_j$	Non-dimensional modal displacement

Greek letters

σ_{ij}	Stress tensor
ε_{kl}	Stain tensor

$\sigma_i \ \ (i, j = 1,...,6)$	Stress components in Voigt-Kelvin notation
$\varepsilon_j \ \ (i, j = 1,...,6)$	Strain components in Voigt-Kelvin notation
ν_{ij}	Poisson's ratio of fiber-reinforced composites
ν	Poisson's ratio of isotropic materials
(α, β, z)	General coordinate system
ϕ	Angle of a fiber with respect to α -axis in the $\alpha\beta$ -plane
ρ	Density
$\sigma_i \ (i = r, \theta, z)$	Normal stress components in cylindrical coordinate system
$\tau_{r\theta}$, τ_{zr} , $\tau_{z\theta}$	Shear stress components in cylindrical coordinate system
ψ_x , ψ_y	Rotational displacements about the *x* and *y* axes
$\gamma_{r\theta}$, γ_{zr} , $\gamma_{z\theta}$	Shear strain components in cylindrical coordinate system
$\varepsilon_i \ \ (i = r, \theta, z)$	Normal strain components in cylindrical coordinate system
Φ	Panel angle
$\sigma_i \ (i = x, y, z)$	Normal stress components in Cartesian coordinate system
τ_{yz} , τ_{xy} , τ_{xz}	Shear stress components in Cartesian coordinate system
Θ	Angle of annular sectorial plate
β_i	Thermal stress modulus
α_i	Thermal expansion coefficient
Ω	Work done by the external forces

η_r, η_z	Non-dimensional radial and axial components, respectively
ϕ_i, ϕ_o	Fiber orientation of two different orthotropic materials
ρ_f	Density of nanotubes
ρ_m	Density of matrix phase
γ_r	Radial volume fraction index
γ_z, γ_x	Axial volume fraction index
α_r , β_r	Radial power-law parameters
$\alpha_z, \beta_z, \alpha_x, \beta_x$	Axial power-law parameters
λ	Lame constant
η_i (i = 1, 2, 3)	Carbon nanotube efficiency parameter
μ, ξ	Agglomeration constants
ω	Natural frequency
δ_d, δ_b	Domain and boundary displacement vectors
$\overline{\sigma}_{ij}$	Non-dimensional stress component
Ω	Non-dimensional natural frequency
λ_{mn}	Non-dimensional natural frequency annular sectoral plate

Chapter 1

Introduction

1.1 Functionally graded materials

In the progress of science and technology, materials have played a crucial role. The scientific application of base materials into diverse inorganic and organic compounds has paved the way for developing the advanced polymers, engineering alloys, structural ceramics, etc. The structure of enhancement of advanced material is illustrated in Figure 1.1. Functionally graded materials (FGMs) are heterogeneous advanced composite materials consisting of two or more constituent phases with a continuously variable distribution [1,2]. The variations in the phase distribution may be reflected in their volume or weight fraction, orientation, and shape. In the vast majority of studies of FGMs in engineering, the researchers aim to achieve their goals with only one of these factors, i.e. the volume fraction being a typical variable. The variation of the volume fractions may be exclusively through the thickness of the structure and/or in any other direction, such as coordinates of a plate or shell. The mechanical properties such as Young's modulus of elasticity, Poisson's ratio, shear

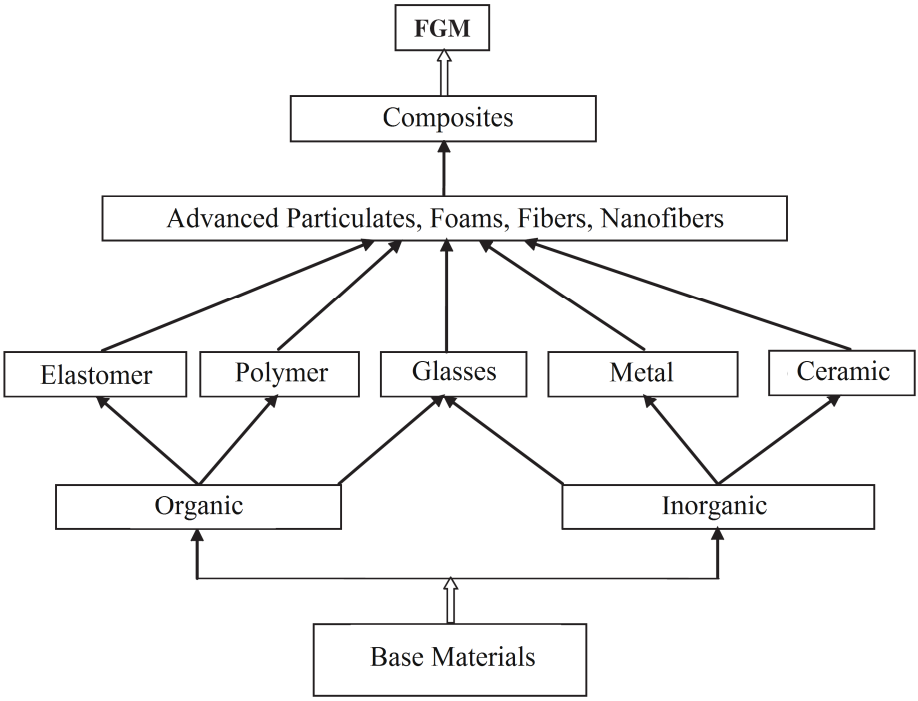

Figure 1.1. Illustration of advanced material hierarchy.

modulus of elasticity, material density, thermal conductivity, and thermal expansion coefficient vary smoothly and continuously in preferred directions in FGMs.

These materials possess numerous advantages over materials composed of similar constituents that make them appropriate in potential applications. Grading or tailoring the internal microstructure of a composite material or a structural component allows the designer to truly integrate both material and structural considerations into the final design and final product. This brings the entire structural design process to the material level in the purest sense, thereby increasing the number of possible material configurations for specific design applications.

Although the concept of FGMs, and our ability to fabricate them, appears to be a modern marvel of engineering innovation, the concept is not new. FGMs have been occurring in nature. Some natural examples have been included in Figure 1.2 for illustration. Bamboo is an excellent example. Bamboo stalks are optimized

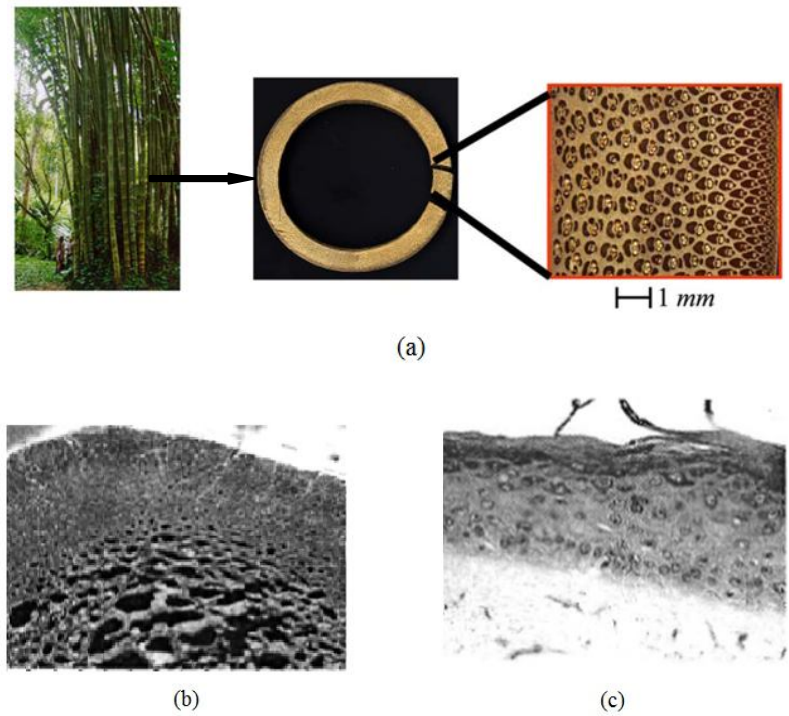

Figure 1.2. Some examples of FGMs in nature; a) Bamboo stalks and cross section of culm showing radial distribution of fibers through the thickness [3], b) Bone, and c) Human skin.

composite materials that naturally exploit the concept of FGMs, as shown in Figure 1.2a [3]. The bamboo culm is an approximately cylindrical shell that is divided periodically by transversal diaphragms at nodes. Between 20% and 30% of the cross-sectional area of the culm is made of longitudinal fibers that are nonuniformly distributed through the wall thickness, the concentration being most dense near the exterior. The orientation of these fibers makes bamboo an orthotropic material with high strength along fiber direction and low strength along its transverse direction [3]. Also, bones have functional grading, as depicted in Figure 1.2b. As shown in Figure 1.2c, even human skin is graded to provide certain toughness, tactile and elastic qualities as a function of skin depth and location on the body.

In the case of FGMs engineered by humans, the concept of FGMs was proposed in 1984 as an alternative to conventional thermal barrier ceramic coatings to overcome their well documented shortcomings, when Japanese scientists researched advanced materials for aerospace industry [4]. FGMs commonly involve two isotropic material phases including metal and ceramic. This type of FGMs is called FG isotropic materials. Constituents often include, but are not limited to, the engineering alloys of magnesium, tungsten, titanium, aluminium, copper, steel, etc. and the structural ceramics such as zirconia, alumina, silicon-carbide and tungsten-carbide. FG isotropic materials are usually associated with particulate composites where the volume fraction of particles varies in one or several directions. While particulate composite materials may be locally isotropic, they are also non-homogeneous due to spatial variations of volume fractions of the phases. An example of such material is shown in Figure 1.3 [5] where spherical or nearly spherical particles are embedded within an isotropic matrix. Besides, orthotropic FGMs that employ spatially variation of fiber volume fractions and/or fiber orientations can be used to provide certain performance characteristics [6]. In recent years, by increasing great interest in carbon nanotube-reinforced composites and urgent need to adjusting distribution of nanotubes in matrix phase, the concept of FGMs has been used in nanocomposites. Accordingly, in the following, incorporation of the concept of FGM in various problems mechanics, including thermo-elastic, static, and vibration analyses of plates and shells, is categorized as 1-D FG fiber-reinforced composites, 2-D FGMs composites and FG carbon nanotubes-reinforced composites.

1.1.1 1-D FG fiber-reinforced composites

Fibers of high strength and stiffness are greatly applied in lightweight structures. Continuous fibers embedded in a matrix, commonly referred to as a lamina or ply, constitute the laminated composites. The fiber-reinforced laminated composites have

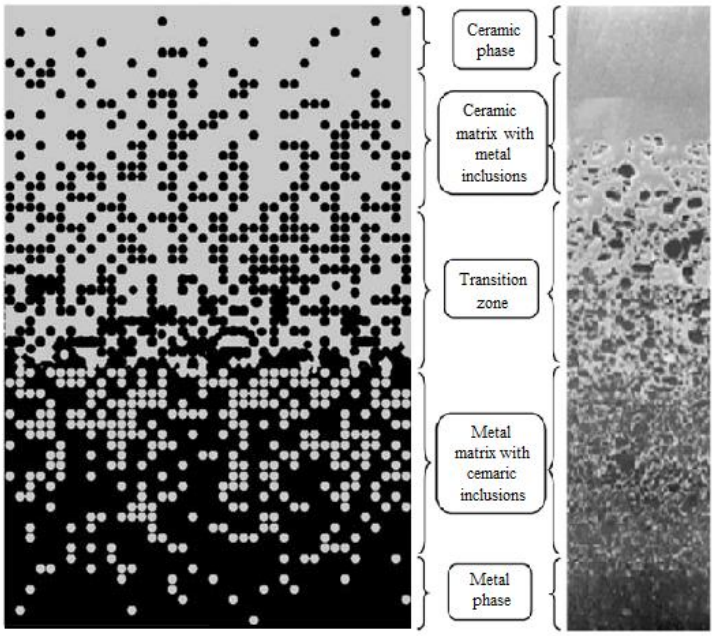

Figure 1.3. A particulate metal-ceramic FGM with the volume fractions of constituent phases graded in one vertical direction [5].

some problems, such as failure owing to delamination and other effects in the material formation, and also effects of transverse shear deformation because of the low ratio of transverse shear modulus to axial modulus [1]. For laminated composite structures, interlaminar stresses encompassing the normal and transverse shear stresses are the profound effects on the delamination phenomena. Such fiber-reinforced composite structures can be tailored to meet various in-plane stiffness or strength requirements by using the idea of FGMs, in which material properties vary smoothly and continuously through the thickness from one surface to another one. Herein, variation of material properties is referred to as gradation of fiber volume fractions and/or fiber orientations. In case of former, fiber volume fractions are graded in the thickness direction according to power law distribution. Arthur W. Leissa and his colleagues in Ohio State University [7-9] are pioneers to this study. The effect of the in-plane fiber volume fraction distribution on the mechanical properties of plates was fully studied by them. Their results show that the natural frequency and buckling load of a plate can be improved and increased by 21% and 38%, respectively with variable fiber spacing.

In case of FG fiber orientations, the fiber-reinforced composite has a continuously graded variation of the fiber orientations through the thickness from one surface to

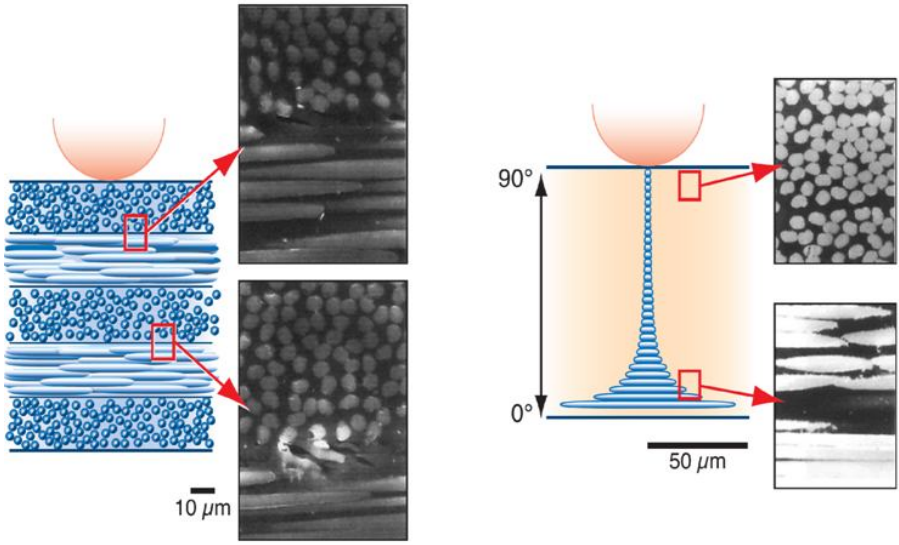

Figure 1.4. Effects of gradations in fiber orientation on indentation damage in laminated composites (a) Symmetric, cross-ply laminated composites with aligned carbon fibers. (b) Cross-sectional optical micrographs after indentation of functionally graded fiber orientation composite [10].

the other one. To provide better explanation of benefits of FG fiber orientations composites over discretely laminated composites, an interesting study is introduced in the following.

Jorgensen et al. [10] as a joint work between MIT and Technical University of Denmark demonstrated the advantage of fiber-reinforced composites with a through-thickness gradient in in-plane fiber orientation. Two kinds of plate were studied and manufactured. One was a so-called cross ply laminate comprising laminas with fiber direction 0° and 90°. The other type was a ply with a graded linear variation of fiber orientation through thickness between 0° and 90°. Results showed that gradients in elastic properties can suppress damage and cracking through redistributing peak stresses to regions beneath the indented surface. Laminated composites with cross-plies of carbon fiber reinforcements in an organic matrix generally developed cracks at interfaces between adjacent laminates, when subjected to indentation, as can be seen in Figure 1.4a. Symmetric cross-ply laminated composites with aligned carbon fibers in an epoxy matrix developed microcracks at interfaces when subjected to indentation, as shown in Figure 1.4a. In the diagram, layers with circular fibers (i.e., top, center, and bottom laminates) represent fibers oriented perpendicularly to the

plane of the figure. The second and fourth layers from the top denote fibers oriented within the plane of the figure. If the carbon fiber orientation was graded in small angular increments between adjacent laminates, these interfacial cracks were completely suppressed during indentation (Figure 1.4b). In Figure 1.4b, cross-sectional optical micrographs after indentation of the same fiber-reinforced composite where the fiber orientation is gradually changed from 0° to 90° is shown. All microcracking at interfaces is completely suppressed as a result of gradients in elastic modulus.

1.1.2 2-D FGMs composites

The high degree of operating temperature involved in several industrial machine elements, like combustion chambers, space shuttles, and ovens, needs effective high temperature resistant materials to progress the strength of such elements.
Steinberg [11] demonstrated the variations of the temperature at different places on the outer surface of the new aerospace craft when the plane is in sustained flight at a speed of Mach 8 and altitude of 29 km. The temperature on the outer surface of such a plane ranges from 1033 K along the top of the fuselage to 2066 K at the nose and from outer surface temperature to room temperature inside the plane. Such type of aerospace craft added a new challenge to develop more high temperature resistant materials that can tolerate high external temperatures which have variation in two or three directions. In 2003, the Columbia space shuttle was lost in a catastrophic

Figure 1.5. Wreckage of Columbia space shuttle in March 2003 at the Kennedy Space Center [12].

breakup due to outer surface insulation that fell loose when the Columbia lifted off. Collected wreckage of Columbia space shuttle is shown in Figure 1.5. The physical cause of the loss of Columbia and its crew was a breach in the thermal protection system on the leading edge of the left wing, caused by a piece of insulating foam. This breach in the thermal protection system allowed superheated air to penetrate through the leading edge insulation and progressively melt the aluminum structure of the left wing, resulting in a weakening of the Orbiter [12,13]. Such damage to the space shuttle's protective thermal tiles can be prevented by using FGMs. It is worth mentioning that a conventional FGM may also not be so effective in such design problems inasmuch as all outer surface of the body have the same composition distribution. This is because temperature distribution in such advanced machine elements change in two or three directions. Hence, if the FGM has two-dimensional dependent material properties, more effective high-temperature resistant material can be gained.

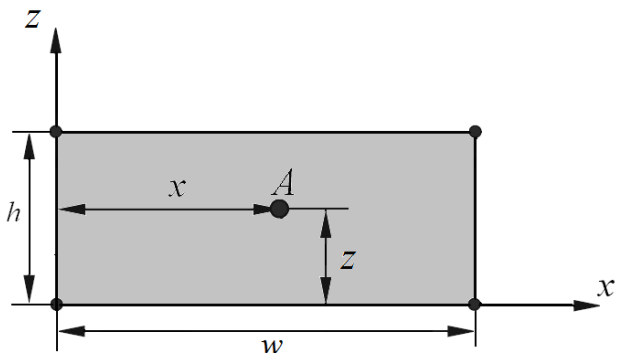

Figure 1.6. Geometrical parameters and coordinate system of the 2-D FGM plate.

What is more, tailoring material properties in two directions will provide the high capability to the designers to modify mechanical responses of structures composed of 2-D FGMs to a required manner. Based on such fact, a 2-D FGM, whose material properties are two-directional dependent, is introduced. In 2-D FGM, volume fractions of the constituents are varied through two-directional, and as a result, material phases are varied continuously in a predetermined composition profile. For further clarification, consider a two-phase (metal and ceramic) plate of width *w* and thickness *h* as shown in Figure 1.6. For any point on the 2-D FGM plate, the volume

fraction of ceramic phase is a continuous function of the coordinates, *x* and *z*, and varies in a predetermined composition profile. The profile is defined by using generalized power-law distribution that will be introduced in detail in Chapter 4. As shown in Figure 1.7, the volume fraction of ceramic phase has a continuous variation through the two directions.

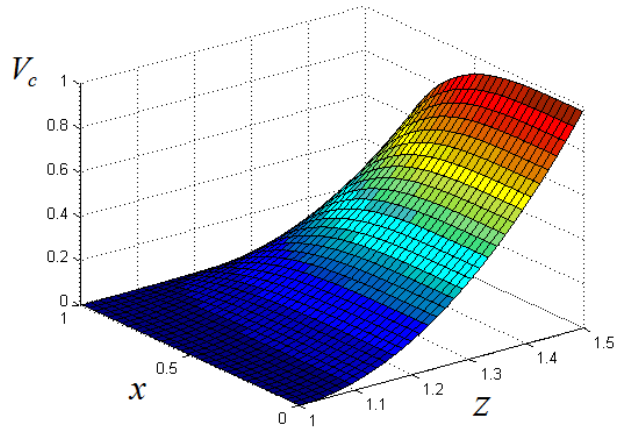

Figure 1.7. The variation of ceramic volume fraction in two directions

1.1.3 FG carbon nanotubes-reinforced composites

The discovery of carbon nanotubes (CNTs) by Iijima in 1991 [14] has generated a great and sustained interest in carbon based materials and nanotechnologies. CNTs have been widely accepted owing to their remarkable mechanical, electrical and thermal properties and the applications of CNTs are thus drawing much attention currently. The discovery of CNTs has led to a new way to improve the properties of resulting composites by changing reinforcement phases to nano-scaled fillers. A detailed summary of the mechanical properties of CNTs can be found in Salvetat and Rubio [15]. The exceptional mechanical properties of CNTs have shown great promise for a wide variety of applications, such as nanotransistors, nanofillers, semiconductors, hydrogen storage devices, structural materials, molecular sensors, field-emission-based displays and fuel cells, to name just a few [16]. The addition of nano-sized fibers or nanofillers, such as CNTs, can further increase the merits of polymer composites [17]. CNT-reinforced composites, easily processed due to the

small diameter of the CNTs, exhibit unique properties [18,19], such as enhanced modulus and tensile strength, high thermal stability and good environmental resistance. This behavior, combined with their low density, makes them suitable for a broad range of technological sectors, such as telecommunications, electronics [20] and transport industries, and in particular for aeronautic and aerospace applications, where the reduction of weight is crucial in order to reduce the fuel consumption. Several investigations have shown that the addition of small amounts of CNT can considerably improve the mechanical, electrical and thermal properties of polymeric composites. On the other hand, mechanical properties of CNT-reinforced composites will deteriorate if the volume fraction increases beyond certain limit [21]. Therefore, in the modeling of CNT-reinforced composites the concept of FGMs might be incorporated to effectively make use of the CNTs.

1.2 Application of FGMs

Generally FGMs offer great promise in applications where the operating conditions are severe, including spacecraft heat shields, fusion reactors, pressure vessels, biomedical implants, flywheels, and plasma facings for fusion reactors, etc. Various combinations of the ordinarily incompatible functions can be implemented to create new materials for aerospace, chemical plants, nuclear energy reactors, etc. As an example, in general, the highest temperature on the surface of space-planes is estimated to reach 2100 K [22]. Hence, materials at the surface must withstand temperatures as high as 2100 K and temperature differences of 1600 K. At high temperatures, metals and metal alloys appear to be very susceptible to oxidation, creep, and generally to loss of structural integrity. On the other hand, the disadvantage of ceramics has always been low strength and low toughness. Thus, a variety of metal/ceramic composites and ceramic thermal barrier coatings have been developed in an effort to take advantage of the respective favorable properties of these two major groups of materials. However, in such composites, to varying degrees, oxidation and low toughness are still a problem, while the drawbacks of ceramic coatings seem to be poor interfacial bonding, high residual and thermal stresses, low toughness, and consequent tendency towards cracking. Another alternative can be bonding a discrete ceramic layer to a metal layer. In this case, the abrupt transition in material properties across the interface between distinct materials can lead to large inter-laminar stresses and cause plastic deformation or cracking [23,24]. These harmful effects can be alleviated by FGMs to have a smooth spatial variation of material composition, with ceramic-rich material placed at the high temperature locations and metal-rich material placed at regions where mechanical properties, such as toughness, need to be high. Further, FGMs composed of a mixture of a ceramic and a metal with a continuously varying volume fraction is a common type of such materials, which can be easily manufactured in practice [25,26].

In engineering applications, although the initial research on FGMs was largely motivated by the practical applications of the concept in a wide variety of thermal shielding problems, materials with graded physical properties have almost unlimited potential in many other technological applications. In the following, some of the current engineering applications of FGMs can be found:

- ✓ The aerospace sector is one of the sectors that shows more interest on the developments of the FGM. NASA has shown crescent interest on the development of these technologies. As the costs for launching space shuttles depend on the weight they lift to the space, creating with less connection elements is a solution. Also, the optimum design, balancing weight and performance can reduce costs for launching. The heat shield of space shuttles can be optimized to reduce weight and increase reliability by using FGMs [27].
- ✓ One application involves the blast or ballistic protection for critical structure or armors for military applications [28,29].
- ✓ In microelectronics, metal-semiconductor FGM has been applied in actuators and transducers [30].
- ✓ High-performance cutting tools can be made of FGM. A design model for functionally graded ceramic tool materials with symmetrical composition distribution was developed by Zhao et al. [31] based on a deep understanding of the requirements of the cutting conditions of ceramic tools. The functionally graded ceramics exhibited higher retained strength under all thermal shock temperature differences compared to the homogeneous ceramics, indicating their higher thermal shock resistance.

Figure 1.8. Schematic view of FGM dental implant with graded material composition.

- ✓ Wide application can be also found in energy conversion, where heat exchangers, combustion systems and fusion reactors, solar energy generators can use FGM components [32].
- ✓ In biomedical area, graded bone and dental implants have shown better performance than monolithic implants [33]. Figure 1.8 presents a schematic of a functionally graded dental implant. The implant is made of hydroxyapatite (HAP), the principal component of bones and teeth, and titanium (Ti), one of the best biocompatible metals. The implant with a functionally graded structure in the longitudinal direction is designed to provide more titanium for the outer part where force is directly applied and more apatite for the inner part which is implanted inside the jaw bone [34]. The main advantages of using FGM dental implant are [35]: 1) reduction of stress effect on the surrounding bones that usually arises in the presence of fully metallic implants, 2) improvement of biocompatibility with bone tissues, 3) preventing the thermal-mechanical failure at the interface of HAP coated metallic implants, and 4) meeting the biomechanical requirements at each region of the bone, while enhance the bone remodeling, hereby maintaining the bone's health status.
- ✓ Filters with porosity gradient show improved efficiency over those with uniform porosity [36].
- ✓ Other applications include optical materials with piezoelectric and thermoelectric devices, vehicle and spaceflight structures [37].

1.3 Objectives of thesis

Taking theoretical numerically modelling and analysis of FGMs into account, this thesis presents the free vibration, static, and thermal analyses of plates and shells composed of FGMs. The specific contributions of the present thesis are as follows:

- 1-D and 2-D generalized power-law distribution for modelling gradation of material properties are introduced. Various material profiles in one or two directions can be illustrated using the generalized power-law distribution. Actually, using the generalized power-law distribution, it is possible to study the influence of the different kinds of material profiles including symmetric and classic on the mechanical responses of FGM structures. Furthermore, responses of the structure are modified to a required manner by selecting suitable different parameters of power-law distribution and volume fractions profiles.
- Some available literatures [38-40] for structures are based on the assumption that the material properties, such as Young's modulus, shear modulus and Poisson's ratio, have a specific variation in one direction. However, it is difficult to tailor the material moduli in practice. Since the designer can control the spatial variation of material composition (i.e., volume fraction and microstructure morphology) during the

fabrication of functionally graded materials but not the material moduli directly, therefore, we used the power-law distribution for variations of volume fractions. Moreover, the various micromechanics models, like Mori-Tanaka scheme, are used for estimating the homogenized material properties of composite materials.

- Most analyses available in the open literatures for FGM plates and shells are based on the assumption that the material properties have a specific variation in one direction. As mentioned earlier in section 1.1.2, a conventional FGM may also not be so effective in such design problems since all outer surface of the body will have the same composition distribution. In this thesis, we also study, for the first time, cylindrical panels with graded volume fractions in radial and axial directions.
- Noda [41] presented an extensive review that covers a wide range of topics, from thermoelastic to thermoinelastic problems. He discussed the effect of temperature-dependent mechanical properties on stresses and suggested that temperature-dependent properties of the material be taken into account to perform more accurate analysis. Therefore, realistic investigations of FGMs should be carried out considering the temperature-dependent properties. In general, the thermal conductivity of most materials has a strong dependence on the temperature which leads to a nonlinear differential equation for the temperature field. Accordingly, in this thesis, thermal analysis of FGMs with temperature-dependent properties is presented to provide more realistic study.
- In the present thesis, both 3-D elasticity and 2-D plate theories for FGM plates and shells are developed. 3-D elasticity solutions for plates and shells are useful since they provide benchmark results to assess the accuracy of various 2-D plate theories and finite element formulations. Because of complexity of solving of governing equations with variable coefficients due to variation material properties based on 3-D elasticity, a powerful numerical method is required. In this thesis, the generalized differential quadrature method (GDQM) approach is used to solve the governing equations of FGMs. The GDQM is found to be a simple and efficient numerical technique for structural analysis [42,43]. Better convergence behavior is observed by GDQM compared with its peer numerical competent techniques viz. the finite element method, the finite difference method, the boundary element method and the meshless technique [44]. The GDQM is effectively used in various problems in free vibration, static, and thermal analyses of FGM plates and shells and the fast rate of convergence of the method is demonstrated, and comparison studies are carried out to establish its very high accuracy and versatility.
- By using the concept of FGM in CNT-reinforced composites, free vibration and mechanical buckling of nanocomposites reinforced by various types of CNT is studied. For the first time, different forms of graded CNT dispersion in the matrix phase including aligned, randomly oriented, and agglomerated CNT are taken into

account. It will be shown that the desired stiffness of the structure can be achieved by properly adjusting the CNTs distribution through the thickness.

1.4 Thesis scopes and methodology

Following above mentioned objectives, in this thesis free vibration, static, and thermal analyses of FGM composite plates and shells are studied. To this end, firstly theoretical formulations of several FGM problems is performed and governing equations are derived. Then, mathematical modelling of FGMs is conducted. In this case, 1-D and 2-D generalized power-law distribution are introduced and discussed. In order to determine effective material properties in FG composites and nanocomposites, homogenization methods are taken into account. Afterwards, a semi-analytical method, GDQM, is adopted for solving coupled governing differential equations with variable coefficients. Eventually, numerical results and discussion are presented. For this purpose, the present thesis is organized as follows:

Chapter 2 is devoted to basic background and literature survey of FGMs. A brief description of composite materials and their macro-mechanical analysis are presented, followed by a general overview regarding shell and plate theories. As a general feature in this thesis, literature review of FGMs is summarized into three parts comprising 1-D FG fiber-reinforced composites, 2-D FGM composites, and FG CNT-reinforced composites.

Chapter 3 deals with theoretical formulations of various problems in free vibration, static, and thermal of FGMs composite plates and shells. Not only based on 3-D elasticity theory governing equations are derived, but also 2-D plate theories are used to formulate various problems.

Chapter 4 is dedicated to mathematical modeling of FGMs. For modelisation of volume fraction and fiber orientation, firstly, the classic form of power-law distribution was introduced. Afterwards, 1-D and 2-D generalized power-law distribution are presented and discussed for the first time in this thesis. To compute effective material properties of FG composites and nanocomposites, commonly used homogenization methods are presented.

Chapter 5 describes solution procedure for solving coupled governing differential equations with variable coefficients derived in the chapter 3. In the present methodology, GDQM as a semi-analytical approach is adopted to solve the governing equations. After brief introduction to GDQM, the method is applied to discretize the governing equations and boundary conditions of various problems in free vibration, static, thermal analyses of structures composed of FGMs.

Chapter 6 presents comprehensive new numerical results and discussion for several problems of FGMs summarized into three parts comprising 1-D FG fiber-reinforced composites, 2-D FGM composites, and FG CNT-reinforced composites.

Chapter 7 elaborates main conclusions of the thesis and makes suggestions for further extension of the present research.

Chapter 2

Background and literature review

2.1 Overview

In this chapter, to properly explain mechanics of FGMs, which are fundamentally composite materials, a short description of composite materials and its macro-mechanical analysis are introduced. Afterwards, a general overview regarding shell and plate theories is presented. Discussion will then be focused on state-of-the-art literature regarding 1-D FG fiber-reinforced composites. In order to give readers a comprehensive literature review of the variety of articles on responses of FGMs, firstly, important literature on the free vibration, static, and thermal stress analysis of FG isotropic composites are presented. Later on, a critical review of studies on FG fiber-reinforced composites will be provided. Afterwards, a comprehensive review on state-of-the-art literature specialized in 2-D FGM composites is carried out. In the next section, available literature focused on making use of the FGM concept in CNT-reinforced composites, termed as FG CNT-reinforced composites, is introduced and discussed. In section 2.5.4 main problems in sandwich structures are explained, and then the way of using the FGM concept to improve their performance is presented. Next available literature on FG sandwich structures is fully reviewed. In the end, a critical review on available papers concentrated on plates and shells resting on elastic foundations is performed.

2.2 Composite Materials

A composite material can be defined as a combination of two or more materials that results in better properties than those of the individual components used alone. In contrast to metallic alloys, each material retains its separate chemical, physical, and mechanical properties. The two constituents are a reinforcement and a matrix. The main advantages of composite materials are their high strength and stiffness, combined with low density, when compared with bulk materials, allowing for a weight reduction in the finished part. The reinforcing phase provides the strength and stiffness. In most cases, the reinforcement is harder, stronger, and stiffer than the matrix. The reinforcement is usually a fiber or a particulate. Particulate composites have dimensions that are approximately equal in all directions. They may be spherical, platelets, or any other regular or irregular geometry. Particulate composites tend to be much weaker and less stiff than continuous fiber composites, but they are usually much less expensive. A fiber has a length that is much greater than its diameter. The length-to-diameter ratio is known as the aspect ratio and can vary greatly. Continuous fibers have long aspect ratios, while discontinuous fibers have short aspect ratios. Continuous-fiber composites normally have a preferred orientation, while discontinuous fibers generally have a random orientation. As a

general rule, the smaller the diameter of the fiber, the higher its strength, but often the cost increases as the diameter becomes smaller. In addition, smaller-diameter high-strength fibers have greater flexibility and are more amenable to fabrication processes such as weaving or forming over radii. Typical fibers include glass, aramid, and carbon, which may be continuous or discontinuous. The continuous phase is the matrix, which is a polymer, metal, or ceramic. Polymers have low strength and stiffness, metals have intermediate strength and stiffness but high ductility, and ceramics have high strength and stiffness but are brittle. The matrix (continuous phase) performs several critical functions, including maintaining the fibers in the proper orientation and spacing and protecting them from abrasion and the environment. In polymer and metal matrix composites that form a strong bond between the fiber and the matrix, the matrix transmits loads from the matrix to the fibers through shear loading at the interface. In ceramic matrix composites, the objective is often to increase the toughness rather than the strength and stiffness; therefore, a low interfacial strength bond is desirable.

2.2.1 Macromechanical analysis of composite materials

The kinematic relations, mechanical and thermodynamic principles are applicable to any continuum irrespective of its physical constitution. Here, we consider equations characterizing the individual material and its reaction to applied loads. These equations are called the constitutive equations. In a composite material, the fibers may be oriented in an arbitrary manner. Depending on the arrangements of the fibers, the material may behave differently in different directions. According to their behavior, composites may be characterized as generally anisotropic, monoclinic, orthotropic, transversely isotropic, or isotropic. In the following, we also present the stress-strain relationships for these types of materials under linearly elastic conditions.

A material body is said to be homogeneous if the material properties are the same throughout the body i.e. independent of position. In a heterogeneous body, the material properties are a function of position. For example, a structure composed of several uniform thickness layers of different materials stacked on top of each other and bonded to each other is heterogeneous through the thickness. Another example of heterogeneous materials is functionally graded materials. An anisotropic body is one that has different values of a material property in different directions at a point; i.e., material properties are direction-dependent. An isotropic body is one for which every material property in all directions at a point is the same. An isotropic or anisotropic material can be nonhomogeneous or homogeneous.

2.2.1.1 Anisotropic Materials

When there are no symmetry planes with respect to the alignment of the fibers the material is referred to as generally anisotropic [45]. The generalized Hooke's law relating stresses to strains in the most general form for infinitesimal deformation (i.e. $|\nabla \mathbf{u}| << 1$) can be written as [45,46]:

$$\sigma_{ij} = C_{ijkl}\varepsilon_{kl} \tag{2.1}$$

where C_{ijkl} is a fourth-order elasticity tensor with 81 components, which include all the material parameters necessary to characterize the material. In the absence of body couples, the principle of conservation of angular momentum requires the stress tensor to be symmetric, $\sigma_{ij} = \sigma_{ji}$. Then it follows from (2.1) that C_{ijkl} must be symmetric in the first two subscripts. Hence the number of independent material stiffness components reduces to 54. Since the strain tensor is symmetric (by its definition), $\varepsilon_{ij} = \varepsilon_{ji}$, then C_{ijkl} must be symmetric in the last two subscripts as well, further reducing the number of independent material stiffness components to 36. If we also assume that the material is hyperelastic, i.e., there exists a strain energy density function $U_0(\varepsilon_{ij})$ such that [47]:

$$\sigma_{ij} = \frac{\partial U_0}{\partial \varepsilon_{ij}} = C_{ijkl}\varepsilon_{kl} \tag{2.2}$$

we have:

$$\frac{\partial^2 U_0}{\partial \varepsilon_{ij}\partial \varepsilon_{kl}} = C_{ijkl} \tag{2.3}$$

Since the order of differentiation is arbitrary, $\partial^2 U_0 / \partial \varepsilon_{ij}\partial \varepsilon_{kl} = \partial^2 U_0 / \partial \varepsilon_{kl}\partial \varepsilon_{ij}$, it follows that $C_{ijkl} = C_{klij}$. This reduces the number of independent material stiffness components to 21. To show this we express Eq. (2.1) in an alternate form using single subscript notation for stresses and strains and two subscript notations for the material stiffness coefficients:

$11 \to 1,\ 22 \to 2,\ 33 \to 3,\ 23 \to 4,\ 13 \to 5,\ 12 \to 6.$

The single subscript notation for stresses and strains is called the engineering notation or Voigt-Kelvin notation. Eq. (2.1) now takes the from

$$\sigma_i = C_{ij}\varepsilon_j \qquad i, j = 1,...,6 \tag{2.4}$$

In matrix notation, Eq. (2.4) can be written as:

$$\begin{bmatrix}\sigma_1\\ \sigma_2\\ \sigma_3\\ \sigma_4\\ \sigma_5\\ \sigma_6\end{bmatrix}=\begin{bmatrix}C_{11} & C_{12} & C_{13} & C_{14} & C_{15} & C_{16}\\ C_{21} & C_{22} & C_{23} & C_{24} & C_{25} & C_{26}\\ C_{31} & C_{23} & C_{33} & C_{34} & C_{35} & C_{36}\\ C_{41} & C_{42} & C_{43} & C_{44} & C_{45} & C_{46}\\ C_{51} & C_{52} & C_{53} & C_{54} & C_{55} & C_{56}\\ C_{61} & C_{62} & C_{63} & C_{64} & C_{65} & C_{66}\end{bmatrix}\begin{bmatrix}\varepsilon_1\\ \varepsilon_2\\ \varepsilon_3\\ \varepsilon_4\\ \varepsilon_5\\ \varepsilon_6\end{bmatrix} \tag{2.5}$$

Now the coefficients C_{ij} must be symmetric $(C_{ij}=C_{ji})$ by virtue of assumption that the material is hyperelastic. Hence, we have 21 independent stiffness coefficients for the most general elastic material, i.e., anisotropic material.

2.2.1.2 Monoclinic Materials

When the elastic coefficients at a point have the same value for every pair of coordinate systems which are the mirror images of each other with respect to a plane, the material is called a monoclinic material [47]. For example, let (x_1, x_2, x_3) and (x_1', x_2', x_3') be two coordinate systems, with the x_1, x_2 -plane parallel to the plane of symmetry. Choose x_3'-axis such that $x_3' = -x_3$ so that one system is the mirror image of the other. The definitions and sign conventions of the stress and strain components show that:

$$\sigma_{23}{}' = -\sigma_{23},\ \sigma_{31}{}' = -\sigma_{31},\ \varepsilon_{23}{}' = -\varepsilon_{23},\ \varepsilon_{31}{}' = -\varepsilon_{31} \tag{2.6}$$

or, in single-subscript notation:

$$\sigma_4{}' = -\sigma_4,\ \sigma_5{}' = -\sigma_5,\ \varepsilon_4{}' = -\varepsilon_4,\ \varepsilon_5{}' = -\varepsilon_5 \tag{2.7}$$

While all their independent stress and strain components remain unchanged in value by the change from one coordinate system to the other. Using the stress-strain relations of the generally anisotropic material, we can write:

$$\sigma_1' = C_{11}\varepsilon_1' + C_{12}\varepsilon_2' + C_{13}\varepsilon_3' + C_{14}\varepsilon_4' + C_{15}\varepsilon_5' + C_{16}\varepsilon_6' \tag{2.8}$$

$$\sigma_1 = C_{11}\varepsilon_1 + C_{12}\varepsilon_2 + C_{13}\varepsilon_3 - C_{14}\varepsilon_4 - C_{15}\varepsilon_5 + C_{16}\varepsilon_6 \tag{2.9}$$

But we also have

$$\sigma_1 = C_{11}\varepsilon_1 + C_{12}\varepsilon_2 + C_{13}\varepsilon_3 + C_{14}\varepsilon_4 + C_{15}\varepsilon_5 + C_{16}\varepsilon_6 \tag{2.10}$$

Note that elastic parameters C_{ij} are the same for two coordinate systems because they are the mirror images in the plane of symmetry. From the above two equations (subtract one from the other) we obtain:

$$C_{14}\varepsilon_4 + C_{15}\varepsilon_5 = 0 \qquad \text{for all values of } \varepsilon_4 \text{ and } \varepsilon_5 \tag{2.11}$$

The above equation holds only if $C_{14} = 0$ and $C_{15} = 0$. Similar discussion with the two alternative expressions of the remaining stress components yield $C_{24} = 0$ and $C_{25} = 0$; $C_{34} = 0$ and $C_{35} = 0$; $C_{46} = 0$ and $C_{56} = 0$. Thus out of 21 material parameters in stiffness matrix of the generally anisotropic material, we only have 21-8=13 independent parameters, as indicated below:

$$[C] = \begin{bmatrix} C_{11} & C_{12} & C_{13} & 0 & 0 & C_{16} \\ C_{12} & C_{22} & C_{23} & 0 & 0 & C_{26} \\ C_{13} & C_{23} & C_{33} & 0 & 0 & C_{36} \\ 0 & 0 & 0 & C_{44} & C_{45} & 0 \\ 0 & 0 & 0 & C_{45} & C_{55} & 0 \\ C_{16} & C_{26} & C_{36} & 0 & 0 & C_{66} \end{bmatrix} \tag{2.12}$$

and the stress-strain relations for a monoclinic material is as follows:

$$\begin{bmatrix} \sigma_1 \\ \sigma_2 \\ \sigma_3 \\ \sigma_4 \\ \sigma_5 \\ \sigma_6 \end{bmatrix} = \begin{bmatrix} C_{11} & C_{12} & C_{13} & 0 & 0 & C_{16} \\ C_{12} & C_{22} & C_{23} & 0 & 0 & C_{26} \\ C_{13} & C_{23} & C_{33} & 0 & 0 & C_{36} \\ 0 & 0 & 0 & C_{44} & C_{45} & 0 \\ 0 & 0 & 0 & C_{45} & C_{55} & 0 \\ C_{16} & C_{26} & C_{36} & 0 & 0 & C_{66} \end{bmatrix} \begin{bmatrix} \varepsilon_1 \\ \varepsilon_2 \\ \varepsilon_3 \\ \varepsilon_4 \\ \varepsilon_5 \\ \varepsilon_6 \end{bmatrix} \tag{2.13}$$

Note that monoclinic materials exhibit shear-extensional coupling; i.e. a shear strain can produce a normal stress; for example, $\sigma_{11} = C_{16}\varepsilon_6$. Therefore, the principal axes of stress do not coincide with those of strain.

2.2.1.3 Orthotropic Materials

When three mutually orthogonal planes of material symmetry exist, the number of elastic coefficients is reduced to 9 using arguments similar to those given for single material symmetry plane, and such materials are called orthotropic. The stress-strain relations for an orthotropic material take the form:

$$\begin{bmatrix}\sigma_1\\ \sigma_2\\ \sigma_3\\ \sigma_4\\ \sigma_5\\ \sigma_6\end{bmatrix}=\begin{bmatrix}C_{11} & C_{12} & C_{13} & 0 & 0 & 0\\ C_{12} & C_{22} & C_{23} & 0 & 0 & 0\\ C_{13} & C_{23} & C_{33} & 0 & 0 & 0\\ 0 & 0 & 0 & C_{44} & 0 & 0\\ 0 & 0 & 0 & 0 & C_{55} & 0\\ 0 & 0 & 0 & 0 & 0 & C_{66}\end{bmatrix}\begin{bmatrix}\varepsilon_1\\ \varepsilon_2\\ \varepsilon_3\\ \varepsilon_4\\ \varepsilon_5\\ \varepsilon_6\end{bmatrix} \tag{2.14}$$

where

$$C_{11}=E_1\frac{1-\nu_{23}\nu_{32}}{\Delta}, \qquad C_{12}=E_2\frac{\nu_{12}+\nu_{32}\nu_{13}}{\Delta}$$

$$C_{13}=E_1\frac{\nu_{31}+\nu_{21}\nu_{32}}{\Delta}, \qquad C_{23}=E_2\frac{\nu_{32}+\nu_{12}\nu_{31}}{\Delta}$$

$$C_{33}=E_3\frac{1-\nu_{12}\nu_{21}}{\Delta}, \qquad C_{22}=E_2\frac{1-\nu_{31}\nu_{13}}{\Delta}$$

$$C_{44}=G_{23}, \qquad C_{55}=G_{13}, \qquad C_{66}=G_{12}$$

$$\Delta=1-\nu_{12}\nu_{21}-\nu_{23}\nu_{32}-\nu_{31}\nu_{13}-2\nu_{21}\nu_{32}\nu_{13} \tag{2.15}$$

where

E_1, E_2, E_3 = Young's (extension) moduli in the 1-,2-, and 3- directions.

ν_{ij} = Poisson's ratio (extension-extension coupling coefficient), i.e., the negative ratio of the transverse strain in the *j*-direction to the strain in *i*-direction when stress is applied in the *i*-direction, i.e.,

$$\nu_{ij}=-\frac{\varepsilon_j}{\varepsilon_i}$$

For $\sigma_i=\sigma$ and all other stresses are zero.

G_{23}, G_{13}, G_{12} = shear moduli in the 2-3, 3-1, and 1-2 planes.

2.2.1.4 Isotropic materials

When there exist no preferred directions in the material (i.e. the material has infinite number of planes of material symmetry), the number of independent elastic coefficients reduces to 2. Such materials are called isotropic. For isotropic materials we have:

$$E_1 = E_2 = E_3 = E\,,\quad G_{12} = G_{13} = G_{12} = G\,,\quad \nu_{12} = \nu_{13} = \nu_{12} = \nu \tag{2.16}$$

Consequently, the stress-strain relations for an isotropic material take the form:

$$\begin{bmatrix}\sigma_1\\ \sigma_2\\ \sigma_3\\ \sigma_4\\ \sigma_5\\ \sigma_6\end{bmatrix} = \Lambda \begin{bmatrix} 1-\nu & \nu & \nu & 0 & 0 & 0\\ \nu & 1-\nu & \nu & 0 & 0 & 0\\ \nu & \nu & 1-\nu & 0 & 0 & 0\\ 0 & 0 & 0 & \frac{1}{2}(1-2\nu) & 0 & 0\\ 0 & 0 & 0 & 0 & \frac{1}{2}(1-2\nu) & 0\\ 0 & 0 & 0 & 0 & 0 & \frac{1}{2}(1-2\nu) \end{bmatrix} \begin{bmatrix}\varepsilon_1\\ \varepsilon_2\\ \varepsilon_3\\ \varepsilon_4\\ \varepsilon_5\\ \varepsilon_6\end{bmatrix} \tag{2.17}$$

where

$$\Lambda = \frac{E}{(1+\nu)(1-2\nu)} \tag{2.18}$$

2.2.1.5 Transformation of stresses and strains

The constitutive relations (2.13) for an orthotropic material were written in terms of the stress and strain components that are referred to a coordinate system that coincides with the principal material coordinate system. The coordinate system used in the problem formulation, in general, does not coincide with the principal material coordinate system. Further, FGM composite materials with graded fiber orientation behave like composite laminates consisting of several layers, each with different orientation of their material coordinates with respect to the laminate coordinates. Thus, there is a need to establish transformation relations among stresses and strains in one coordinate system to the corresponding quantities in other coordinate system. These relations can be used to transform constitutive equations from the material coordinates of each layer to the coordinates used in the problem description.

Let (α, β, z) denote the coordinate system used to write the governing equations of a fiber-reinforced composite material, and let (x_1, x_2, x_3) be the principal material

coordinates of the material such that x_3 – axis is parallel to the z -axis (i.e. the x_1x_2 -plane and the $\alpha\beta$ -plane are parallel) and the x_1 – axis is oriented at an angle of $+\phi$ counterclockwise (when looking down on the material) from the α -axis, as shown in Figure 2.1). The transformation of stresses (and strains) from the (x_1, x_2, x_3) coordinate to the (α, β, z) coordinate can be performed by [47]:

$$T = \begin{bmatrix} m^2 & n^2 & 0 & 0 & 0 & 2mn \\ n^2 & m^2 & 0 & 0 & 0 & -2mn \\ 0 & 0 & 1 & 0 & 0 & 0 \\ 0 & 0 & 0 & m & -n & 0 \\ 0 & 0 & 0 & n & m & 0 \\ -mn & mn & 0 & 0 & 0 & m^2 - n^2 \end{bmatrix} \tag{2.19}$$

where $m = \cos(\phi)$ and $n = \sin(\phi)$. Note that the inverse of the transformation matrix *T* can be found by replacing ϕ with $-\phi$.

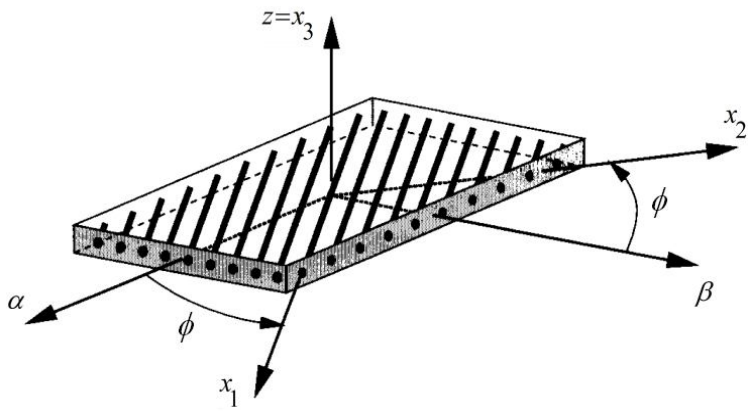

Figure 2.1. A lamina with material and coordinate system

The transformation from fiber coordinates 1 and 2 to global coordinate α and β can be done now as follows:

$$\begin{bmatrix}\sigma_\alpha\\ \sigma_\beta\\ \sigma_z\\ \sigma_{\beta z}\\ \sigma_{\alpha z}\\ \sigma_{\alpha\beta}\end{bmatrix} = T^{-1}\begin{bmatrix}\sigma_1\\ \sigma_2\\ \sigma_3\\ \sigma_4\\ \sigma_5\\ \sigma_6\end{bmatrix}, \qquad \begin{bmatrix}\varepsilon_\alpha\\ \varepsilon_\beta\\ \varepsilon_z\\ \gamma_{\beta z}\\ \gamma_{\alpha z}\\ \gamma_{\alpha\beta}\end{bmatrix} = T^{-1}\begin{bmatrix}\varepsilon_1\\ \varepsilon_2\\ \varepsilon_3\\ \varepsilon_4\\ \varepsilon_5\\ \varepsilon_6\end{bmatrix} \tag{2.20}$$

The material stiffness in global coordinate can be found as:

$$\left[\bar{C}\right] = [T][C][T]^T \tag{2.21}$$

where $[C]$ is the material stiffness of an orthotropic material. Performing the matrix multiplication in the above equation, the material stiffness $\bar{C}_{ij}$ can be written as

$$\bar{C}_{11} = C_{11}\cos^4\phi + 2(C_{12} + 2C_{66})\cos^2\phi\sin^2\phi + C_{22}\sin^4\phi$$

$$\bar{C}_{12} = (C_{11} + C_{22} - 4C_{66})\cos^2\phi\sin^2\phi + C_{12}(\cos^4\phi + \sin^4\phi)$$

$$\bar{C}_{13} = C_{13}\cos^2\phi + C_{23}\sin^2\phi$$

$$\bar{C}_{16} = (C_{11} - C_{12} - 2C_{66})\cos^3\phi\sin\phi + (C_{12} - C_{22} + 2C_{66})\cos\phi\sin^3\phi$$

$$\bar{C}_{22} = C_{11}\sin^4\phi + 2(C_{12} + 2C_{66})\cos^2\phi\sin^2\phi + C_{22}\cos^4\phi$$

$$\bar{C}_{23} = C_{23}\cos^2\phi + C_{13}\sin^2\phi$$

$$\bar{C}_{33} = C_{33}$$

$$\bar{C}_{26} = (C_{11} - C_{12} - 2C_{66})\cos\phi\sin^3\phi + (C_{12} - C_{22} + 2C_{66})\cos^3\phi\sin\phi$$

$$\bar{C}_{36} = (C_{13} - C_{23})\cos\phi\sin\phi$$

$$\bar{C}_{66} = (C_{11} + C_{22} - 2C_{12} - 2C_{66})\cos^2\phi\sin^2\phi + C_{66}(\cos^4\phi + \sin^4\phi)$$

$$\bar{C}_{44} = C_{44}\cos^2\phi + C_{55}\sin^2\phi$$

$$\bar{C}_{55} = C_{55}\cos^2\phi + C_{44}\sin^2\phi$$

$$\bar{C}_{45} = (C_{55} - C_{44})\cos\phi\sin\phi \tag{2.22}$$

2.3 3-D elasticity theory

The theory of elasticity is an elegant and fascinating subject that treats explicitly a special response of materials to applied forces, namely the elastic response, in which the stress at every point in a material body (continuum) depends at all times solely on the simultaneous deformation in the immediate neighborhood of the point [45]. If the relationship of the stress and the deformation is linear, the material is said to be linearly elastic, and the corresponding theory is called the linear theory of elasticity. Actually, the linear theory of elasticity deals with problems in which deformations, displacements, and rotations are "small". In 3-D elasticity theory, a shell is a three-dimensional body confined by two parallel (unless the thickness is varying) surfaces. In general, the distance between those surfaces is small compared with other shell parameters. The classical method of analysis in elasticity and thermoelasticity is to combine the equilibrium equations with the stress-strain and strain-displacement relations to derive the governing equations in term of the displacement components. This approach is called Navier method. The methods to solve the Navier equations are through either the potential function method, i.e. non-direct method, or direct method. The non-direct method is used for isotropic materials [48,49], as well as FGMs [50]. The non-direct method proposes the harmonic and biharmonic functions for temperature field or displacements which satisfy the Navier equation. The method, however, has some limitations. The main limitation of the potential function method is the ability to handle the general type of boundary conditions. Also, satisfying the mixed boundary conditions by the potential function method is a difficult mathematics problem. In this thesis, first the Navier equations are derived, and then non-direct method is proposed.

2.3.1 Equations of motion

In this section, we derive the 3-D elasticity equations of motion for any continuum in motion. The basic postulate is that each particle of the continuum must satisfy Newton's law of motion. Figure 2.2 shows the stress vectors that are acting on the six faces of a small rectangular element that is isolated from the continuum in the neighborhood of the position designated by x_i .

Let $\mathbf{B} = B_i\mathbf{e}_i$ be the body force (such as weight) per unit mass, ρ be the mass density at x_i and $\mathbf{a}$ the acceleration of a particle currently at the position x_i ; then Newton's law of motion takes the form, valid in rectangular Cartesian coordinate systems [51]:

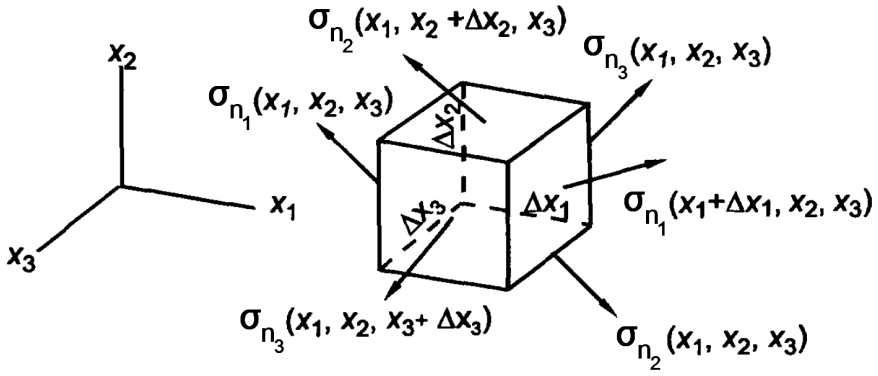

Figure 2.2. Stress vectors acting on the six faces of a small rectangular element [51].

$$\left(\frac{\boldsymbol{\sigma}_{\mathbf{e}_1}(x_1+\Delta x_1,x_2,x_3)-\boldsymbol{\sigma}_{\mathbf{e}_1}(x_1,x_2,x_3)}{\Delta x_1}\right)+\left(\frac{\boldsymbol{\sigma}_{\mathbf{e}_2}(x_1,x_2+\Delta x_2,x_3)-\boldsymbol{\sigma}_{\mathbf{e}_2}(x_1,x_2,x_3)}{\Delta x_1}\right)+$$
$$\left(\frac{\boldsymbol{\sigma}_{\mathbf{e}_3}(x_1,x_2,x_3+\Delta x_3)-\boldsymbol{\sigma}_{\mathbf{e}_3}(x_1,x_2,x_3)}{\Delta x_1}\right)\Delta x_1\Delta x_2\Delta x_3+\rho\mathbf{B}\Delta x_1\Delta x_2\Delta x_3=(\rho\mathbf{a})\Delta x_1\Delta x_2\Delta x_3 \tag{2.23}$$

Dividing by $\Delta x_1\Delta x_2\Delta x_3$ and letting $\Delta x_i \to 0$, we have:

$$\frac{\partial\boldsymbol{\sigma}_{\mathbf{e}_1}}{\partial x_1}+\frac{\partial\boldsymbol{\sigma}_{\mathbf{e}_2}}{\partial x_2}+\frac{\partial\boldsymbol{\sigma}_{\mathbf{e}_3}}{\partial x_3}+\rho\mathbf{B}=\rho\mathbf{a} \tag{2.24}$$

Since $\boldsymbol{\sigma}_{\mathbf{e}_i}=\boldsymbol{\sigma}\mathbf{e}_i=\sigma_{ji}\mathbf{e}_j$ [51], therefore we have (noting that all $\mathbf{e}_i$ are of fixed directions in Cartesian coordinates:

$$\frac{\partial\sigma_{ij}}{\partial x_j}\mathbf{e}_i+\rho B_i\mathbf{e}_i=\rho a_i\mathbf{e}_i \tag{2.25}$$

and in Cartesian component form:

$$\frac{\partial\sigma_{ij}}{\partial x_j}+\rho B_i=\rho a_i \tag{2.26}$$

and in cylindrical coordinates:

$$\frac{\partial\tau_{zr}}{\partial z}+\frac{1}{r}\frac{\partial\tau_{r\theta}}{\partial\theta}+\frac{\partial\sigma_r}{\partial r}+\frac{\sigma_r-\sigma_\theta}{r}+\rho B_r=\rho a_r \tag{2.27a}$$

$$\frac{\partial \tau_{\theta z}}{\partial z}+\frac{\partial \sigma_{\theta}}{r\partial \theta}+\frac{\partial \tau_{r\theta}}{\partial r}+\frac{2\tau_{r\theta}}{r}+\rho B_{\theta}=\rho a_{\theta} \tag{2.27b}$$

$$\frac{\partial \sigma_{z}}{\partial z}+\frac{\partial \tau_{z\theta}}{r\partial \theta}+\frac{\partial \tau_{rz}}{\partial r}+\frac{\tau_{rz}}{r}+\rho B_{z}=\rho a_{z} \tag{2.27c}$$

2.4 2-D plate theories

The 3-D elasticity theory is reduced to a 2-D theory using the assumption that the normal strains acting upon the plane parallel to the middle surface are negligible compared with other strain components. In 2-D theories, the displacements are expanded in terms of thickness. Many classical theories were originally developed for thin elastic plates and shells, and are based on the Love-Kirchhoff assumptions, which are [52]:

(1) Straight lines normal to the middle-surface remain straight and normal to the deformed middle surface.

(2) The transverse normals do not experience elongation.

(3) The transverse normals rotate such that they remain perpendicular to the mid-surface after deformation.

The first two assumptions imply that the transverse displacement is independent of the transverse (or thickness) coordinate and the transverse normal strain is zero. The third assumption leads to zero transverse shear strains. With these assumptions, the theory is known as the Kirchhoff plate theory or classical plate theory (CPT). To improve the situation, various refined theories including First-order Shear Deformation Theories (FSDT) and Higher-order Shear Deformation Theories (HSDT) have been developed. The FSDT is often called Mindlin theory. In the FSDT, the Love-Kirchhoff assumptions are relaxed by removing the third part; i.e. the transverse normals do not remain perpendicular to the mid-surface after deformation. This leads to including transverse shear strains in the theory. HSDT can represent the kinematics better and can yield accurate results, especially for thick plates and shells. However, they involve more computational effort. In HSDT, we relax the assumption on the straightness and normality of the transverse normals after deformation by expanding displacements. Among various HSDT, including the second-order shear deformation formulation of Whitney and Sun [53] and the Third-order Shear Deformation Theory (TSDT) of Lo et al. [54] with 11 unknowns, Kant [55] with six unknowns, Bhimaraddi and Stevens [56] with five unknowns and Hanna and Leissa [57] with four unknowns, the TSDT of Reddy [58] with five unknowns is the most widely adopted model in the study of shells, especially FGM ones, due to its high efficiency and simplicity. The displacement fields of CPT, FSDT, and TSDT are in the form:

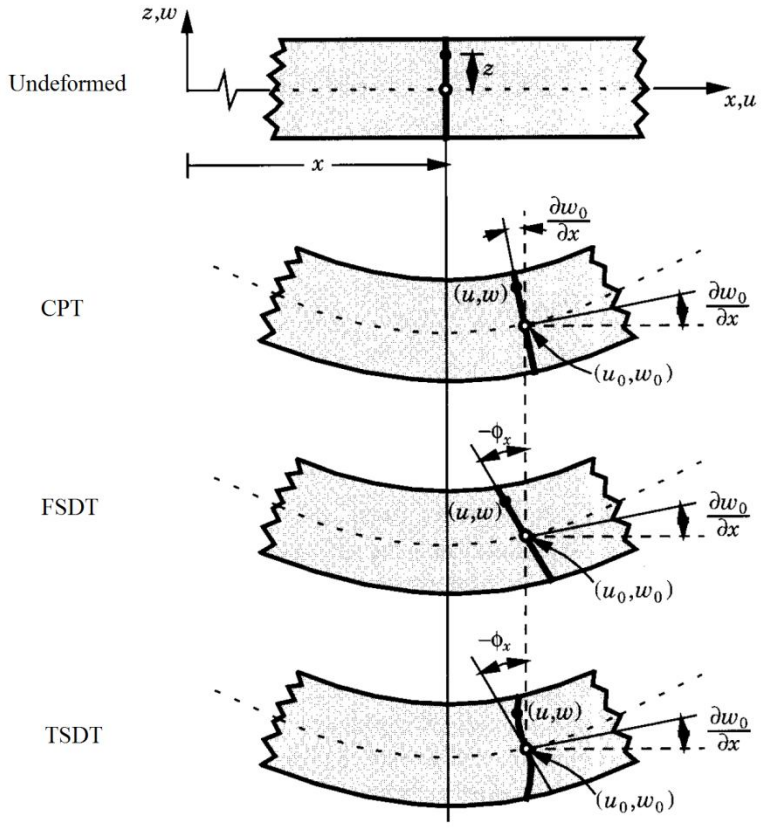

Figure 2.3. Deformation for the CPT, FSDT and TSDT [47].

CPT:

$$u(x,y,z,t) = u_0(x,y,t) + z\frac{\partial w_0}{\partial x}$$

$$v(x,y,z,t) = v_0(x,y,t) + z\frac{\partial w_0}{\partial y}$$

$$w(x,y,z,t) = w_0(x,y,t) \tag{2.28}$$

FSDT:

$$u(x,y,z,t) = u_0(x,y,t) + z\psi_x(x,y,t)$$

$$v(x,y,z,t) = v_0(x,y,t) + z\psi_y(x,y,t)$$

$$w(x,y,z,t) = w_0(x,y,t) \tag{2.29}$$

TSDT:

$$\begin{aligned} u(x,y,z,t) &= u_0 + z\psi_x + z^2\theta_x + z^3\lambda_x \\ v(x,y,z,t) &= v_0 + z\psi_y + z^2\theta_y + z^3\lambda_y \\ w(x,y,z,t) &= w_0 \end{aligned} \tag{2.30}$$

where (u_0, v_0, w_0) are the displacement components along the (x, y, z) coordinate directions, respectively, of a point on the mid-surface, and ψ_x and ψ_y are rotational displacements about the *x* and *y* axes at the middle surface of the plate, respectively, (θ_x, θ_y) and (λ_x, λ_y) are unknown functions to be determined. Figure 2.3 shows the kinematics of the deformation for the CPT, FSDT and TSDT.

2.5 Literature review

The literature review carried out here, is categorized according to classification of FGM concept in three categories, including FG fiber-reinforced composites, 2-D FGM composites, and FG CNT-reinforced composites. Furthermore, the following review provides a discussion of the more prevalent literature based on different types of analysis, elastic foundations, and FG sandwich structures.

2.5.1 1-D FG fiber-reinforced composites

In order to give readers a full literature review of the variety of studies on mechanical responses of FGMs, in each section, firstly, recent state-of-the-art literature on the free vibration, static, and thermal stress analyses of FG isotropic composites are introduced. Then, a critical review of the reported studies on FG fiber-reinforced composites will be provided. An effort will be made here, to include all important contributions in the current area of interest.

2.5.1.1 Free vibration and static analyses

An exact, three-dimensional method was developed by Chen et al. [59] to analyze the free vibration of a spherically isotropic hollow sphere made of a functionally graded material and filled with a compressible fluid medium. Based on the theory of elasticity, an exact free vibration solution of simply supported FGM sandwich cylindrical panel was presented by Alibeigloo and Liew [60]. They concluded that

for a FGM sandwich cylindrical panel higher mode of vibration is significantly affected by mid-radius to thickness ratio *S*, as shown in Figure 2.4. It is noted that *m* and *n* are axial and circumferential wave numbers, respectively. It is also observed that the influence of *S* on the first natural frequency of any mode for the thick panel is more significant than that for the moderately thick panel. It is concluded that the

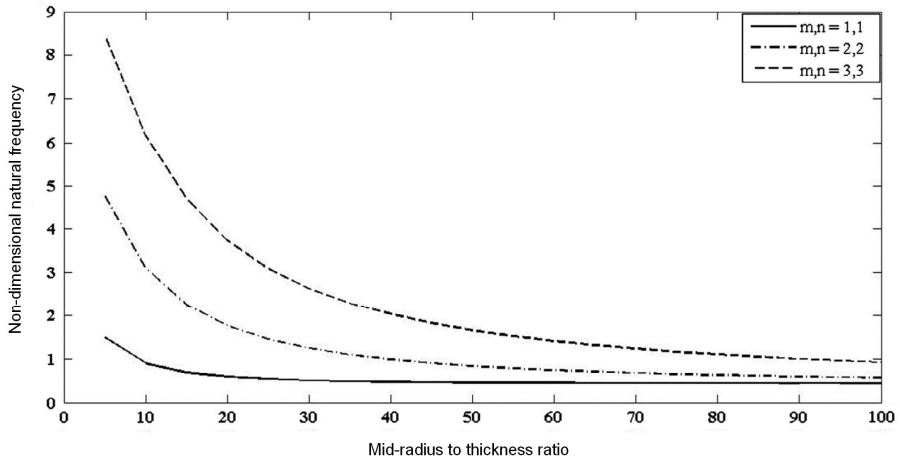

Figure 2.4. Effect of mid-radius to thickness ratio *S* on dimensionless first natural frequency of sandwich cylindrical FGM panel for various mode numbers [60].

variation of first natural frequency for the lower mode via *S*, contrary to the higher mode, can be neglected. A coupled technique, using the Fourier series expansion along the axial and circumferential directions and state space technique in the radial direction, was used to obtain the solution. Malekzadeh et al. [61] studied a three-dimensional free vibration analysis of the functionally graded truncated conical shells subjected to thermal environment. They used the differential quadrature method to solve the thermo-mechanical governing equations. Santos et al. [62] developed an axisymmetric finite element model to study the free vibrations of FGM cylindrical shells using the 3-D theory of elasticity. They reduced the 3-D equations of motion to 2-D representations by expanding the displacement field in terms of Fourier series for the circumferential variable. Qu and Meng [63,54] presented a novel semi-analytical method and its associated applications for linear vibration analyses of functionally graded bodies (either hollow or solid) of revolution with arbitrary boundary conditions. A modified variational principle combined with a multi-segment partitioning procedure was employed to formulate the theoretical model in the context of three-dimensional theory of elasticity. Three-dimensional free

vibration characteristic of thick circular/annular functionally graded plates with surface-bonded piezoelectric layers on the basis of 3-D Ritz solution was studied by Hosseini-Hashemi et al. [65]. Three displacement components along with electrical potential field of the plate were expressed by a set of Chebyshev polynomials multiplied by geometry boundary functions. The large amplitude vibration behavior of a shear deformable FGM cylindrical panel resting on elastic foundations in thermal environments was studied by Shen and Wang [66]. Two kinds of micromechanics models, namely, Voigt model and Mori–Tanaka model, are considered. Matsunaga [67] studied natural frequencies and buckling stresses of shallow shells made of functionally graded materials by taking into account the effects of transverse shear and normal deformations, and rotatory inertia. The modulus of elasticity of shells was assumed to vary according to a power law distribution in terms of the volume fractions of the constituents. Zhao et al. [68] investigated the static response and free vibration of FGM shells subjected to mechanical or thermo-mechanical loading based on Sander's first order shear deformation shell theory by using the element-free *kp*-Ritz method. Tornabene et al. [69] used generalized differential quadrature method to analyze the dynamic behavior of FGM conical, cylindrical shells and annular plates. One of the interesting results of their study is that as can be seen from Figure 2.5, natural frequencies of FGM panels fall between the natural frequencies of the limit cases of homogeneous shell panels of zirconia (p=0) and of aluminum (p=∞). It is interesting to note that the frequencies attain a minimum value for a shell made only of metal, due to the fact that aluminum has a much smaller Young's modulus that zirconia. In particular, it

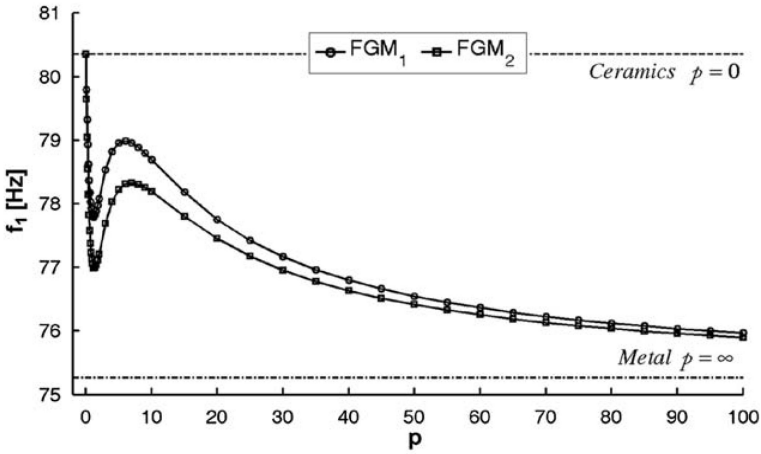

Figure 2.5. Influence of the power-law exponent p on the frequency characteristics of FGM conical panel [69].

can be noted that the most of frequencies exhibits a fast descending behavior from the ceramic limit case (p=0) varying the power-law index from p=0 to 1, while for values of p greater than unity frequencies increase until a maximum value. After this maximum, frequencies slowly decrease by increasing the power-law exponent p and tend to the metallic limit case (p=∞).

As aforementioned above, most of the studies regarding the FGM plate and shells are confined to isotropic material properties. By increasing interest towards using the concept of FGM in fiber-reinforced composites, in recent years some literature has been allocated to free vibration and static analyses of FG orthotropic (fiber-reinforced) materials, although they are few to number. Batra and Jin [70] studied natural frequencies of a functionally graded orthotropic material in which the gradation of material properties is achieved by varying the fiber orientation angle smoothly through the thickness. Nie and Batra [71] studied analytically static plane-strain deformations of functionally graded polar-orthotropic cylinders with elliptic inner and circular outer surfaces by employing the Fourier and the Frobenius series. Interlaminar stress distribution of composite laminated plates with functionally graded fiber volume fraction was studied by Fu et al. [72]. Classic state space method as well as differential quadrature state space method were utilized for different boundary and plied conditions. Numerical examples indicated that the non-uniform distribution of fibers rearranges the stress field, of which the in-plane stresses are sensitive to the fibers' distribution, while the transverse stresses are not affected so much. Vel [73] presented a 3-D elasticity solution for the vibration of FG cylindrical shells. Results were presented for two-constituent isotropic and fiber-reinforced composite materials. Shen and Zhang [74,75] studied the large amplitude vibration, non-linear bending and postbuckling of fiber reinforced composite laminated plates resting on an elastic foundation in hygrothermal environments. A two-step perturbation technique was employed to determine the non-linear to linear frequency ratios of plate vibration, the load-deflection and load-bending moment curves of plate bending, and postbuckling equilibrium paths of laminated plates. Li et al. [76] presented isogeometric analysis based on nonuniform rational B-splines (NURBS) for static and free vibration of laminated composite plates by using the TSDT. Due to the noninterpolatory nature of NURBS basis functions, a penalty method was applied to enforce the essential boundary conditions. A boundary layer theory for the nonlinear flexural vibration of anisotropic shear deformable laminated cylindrical shells was developed by Shen [77]. Two kinds of fiber reinforced composite laminated cylindrical shells, namely, uniformly distributed and FG reinforcements, were considered. The results showed that a FG reinforcement has a moderately effect on the linear and nonlinear vibration characteristics of shells. Naderi and Saidi [78] investigated static analysis of moderately thick composite beams, whose fiber orientation angle varies continuously through the thickness direction. Since

anisotropic beams have a monoclinic stiffness matrix form, the strain components, which are ignored for isotropic beams must be taken into account. To this end, a refined displacement field taking into account the entire shear strains was used.

2.5.1.2 Thermal stress analysis

Obata and Noda [79] carried out one-dimensional thermal stress analysis of a hollow circular cylinder and a hollow sphere made of functionally graded materials under a steady state condition using the perturbation method. Thermal stresses in a functionally graded cylindrical shell due to fluid have been found and reported by Takezono et al. [80]. They derived governing equations using the Sanders elastic shell theory and solved the equations with the help of the finite difference method. Tutuncu and Ozturk [81] obtained stress and displacement fields in functionally graded cylindrical and spherical structures subjected to internal pressure, using the theory of elasticity. Cheng and Batra [82] and Reddy and Cheng [83] have used the method of asymptotic expansion to study the three-dimensional thermoelastic deformations of functionally graded elliptic and rectangular plates, respectively. Vel and Batra [84, 85] have presented exact three-dimensional solutions for the steady-state and quasi-static transient thermoelastic response of functionally graded thick plates with an arbitrary variation of material properties in the thickness direction. Qian and Batra [86] have obtained results for the steady-state and transient thermoelastic response of functionally graded plates using the meshless local Petrov-Galerkin method that compare well with the exact solution of Vel and Batra [84,85]. Darabseh et al. [87] studied the transient thermoelastic response of a thick hollow cylinder made of functionally graded material under thermal loading. The generalized theory of thermoelasticity based on Green-Lindsay model was used. The thermal and mechanical properties of the functionally graded material were assumed to be varied in the radial direction according to a power law variation as a function of the volume fractions of the constituents. Ghosh and Kanoria [88] investigated thermoelastic displacements and stresses in a functionally graded spherically isotropic hollow sphere due to prescribed temperature in the context of the linear theory of generalized thermoelasticity with two relaxation time parameters. It was found that the variation of the thermophysical properties of a material as well as the thickness of the body strongly influence the response to loading. Theoretical treatment of transient thermoelastic problem involving an orthotropic functionally graded rectangular plate due to nonuniform heat supply were studied by Ootao and Tanigawa [89]. The thermal and thermoelastic constants of the rectangular plate were assumed to vary exponentially in the thickness direction. Based on the 3-D thermoelasticity theory, the thermoelastic analysis of laminated cylindrical panels with finite length and functionally graded layers subjected to three-dimensional

thermal loading were presented by Malekzadeh and Ghaedsharaf [90]. Thermal-mechanical behavior of functionally graded thick plates, with one pair of opposite edges simply supported, was investigated by Ying et al. [91] based on 3D thermoelasticity. As for the arbitrary boundary conditions, a semi-analytical solution was presented via a hybrid approach combining the state space method and the technique of differential quadrature. Analysis of thermoelastic characteristics of a thin circular functionally graded material rotating disk having a concentric hole and subjected to a thermal load was presented by Go et al. [92]. The Young's modulus, coefficient of thermal expansion, and density of the disk were assumed to vary exponentially in the radial direction only while the Poisson's ratio is assumed to be constant.

Based on the author's knowledge, available literature on the thermal analysis of FG fiber-reinforced composites is limited. Wang and Sudak [93] studied thermoelastic of a multi-layered cylindrical panel made of an oblique pile of functionally graded layers having orthotropic material properties. The influence of the gradation of the

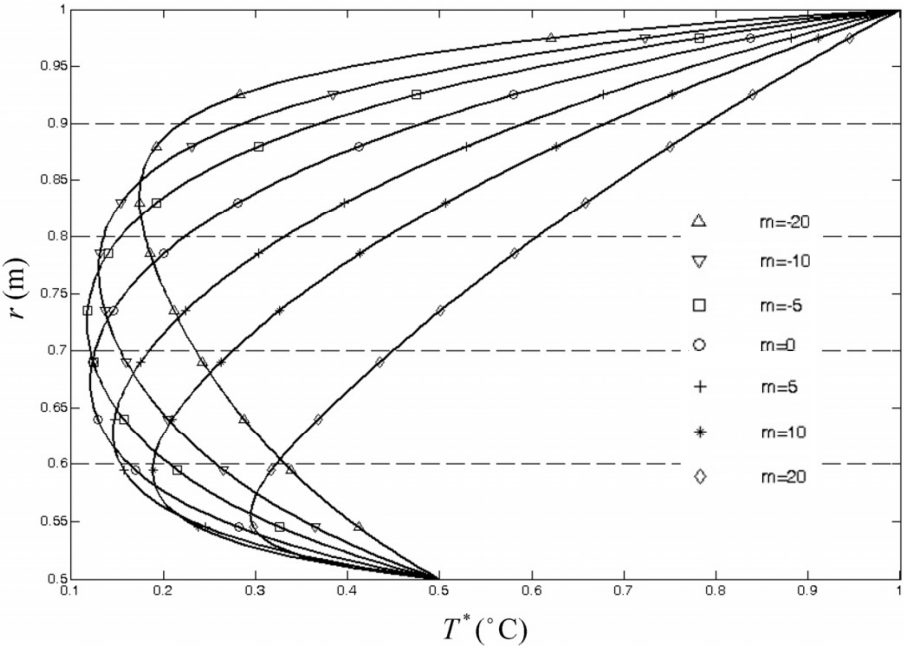

Figure 2.6. The temperature variations along the radial direction under different values of gradient parameter *m* [93].

material and ply angle on the distribution of temperature, displacements and stresses were investigated. As shown in Figure 2.6, it has been concluded that material gradation and ply angle significantly influence the elastic and temperature fields. Controlling thermal deformation by using composite materials having variable fiber volume fraction was studied by Bouremana et al. [94]. Continuous gradation of the fiber volume fraction in the FGM layer was modelled in the form of a *m*th power polynomial of the coordinate axis in thickness direction of the beam. The influence of volume fiber fraction distributions were studied to match or eliminate an in-plane expansion coefficient, or to match a desired axial stiffness. Pelletier and Vel [95] analyzed the steady-state response of a functionally graded thick cylindrical shell subjected to thermal and mechanical loads. The analytically obtained displacements and stresses were compared with those obtained using Flügge and Donnell shell theories for FG shells for a wide range of geometric parameters.

2.5.2 2-D FGM composites

Recently, many investigations on the 2-D FGM composites have been carried out. The thermal stresses in a two-directionally graded aerospace shuttles and crafts were later studied by Nemat-Alla [96] using a finite element model. The same technique was later applied by Hedia [97] for the stress analysis on backing shell of the cemented acetabular cup made of FGMs. He found that some critical stresses of concern for shells fabricated by unidirectional or 2-D FGMs were reduced by more than 50% compared with shells made of homogeneous materials. Further reduction of stresses was achieved using 2-D FGMs rather than unidirectional FGMs when designing cementless hip stems [98]. Sutradhar and Paulino [99] used the boundary element method to investigate the heat conduction problems of 2-D FGMs, while the Green functions were obtained by Chan et al. [100] for 2-D unbounded spaces with the shear modulus varying in two directions. Qian and Batra [101] made use of the meshless local Petrov-Galerkin (MLPG) method to obtain numerical solutions for static, free, and forced vibrations of a cantilever beam, for which material properties are power-law functions of the two coordinates. Nemat-Alla et al. [102] studied the elastic-plastic analysis of 2-D FGM under thermal loading. They showed that heat conductivity of the metallic constituents of FGM has great effect on the temperature distribution that resulting from the thermal loads.

It is worth noting that some literature on 2-D FGMs [103-108] has considered exponential functions for continuous gradation of the material properties, such as Young's modulus, shear modulus and Poisson's ratio. Nonetheless, it is difficult to tailor the material moduli in practice. It is because the designer can control the spatial variation of material composition (i.e., volume fraction and microstructure morphology) during the fabrication of functionally graded materials but not the

material moduli directly. A few researchers attempted to employ power-law distribution for variations of volume fractions in two directions. Aboudi et al. [109] proposed a higher-order micro-mechanical theory for thermoelastic/plastic problems of materials functionally graded in two directions. In their analysis, stiffness coefficients were computed directly from the micro-mechanical level rather than using the homogeneous elastic constants and geometric size. Cho and Ha [110] have optimized the volume fractions distributions of FGM for relaxing the effective thermal stress. They obtained the optimal volume fractions distribution in two directions for the FGM. The obtained optimum volume fractions have a random distribution, which is very difficult to represent or simulate as that of conventional FGM that have continuous variations of the composition. While FGM may serve as an excellent optimization and material tailoring tool, the ability to incorporate optimization techniques and solutions in practical design depend on the capacity to manufacture these materials to required specifications, and it may be difficult to achieve an optimized grading in FGM in practice. Nemat-Alla [96] introduced the concept of adding a third material constituent to the conventional FGM to withstand the induced sever thermal stresses. The rules of mixture for the introduced 2-D FGM were used to calculate the effective material properties of SiC/Al1100/Ti-6Al-4V 2-D FGM plate, with temperature-independent material properties. They found that it is possible to reduce the magnitude of thermal stresses by a proper management of the material properties in two directions. Asgari and Akhlaghi [112] investigated the transient thermal stresses in a 2-D FG thick hollow cylinder with finite length based on the classical thermoelasticity. The proposed 2-D FGM model was made of four distinct materials consisting of two distinct ceramics on the inner surface and two metals on the outer surface. The material properties at each point were obtained by using the linear rules of mixture. The same authors [113] studied the transient heat conduction in two-dimensional functionally graded hollow cylinder with finite length. For modelling and simulation of governing equations, finite element method with graded material properties within each element was used that had some advantages over the conventional finite element method.

In all aforementioned research works, the material properties at different positions within the 2-D FGM have been calculated using the rules of mixture. In addition, available power-law distributions for 2-D FGMs are not applicable to other homogenization schemes. Motivated by these ideas, in chapter 4, new 2-D power-law distributions, which are applicable to other homogenization methods, will be presented for variation of volume fractions in two directions. Various material profiles in radial and axial directions can be illustrated using the new 2-D power-law distribution.

2.5.3 FG CNT-reinforced composites

As discussed in section 1.1.3, in order to effectively make use of the CNTs, the concept of FGMs can be incorporated in CNT-reinforced composites. Shen [114] studied the nonlinear bending behavior of CNT-reinforced composites plates and

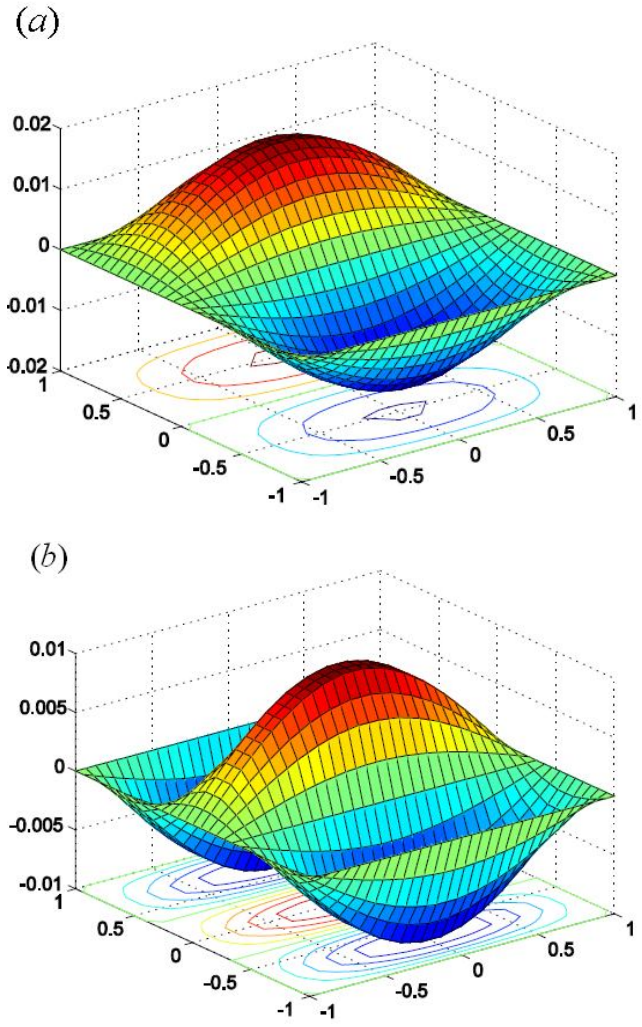

Figure 2.7. The vibration modes shape of an FG CNT-reinforced square plate, a) Second mode, b) Third mode [117].

found that the load-bending moment curves of the plates can be considerably improved through the use of a functionally graded distribution of CNTs in the matrix. Applying the idea of FGM to the nanocomposites, compressive postbuckling and thermal postbuckling strength of CNT-reinforced composites plates under a low nanotube volume fraction were studied by Shen et al. [115,116]. They found that in some cases the CNT-reinforced composites plate with intermediate CNT volume fraction does not have intermediate buckling temperature and initial thermal postbuckling strength. Zhu et al. [117] carried out bending and free vibration analyses of thin-to-moderately thick FG composite plates reinforced by single-walled CNT (SWCNTs) using the finite element method based on the first order shear deformation plate theory. Figure 2.7 gives the second and third mode shape of an FG CNT-reinforced square plate. They inferred that because the reinforcement only aligns in *x* direction, the mechanical properties of transverse direction (in *y* axis) of the plate are weaker and then the mode sequence is dissimilar to that for an isotropic plate. Wang and Shen [118] investigated nonlinear bending and vibration behavior of FG sandwich plate with CNT-reinforced composites face sheets by using multiscale approach and two-step perturbation technique. Based on three-dimensional theory of elasticity, Alibeigloo [119] discussed static analysis of functionally graded carbon nanotube reinforced composite plate imbedded in piezoelectric layers with three cases of CNT distribution. Lie et al. [120] presented free vibration analysis of functionally graded nanocomposite plates reinforced by SWCNTs using the element-free kp-Ritz method. It was concluded that reinforcements distributed close to top and bottom are more efficient than those distributed near the mid-plane for increasing the stiffness of FG CNT-reinforced plates. Axisymmetric natural frequencies of nanocomposite cylinders reinforced by straight single-walled carbon nanotubes were studied by Moradi et al [121] based on a mesh-free method. It was observed that the kind of distributions, aggregation or even randomly orientations of CNTs have significant effect on the effective stiffness and frequency parameter.

Yas and Heshmati [122] studied the vibrational properties of FG nanocomposite beams reinforced by SWCNTs under the action of moving load. They used the Eshelby-Mori-Tanaka approach based on an equivalent fiber to investigate the material properties of the beam. They used FEM to discretize the model and obtain a numerical approximation of the motion equation. Jam et al. [123] used the extended rule of mixture to show the effects of waviness and aspect ratio of CNT on the vibrational behavior of a nanocomposite cylindrical panel. They showed that the waviness has a significant effect on the natural frequency of this cylindrical panel.

2.5.4 Plates and shells resting on elastic foundations

Plates resting on elastic foundations have been widely adopted by many researchers to model interaction between elastic media and plates for various engineering problems such as reinforced-concrete pavements of highways, airport runways, foundation of storage tanks, and swimming pools together with foundation slabs of buildings, etc. In addition, cylindrical shells are usually laid on or placed in a soil medium as an elastic foundation, thus there is a great interest in analysis of the shells on elastic foundations. The underlying layers are modeled by a Winkler-type elastic foundation. The most serious deficiency of the Winkler foundation model is to have no interaction between the springs. The Winkler foundation model is fairly improved by adopting the Pasternak [124,125] foundation model, a two-parameter model, in which the shear stiffness of the foundation is considered. Despite the evident importance in practical applications, investigations on the plates and shell resting on elastic foundations are still limited in number. Cheng and Batra [126] used Reddy's third-order plate theory to study steady state vibrations and buckling of a simply supported functionally gradient isotropic polygonal plate resting on a Pasternak elastic foundation and subjected to uniform in-plane hydrostatic loads. An analytical solution for free vibration analysis of moderately thick FGM rectangular plates, resting on either Winkler or Pasternak elastic foundations, presented for all six possible combinations of boundary conditions by Hosseini-Hashemi et al. [127].

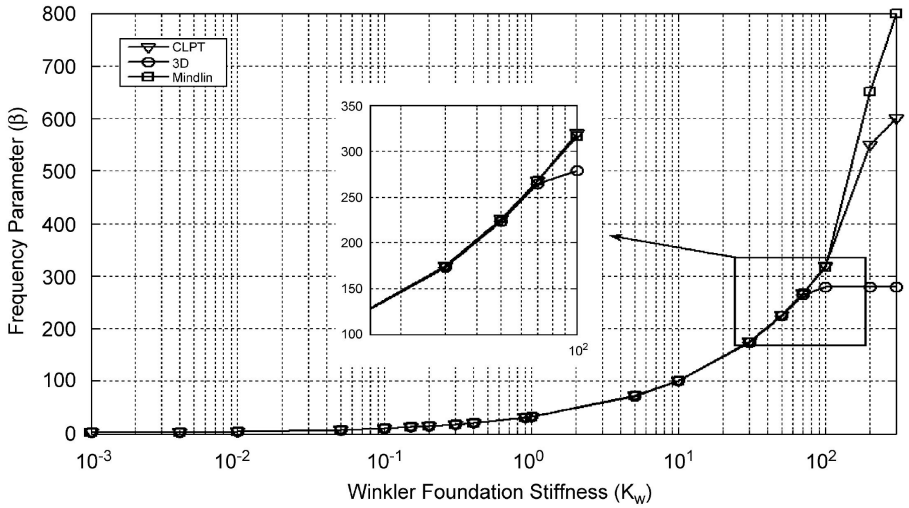

Figure 2.8. The frequency parameter versus the Winkler foundation stiffness K_w for a thin annular plate resting on elastic foundation [130].

Zenkour et al. [128] and [129] have employed the sinusoidal shear deformation plate theory to explain the bending behavior of FGM and fiber-reinforced viscoelastic structures resting on two-parameter elastic foundations. Based on the elasticity theory, a comprehensive study of the 3-D vibration analysis of annular plates resting on Pasternak elastic was studied by Hosseini-Hashemi et al. [130]. The validity and the range of applicability of the results obtained on the basis of the Mindlin and classical plate theories (CLPT) for annular plates with different values of the Winkler foundation stiffness was investigated. As depicted in Figure 2.8, unlike the 3-D results, the frequency parameters in the Mindlin and the CLPT diverged with increasing Winkler foundation stiffness K_w. In other words, as the Winkler foundation stiffness increased, the CLPT curve could follow the 3-D one better in comparison with the Mindlin results. They concluded that in the CLPT and Mindlin theory, the foundation was applied on the middle surface of the plate but not on the lower surface. That was why the Mindlin theory and CLPT gave incorrect results as the Winkler foundation stiffness takes large values. The free vibration of functionally graded rectangular plates resting on two-parameter elastic foundation was studied by Sheikholeslami and Saidi [131] using the higher-order shear and normal deformable plate theory of Batra and Vidoli by an analytical approach. Huang et al. [132] presented an exact three-dimensional elasticity solution for FGM thick plates resting on a Winkler–Pasternak elastic foundation, using the state space method.

The available literature on the shells, especially made of FGMs, resting on elastic foundations is sparse. Paliwal et al. [133,134] investigated the free vibration of whole buried cylindrical shells with simply supported ends in contact with Winkler and Pasternak foundations using direct solution to the governing classical shell theory equations of motion. Yang et al. [135] investigated the behavior of whole buried pipelines subjected to sinusoidal seismic waves by the finite element method. Cai et al. [136] investigated free vibration of a cylindrical panel supported on Kerr foundation. Kerr model can be reduced to either a Pasternak model or a Winkler one by selecting certain values of foundation parameters. Gunawan et al. [137] examined the free vibrations of cylindrical shells partially buried in elastic foundations based on the finite element method. Farid et al. [138] studied three-dimensional temperature dependent free vibration analysis of functionally graded material curved panels resting on two-parameter elastic foundation subjected to thermal environment. Shen [139] studied nonlinear thermal bending for a functionally graded cylindrical panel resting on an elastic foundation. The formulations were based on a higher order shear deformation shell theory with a von Kármán-type of kinematic nonlinearity and included shell panel-foundation interaction and the thermal effects. Shah et al. [140] performed the vibrations of functionally graded cylindrical shells based on the

Winkler and Pasternak foundations. A wave propagation approach was employed to solve the equations of motion of the shell involving the elastic foundation.

2.5.5 FG sandwich structures

Sandwich structures are used in a variety of engineering applications including aircraft, construction and transportation where strong, stiff and light structures are required [141]. Due to the mismatch of stiffness properties between the face sheets and the core, sandwich panels are susceptible to face sheet/core debonding, which is a major problem in sandwich construction, especially under impact loading [142]. Figure 2.9 shows damage in a sandwich laminated plate that was subjected to thermal shock [143]. One sees two types of cracks: cracking of the matrix material within a ply, and separation cracks (delaminations) at the boundary between plies. To increase the resistance of sandwich panels to this type of failure, the concept of a FGM is being actively explored in sandwich panel design.

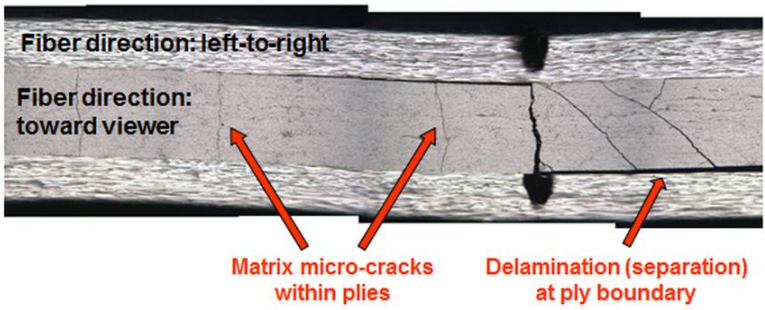

Figure 2.9. Damage in a sandwich laminated plate that was subjected to thermal [143].

Although there is several research work reported on general sandwich structures, studies related to FGM sandwich (FGSW) structures are few in numbers. Li et al. [144] studied the free vibration of FGSW rectangular plates with simply supported and clamped edges based on the three-dimensional linear theory of elasticity. They considered two common types of FGSW plates, namely the sandwich plate with FG face sheet and homogeneous core and the sandwich plate with homogeneous face sheet and FG core. They expanded the three displacement components of the plates by a series of Chebyshev. To investigate the effect of FGM core on performance of sandwich panels, Anderson [145] developed 3D elasticity solution for a sandwich

panel with orthotropic face sheets and an isotropic functionally graded core subjected to transverse loading. Exponential variation of the Young's modulus with respect to transverse direction was assumed. Xiang and Yang [146] presented the free and forced vibration of a laminated functionally graded Timoshenko beam of variable thickness, which consists of a homogeneous substrate and two inhomogeneous functionally graded layers, subjected to one-dimensional steady heat conduction in the thickness direction, employing the differential quadrature method. Zenkour [147,148] presented a two-dimensional solution to study the bending, buckling and free vibration of simply supported FG ceramic-metal sandwich plates. The sandwich plate faces assumed to have isotropic, two-constituent material distribution through the thickness, and the modulus of elasticity and Poisson's ratio of the faces assumed to vary according to a power law distribution in terms of the volume fractions of the constituents. Kashtalyan and Menshykova [149] presented a 3-D elasticity analysis of sandwich panels with a FG core subjected to transverse loading. Their analysis revealed that the use of a graded core instead of a conventional homogeneous one eliminates discontinuity of the in-plane normal and shear stresses across the face sheet-core interfaces, which contribute to the structural failure of the panel. Bhangale and Ganesan [150] studied buckling and vibration behavior of a FGSW beam having constrained viscoelastic layer in thermal environment using finite element formulation.

2.6 Summary and conclusions

This chapter has been devoted to basic useful background and literature survey of FGMs. In order to be familiar with constitutive modelling of FGM problems, which will be formulated in the next chapter, a short description of composite materials and their macro-mechanical analysis were provided. Besides, 3-D elasticity theory has been introduced, followed by an overview on the 2-D plate theories. This chapter aimed at providing the basic concepts of shell and plate theories whereas in the next chapter the basic assumptions will be taken to formulate state-of-the-art problems.

As a general feature in this thesis, literature review of FGMs has been summarized into three parts comprising 1-D FG fiber-reinforced composites, 2-D FGM composites, and FG CNT-reinforced composites. An effort was made to include all important contributions in the area of interest. By a comprehensive literature review, it has been shown that new studies on the mechanical responses 1-D FG fiber-reinforced composites are still required because of lack of prevalent literature. Motivated by these shortcomings, presenting detailed parametric studies on the free vibration, static, and thermal problems of 1-D FG fiber-reinforced composites is of this thesis's contributions. On the other hand, in case of mathematical modelling of

2-D FGM composites, generalized 2-D power-law distributions, which are applicable to different homogenization methods, is required that will be presented in chapter 4 for variation of volume fractions in two directions. In addition, no reposted study on the realistic investigation of thermal stress analysis of 2-D FGM composites with temperature-dependent properties was found. Regarding FG CNT-reinforced composites, available literature is very few to number. As a consequence, studies on mechanical responses of FG CNT-reinforced composites can undoubtedly contribute towards better understanding of structural responses of such composites. It can be concluded form the literature survey that most studies have been devoted into graded aligned CNTs dispersed in matrix phase. It can be of great interest to study other dispersion forms of CNTs including randomly orientation and agglomeration.

Chapter 3

Theoretical formulations

3.1 Overview

In this chapter, theoretical formulations of various problems in the mechanics of FGMs are presented. Based on types of theory, basic formulations are divided into two categories including 3-D elasticity and 2-D plate theories. Then, free vibration, static, and thermal stress analyses of FGMs based on 3-D elasticity theory will be formulated in section 3.2.1. Depending on the geometry of different structures composed of FGM, section 3.2.1 will be divided into several subsections, consisting of cylindrical panel, sandwich panel, rectangular plate, and annular sectorial plate. Eventually, the derivation of governing equations for free vibration, mechanical buckling, and thermal problems of FGMs based on 2-D theories will be explained.

3.2 3-D elasticity

The analysis of plate and shell structures based on 3-D elasticity theory become more complex if one or more of the several complicating effects, such as gradation of material properties (as seen in FGMs), are included. Including the effects of variation of material properties through one or two directions, which is necessary for most FGM composites, increases the complexity of governing equations with variable coefficients. This complexity rises by temperature-dependent material properties in thermal stress analysis, thereby causing the material properties to be function of both temperature and positions. In order to better elaborate the discussion, theoretical formulations based on elasticity theory is classified according to the type of analysis.

3.2.1 Free vibration and static analyses

In the following, we will formulate various problems in free vibration, static and thermal stress analyses of plates and shells composed of FGMs. In each problem, specific assumptions and structure are introduced so as to provide comprehensive studies on the analysis of FGMs. In order to better elaborate the study, this section is divided into following subsections depending on the type of geometries of the structure.

3.2.1.1 Cylindrical panel

We describe the geometry of an FG cylindrical panel a standard, global, cylindrical coordinate system, with coordinates r, θ and z denoting the radial, circumferential and axial coordinate directions, respectively, as depicted in Figure 3.1. Here, the general form of the problem for a panel with a smooth variation of fiber volume fractions, and/or in-plane fiber orientations, through the radial direction and variation of fiber volume fraction in the axial direction is defined and governing equations are

derived. In the general form, it is assumed that the panel is composed of monoclinic materials.

Strain-displacement relations in cylindrical coordinate are expressed as [45]:

$$\varepsilon_\theta = \frac{u_r}{r} + \frac{\partial u_\theta}{r\partial\theta} \;,\quad \varepsilon_r = \frac{\partial u_r}{\partial r} \;,\quad \varepsilon_z = \frac{\partial u_z}{\partial z} \;,\quad \gamma_{r\theta} = \frac{-u_\theta}{r} + \frac{\partial u_\theta}{\partial r} + \frac{\partial u_r}{r\partial\theta} \;,$$

$$\gamma_{zr} = \frac{\partial u_z}{\partial r} + \frac{\partial u_r}{\partial z}, \qquad \gamma_{z\theta} = \frac{\partial u_\theta}{\partial z} + \frac{\partial u_z}{r\partial\theta} \tag{3.1}$$

where u_r, u_θ and u_z are radial, circumferential and axial displacement components, respectively. Substitution of Eq. (3.1) into Eq. (2.13) in cylindrical coordinates and then into Eq. (2.27), the following equations of motion are obtained in terms of displacement components:

$$\frac{\partial C_{45}}{\partial z}(\frac{-u_\theta}{r} + \frac{\partial u_\theta}{\partial r} + \frac{\partial u_r}{r\partial\theta}) + C_{45}(-\frac{1}{r}\frac{\partial u_\theta}{\partial z} + \frac{\partial^2 u_\theta}{\partial r\partial z} + \frac{1}{r}\frac{\partial^2 u_r}{\partial\theta\partial z}) + \frac{\partial C_{55}}{\partial z}(\frac{\partial u_z}{\partial r} + \frac{\partial u_r}{\partial z})$$

$$+C_{55}(\frac{\partial^2 u_z}{\partial r\partial z} + \frac{\partial^2 u_r}{\partial z^2})C_{44} + \frac{1}{r}(-\frac{1}{r}\frac{\partial u_\theta}{\partial\theta} + \frac{\partial^2 u_\theta}{\partial r\partial\theta} + \frac{1}{r}\frac{\partial^2 u_r}{\partial\theta^2}) + C_{45}\frac{1}{r}(\frac{\partial^2 u_z}{\partial r\partial\theta} + \frac{\partial^2 u_r}{\partial\theta\partial z})$$

$$+\frac{\partial C_{13}}{\partial r}\frac{\partial u_z}{\partial z} + C_{13}\frac{\partial^2 u_z}{\partial r\partial z} + \frac{\partial C_{23}}{\partial r}(\frac{u_r}{r} + \frac{\partial u_\theta}{r\partial\theta}) + C_{23}\frac{1}{r}\frac{\partial^2 u_\theta}{\partial r\partial\theta} + \frac{\partial C_{36}}{\partial r}(\frac{\partial u_\theta}{\partial z} + \frac{\partial u_z}{r\partial\theta})$$

$$+C_{36}(\frac{\partial^2 u_\theta}{\partial r\partial z} + \frac{1}{r}\frac{\partial^2 u_z}{\partial r\partial\theta}) + C_{13}\frac{1}{r}\frac{\partial u_z}{\partial z} + C_{33}\frac{1}{r}\frac{\partial u_r}{\partial r} + C_{36}\frac{1}{r}\frac{\partial u_\theta}{\partial z} - C_{12}\frac{1}{r}\frac{\partial u_z}{\partial z}$$

$$-\bar{C}_{22}\frac{1}{r}(\frac{u_r}{r} + \frac{\partial u_\theta}{r\partial\theta}) - \frac{1}{r}C_{26}(\frac{\partial u_\theta}{\partial z} + \frac{\partial u_z}{r\partial\theta}) = \rho\frac{\partial^2 u_r}{\partial t^2} \tag{3.2}$$

$$C_{16}\frac{\partial u_z}{\partial z} + C_{26}(\frac{u_r}{r} + \frac{\partial u_\theta}{r\partial\theta}) + C_{36}\frac{\partial u_r}{\partial r} + C_{66}(\frac{\partial u_\theta}{\partial z} + \frac{\partial u_z}{r\partial\theta}) + \frac{\partial C_{16}}{\partial z}\frac{\partial u_z}{\partial z} + C_{16}\frac{\partial^2 u_z}{\partial z^2}$$

$$+\frac{\partial C_{26}}{\partial z}(\frac{u_r}{r} + \frac{\partial u_\theta}{r\partial\theta}) + C_{26}\frac{1}{r}(\frac{\partial u_r}{\partial z} + \frac{\partial^2 u_\theta}{\partial\theta\partial z}) + \frac{\partial C_{36}}{\partial z}\frac{\partial^2 u_r}{\partial r\partial z} + \frac{\partial C_{66}}{\partial z}(\frac{\partial u_\theta}{\partial z} + \frac{1}{r}\frac{\partial u_z}{\partial\theta})$$

$$+C_{66}(\frac{\partial^2 u_\theta}{\partial z^2} + \frac{1}{r}\frac{\partial^2 u_z}{\partial z\partial\theta}) + C_{12}\frac{\partial u_z}{\partial z} + \bar{C}_{22}(\frac{u_r}{r} + \frac{\partial u_\theta}{r\partial\theta}) + C_{23}\frac{\partial u_r}{\partial r} + C_{26}(\frac{\partial u_\theta}{\partial z} + \frac{\partial u_z}{r\partial\theta})$$

$$+C_{12}\frac{1}{r}\frac{\partial^2 u_z}{\partial\theta\partial z} + \bar{C}_{22}\frac{1}{r^2}(\frac{\partial u_r}{\partial\theta} + \frac{\partial^2 u_\theta}{\partial\theta^2}) + C_{23}\frac{1}{r}\frac{\partial^2 u_r}{\partial r\partial\theta} + C_{26}\frac{1}{r}(\frac{\partial^2 u_\theta}{\partial\theta\partial z} + \frac{1}{r}\frac{\partial^2 u_z}{\partial\theta^2})$$

$$+\frac{\partial C_{44}}{\partial r}\left(\frac{-u_\theta}{r}+\frac{\partial u_\theta}{\partial r}+\frac{\partial u_r}{r\partial\theta}\right)+C_{44}\left(\frac{\partial^2 u_\theta}{\partial r^2}+\frac{1}{r}\frac{\partial^2 u_r}{\partial r\partial\theta}\right)+C_{44}\left(\frac{-u_\theta}{r^2}+\frac{1}{r}\frac{\partial u_\theta}{\partial r}+\frac{1}{r^2}\frac{\partial u_r}{\partial\theta}\right)$$

$$+C_{45}\frac{2}{r}\left(\frac{\partial u_z}{\partial r}+\frac{\partial u_r}{\partial z}\right)=\rho\frac{\partial^2 u_\theta}{\partial t^2} \tag{3.3}$$

$$\frac{\partial C_{11}}{\partial z}\frac{\partial u_z}{\partial z}+C_{11}\frac{\partial^2 u_z}{\partial z^2}+\frac{\partial C_{12}}{\partial z}\left(\frac{u_r}{r}+\frac{\partial u_\theta}{r\partial\theta}\right)+C_{12}\left(\frac{1}{r}\frac{\partial u_r}{\partial z}+\frac{\partial^2 u_\theta}{r\partial\theta\partial z}\right)+\frac{\partial C_{13}}{\partial z}\frac{\partial u_r}{\partial r}+C_{13}\frac{\partial^2 u_r}{\partial r\partial z}$$

$$+\frac{\partial C_{16}}{\partial z}\left(\frac{\partial u_\theta}{\partial z}+\frac{\partial u_z}{r\partial\theta}\right)+C_{16}\left(\frac{\partial^2 u_\theta}{\partial z^2}+\frac{\partial^2 u_z}{r\partial\theta\partial z}\right)+C_{16}\frac{1}{r}\frac{\partial^2 u_z}{\partial\theta\partial z}+C_{26}\frac{1}{r^2}\frac{\partial^2 u_r}{\partial\theta^2}+C_{36}\frac{1}{r}\frac{\partial^2 u_r}{\partial r\partial\theta}$$

$$+C_{66}\frac{1}{r}\left(\frac{\partial^2 u_\theta}{\partial\theta\partial z}+\frac{1}{r}\frac{\partial^2 u_z}{\partial\theta^2}\right)+C_{45}\left(\frac{-u_\theta}{r}+\frac{\partial u_\theta}{\partial r}+\frac{1}{r}\frac{\partial u_r}{\partial\theta}\right)+C_{55}\left(\frac{\partial u_z}{\partial r}+\frac{\partial u_r}{\partial z}\right)$$

$$+\frac{\partial C_{45}}{\partial r}\left(\frac{-u_\theta}{r}+\frac{\partial u_\theta}{\partial r}+\frac{\partial u_r}{r\partial\theta}\right)+\frac{\partial C_{55}}{\partial r}\left(\frac{\partial u_z}{\partial r}+\frac{\partial u_r}{\partial z}\right)+C_{55}\left(\frac{\partial^2 u_z}{\partial r^2}+\frac{\partial^2 u_r}{\partial r\partial z}\right)$$

$$+C_{55}\frac{1}{r}\left(\frac{\partial u_z}{\partial r}+\frac{\partial u_r}{\partial z}\right)+C_{45}\left(\frac{\partial^2 u_\theta}{\partial r^2}+\frac{1}{r}\frac{\partial^2 u_r}{\partial r\partial\theta}\right)=\rho\frac{\partial^2 u_z}{\partial t^2} \tag{3.4}$$

Eqs. (3-2) to (3.4) can be written in a matrix form as:

$$\begin{bmatrix} K_{1r} & K_{1\theta} & K_{1z} \\ K_{2r} & K_{2\theta} & K_{2z} \\ K_{3r} & K_{3\theta} & K_{3z} \end{bmatrix} \begin{Bmatrix} u_r \\ u_\theta \\ u_z \end{Bmatrix} = \rho \begin{Bmatrix} \ddot{u}_r \\ \ddot{u}_\theta \\ \ddot{u}_z \end{Bmatrix} \tag{3.5}$$

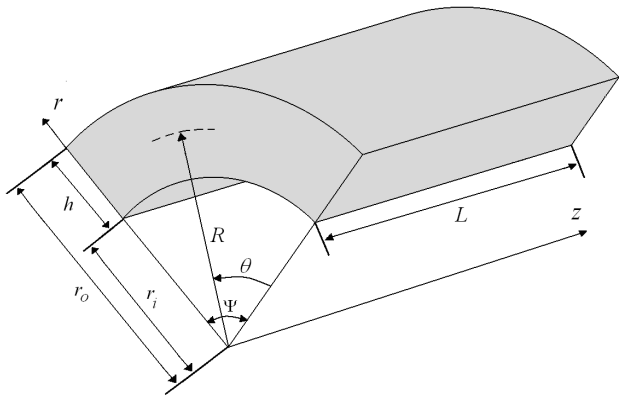

Figure 3.1. Geometry of a cylindrical panel.

Eqs. (3-2) to (3.4) are the governing equations for a finite cylindrical panel with monoclinic materials or with FG fiber orientation materials. It is because when there is a smooth variation in fiber orientation from the inner surface to the outer surface, in each point through the radial direction, we have a fiber oriented by different angle with the axial direction. In case of panel with graded volume fraction of fibers, elements of C_{16}, C_{26}, C_{36}, and C_{45} in Eqs. (3-2) to (3.4) are equal to zero for an orthotropic material.

The outer and inner surfaces of the cylindrical panel in the state of free vibration are tractions free as:

$$\sigma_r = \tau_{rx} = \tau_{r\theta} = 0, \quad \text{at} \quad r = r_i \quad \text{and} \quad r_o \tag{3.6}$$

Surface boundary conditions in the state of static loading are:

$$\sigma_r = \tau_{rz} = \tau_{r\theta} = 0 \qquad \text{at} \qquad r = r_i \tag{3.7}$$

$$\tau_{rz} = \tau_{r\theta} = 0 \qquad \sigma_r = q, \qquad \text{at} \qquad r = r_o \tag{3.8}$$

The following boundary conditions for Simply (S) support, Clamped (C) support and Free (F) at the $z = 0, L$ edges are assumed:

$$\text{S}: \quad u_r = u_\theta = \sigma_z = 0$$

$$\text{C}: \quad u_r = u_\theta = u_z = 0$$

$$\text{F}: \quad \sigma_z = \sigma_{z\theta} = \sigma_{rz} = 0 \tag{3.9}$$

3.2.1.2 Sandwich panel

Consider an FG Sandwich (FGSW) panel using a global, cylindrical coordinate system, with coordinates r, θ and z denoting the radial, circumferential and axial coordinate directions, respectively, as depicted in Figure 3.2. The core has thickness h_c, and the face sheets have thickness h_f. The constitutive relations for the *k*th layer of the FGSW panel can be written according to Eq. (2.13) for a monoclinic material. The face sheets are assumed to be perfectly bonded to the core, so the continuity conditions to be enforced at any arbitrary interior *k*th interface can be written as:

$$\sigma_r^{\,k} = \sigma_r^{\,k+1} \qquad \tau_{r\theta}^{\,k} = \tau_{r\theta}^{\,k+1} \qquad \tau_{rz}^{\,k} = \tau_{rz}^{\,k+1}$$

$$u_r^{\,k} = u_r^{\,k+1} \qquad u_\theta^{\,k} = u_\theta^{\,k+1} \qquad u_z^{\,k} = u_z^{\,k+1} \tag{3.10}$$

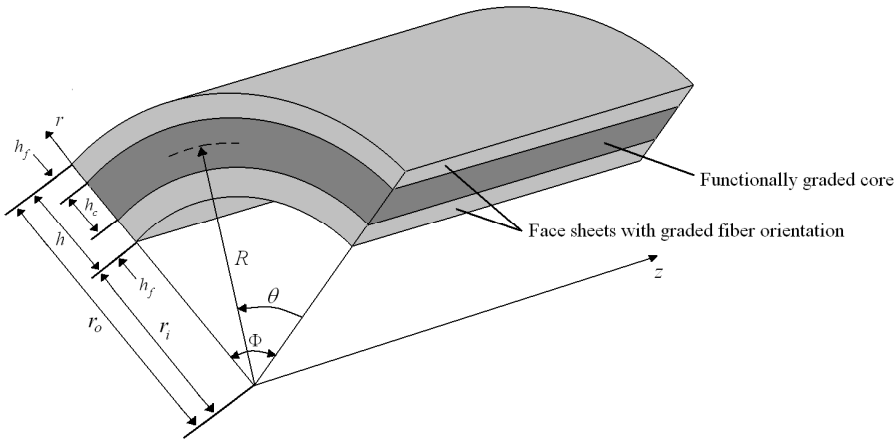

Figure 3.2. Geometry and coordinates of the FGSW panel.

3.2.1.3 Rectangular plate

Consider a functionally graded plate rested on two-parameter elastic foundations as shown in Figure 3.3. A Cartesian coordinate system (*x,y,z*) is used to label the material point of the plate in the unstressed reference configuration. The lower surface is continuously in contact with an elastic medium that acts as an elastic foundation represented by the Winkler/Pasternak model with radial stiffness k_w and shear stiffness k_g. The Pasternak model is used to describe the reaction of the elastic foundation on the thick simply supported plate. The plate has continuous grading of volume fraction of fiber reinforcement in the thickness direction.

The infinitesimal strain tensor is related to the displacements in Cartesian coordinate as follows:

$$\varepsilon_z = \frac{\partial w}{\partial z}, \quad \varepsilon_y = \frac{\partial v}{\partial y}, \quad \varepsilon_x = \frac{\partial u}{\partial x}, \quad \gamma_{xy} = \frac{\partial v}{\partial x} + \frac{\partial u}{\partial y},$$

$$\gamma_{xz} = \frac{\partial w}{\partial x} + \frac{\partial u}{\partial z}, \quad \gamma_{yz} = \frac{\partial v}{\partial z} + \frac{\partial w}{\partial y}, \tag{3.11}$$

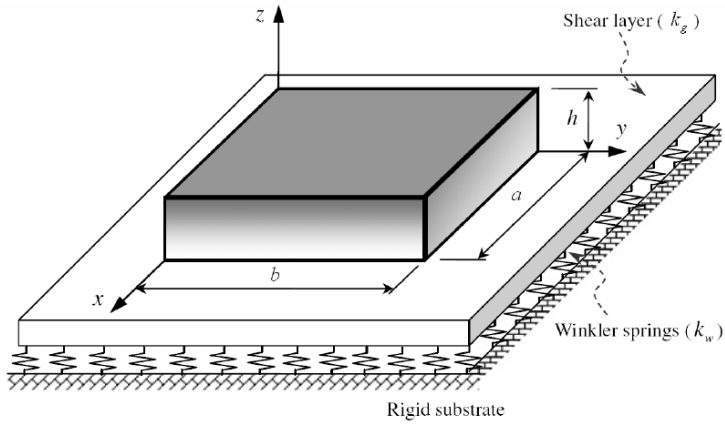

Figure 3.3. A plate resting on elastic foundation.

where u, v and w are displacement components along the *x*, *y* and *z* axes respectively. Substitution of Eq. (3.11) into (2.14) in Cartesian coordinates and then into Eq. (2.26), the following equations of motion as matrix form are obtained in terms of displacement components:

$$C_{11}\frac{\partial^2 u}{\partial x^2}+C_{12}\frac{\partial^2 v}{\partial x\partial y}+C_{13}\frac{\partial^2 w}{\partial x\partial z}+C_{66}\frac{\partial^2 u}{\partial y^2}+C_{66}\frac{\partial^2 v}{\partial x\partial y}+\frac{\partial C_{55}}{\partial z}\frac{\partial w}{\partial x}$$
$$+C_{55}\frac{\partial^2 w}{\partial x\partial z}+\frac{\partial C_{55}}{\partial z}\frac{\partial u}{\partial z}+\bar{C}_{55}\frac{\partial^2 u}{\partial z^2}=\rho\frac{\partial^2 u}{\partial t^2}, \tag{3.12}$$

$$C_{66}\frac{\partial^2 u}{\partial x\partial y}+C_{66}\frac{\partial^2 v}{\partial x^2}+C_{12}\frac{\partial^2 u}{\partial x\partial y}+C_{22}\frac{\partial^2 v}{\partial y^2}+C_{23}\frac{\partial^2 w}{\partial y\partial z}+\frac{\partial C_{44}}{\partial z}\frac{\partial v}{\partial z}$$
$$+C_{44}\frac{\partial^2 v}{\partial z^2}+\frac{\partial C_{44}}{\partial z}\frac{\partial w}{\partial y}+C_{44}\frac{\partial^2 w}{\partial y\partial z}=\rho\frac{\partial^2 v}{\partial t^2}, \tag{3.13}$$

$$C_{55}\frac{\partial^2 w}{\partial x^2}+C_{55}\frac{\partial^2 u}{\partial x\partial z}+C_{44}\frac{\partial^2 v}{\partial y\partial z}+C_{44}\frac{\partial^2 w}{\partial y^2}+\frac{\partial C_{13}}{\partial z}\frac{\partial u}{\partial x}+C_{13}\frac{\partial^2 u}{\partial x\partial z}$$
$$+\frac{\partial C_{23}}{\partial z}\frac{\partial v}{\partial y}+C_{23}\frac{\partial^2 v}{\partial y\partial z}+\frac{\partial C_{33}}{\partial z}\frac{\partial w}{\partial z}+C_{33}\frac{\partial^2 w}{\partial z^2}=\rho\frac{\partial^2 w}{\partial t^2}, \tag{3.14}$$

Above equations in a matrix form can be organized as:

$$\begin{bmatrix} L_{1x} & L_{1y} & L_{1z} \\ L_{2x} & L_{2y} & L_{2z} \\ L_{3x} & L_{3y} & L_{3z} \end{bmatrix} \begin{Bmatrix} u \\ v \\ w \end{Bmatrix} = \rho \begin{Bmatrix} \ddot{u} \\ \ddot{v} \\ \ddot{w} \end{Bmatrix} \tag{3.15}$$

The following simply supported conditions are imposed at the edges of the plate:

$$u = w = \sigma_y = 0 \quad \text{at} \quad x = 0, a \quad \text{and} \quad y = 0, b \tag{3.16}$$

Moreover the lower and upper surfaces of the plate are traction free:

$$\tau_{zx} = \tau_{zy} = 0 \quad \text{and} \quad \sigma_z = k_w w - k_g \Delta w \quad \text{at} \quad z = 0$$

$$\sigma_z = \tau_{zx} = \tau_{zy} = 0 \quad \text{at} \quad z = h \tag{3.17}$$

Where k_w and k_g are the Winkler and shearing layer elastic coefficients of the foundations.

3.2.1.4 Annular sectorial plates

Consider a annular sectorial plate having inner radius r_i, outer radius r_o, and thickness h resting on a Pasternak elastic foundation, as shown in Figure. 3.8. The bottom surface is continuously in contact with an elastic medium that acts as an elastic foundation represented by the Winkler/Pasternak model with Winkler elastic coefficient k_w and shearing layer elastic coefficient k_s. To deal with a plate with

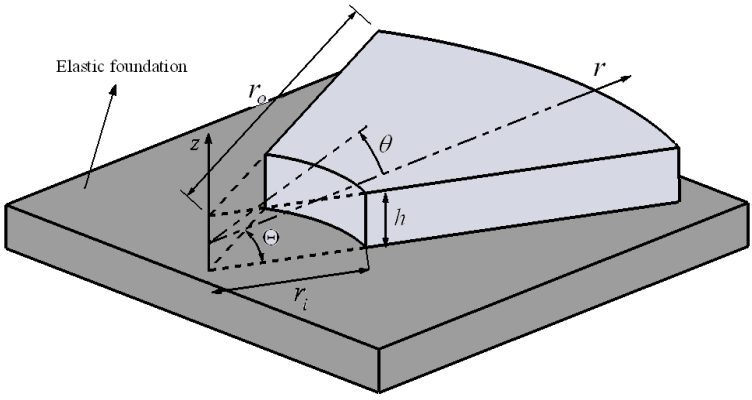

Figure 3.4. Geometry of an annular sectorial plate resting on an elastic foundation.

3-D flexibility, we use cylindrical polar coordinate to describe the geometry of the plate. An annular sectorial plate in cylindrical polar coordinate system (r,θ,z) is shown in Figure 3.4 with the displacement components u_r , u_θ , u_z at a generic point in the radial, circumferential and thickness directions.
The related boundary conditions at the lower and upper surfaces of the annular sectorial plate are as follows:

$$\begin{aligned} &\tau_{zr}=\tau_{z\theta}=0, \quad \sigma_z=k_w u_z-k_s\nabla^2 u_z && \text{at} && z=0 \\ &\sigma_z=\tau_{zr}=\tau_{z\theta}=0 && \text{at} && z=h \end{aligned} \tag{3.18}$$

where $\nabla^2(*)=\partial^2(*)\big/\partial r^2+(1\big/r)(*)\big/\partial r+(1\big/r^2)\,\partial^2(*)\big/\partial\theta^2$.

3.2.2 Thermal stress analysis

Most materials tend to expand if their temperature increases and, to a first approximation, the expansion is proportional to the temperature change. If the expansion is unrestrained, all dimensions will expand equally. Notice that no shear strains are induced in unrestrained thermal expansion, so that a body which is heated to a uniformly higher temperature will get larger, but will retain the same shape. The mechanical constitutive relations for a cylindrical panel, shown in Figure 3.1, composed of orthotropic material are as follows [47]:

$$\begin{Bmatrix}\sigma_z\\ \sigma_\theta\\ \sigma_r\\ \tau_{r\theta}\\ \tau_{zr}\\ \tau_{z\theta}\end{Bmatrix}=\begin{bmatrix}C_{11}&C_{12}&C_{13}&0&0&0\\ C_{12}&C_{22}&C_{23}&0&0&0\\ C_{13}&C_{23}&C_{33}&0&0&0\\ 0&0&0&C_{44}&0&0\\ 0&0&0&0&C_{55}&0\\ 0&0&0&0&0&C_{66}\end{bmatrix}\begin{Bmatrix}\varepsilon_z\\ \varepsilon_\theta\\ \varepsilon_r\\ \gamma_{r\theta}\\ \gamma_{zr}\\ \gamma_{z\theta}\end{Bmatrix}-\begin{bmatrix}\beta_1\\ \beta_2\\ \beta_3\\ 0\\ 0\\ 0\end{bmatrix}T \tag{3.19}$$

Where C_{ij} are elastic stiffnesses and β_i are the stresses moduli that are related to the thermal expansion coefficients α_i as follows:

$$\begin{Bmatrix}\beta_1\\ \beta_2\\ \beta_3\end{Bmatrix}=\begin{Bmatrix}C_{11}\alpha_1+C_{12}\alpha_2+C_{13}\alpha_3\\ C_{12}\alpha_1+C_{22}\alpha_2+C_{23}\alpha_3\\ C_{13}\alpha_1+C_{23}\alpha_2+C_{33}\alpha_3\end{Bmatrix} \tag{3.20}$$

Since the shell is graded in the radial direction, the material properties k_i, C_{ij} and α_i are functions of the radial coordinate *r*.

The three-dimensional steady-state heat conduction equation, expressed in terms of the local coordinates, is [151]:

$$\frac{\partial q_r}{\partial r}+\frac{1}{r}\frac{\partial q_\theta}{\partial \theta}+\frac{\partial q_z}{\partial z}+\frac{q_r}{r}=0 \tag{3.21}$$

where q_θ, q_r and q_z are the components of the heat flux vector. Fourier's law of heat conduction, which relates the heat flux to the temperature gradient, is:

$$\begin{Bmatrix}q_z\\ q_\theta\\ q_r\end{Bmatrix}=-\begin{Bmatrix}k_{11} & 0 & 0\\ 0 & k_{22} & 0\\ 0 & 0 & k_{33}\end{Bmatrix}\begin{Bmatrix}\dfrac{\partial T}{\partial z}\\ \dfrac{1}{r}\dfrac{\partial T}{\partial \theta}\\ \dfrac{\partial T}{\partial r}\end{Bmatrix} \tag{3.22}$$

where *T* is the change in temperature of a material particle from that in the stress-free reference configuration and k_i are the thermal conductivities. Upon Eq. (3.1) into Eq. (3.19) and then into (2.27), also Eq. (3.22) into (3.21), the following equations of motion in matrix form are obtained

$$\begin{bmatrix}L_{1r} & L_{1\theta} & L_{1z} & L_{1T}\\ L_{2r} & L_{2\theta} & L_{2z} & L_{2T}\\ L_{3r} & L_{3\theta} & L_{3z} & L_{3T}\\ 0 & 0 & 0 & L_{4T}\end{bmatrix}\begin{Bmatrix}u_r\\ u_\theta\\ u_z\\ T\end{Bmatrix}=\{0\} \tag{3.23}$$

where

$$L_{1r} = C_{55}\frac{\partial^2}{\partial z^2} + C_{44}\frac{1}{r^2}\frac{\partial^2}{\partial\theta^2} + \frac{\partial C_{23}}{\partial r}\frac{1}{r} + C_{23}\frac{1}{r}\frac{\partial}{\partial r} + \frac{\partial C_{33}}{\partial r}\frac{\partial}{\partial r} - C_{22}\frac{1}{r^2}$$

$$+C_{33}\left(\frac{1}{r}\frac{\partial}{\partial r} + \frac{\partial^2}{\partial r^2}\right) - C_{23}\frac{1}{r}\frac{\partial}{\partial r}, \tag{3.24}$$

$$L_{1\theta} = -C_{44}\frac{1}{r^2}\frac{\partial}{\partial\theta} + C_{44}\frac{1}{r}\frac{\partial^2}{\partial r\partial\theta} + \frac{\partial C_{23}}{\partial r}\frac{1}{r}\frac{\partial}{\partial\theta} + C_{23}\frac{1}{r}\frac{\partial^2}{\partial r\partial\theta} - C_{22}\frac{1}{r^2}\frac{\partial}{\partial\theta}, \tag{3.25}$$

$$L_{1z} = C_{55}\frac{\partial^2}{\partial r\partial z} - C_{12}\frac{1}{r}\frac{\partial}{\partial z} + \frac{\partial C_{13}}{\partial r}\frac{\partial}{\partial z} + C_{13}\frac{\partial^2}{\partial r\partial z} + C_{13}\frac{1}{r}\frac{\partial}{\partial z}, \tag{3.26}$$

$$L_{1T} = -\frac{\partial\beta_3}{\partial r} - \beta_3\frac{\partial}{\partial r} - \frac{1}{r}\beta_3 + \beta_2\frac{1}{r} \tag{3.27}$$

$$L_{2r} = C_{22}\frac{1}{r^2}\frac{\partial}{\partial\theta} + C_{23}\frac{1}{r}\frac{\partial^2}{\partial r\partial\theta} + \frac{\partial C_{44}}{\partial r}\frac{1}{r}\frac{\partial}{\partial\theta} - C_{44}\frac{1}{r^2}\frac{\partial}{\partial\theta} + C_{44}\frac{1}{r}\frac{\partial^2}{\partial r\partial\theta} + C_{44}\frac{2}{r^2}, \tag{3.28}$$

$$L_{2\theta} = \frac{1}{r}\frac{\partial^2}{\partial\theta\partial z}\left(C_{66} + C_{12}\right) \tag{3.29}$$

$$L_{2z} = C_{66}\frac{\partial^2}{\partial z^2} + C_{22}\frac{1}{r^2}\frac{\partial^2}{\partial\theta^2} + \frac{\partial C_{44}}{\partial r}\frac{\partial}{\partial r} + C_{44}\frac{\partial^2}{\partial r^2} - \frac{\partial C_{44}}{\partial r}\frac{1}{r} - C_{44}\frac{1}{r}\left(\frac{1}{r} + \frac{\partial}{\partial r}\right), \tag{3.30}$$

$$L_{2T} = -\frac{1}{r}\beta_2\frac{\partial}{\partial\theta}, \tag{3.31}$$

$$L_{3r} = C_{13}\frac{\partial^2}{\partial r\partial z} + C_{12}\frac{1}{r}\frac{\partial}{\partial z} + \frac{\partial C_{55}}{\partial r}\frac{\partial}{\partial z} + C_{55}\frac{\partial^2}{\partial r\partial z} + C_{55}\frac{1}{r}\frac{\partial}{\partial z}, \tag{3.32}$$

$$L_{3\theta} = C_{12}\frac{1}{r}\frac{\partial^2}{\partial\theta\partial z} + C_{66}\frac{1}{r}\frac{\partial^2}{\partial\theta\partial z}, \tag{3.33}$$

$$L_{3z} = C_{11}\frac{\partial^2}{\partial z^2} + C_{66}\frac{1}{r^2}\frac{\partial^2}{\partial\theta^2} + \frac{\partial C_{55}}{\partial r}\frac{\partial}{\partial r} + C_{55}\frac{\partial^2}{\partial r^2} + C_{55}\frac{1}{r}\frac{\partial}{\partial r}, \tag{3.34}$$

$$L_{3T} = -\beta_1 \frac{\partial}{\partial z}, \tag{3.35}$$

$$L_{4T} = \frac{\partial k_3}{\partial r}\frac{\partial}{\partial r} + k_3 \frac{\partial^2}{\partial r^2} + k_2 \frac{1}{r^2}\frac{\partial^2}{\partial \theta^2} + k_1 \frac{\partial^2}{\partial z^2} + k_3 \frac{1}{r}\frac{\partial}{\partial r} \tag{3.36}$$

The following simply supported conditions are imposed at the edges of the cylindrical panel:

$$u_r = \sigma_\theta = 0 \ , \quad T = 0 \qquad \text{at} \qquad \theta = 0, \Phi \tag{3.37}$$

$$u_r = \sigma_z = 0 \ , \quad T = 0 \qquad \text{at} \qquad z = 0, L \tag{3.38}$$

Moreover the boundary conditions on the inner and outer surfaces of the panel are as follows:

$$\sigma_r = \tau_{rz} = \tau_{r\theta} = 0 \quad , \quad T = 0 \qquad \text{at} \qquad r = r_i \tag{3.39}$$

$$\sigma_r = \tau_{rz} = \tau_{r\theta} = 0 \quad , \quad T = T_o \qquad \text{at} \qquad r = r_o \tag{3.40}$$

3.3 2-D plate theories

Now, based on 2-D theories we formulate free vibration, mechanical buckling, and thermal problems of plates and shells composed of FGMs. As discussed in section 2.5, in 2-D theories, the displacements are expanded in terms of thickness and transverse displacement is independent of the transverse (or thickness) coordinate. This leads coupled governing equations to be independent of transverse displacement. Hence, solutions of such set of equations can be easier than that of 3-D elasticity. It is worth noting that we have compared 3-D elasticity solutions with those of 2-D theories in recent publication [152] and an excellent agreement obtained between the 3-D elasticity results and those of 2-D theories.

3.3.1 First-order shear deformation theory

In this section, theoretical formulations based on FSDT for free vibration and mechanical buckling of CNT-reinforced plates are carried out.

3.3.1.1 Free vibration

A flat, nanocomposite rectangular plate of length *a*, width *b*, and uniform thickness

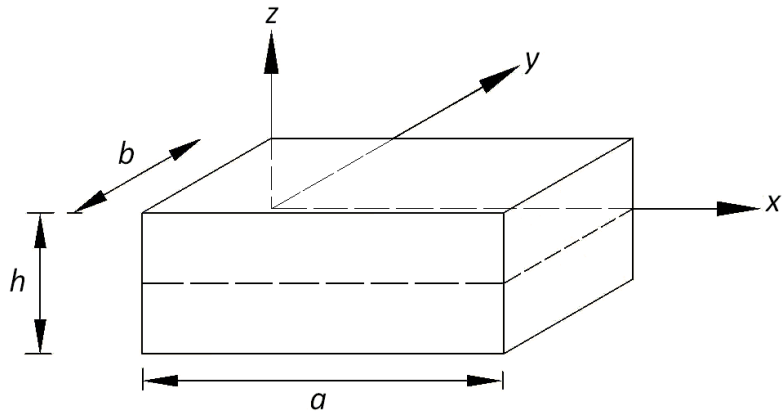

Figure 3.5. Configuration of a rectangular plate

h, made of graded CNT dispersed in the matrix phase, is depicted in Figure 3.5. The Cartesian coordinate system (*x*,*y*,*z*) is considered to extract mathematical formulations when *x* and *y* axes are located in the undeformed mid-plane of the plate. According to FSDT, the in-plane displacements are expanded as linear functions of the thickness coordinate and the transverse deflection is constant through the plate thickness. Thus, displacement components of the middle surface of the rectangular plate along the *x*, *y*, and *z* axes, designated by u, v and w, are expressed by Eq. (2.29). By substituting Eq. (2.29) into strain-displacement relations in Cartesian coordinate, Eq. (3.11), the relations of strain-displacement are derived:

$$\left\{\varepsilon_{ij}\right\} = \left\{\varepsilon^{0}{}_{ij}\right\} + z\left\{\varepsilon^{1}{}_{ij}\right\} \qquad i, j = x, y, z \tag{3.41}$$

where

$$\begin{Bmatrix} \varepsilon^0_{xx} \\ \varepsilon^0_{yy} \\ \gamma^0_{yz} \\ \gamma^0_{xz} \\ \gamma^0_{xy} \end{Bmatrix} = \begin{Bmatrix} u_{0,x} \\ v_{0,y} \\ w_{0,y} + \psi_y \\ w_{0,x} + \psi_x \\ u_{0,y} + v_{0,x} \end{Bmatrix}, \qquad \begin{Bmatrix} \varepsilon^1_{xx} \\ \varepsilon^1_{yy} \\ \gamma^1_{yz} \\ \gamma^1_{xz} \\ \gamma^1_{xy} \end{Bmatrix} = \begin{Bmatrix} \psi_{x,x} \\ \psi_{y,y} \\ 0 \\ 0 \\ \psi_{x,y} + \psi_{y,x} \end{Bmatrix} \tag{3.42}$$

The stress resultant-displacement relations are given by:

$$(N_i, M_i) = \int_{-h/2}^{h/2} \sigma_i\,(1, z)\,dz \qquad i = xx, yy, xy \tag{3.43}$$

$$Q_i = k' \int_{-h/2}^{h/2} \sigma_{iz}\, dz \qquad i = x, y \tag{3.44}$$

in which k' is the transverse shear correction coefficient, applied to the transverse shear forces due to the fact that the transverse shear strains (γ_{xz} and γ_{yz}) have a nearly parabolic dependency on the thickness coordinate and in this study is taken as $k' = 5/6$. Substituting Eqs. (3.41) and (3.42) into Eq. (2.14) and then into Eqs. (3.43) and (3.44) gives the forces and the resultant moments (N_{ij} and M_{ij}), and the transverse shear forces (Q_i) per unit length as follows:

$$N_{xx} = \frac{1}{1-\nu_{12}^2}\left[\left(E_{1a}+E_{1d}\right)\left(\varepsilon_{xx}^0+\nu_{21}\varepsilon_{yy}^0\right)+\left(E_{1b}+E_{1e}\right)\left(\varepsilon_{xx}^1+\nu_{12}\varepsilon_{yy}^1\right)\right]$$

$$N_{yy} = \frac{1}{1-\nu_{12}^2}\left[\left(E_{2a}+E_{2d}\right)\left(\varepsilon_{yy}^0+\nu_{12}\varepsilon_{xx}^0\right)+\left(E_{2b}+E_{2e}\right)\left(\varepsilon_{yy}^1+\nu_{12}\varepsilon_{xx}^1\right)\right]$$

$$N_{xy} = \left(G_{12a}+G_{12d}\right)\gamma_{xy}^0+\left(G_{12b}+G_{12e}\right)\gamma_{xy}^1$$

$$M_{xx} = \frac{1}{1-\nu_{12}^2}\left[\left(E_{1b}+E_{1e}\right)\left(\varepsilon_{xx}^0+\nu_{12}\varepsilon_{yy}^0\right)+\left(E_{1c}+E_{1f}\right)\left(\varepsilon_{xx}^1+\nu_{12}\varepsilon_{yy}^1\right)\right]$$

$$M_{yy} = \frac{1}{1-\nu_{12}^2}\left[\left(E_{2b}+E_{2e}\right)\left(\varepsilon_{yy}^0+\nu_{12}\varepsilon_{xx}^0\right)+\left(E_{2c}+E_{2f}\right)\left(\varepsilon_{yy}^1+\nu_{12}\varepsilon_{xx}^1\right)\right]$$

$$M_{xy} = \left(G_{12b}+G_{12e}\right)\gamma_{xy}^0+\left(G_{12c}+G_{12f}\right)\gamma_{xy}^1$$

$$Q_x = k\left(G_{12a}+G_{12d}\right)\gamma_{xz}^0$$

$$Q_y = k\left(G_{12a}+G_{12d}\right)\gamma_{yz}^0 \tag{3.45}$$

where coefficients E_{ii}, G_{ij} are:

$$\left(E_{1a}, E_{1b}, E_{1c}\right) = \int_{-h/2}^{0} E_{11}\left(1, z, z^2\right) dz$$

$$\left(E_{1d}, E_{1e}, E_{1f}\right) = \int_{0}^{h/2} E_{11}\left(1, z, z^2\right) dz$$

$$\left(E_{2a}, E_{2b}, E_{2c}\right) = \int_{-h/2}^{0} E_{22}\left(1, z, z^2\right) dz$$

$$\left(E_{2d}, E_{2e}, E_{2f}\right) = \int_{0}^{h/2} E_{22}\left(1, z, z^2\right) dz$$

$$\left(G_{12a}, G_{12b}, G_{12c}\right) = \int_{-h/2}^{0} G_{12}\left(1, z, z^2\right) dz$$

$$\left(G_{12d}, G_{12e}, G_{12f}\right) = \int_{0}^{h/2} G_{12}\left(1, z, z^2\right) dz \tag{3.46}$$

Hamilton's principle is used to derive equations of motion based on the FSDT. The principle can be stated as follows:

$$\int_{t_1}^{t_2} \left(\delta K_e - \delta P_e\right) dt = 0 \tag{3.47}$$

Where

$$\delta K_e = \int_{\Omega_0} \{\int_{-\frac{h}{2}}^{\frac{h}{2}} \rho\,[\left(\dot{u}_0 + z\dot{\psi}_x\right)\left(\delta\dot{u}_0 + z\delta\dot{\psi}_x\right) + \left(\dot{v}_0 + z\dot{\psi}_y\right)\left(\delta\dot{v}_0 + z\delta\dot{\psi}_y\right) + \dot{w}_0\delta\dot{w}_0]dz\}dxdy\,, \tag{3.48}$$

$$\delta P_e = \int_{\Omega_0} \{\int_{-h/2}^{h/2} [\sigma_{xx}\left(\delta\varepsilon_{xx}^{(0)} + z\delta\varepsilon_{xx}^{(1)}\right) + \sigma_{yy}\left(\delta\varepsilon_{yy}^{(0)} + z\delta\varepsilon_{yy}^{(1)}\right) + \sigma_{xy}\left(\delta\gamma_{xy}^{(0)} + z\delta\gamma_{xy}^{(1)}\right) + \sigma_{xz}\delta\gamma_{xz}^{(0)} + \sigma_{yz}\delta\gamma_{yz}^{(0)}]dz\}dxdy\,, \tag{3.49}$$

where K_e is the kinetic energy of the plate and P_e is the elastic potential energy of the nanocomposite plate. Simplifying Eqs. (3.48) and (3.49) and inserting the results into Eq. (3.47) and performing the integrations by parts in Hamilton's equation (3.45), one obtains:

$$\begin{aligned}
&N_{xx,x} + N_{xy,y} = I_0\ddot{u}_0 + I_1\ddot{\psi}_x \\
&N_{xy,x} + N_{yy,y} = I_0\ddot{v}_0 + I_1\ddot{\psi}_y \\
&Q_{x,x} + Q_{y,y} = I_0\ddot{w}_0 \\
&M_{xx,x} + M_{xy,y} - Q_x = I_1\ddot{u}_0 + I_2\ddot{\psi}_x \\
&M_{xy,x} + M_{yy,y} - Q_y = I_1\ddot{v}_0 + I_2\ddot{\psi}_y
\end{aligned} \tag{3.50}$$

where

$$I_i = \int_{-h/2}^{h/2} (z)^i \rho(z) dz \qquad i = 0,1,2 \tag{3.51}$$

For a simply supported rectangular plate, the boundary conditions can be expressed on the *x*-constant and *y*-constant edges as:

$$v_0 = w_0 = N_{xx} = M_{xx} = \psi_y = 0 \qquad at \qquad x = 0, a \tag{3.52}$$

$$u_0 = w_0 = N_{yy} = M_{yy} = \psi_x = 0 \qquad at \qquad y = 0, b \tag{3.53}$$

3.3.1.2 Mechanical Buckling

As it is shown in Figure 3.5, a polymer rectangular plate with length *a*, width *b* and thickness *t* reinforced by graded SWCNTs distribution in the thickness direction is assumed. It is also assumed that the mentioned nanocomposite plate is being influenced by plane forces N_x and N_y , which are in *x* and *y* direction respectively. In order to obtain the equilibrium relations, the energy method will be used. Therefore, the plate overall potential energy is written as follows:

$$\overline{V} = P_e + \Omega \tag{3.54}$$

In which $\overline{V}$ is the overall potential energy and Ω is work done by the external forces the relations which are written:

$$P_e = \frac{1}{2}\iint \int_{-t/2}^{t/2} \left(\sigma_x \varepsilon_x + \sigma_y \varepsilon_y + \sigma_z \varepsilon_z + \tau_{xy}\gamma_{xy} + \tau_{yz}\gamma_{yz} + \tau_{zx}\gamma_{zx}\right) dzdxdy$$

$$\Omega = \iint \left(\frac{1}{b} p_x u_{,x} + \frac{1}{a} p_y v_{,y} - p_n w\right) dxdy = \iint \left(\frac{1}{b} p_x \frac{\partial \psi_x}{\partial x} + \frac{1}{a} p_y \frac{\partial \psi_y}{\partial y} - p_n w\right) dxdy \tag{3.55}$$

By substituting the stress components of Eq. (2.14) into Eq. (3.55), and calculating the total potential energy, (*V*), the functional of energy is obtained as:

$$\begin{aligned} F = {} & \frac{1}{2\left(1-\nu_{12}\nu_{21}\right)}\Big[\left(E_{1a}+E_{1d}\right)\left(\varepsilon_{xx}^{0\,2} + \nu_{21}\varepsilon_{xx}^{0}\varepsilon_{yy}^{0}\right) + \left(E_{1b}+E_{1e}\right)\left(2\varepsilon_{xx}^{0}\varepsilon_{xx}^{1} + \nu_{21}\varepsilon_{xx}^{0}\varepsilon_{yy}^{1} + \nu_{21}\varepsilon_{xx}^{1}\varepsilon_{xx}^{0}\right) \\ & + \left(E_{1c}+E_{1f}\right)\left(\varepsilon_{xx}^{1\,2} + \nu_{21}\varepsilon_{xx}^{1}\varepsilon_{yy}^{1}\right) + \left(E_{2a}+E_{2d}\right)\left(\varepsilon_{yy}^{0\,2} + \nu_{12}\varepsilon_{xx}^{0}\varepsilon_{yy}^{0}\right) + \left(E_{2b}+E_{2e}\right) \\ & \times\left(2\varepsilon_{yy}^{0}\varepsilon_{yy}^{1} + \nu_{12}\varepsilon_{xx}^{0}\varepsilon_{yy}^{1} + \nu_{12}\varepsilon_{xx}^{1}\varepsilon_{yy}^{0}\right) + \left(E_{2c}+E_{2f}\right)\left(\varepsilon_{yy}^{1\,2} + \nu_{12}\varepsilon_{yy}^{1}\varepsilon_{xx}^{1}\right)\Big] + \left(G_{12b}+G_{12e}\right)\gamma_{xy}^{0}\gamma_{xy}^{1} \\ & + \frac{1}{2}\left(G_{12c}+G_{12f}\right)\gamma_{xy}^{1\,2} + \frac{1}{2}\left(G_{12a}+G_{12d}\right)\left(\gamma_{xy}^{0\,2} + \gamma_{yz}^{0\,2} + \gamma_{zx}^{0\,2}\right) + \frac{1}{b} p_x z\psi_{x,x} + \frac{1}{a} p_y z\psi_{y,y} - p_n w \end{aligned} \tag{3.56}$$

Now by applying the Euler-Lagrange equations to the above equation, the equilibrium equations of the nanocomposite plate are obtained based on FSDT in the form:

$$\begin{aligned} & M_{x,x} + M_{xy,y} - Q_x = 0 \\ & M_{y,y} + M_{xy,x} - Q_y = 0 \\ & \left(Q_{x,x} + Q_{y,y}\right) + \frac{\partial}{\partial x}\left(N_x \frac{\partial w}{\partial x} + N_{xy}\frac{\partial w}{\partial y}\right) + \frac{\partial}{\partial y}\left(N_{xy}\frac{\partial w}{\partial x} + N_y \frac{\partial w}{\partial y}\right) = 0 \end{aligned} \tag{3.57}$$

In the following, the stability equations of the FG nanocomposite rectangular plate are derived by using the adjacent equilibrium criterion [153]. We give small increments to the displacement and rotation variables and examine the two adjacent configurations represented by the displacements and rotations before and after the

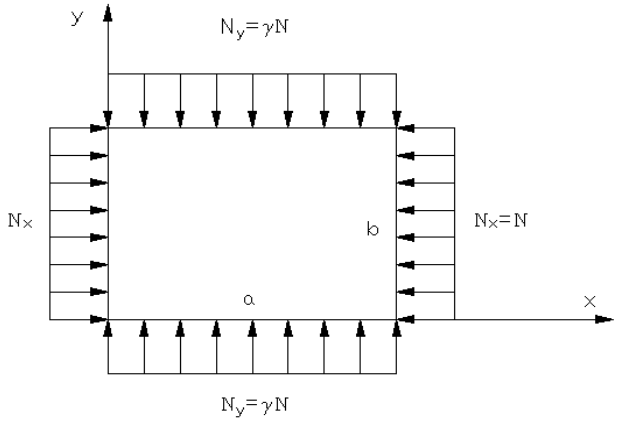

Figure 3.6. Nanocomposite rectangular plate reinforced by SWCNTs under the plane forces in *x* and *y* directions ($N_x=N$, $N_y=\gamma N_x$)

increment, i.e.:

$$\psi_x \to \psi_{x0} + \psi_{x1}$$
$$\psi_y \to \psi_{y0} + \psi_{y1} \tag{3.58}$$
$$w \to w_0 + w_1$$

In which the subscript 0 indicates the equilibrium state and the subscript 1 expresses a minute change in the plate equilibrium condition. Regarding the incremented variation to the rotation and the displacement components, the overall strain is expressed as follows:

$$\{\varepsilon\} = \{\varepsilon_0^0 + \varepsilon_1^0\} + z\{\varepsilon_0^1 + \varepsilon_1^1\} \tag{3.59}$$

Subsequently the relations of the forces and moments are written:

$$N_i = N_{i0} + N_{i1} \qquad i = x, y, xy$$
$$M_i = M_{i0} + M_{i1} \qquad i = x, y, xy \tag{3.60}$$
$$Q_i = Q_{i0} + Q_{i1} \qquad i = x, y$$

Now, by applying equations (3.58) and (3.59) into (3.60), the relations of the forces and moments are written in the form below:

$$N_{x0} = \frac{1}{1-\nu_{12}\nu_{21}}\left(E_{1b} + E_{1e}\right)\left(\psi_{x0,x} + \upsilon_{21}\psi_{y0,y}\right)$$

$$N_{x1} = \frac{1}{1-\nu_{12}\nu_{21}}\left(E_{1b}+E_{1e}\right)\left(\psi_{x1,x}+\upsilon_{21}\psi_{y1,y}\right)$$

$$N_{y0} = \frac{1}{1-\nu_{12}\nu_{21}}\left(E_{2b}+E_{2e}\right)\left(\psi_{y0,y}+\upsilon_{12}\psi_{x0,x}\right)$$

$$N_{y1} = \frac{1}{1-\nu_{12}\nu_{21}}\left(E_{2b}+E_{2e}\right)\left(\psi_{y1,y}+\upsilon_{12}\psi_{x1,x}\right)$$

$$M_{yy0} = \frac{1}{1-\nu_{12}\nu_{21}}\left(E_{2c}+E_{2f}\right)\left(\psi_{y0,y}+\upsilon_{12}\psi_{x0,x}\right)$$

$$M_{yy1} = \frac{1}{1-\nu_{12}\nu_{21}}\left(E_{2c}+E_{2f}\right)\left(\psi_{y1,y}+\upsilon_{21}\psi_{x1,x}\right)$$

$$M_{xx0} = \frac{1}{1-\nu_{12}\nu_{21}}\left(E_{1c}+E_{1f}\right)\left(\psi_{x0,x}+\upsilon_{21}\psi_{y0,y}\right)$$

$$M_{xx1} = \frac{1}{1-\nu_{12}\nu_{21}}\left(E_{1c}+E_{1f}\right)\left(\psi_{x1,x}+\upsilon_{21}\psi_{y1,y}\right)$$

$$N_{xy0} = \left(G_{12b}+G_{12e}\right)\left(\psi_{x0,y}+\psi_{y0,y}\right)$$

$$N_{xy1} = \left(G_{12b}+G_{12e}\right)\left(\psi_{x1,y}+\psi_{y1,y}\right)$$

$$M_{xy0} = \left(G_{12c}+G_{12f}\right)\left(\psi_{x0,y}+\psi_{y0,x}\right)$$

$$M_{xy1} = \left(G_{12c}+G_{12f}\right)\left(\psi_{x1,y}+\psi_{y1,x}\right)$$

$$Q_{x0} = k\left(G_{12a}+G_{12d}\right)\left(\psi_{x0}+w_{0,x}\right)$$

$$Q_{x1} = k\left(G_{12a}+G_{12d}\right)\left(\psi_{x1}+w_{1,x}\right)$$

$$Q_{y0} = k\left(G_{12a}+G_{12d}\right)\left(\psi_{y0}+w_{0,y}\right)$$

$$Q_{y1} = k\left(G_{12a}+G_{12d}\right)\left(\psi_{y1}+w_{1,y}\right) \tag{3.61}$$

By substituting the aforementioned relations into the equilibrium equations and applying the following assumptions; the linear stability equations will be obtained in the form of the Eq. (3.62).

a) w_0 and all its derivatives are zero.

b) The expressions conclude the N_{i0}, M_{i0} and Q_{i0} indicate the initial equilibrium condition and should be eliminated.

c) The expressions consists of multiplying the (Q_{i0}, M_{i0} and N_{i0}) in (w_{i0}, ψ_{x0} and ψ_{y0}) are negligible and should be eliminated.

$$M_{x1,x} + M_{xy1,y} - Q_{x1} = 0$$

$$M_{y1,y} + M_{xy1,x} - Q_{y1} = 0 \tag{3.62}$$

$$\left(Q_{x1,x} + Q_{y1,y}\right) + \frac{\partial}{\partial x}\left(N_{x0}\frac{\partial w_1}{\partial x} + N_{xy0}\frac{\partial w_1}{\partial y}\right) + \frac{\partial}{\partial y}\left(N_{xy0}\frac{\partial w_1}{\partial x} + N_{y0}\frac{\partial w_1}{\partial y}\right) = 0$$

Herein, the determination of the critical buckling force of the functionally graded composite plate under the effect of plane forces using analytical method is discussed. It is assumed that the forces are N_x and N_y in x and y directions respectively and their relation is $N_y=\gamma N_x$, as shown in Figure 3.6. By substituting the Eq. (3.61) in to Eq. (3.62) the stability equations will be written in terms of the displacement components:

$$\frac{1}{\left(1-\nu_{12}\nu_{21}\right)}\left(E_{1c}+E_{1f}\right)\left(\psi_{x1,xx}+\nu_{21}\psi_{y1,yx}\right)+\left(G_{12c}+G_{12cf}\right)\left(\psi_{x1,yy}+\nu_{21}\psi_{y1,xy}\right)-$$

$$k\left(G_{12a}+G_{12d}\right)\left(\psi_{x1}+w_{1,x}\right)=0,$$

$$\frac{1}{\left(1-\nu_{12}\nu_{21}\right)}\left(E_{2c}+E_{2f}\right)\left(\psi_{y1,yy}+\nu_{12}\psi_{x1,yx}\right)$$

$$+\left(G_{12c}+G_{12cf}\right)\left(\psi_{x1,yx}+\nu_{21}\psi_{y1,xx}\right)-k\left(G_{12a}+G_{12d}\right)\left(\psi_{y1}+w_{1,y}\right)=0,$$

$$-k\left(G_{12a}+G_{12d}\right)\left(\psi_{x1,x}+w_{1,xx}+\psi_{y1,y}+w_{1,yy}\right)$$

$$+\frac{\partial}{\partial x}\left(N_{x0}\frac{\partial w_1}{\partial x}+N_{xy0}\frac{\partial w_1}{\partial y}\right)+\frac{\partial}{\partial y}\left(N_{xy0}\frac{\partial w_1}{\partial x}+N_{y0}\frac{\partial w_1}{\partial y}\right)=0, \tag{3.63}$$

By applying plate boundary condition into Eq. (3.63) and regarding that N_x and N_y are the plane forces per unit length applied on the plate edges, one would get:

$$N_x = -\frac{p_x}{a} \qquad N_y = -\frac{p_y}{b} \tag{3.64}$$

$$-k\left(G_{12a}+G_{12d}\right)\left(\psi_{x1,x}+w_{1,xx}+\psi_{y1,y}+w_{1,yy}\right)-\frac{p_y}{a}w_{1,yy}-\frac{p_x}{b}w_{1,xx}=0 \tag{3.65}$$

In which P_x and P_y are the total imposed forces on the plate in the direction of x and y, respectively. According to the simply supported boundary conditions for the mentioned plate edges, the following functions have been assumed for quantities of w_1, ψ_{x1} and ψ_{y1}:

$$\begin{aligned} w_1(x,y) &= \sum_{n=1}^{\infty}\sum_{m=1}^{\infty} W_{mn}\sin\alpha x\sin\beta y \\ \psi_{x1}(x,y) &= \sum_{n=1}^{\infty}\sum_{m=1}^{\infty} X_{mn}\cos\alpha x\sin\beta y \\ \psi_{y1}(x,y) &= \sum_{n=1}^{\infty}\sum_{m=1}^{\infty} Y_{mn}\sin\alpha x\cos\beta y \end{aligned} \tag{3.66}$$

in which W_{mn} , X_{mn} and Y_{mn} are the amplitude of the above-mentioned functions. m and n indicate also number of half wave in x and y directions, respectively, and following relations express the relationship between m and n with α and β :

$$\alpha = \frac{m\pi}{a} \qquad \beta = \frac{n\pi}{b} \tag{3.67}$$

After substituting the Eq. (3.66) in to Eq. (3.65), we reach a system of three equations for finding the W_{mn}, X_{mn} and Y_{mn} as follows:

$$\begin{bmatrix} s_{11}-N_y\left(\beta^2+\gamma\alpha^2\right) & s_{12} & s_{13} \\ s_{21} & s_{22} & s_{23} \\ s_{31} & s_{32} & s_{33} \end{bmatrix} \begin{Bmatrix} W_{mn} \\ X_{mn} \\ Y_{mn} \end{Bmatrix} = 0$$

By equalling the determinant of coefficient to zero we have:

$$\begin{aligned} s_{11} &= N_y\beta^2 + N_x\alpha^2 = -k\left(G_{12a}+G_{12d}\right)\left(\alpha^2+\beta^2\right)+N_y\left(\beta^2+\gamma\alpha^2\right) \\ s_{12} &= -k\left(G_{12a}+G_{12d}\right)\alpha \\ s_{13} &= -k\left(G_{12a}+G_{12d}\right)\beta \\ s_{21} &= s_{12} \\ s_{22} &= \frac{-1}{1-\upsilon_{12}\upsilon_{21}}\left(E_{1c}+E_{1f}\right)\alpha^2-\left(G_{12c}+G_{12f}\right)\beta^2-k\left(G_{12a}+G_{12d}\right) \end{aligned} \tag{3.68}$$

$$s_{23} = \frac{-\upsilon_{21}}{1-\upsilon_{12}\upsilon_{21}}\left(E_{1c}+E_{1f}\right)\alpha\beta - \left(G_{12c}+G_{12f}\right)\alpha\beta$$

$$s_{31} = s_{13}$$

$$s_{32} = s_{23}$$

$$s_{33} = \frac{-1}{1-\upsilon_{12}\upsilon_{21}}\left(E_{2c}+E_{2f}\right)\beta^2 - \left(G_{12c}+G_{12f}\right)\alpha^2 - k\left(G_{12a}+G_{12d}\right) \quad (3.69)$$

In Eqs. (3.69), N_x or N_y ($N_x=\gamma N_y$) indicated the critical mechanical buckling load as:

$$N^{cr} = -\frac{s_d}{\pi^2\left(\frac{m^2\gamma}{a^2}+\frac{n^2}{b^2}\right)s_c} \quad (3.70)$$

in which s_d and s_c are given as follows:

$$s_d = 2s_{13}s_{12}s_{23} - s_{22}s_{13}^2 + s_{11}s_{22}s_{33} - s_{11}s_{23}^2 - s_{33}s_{12}^2$$

$$s_c = s_{22}s_{33} - s_{23}^2 \quad (3.71)$$

3.3.2 Third-order shear deformation theory

In the following, for the first time, thermal stress analysis of a 2-D FGM cylindrical panel is formulated based on the Reddy's TSDT, and governing equations and heat conduction equation are derived.

3.3.2.1 Thermal stress analysis

Let us consider a 2-D FGM cylindrical panel of length L, mean radius Z_m, uniform thickness h, as shown in Figure 3.7. An orthogonal cylindrical coordinate system (x,θ,z) is used to label the material point of the shell in the unstressed reference configuration.

According to the Reddy's TSDT [47], straight lines normal to midsurface before deformation will no longer remain straight. Satisfying zero shear stress boundary conditions at the top and bottom of the shell, the displacement components of an arbitrary point within the shell domain, designated by U, V and W, are expressed as:

$$U = \overline{u}(x,\theta) + z\psi_1(x,\theta) - nz^3(\psi_1 + \frac{\partial \overline{w}}{\partial x})$$

$$V = \overline{v}(x,\theta) + z\psi_2(x,\theta) + nz^3\left(\frac{\overline{v}}{Z_m} - \psi_2 - \frac{\partial \overline{w}}{Z_m \partial \theta}\right)$$

$$W = \overline{w}(x,\theta) \tag{3.72}$$

where $n = 4/3h^2$. Substituting Eq. (3.72) into the linear strain-displacement relations, Eq. (3.1), leads to:

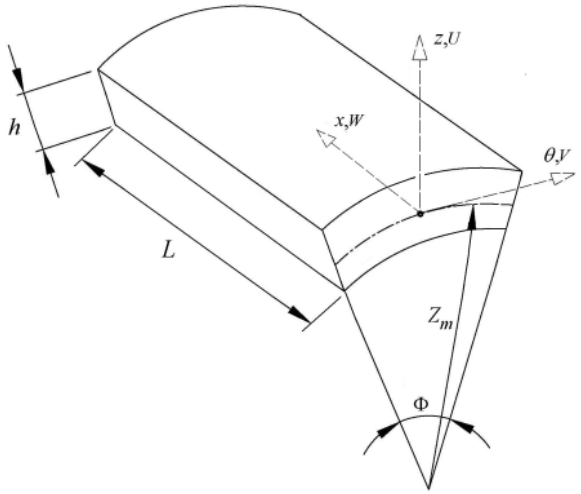

Figure 3.7. Geometry of a 2-D FGM cylindrical panel in 2-D theories.

$$\begin{aligned}
\varepsilon_{xx} &= \varepsilon^0_{xx} + z\varepsilon'_{xx} + z^2\varepsilon''_{xx} + z^3\varepsilon'''_{xx} \\
\varepsilon_{\theta\theta} &= \varepsilon^0_{\theta\theta} + z\varepsilon'_{\theta\theta} + z^2\varepsilon''_{\theta\theta} + z^3\varepsilon'''_{\theta\theta} \\
\varepsilon_{x\theta} &= \varepsilon^0_{x\theta} + z\varepsilon'_{x\theta} + z^2\varepsilon''_{x\theta} + z^3\varepsilon'''_{x\theta} \\
\varepsilon_{xz} &= \varepsilon^0_{xz} + z\varepsilon'_{xz} + z^2\varepsilon''_{xz} + z^3\varepsilon'''_{xz} \\
\varepsilon_{\theta z} &= \varepsilon^0_{\theta z} + z\varepsilon'_{\theta z} + z^2\varepsilon''_{\theta z} + z^3\varepsilon'''_{\theta z}
\end{aligned} \tag{3.73}$$

where

$$\varepsilon^0_{xx} = \overline{u}_{,xx} \qquad \varepsilon'_{xx} = \psi_{1,x} \qquad \varepsilon''_{xx} = 0 \qquad \varepsilon'''_{xx} = -n(\psi_{1,x} + \overline{w}_{,xx})$$

$$\varepsilon_{\theta\theta}^{0} = (1/Z_m)\overline{v}_{,\theta} + \overline{w}/Z_m \qquad \varepsilon_{\theta\theta}' = (1/Z_m)\psi_{2,\theta} \qquad \varepsilon_{\theta\theta}'' = 0$$

$$\varepsilon_{\theta\theta}'' = n\left((1/Z_m)\overline{v}_{,\theta} - (1/Z_m)\psi_{2,\theta} - (1/Z_m)\overline{w}_{,\theta\theta}\right)$$

$$\varepsilon_{x\theta}^{0} = (1/Z_m)\overline{u}_{,\theta} + \overline{v}_{,x} \qquad \varepsilon_{x\theta}' = (1/Z_m)\psi_{1,\theta} + \psi_{2,x} \qquad \varepsilon_{x\theta}'' = 0$$

$$\varepsilon_{x\theta}''' = -(n/Z_m)\psi_{1,\theta} - (n/Z_m)\,\overline{w}_{,x\theta} + (n/Z_m)\overline{v}_{,x} - n\psi_{2,x}$$

$$\varepsilon_{xz}^{0} = \psi_1 + \overline{w}_{,x} \qquad \varepsilon_{xz}' = 0 \qquad \varepsilon_{xz}'' = -3n(\psi_1 + \overline{w}_{,x})$$

$$\varepsilon_{xz}''' = 0 \qquad \varepsilon_{\theta z}^{0} = \psi_2 + (1/Z_m)\overline{w}_{,x} \qquad \varepsilon_{\theta z}' = 0$$

$$\varepsilon_{\theta z}'' = 3n\left(-(1/Z_m)\overline{w}_{,\theta} - \psi_2 + (\overline{v}/Z_m)\right) \qquad \varepsilon_{\theta z}''' = 0 \tag{3.74}$$

The forces and moments of the thick shells can be defined as:

$$\begin{Bmatrix} N_{xx} \\ M_{xx} \\ P_{xx} \\ N_{x\theta} \\ M_{x\theta} \\ P_{x\theta} \end{Bmatrix} = \int_{-h/2}^{h/2} \begin{Bmatrix} \sigma_{xx} \\ z\sigma_{xx} \\ z^3\sigma_{xx} \\ \sigma_{x\theta} \\ z\sigma_{x\theta} \\ z^3\sigma_{x\theta} \end{Bmatrix} dz, \quad \begin{Bmatrix} N_{\theta\theta} \\ M_{\theta\theta} \\ P_{\theta\theta} \\ N_{\theta x} \\ M_{\theta x} \\ P_{\theta x} \end{Bmatrix} = \int_{-h/2}^{h/2} \begin{Bmatrix} \sigma_{\theta\theta} \\ z\sigma_{\theta\theta} \\ z^3\sigma_{\theta\theta} \\ \sigma_{\theta x} \\ z\sigma_{\theta x} \\ z^3\sigma_{\theta x} \end{Bmatrix} dz$$

$$\begin{Bmatrix} Q_{xz} \\ R_{xz} \\ P_{xz} \end{Bmatrix} = \int_{-h/2}^{h/2} \begin{Bmatrix} \sigma_{xz} \\ z^2\sigma_{xz} \\ z^3\sigma_{xz} \end{Bmatrix} dz, \quad \begin{Bmatrix} Q_{\theta z} \\ R_{\theta z} \\ P_{\theta z} \end{Bmatrix} = \int_{-h/2}^{h/2} \begin{Bmatrix} \sigma_{\theta z} \\ z^2\sigma_{\theta z} \\ z^3\sigma_{\theta z} \end{Bmatrix} dz \tag{3.75}$$

It should be noted that the panel is assumed to be composed of ceramic and metal. The material properties of the panel of ceramic and metal are continuous functions of the radial and axial coordinates and the volume fractions of the constituents vary in a predetermined composition profile. The mathematical modelling for smooth variation of volume fractions will be elaborated in the next chapter. For reliable and accurate prediction of the structural response of 2-D FGM composites, temperature-dependent material properties are taken into account. Without loss of generality, a typical temperature-dependent material property *P*, such as the modulus of elasticity E, the thermal conductivity k and the thermal expansion coefficient α can be expressed as the non-linear functions of environment temperature $T(K)$ as [58]

$$P = P_0\left(P_{-1}T^{-1} + 1 + P_1T + P_2T^2 + P_3T^3\right) \tag{3.76}$$

where P_0, P_{-1}, P_1, P_2 and P_3 are constants in the cubic fit of the material property. The material properties are expressed in this way so that the higher order effects of the temperature on material properties can be readily discernible. The values of each of the coefficients appearing in the preceding equation are listed in Table 3.1 for titanium (Ti-6Al-4V) and zirconium oxide (ZrO_2). Substituting Eq. (2.17) for isotropic materials and Eq. (3.73) into Eq. (3.75) we have:

$$N_{xx} = A_{x0}\varepsilon^0_{xx} + A_{x1}\varepsilon'_{xx} + A_{x2}\varepsilon''_{xx} + A_{x3}\varepsilon'''_{xx} + T_{x0}$$

$$M_{xx} = A_{x1}\varepsilon^0_{xx} + A_{x2}\varepsilon'_{xx} + A_{x3}\varepsilon''_{xx} + A_{x4}\varepsilon'''_{xx} + T_{x1}$$

$$P_{xx} = A_{x3}\varepsilon^0_{xx} + A_{x4}\varepsilon'_{xx} + A_{x5}\varepsilon''_{xx} + A_{x6}\varepsilon'''_{xx} + T_{x3}$$

$$N_{x\theta} = B_{x0}\varepsilon^0_{x\theta} + B_{x1}\varepsilon'_{x\theta} + B_{x2}\varepsilon''_{x\theta} + B_{x3}\varepsilon'''_{x\theta}$$

$$M_{x\theta} = B_{x1}\varepsilon^0_{x\theta} + B_{x2}\varepsilon'_{x\theta} + B_{x3}\varepsilon''_{x\theta} + B_{x4}\varepsilon'''_{x\theta}$$

$$P_{x\theta} = B_{x3}\varepsilon^0_{x\theta} + B_{x4}\varepsilon'_{x\theta} + B_{x5}\varepsilon''_{x\theta} + B_{x6}\varepsilon'''_{x\theta}$$

$$N_{\theta\theta} = A_{x0}\varepsilon^0_{\theta\theta} + A_{x1}\varepsilon'_{\theta\theta} + A_{x2}\varepsilon''_{\theta\theta} + A_{x3}\varepsilon'''_{\theta\theta} + T_{\theta 0}$$

$$M_{\theta\theta} = A_{x1}\varepsilon^0_{\theta\theta} + A_{x2}\varepsilon'_{\theta\theta} + A_{x3}\varepsilon''_{\theta\theta} + A_{x4}\varepsilon'''_{\theta\theta} + T_{\theta 1}$$

$$P_{\theta\theta} = A_{x3}\varepsilon^0_{\theta\theta} + A_{x4}\varepsilon'_{\theta\theta} + A_{x5}\varepsilon''_{\theta\theta} + A_{x6}\varepsilon'''_{\theta\theta} + T_{\theta 3}$$

Table 3.1. Material properties of titanium and zirconium oxide.

Materials		P_0	P_{-1}	P_1	P_2	P_3
titanium	E (Pa)	1.22.56e+9	0	-4.586e-4	0	0
	α (1/K)	7.5788e-6	0	6.638e-4	-3.147e-6	0
	k (W/mK)	1	0	1.704e-2	0	0
	ν	0.3				
zirconium oxide	E (Pa)	244.27e9	0	-1.371e-3	1.214e-6	-3.681e-10
	α (1/K)	12.766e-6	0	-1.491e-3	1.006e-5	-6.778e-11
	k (W/mK)	1.7	0	1.276e-4	6.648e-8	0
	ν	0.3	0	0	0	0

$$Q_{xz} = B_{x0}\varepsilon_{xz}^{0} + B_{x1}\varepsilon_{xz}' + B_{x2}\varepsilon_{xz}'' + B_{x3}\varepsilon_{xz}'''$$

$$R_{xz} = B_{x2}\varepsilon_{xz}^{0} + B_{x3}\varepsilon_{xz}' + B_{x4}\varepsilon_{xz}'' + B_{x5}\varepsilon_{xz}'''$$

$$P_{xz} = B_{x3}\varepsilon_{xz}^{0} + B_{x4}\varepsilon_{xz}' + B_{x5}\varepsilon_{xz}'' + B_{x6}\varepsilon_{xz}'''$$

$$R_{\theta z} = B_{x2}\varepsilon_{\theta z}^{0} + B_{x3}\varepsilon_{\theta z}' + B_{x4}\varepsilon_{\theta z}'' + B_{x5}\varepsilon_{\theta z}'''$$

$$Q_{\theta z} = B_{x0}\varepsilon_{\theta z}^{0} + B_{x1}\varepsilon_{\theta z}' + B_{x2}\varepsilon_{\theta z}'' + B_{x3}\varepsilon_{\theta z}'''$$

$$P_{\theta z} = B_{x3}\varepsilon_{\theta z}^{0} + B_{x4}\varepsilon_{\theta z}' + B_{x5}\varepsilon_{\theta z}'' + B_{x6}\varepsilon_{\theta z}''' \tag{3.77}$$

where

$$A_{x0} = \int_{-h/2}^{h/2} \frac{E(x,z)}{1-\nu^2} dz \qquad A_{x1} = \int_{-h/2}^{h/2} \frac{E(x,z)z}{1-\nu^2} dz$$

$$A_{x2} = \int_{-h/2}^{h/2} \frac{E(x,z)z^2}{1-\nu^2} dz \qquad A_{x3} = \int_{-h/2}^{h/2} \frac{E(x,z)z^3}{1-\nu^2} dz$$

$$T_{x0} = -\int_{-h/2}^{h/2} \frac{E(x,z)\beta_{11}T}{1-\nu^2} dz \qquad T_{x1} = -\int_{-h/2}^{h/2} \frac{E(x,z)z\beta_{11}T}{1-\nu^2} dz$$

$$T_{x3} = -\int_{-h/2}^{h/2} \frac{E(x,z)z^3\beta_{11}T}{1-\nu^2} dz \qquad B_{x0} = \int_{-h/2}^{h/2} \frac{E(x,z)}{2(1+\nu)} dz$$

$$B_{x1} = \int_{-h/2}^{h/2} \frac{E(x,z)z}{2(1+\nu)} dz \qquad B_{x2} = \int_{-h/2}^{h/2} \frac{E(x,z)z^2}{2(1+\nu)} dz$$

$$B_{x3} = \int_{-h/2}^{h/2} \frac{E(x,z)z^3}{2(1+\nu)} dz \quad B_{x4} = \int_{-h/2}^{h/2} \frac{E(x,z)z^4}{2(1+\nu)} dz \qquad B_{x5} = \int_{-h/2}^{h/2} \frac{E(x,z)z^5}{2(1+\nu)} dz$$

$$B_{x6} = \int_{-h/2}^{h/2} \frac{E(x,z)z^6}{2(1+\nu)} dz \qquad T_{\theta 0} = -\int_{-h/2}^{h/2} \frac{E(x,z)\beta_{22}T}{1-\nu^2} dz$$

$$T_{\theta 1} = -\int_{-h/2}^{h/2} \frac{E(x,z)\beta_{22}T}{1-\nu^2}\,dz \qquad T_{\theta 3} = -\int_{-h/2}^{h/2} \frac{E(x,z)\beta_{22}z^3T}{1-\nu^2}\,dz \tag{3.78}$$

Now, using Hamilton principle the governing equations of the third order shear deformation theory of 2-D FGM cylindrical panel can be obtained as:

$$\frac{Z_m\partial N_{xx}}{\partial x} - \frac{\partial N_{x\theta}}{\partial \theta} = 0$$

$$\frac{\partial N_{\theta\theta}}{\partial \theta} + \frac{Z_m\partial N_{x\theta}}{\partial x} + Q_{\theta z} + \frac{n}{Z_m}\frac{\partial P_{\theta\theta}}{\partial \theta} + n\frac{\partial P_{x\theta}}{\partial x} - 3nR_{\theta z} + \frac{n}{Z_m}P_{\theta z} = 0$$

$$-nZ_m\frac{\partial^2 P_{xx}}{\partial x^2} + N_{\theta\theta} - \frac{n}{Z_m}\frac{\partial^2 P_{\theta\theta}}{\partial \theta^2} - n\frac{\partial^2 P_{x\theta}}{\partial x\partial \theta} - Z_m\frac{\partial Q_{xz}}{\partial x} + 3nZ_m\frac{\partial R_{xz}}{\partial x}$$

$$-\frac{\partial Q_{\theta z}}{\partial \theta} + 3n\frac{\partial R_{\theta z}}{\partial \theta} - \frac{n}{Z_m}\frac{\partial P_{\theta z}}{\partial \theta} = 0$$

$$\frac{Z_m\partial M_{xx}}{\partial x} - nZ_m\frac{\partial P_{xx}}{\partial x} + \frac{\partial M_{x\theta}}{\partial \theta} + n\frac{\partial P_{x\theta}}{\partial \theta} + 3nZ_mR_{xz} - RQ_{xz} = 0$$

$$\frac{\partial M_{\theta\theta}}{\partial \theta} + n\frac{\partial P_{\theta\theta}}{\partial \theta} - nP_{xx} - Z_m\frac{\partial M_{x\theta}}{\partial x} + nZ_m\frac{\partial P_{x\theta}}{\partial x} - 3nR_{\theta z} + Z_mQ_{\theta z} + nP_{\theta z} = 0 \tag{3.79}$$

In the present study, the following boundary conditions viz. Simply (S) support and Clamped (C) support at the $x = 0, L$ edges are assumed:

$$\text{S}: \quad v = w = \psi_2 = N_{xx} = M_{xx} = P_{xx} = 0$$

$$\text{C}: \quad u = v = w = \psi_1 = \psi_2 = \partial w/\partial x = 0 \tag{3.80}$$

Without the existence of heat sources, the equation of steady-state heat transfer is obtained as [95]:

$$\frac{\partial k}{\partial z}\frac{\partial T}{\partial z} + k\frac{\partial^2 T}{\partial z^2} + \left(\frac{Z_m}{Z_m+z}\right)^2 k\frac{\partial T^2}{\partial \theta^2} + \frac{\partial k}{\partial x}\frac{\partial T}{\partial x} + k\frac{\partial^2 T}{\partial x^2} + \frac{1}{Z_m+z}k\frac{\partial T}{\partial z} = 0 \tag{3.81}$$

where the thermal conductivity $k(z,x,T)$ is assumed to be temperature-dependent.

3.4 Summary and conclusions

In this chapter, theoretical formulations of various problems in free vibration, static, and thermal analyses of plates and shells composed of FGMs have been performed. Not only based on 3-D elasticity theory governing equations have been derived, but also 2-D plate theories have been used to formulate various problems. First of all, 3-D elasticity equations of motion for cylindrical panels composed of FG monoclinic materials, in a general form, have been derived. Derived formulations possess the potential to be simplified to cylindrical panels composed of FG orthotropic materials. Then, basic formulations for sandwich panels have been explained. Afterwards, the attention has been paid to formulations of FG rectangular plates and annular sectorial plates resting on elastic foundations based on 3-D elasticity theory. Contrary to 2-D plate theories, by using 3-D elasticity theory, the foundation has been applied on the lower surface of plates but not on the middle surface. This can cause more accurate results compared with 2-D theories [130]. In the next section, thermo-elastic governing equations for FG orthotropic cylindrical panels based on 3-D elasticity have been obtained. Formulating based on 2-D theories, the displacements were expanded in terms of thickness and transverse displacement was independent of the transverse coordinate. Based on FSDT, theoretical formulations for free vibration of CNT-reinforced plates have been carried out. Then, the equilibrium and stability equations for mechanical buckling of CNT-reinforced plates were derived using the FSDT and variational approach. Last but not least, for the first time, thermal stress analysis of a 2-D FGM cylindrical panel was formulated based on the Reddy's TSDT, and governing equations and heat conduction equation were derived.

Chapter 4

Mathematical modeling of FGMs

4.1 Overview

The main aim of this chapter is to present a comprehensive description of mathematical modeling of FGMs. For modelisation of volume fraction and fiber orientation, firstly, the classic form of power-law distribution will be described. Furthermore, various profiles for volume fractions of CNT in FG CNT-reinforced composites are introduced. Afterwards, 1-D and 2-D generalized power-law distribution are presented and discussed. In the end, commonly used homogenization methods to compute effective material properties in composites and nanocomposites are presented.

4.2 Power-law distribution

Although FGMs are highly heterogeneous, it is very useful to idealize them as continua with their mechanical properties changing smoothly with respect to the spatial coordinates [154]. The homogenization schemes are necessary to simplify their complicated heterogeneous microstructures in order to analyze FGM in an efficient manner. The distribution of material in FG structures may be designed to various spatial specifications by using power-law distribution. In the following, we aim to present the classic from of power-law distribution that can be found in most literature. Subsequently, the generalization form will be explained and benefits over classic one are discussed.

4.2.1 Classic power-law distribution

Since the volume fraction of each phase in FGMs gradually varies in the gradation direction, the effective properties of FGMs change along this direction. Therefore, there are two possible approaches to model FGMs. For the first choice, a piecewise variation of the volume fraction of ceramic or metal is assumed, and the FGM is taken to be layered with the same volume fraction in each region, i.e., quasihomogeneous ceramic-metal layers, as shown in Figure 4.1a. For the second choice, as Reddy and his collaborators [155-157] as well as numerous other researchers [158,159] assumed, a continuous variation of the volume fraction is represented, depicted in Figure 4.1b, and the volume fraction can be represented as the following function of the thickness coordinate. Herein, for the fiber-reinforced composite cylindrical panel shown in Figure 3.1, we assume the following classic power-law distribution of the reinforcement volume fraction [156]:

$$V = V_i + (V_o - V_i)\left(\frac{r - r_i}{r_o - r_i}\right)^p \tag{4.1}$$

where V_i and V_o which have values that range from 0 to 1, denote the volume fractions on the inner and outer surfaces, respectively. The exponent p controls the

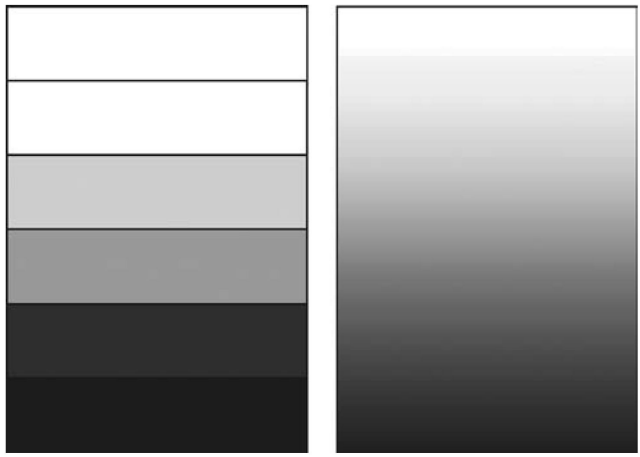

(a) **(b)**

Figure 4.1. Modeling of FGM: a) piecewise variation, b) continuous variation of the volume fraction.

volume fraction profile through the shell's thickness. The volume fraction profile through the thickness is illustrated in Figure 4.2. In this figure, it is assumed that the

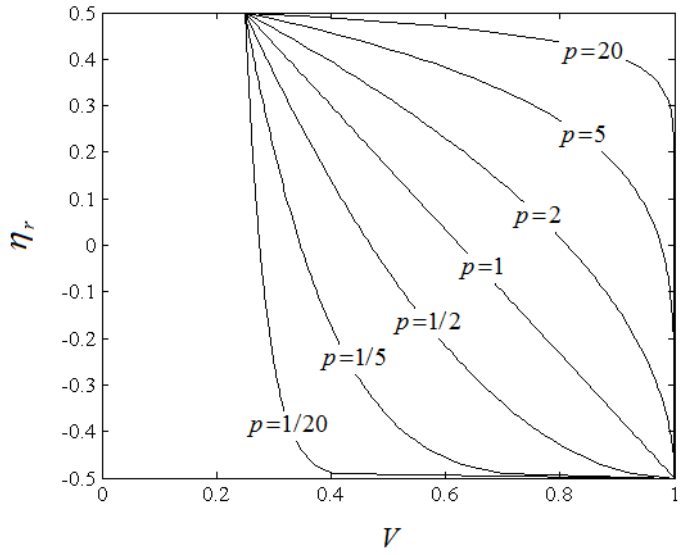

Figure 4.2. Variations of the volume fraction of the matrix phase V through the thickness for different values of p.

matrix volume fractions for an orthotropic shell with graded fiber volume fraction are $V_i = 1$ (100% matrix constituent) and $V_o = 0.25$ (25% matrix constituent) on the inner and outer surfaces, respectively. It is noted that η_r is a non-dimensional radial component $\left(\eta_r = (r-R)/h\right)$. In this figure, the matrix volume fraction decreases from 1 at $\eta_r = -0.5$ to 0.25 at $\eta_r = 0.5$. At η_r away from $\eta_r = 0.5$, the rate of increase of the matrix volume fraction for $p < 1$ is high compared to $p > 1$ and at η_r closer to $\eta_r = 0.5$ the rate of increase of the matrix volume fraction for $p > 1$ is much higher than for $p < 1$.

On the other hand, in fiber-reinforced composites, fiber orientation ϕ with respect to the *z*-axis in the $z-\theta$ surface can vary through the thickness by the following classic power-law:

$$\phi = \phi_i + (\phi_o - \phi_i)\left(\frac{r - r_i}{r_o - r_i}\right)^q \tag{4.2}$$

where ϕ_i and ϕ_0 denote the fiber orientations on the inner and outer surfaces, respectively and may typically range from 0^0 to 90^0. The power q denotes the

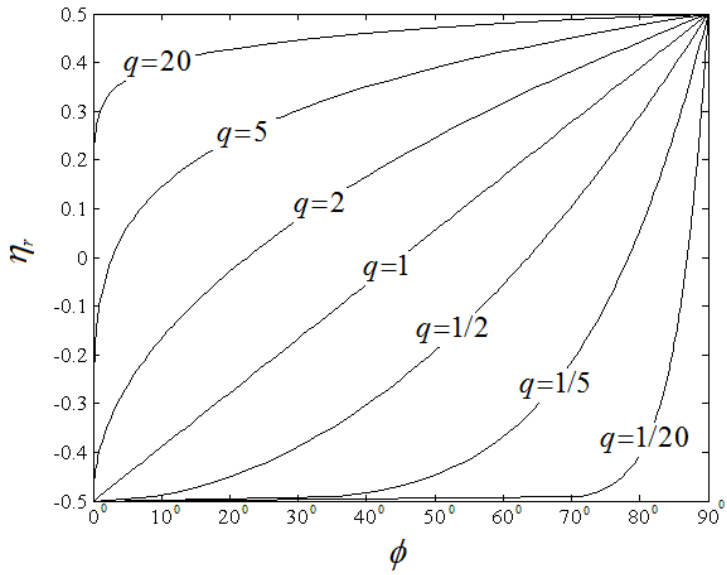

Figure 4.3. Variations of the fiber orientations (ϕ) through the thickness for different values of *q*.

manner in which the orientation of the fibers varies through the shell's thickness. Figure 4.3 shows the variations of the fiber orientations through the thickness. In this figure the fiber orientations are assumed as $\phi_i = 0^0$ and $\phi_0 = 90^0$ on the inner and outer surfaces respectively. It is noticed that the fiber orientation increases from 0^0 at $\eta_r = -0.5$ to 90^0 at $\eta_r = 0.5$. At η_r away from $\eta_r = -0.5$, the rate of increase of the fiber orientation for $q > 1$ is considerably high, compared to $q < 1$, and at locations closer to $\eta_r = -0.5$ the rate of increase of the fiber orientation for $q < 1$ is much higher than that of $q > 1$.

In order to study the effect of different CNTs distribution on the free vibration characteristics of FG CNT-reinforced composites, various types of material profiles through the shell thickness are considered. We assume linear distribution of CNTs volume fraction for the different types of the nanocomposite cylindrical panel as follows:

$$\text{Profile}-\text{V}: \quad V_f = 2\left(\frac{r-R}{h} + 0.5\right)V_{CN}^* \tag{4.3}$$

$$\text{Profile}-\Lambda: \quad V_f = -2\left(\frac{r-R}{h} - 0.5\right)V_{CN}^* \tag{4.4}$$

$$\text{Profile}-\text{X}: \quad V_f = 4\left(\frac{|r-R|}{h}\right)V_{CN}^* \tag{4.5}$$

$$\text{Profile}-\Diamond: \quad V_f = 4\left(0.5 - \frac{|r-R|}{h}\right)V_{CN}^* \tag{4.6}$$

where V_{CN}^* is the volume fraction of CNTs [160] that is calculated from the mass fraction of nanotubes, m_f, assuming two phases and no trapped air, using:

$$V_{CN}^* = \left[\frac{\rho_r}{m_f} - \rho_r + 1\right]^{-1} \tag{4.7}$$

where $\rho_r = \rho_f / \rho_m$ is the ratio of nanotube to matrix density. Note that $V_f = V_{CN}^*$ corresponds to the uniformly distributed CNT-reinforced cylindrical panel, referred to as Profile$-$UD. With V_{CN}^* defined in Eq. (4.7), both the FG shell and

Profile−UD shell have the same value of CNTs mass fraction. For type V, the outer surface of the shell is CNT-rich, referred to as Profile−V. As can be seen from Figure 4.4, for Type Λ, the distribution of CNTs reinforcements is inversed and the inner surface of the shell is CNT-rich, referred to as Profile−Λ. For Type X, a mid-plane symmetric graded distribution of CNTs reinforcements is achieved and both outer and inner surfaces are CNT-rich, referred to as Profile−X. For Type ◊, the distribution of CNTs reinforcements is inversed and both outer and inner surfaces are CNT-poor, whereas the reference surface is CNT-rich, referred to as Profile−◊.

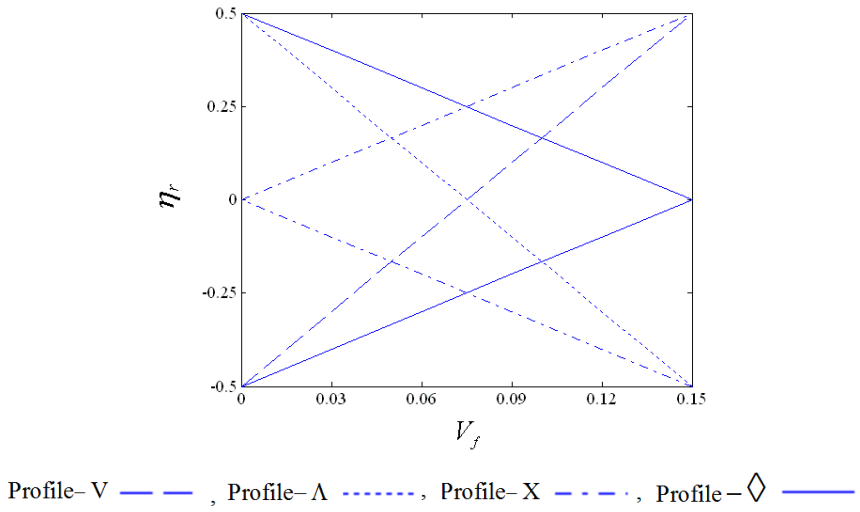

Figure 4.4. Variations of CNTs volume fractions through the thickness for different types of CNT distributions.

4.2.2 Generalized power-law distribution

In the last years, in most studies dedicated to studying of mechanical responses of FGMs, it was assumed that material properties follow a through-thickness variation according to a classic power-law distribution in terms of the volume fractions of constituents. Shah et al. [161] studied the vibration frequency analysis by proposing a volume fraction law in a general exponential form. A comparative study of shell frequencies was given by Arshad et al. [162] for polynomial, exponential, and trigonometric power-law distribution. Viola and Tornabene [163] presented three-

parameter power-law distribution for dynamic behaviour of moderately thick functionally graded parabolic panels of revolution. Further studies were done on free vibrations of four-parameter functionally graded parabolic panels and shells by Viola and Tornabene [164] and Tornabene [165]. Vel [73] proposed a power-law distribution for sigmoidal variation of fibers through the thickness of the FGM shell. In the following, we will introduce brand-new generalized power-law distribution for defining variation of volume fraction or fiber orientation in FGMs composites. By using generalized power-law distribution, it is possible to study the effect of the different kinds of material profiles including symmetric, asymmetric and classic on mechanical behavior of a FGM structures. Furthermore, distribution and magnitude of thermal stresses/frequency characteristics or modal displacements can be reduced/increased to a required manner by selecting appropriate different parameters of power-law distribution and volume fractions profiles in the required direction(s). Another advantage of generalized power-law distribution is to have a desirable volume fraction of the material on the inner or outer surface while we have a smooth gradation of volume fraction through the required direction.

4.2.2.1 1-D generalized power-law distribution

For an orthotropic material, the volume fraction of the matrix phase is given by the

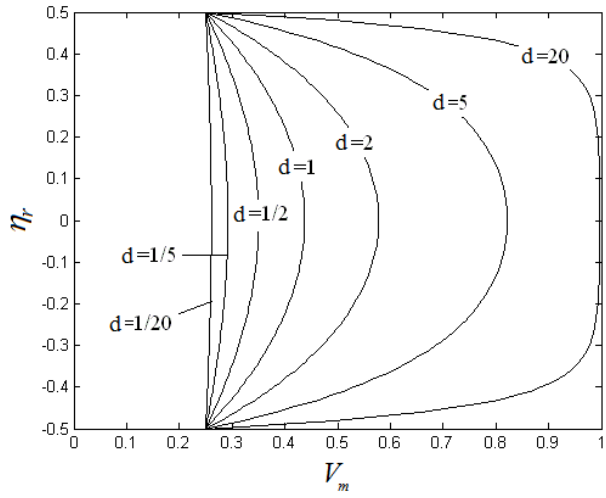

Figure 4.5. Variations of the volume fractions of the matrix phase V_m through the thickness for different values of the power-law index d (a=1, b=1, c=2)

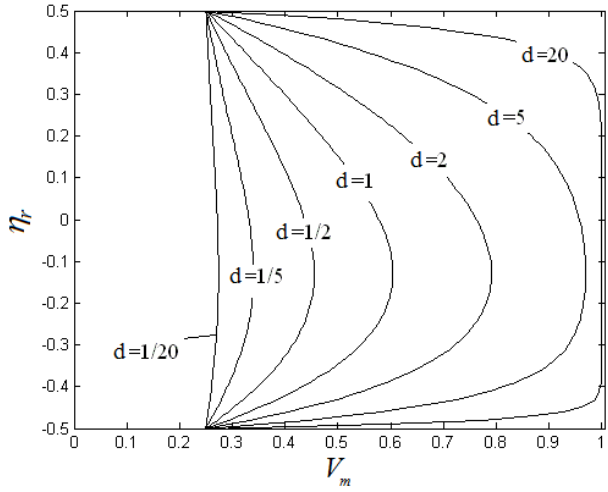

Figure 4.6. Variations of the volume fractions of the matrix phase V_m through the thickness for different values of the power-law index d (a=1, b=1, c=4)

following function:

$$V_m = V_i + (V_0 - V_i)V_{fm} \tag{4.8}$$

Now, for variation of V_{fm} through the thickness of the shell, 1-D generalized power-law distribution is introduced as:

$$V_{fm} = \left(1 - a\left(\frac{1}{2} - \frac{r-R}{H}\right) + b\left(\frac{1}{2} - \frac{r-R}{H}\right)^c\right)^d \tag{4.9}$$

where the volume fraction index d $(0 \le d \le \infty)$ and the parameters a, b, c dictate the material variation profile through the shell thickness. For example, if we assume $V_i = 1$ and $V_o = 0.25$, some material profiles through the thickness are illustrated in Figures 4.5 to 4.8. The classical volume fraction profile are presented as special case of the general distribution laws (4.9) by setting a=1 and b=0, as shown in Figure 4.2.

With another choice of the parameters a, b, c, it is possible to obtain symmetric and

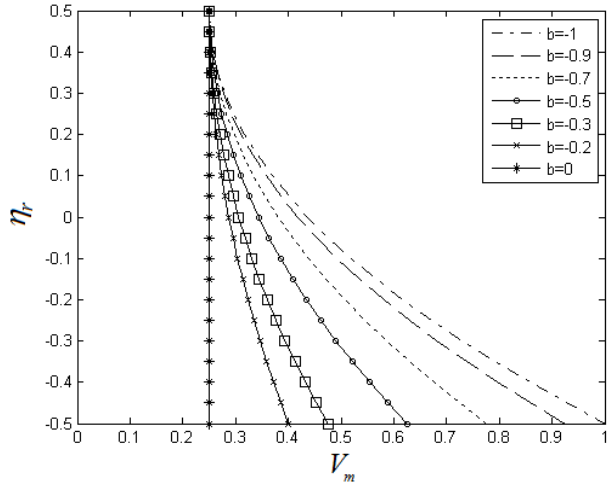

Figure 4.7. Variations of the volume fractions of the matrix phase V_m through the thickness for d=1 **(**a=0, c=2**)**

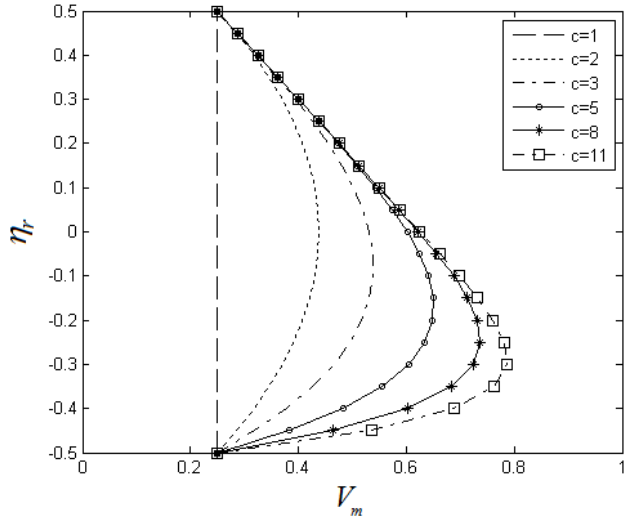

Figure 4.8. Variations of the volume fractions of the matrix phase V_m through the thickness for d=1 **(**a=1, b=1**)**

asymmetric volume fraction profiles as shown in Figures 4.5 to 4.8. In Figure 4.5, by setting a=1, b=1, and c=2 in Eq. (4.9) symmetric volume fraction with respect to the

reference surface is obtained. Figure 4.6 illustrates asymmetric profiles obtained by setting *a*=1, *b*=1 and *c*=4. As shown from figures under consideration, we have the same constituent at the inner and outer surface but, unlike the previous case (Figure 4.5), profiles are not symmetric with respect to the reference surface of the panel. Figures 4.7 and 4.8 show various power-law distributions obtained by modifying parameters *b* and *c*. These profiles are characterized by the fact that on the outer surface we have $V_m = V_o$, while inner surface presents a mixture of V_i and V_o (volume fractions of the matrix phase orthotropic material 1 and 2). In Figure 4.7, by varying parameter *b*, profile of the matrix volume fraction along the thickness as well as matrix volume fraction on the inner surface alters. This interesting trend cannot be seen by using classic power-law distribution. In Figure 4.8, matrix phase volume fraction profile along radial direction became asymmetric with increasing parameter *c*, also matrix phase volume fraction on the inner and outer surface for the different values of parameter *c* is the same $(V_m = V_o)$.

In the following, by using generalized power-law distribution, mathematical modeling for material profiles of FGSW panel, as depicted in Figure 3.6, is introduced. It is assumed that the fiber orientation ϕ of each layer has the following power-law variation:

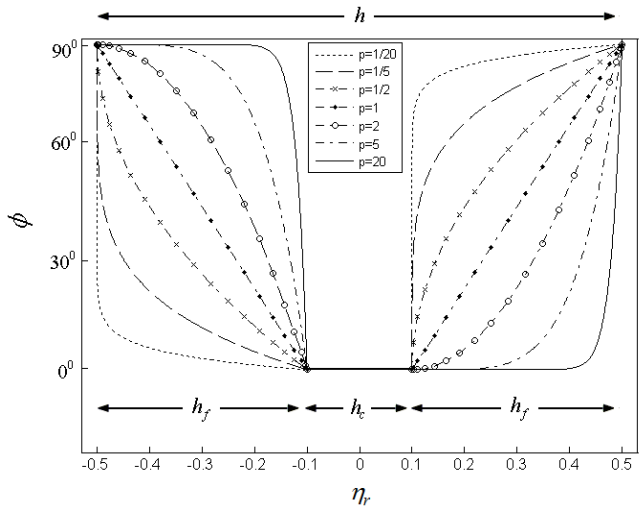

Figure 4.9. Variations of the fiber orientation through the thickness in the FGSW panel for different values of the power-law index *p* (*a*=1, *b*=0, $\phi_i = 0^0$, $\phi_o = 90^0$)

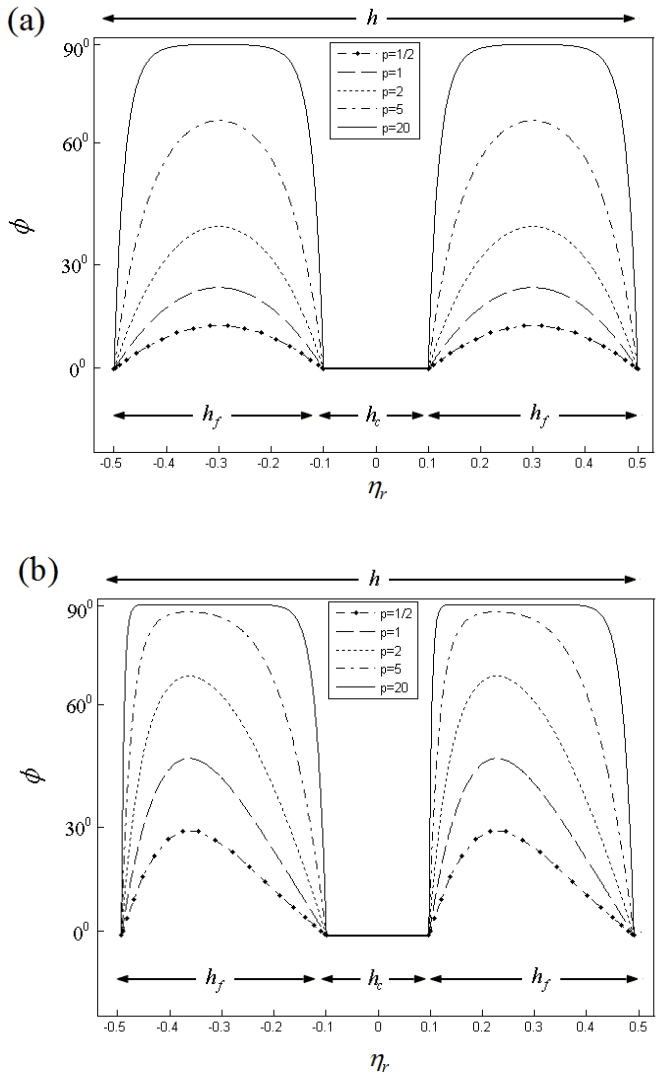

Figure 4.10. Variations of the fiber orientation through the thickness for different values of the power-law index p (**(a):** a=1, b=1, c=2 ; **(b):** a=1, b=1, c=5 , $\phi_i = 90^0, \phi_o = 0^0$)

$$\phi(r)=\begin{cases} 90^0\left(1-\left(1-a\left(\frac{1}{2}-\frac{r-R_1}{h_f}\right)+b\left(\frac{1}{2}-\frac{r-R_1}{h_f}\right)^c\right)^p\right), & r_i \le r \le r_i+h_f \\ 0^0\ , & r_i+h_f \le r \le r_o-h_f \\ \phi_i+(\phi_o-\phi_i)\left(1-a\left(\frac{1}{2}-\frac{r-R_3}{h_f}\right)+b\left(\frac{1}{2}-\frac{r-R_3}{h_f}\right)^c\right)^p, & r_o-h_f \le r \le r_o \end{cases} \tag{4.10}$$

where ϕ_i and ϕ_o denote the fiber orientation of two different orthotropic materials. The power-law index *p* and the parameters *a*, *b*, *c* dictate the fiber orientation variation profile through the FGSW shell thickness. The through-thickness variations of the fiber orientation for some profiles are illustrated in Figures 4.9 to 4.12. In Figure 4.9, the classical fiber orientation profile is presented as special cases of the general distribution laws (4.10) by setting *a*=1 and *b*=0. With another choice of the parameters *a*, *b*, *c*, it is possible to obtain symmetric and asymmetric fiber orientation profiles as shown in Figure 4.10. In Figure 4.10a, by setting *a*=1, *b*=1, and *c*=2, the fiber orientation distribution presents the same profiles by varying the power-law index *p* and are symmetric with respect to the reference surfaces of top and bottom

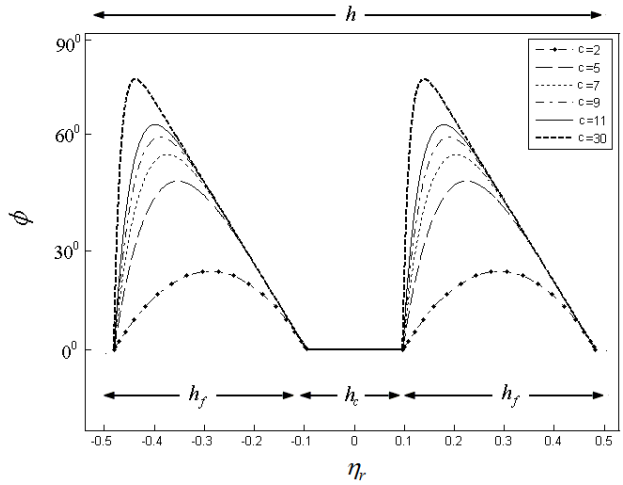

Figure 4.11. Variations of the fiber orientation through the thickness in the FGSW panel (*p*=1, *a*=1, *b*=1, $\phi_i = 90^0$, $\phi_o = 0^0$)

faces of the shell. Figure 4.10b illustrates asymmetric profiles obtained by setting a=1, b=1 and c=5. Fiber orientation profile for the different values of parameters c is shown in Figure 4.11 by considering p=1. In Figure 4.11, fiber orientation profile along radial direction became asymmetric with increasing parameter c, also fiber orientation on the inner and outer surfaces of top and bottom faces for the different values of parameter c is the same. The fiber volume fraction of FGSW panel is assumed as follows:

$$V_f(r)=\begin{cases} V_i\ , & r_i \le r \le r_i + h_f \\ V_i + (V_o - V_i)\left(\dfrac{r-R}{h_c}\right)^q\ , & r_i + h_f \le r \le r_o - h_f \\ V_o\ , & r_o - h_f \le r \le r_o \end{cases} \tag{4.11}$$

The exponent q governs the through-thickness fiber volume fraction profile. The through-thickness variations of the fiber volume fractions are depicted in Figure 4.12. As shown in Figure 4.12, the fiber volume fraction of core varies from 0.2 to 0.8 as η_r varies from $-h_c/2$ to $+h_c/2$, while the fiber volume fractions of top and

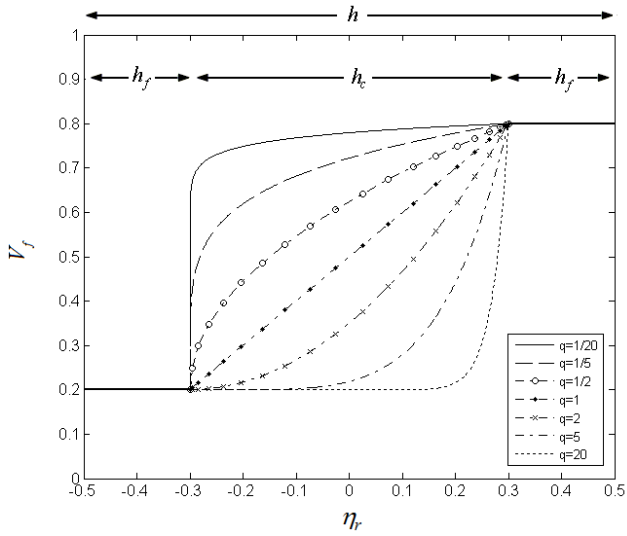

Figure 4.12. Variations of the fiber volume fraction through the thickness in the FGSW panel for different values of the power-law index q ($V_i = 0.2, V_0 = 0.8$)

bottom faces are 0.8 and 0.2, respectively. The rate of increments in V_f depends on values of thickness variable η_r and power-aw exponent *q*.

4.2.2.2 2-D generalized power-law distribution

For the 2-D FGMs, the material properties are continuous functions of the coordinates and the volume fractions of the constituents vary in a predetermined composition profile in two directions. Consider a two-phase graded material with a power law variation of the volume fraction of the constituents through the radial and axial directions of the cylindrical panel, which was depicted in Figure 3.1. It is proposed that the volume fraction of the ceramic phase follows 2-D six-parameter power-law distribution:

$$V_c = \left((V_o - V_i)\left(\left(\frac{1}{2} - \frac{r-R}{r_o - r_i} \right) + \alpha_z \left(\frac{1}{2} + \frac{r-R}{r_o - r_i} \right)^{\beta_r} \right)^{\gamma_r} + V_a \right) \left(1 - \left(\frac{z}{L} \right) + \alpha_z \left(\frac{z}{L} \right)^{\beta_z} \right)^{\gamma_z} \tag{4.12}$$

where the radial volume fraction index γ_r, the axial volume fraction index γ_z and

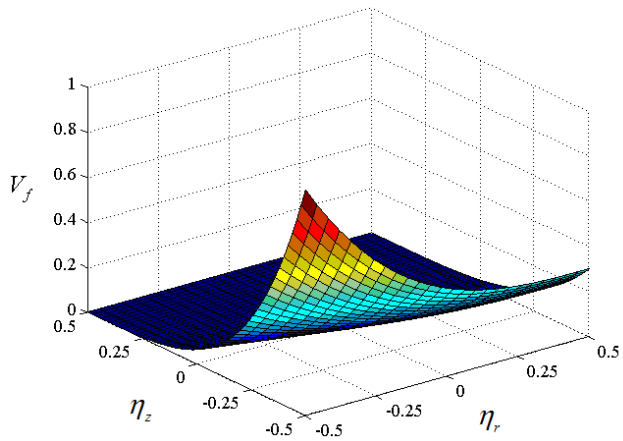

Figure 4.13. Variations of the classical volume fraction profile through the radial and axial directions $(\alpha_r = \alpha_z = 0,\ \gamma_r = \gamma_z = 4)$

parameters α_r , $\beta_r, \alpha_z, \beta_z$ govern the material variation profile through the radial and axial directions, respectively. With assumption $V_o = 1$ and $V_i = 0.3$, some material profiles through the radial and axial directions are illustrated in Figures 4.13 to 4.15. As can be seen from Figure 4.13, the classical volume fraction profile through the radial and axial directions are presented as special case of the 2-D power-law distribution, Eq. (4.12), by setting $\alpha_r = \alpha_z = 0$ and $\gamma_r = \gamma_z = 4$. In Figure 4.13, for the 2-D power-law distribution, Eq. (4.12), the ceramic volume fraction decreases through the thickness from 1 at $\eta_r = -0.5$ to 0.3 at $\eta_r = 0.5$.

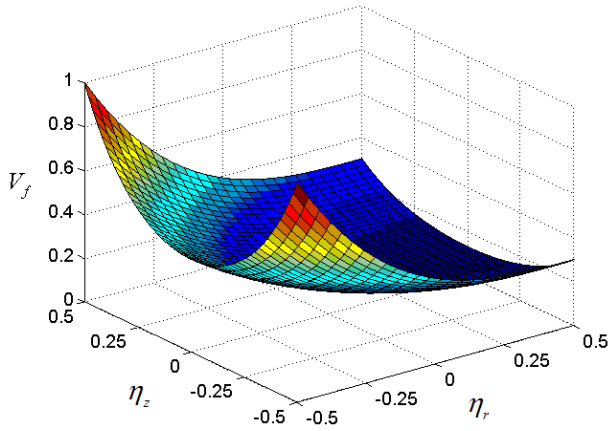

Figure 4.14. Variations of the volume fraction profile through the radial and axial directions $(\gamma_r = \gamma_z = 3, \alpha_r = 1, \beta_r = 2, \alpha_z = 0)$

Likewise, the ceramic volume fraction decreases through the axial direction from 1 at $\eta_z = -0.5$ to 0 at $\eta_z = 0.5$. With another choice of the parameters $\alpha_r, \beta_r, \alpha_z$ and β_z, it is possible to obtain symmetric volume fraction profiles through the radial and axial directions as shown in Figure 4.14. Classical and symmetric profiles through the radial and axial directions are obtained by setting $\alpha_r = 0, \alpha_z = 1$ and $\beta_z = 2$ in

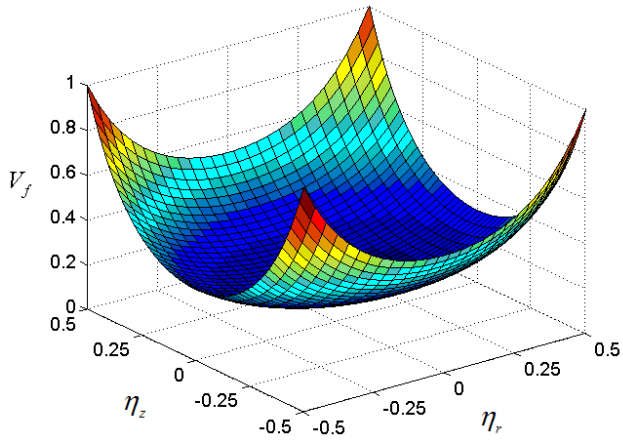

Figure 4.15. Variations of the symmetric volume fraction profiles through the radial and axial directions $(\alpha_r = \alpha_z = 1, \beta_r = \beta_z = 2, \gamma_r = \gamma_z = 3)$

Eq. (4.12). Figure 4.14 shows classic profile versus η_r and symmetric profile versus η_z . As observed the ceramic volume fraction on the lower edge is the same as that on the upper edge. Figure 4.15 illustrates symmetric profiles through the radial and axial directions obtained by setting $\alpha_r = 1, \alpha_z = 1$ and $\beta_r = 2, \beta_z = 2$ .Now we introduce a new-brand of 2-D power-law distribution, which allows to study the impact of the various kinds of two directional material profiles including sigmoidal radial variation as well as symmetrical or classical variation. This model permits volume fraction of conventional 1-D FGM to have a sigmoidal radial variation, as a special case of 2-D power-law distribution, and the volume fraction of the ceramic phase approaches a discretely laminated composite with a sharp transition in contained quantity of ceramic at the midsurface by increasing sigmoid exponent. For the cylindrical panel shown in Figure 3.7, it is propounded that the volume fraction of the ceramic phase follows 2-D power-law distribution:

$$V_c = \left((V_b - V_a) \left(\frac{e^{s((z/h)+0.5)} - 1}{\left(e^{s/2} - 1\right)\left(e^{s(z/h)} + 1\right)} \right) - V_a \right)^{\gamma_z} \left(1 - \frac{x}{L} + \alpha_x \left(\frac{x}{L} \right)^{\beta_x} \right)^{\gamma_x} \tag{4.13}$$

where the sigmoid exponent *s*, radial volume fraction index γ_z, the parameters α_x, β_x and axial volume fraction index γ_x govern the material variation profile through the radial and axial directions, respectively. By considering Eq. (4.13),

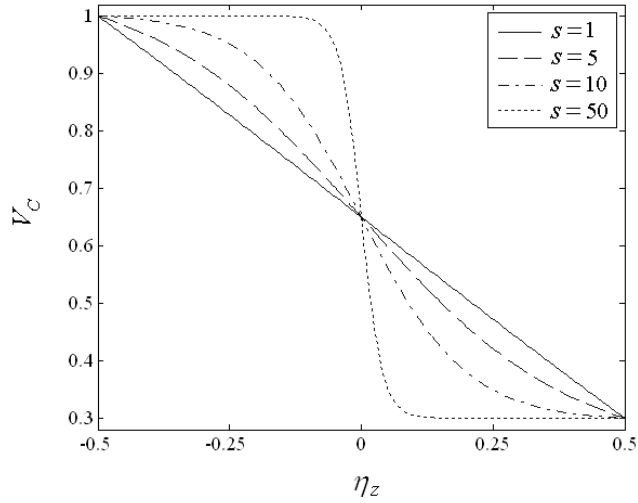

Figure 4.16. Sigmoidal radial variation of ceramic volume fraction for 1-D FGM corresponding to different sigmoid exponents $(\gamma_z = 1,\ \gamma_x = 0)$

when the axial volume fraction index γ_x is set equal to zero, 1-D FGM with sigmoidal radial variation is obtained as a special case of 2-D power-law distribution. The radial variation of the ceramic volume fraction is shown in Figure 4.16 for four different sigmoid exponents *s*=1, 5, 10 and 50. The volume fraction of the ceramic phase has an almost linear variation from 1 to 0.3 in radial direction when *s*=1. As the sigmoid exponent *s* increases, the ceramic volume fraction approaches a discrete [1/0.3] laminate with a sharp transition in ceramic volume fraction from 1 to 0.3 at the midsurface. With appropriate choice of the parameters α_x and β_x, it is possible to obtain classical and symmetrical volume fraction profiles through the axial direction while ceramic volume fraction has a sigmoidal variation through the radial direction as shown in Figures. 4.17a and 4.17b. Classical and symmetrical profiles through the axial directions are obtained by setting $\alpha_x = 0$ and $\alpha_x = 1, \beta_x = 2$ in Eq. (4.13), respectively. In Figure 4.17a, the ceramic volume fraction decreases through the thickness from 1 at $\eta_z = -0.5$ to 0.3 at $\eta_z = 0.5$ with a sigmoid variation. Similarly, the ceramic volume fraction decreases through the axial direction from 1 at $\eta_x = -0.5$ to 0 at $\eta_x = 0.5$. As can be seen from Figure 4.17b, the ceramic volume fraction profile is symmetric with respect to the reference surface

$\eta_x = 0$ of the shell. Furthermore, this distribution is characterized by the fact that volume fraction varies gradually according to the sigmoidal variation through the radial direction.

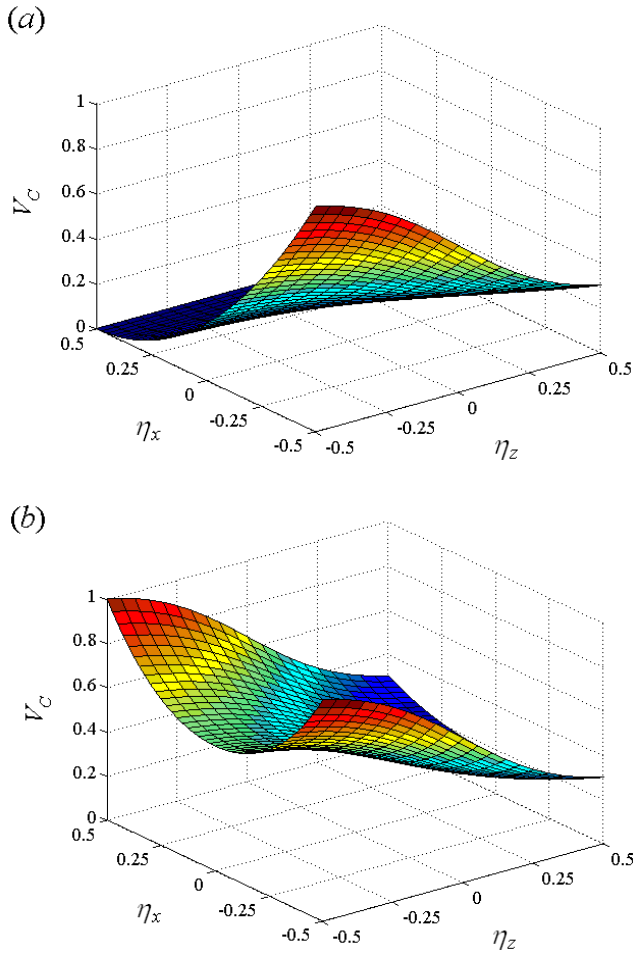

Figure 4.17. Variations of the ceramic volume fraction profile through the radial and axial directions ($\gamma_z = 1, s = 5, \gamma_x = 2$) (Fig. (**a**): $\alpha_x = 0$, Fig. (**b**): $\alpha_x = 1, \beta_x = 2$)

4.3 Effective material properties

Conventional composite materials generally consist of a suspension of discrete reinforcements distributed in a continuous matrix with a more or less constant volume fraction. FG composite structures often possess large variations in constituent material volume fractions through the structure. Several homogenization methods have been developed over the years to infer the effective properties of FG composite materials. The principal difference in the results available from various micromechanical models is related to the degree of those methods, which account for the interactions of adjacent inclusions. After modelling the variation of volume fractions within the FG composite in sections 4.1 and 4.2, herein various homogenization methods for determining effective material properties of the FG composite are summarized.

4.3.1 Rule of Mixture

A general from of rule of mixtures is a weighted mean used to predict various properties of a composite material. In isotropic material, the effective material properties P_f of the FG composite, like Young's modulus and thermal expansion coefficient, can then be expressed as [154]

$$P_f = \sum_{j=1} P_j V_j \tag{4.14}$$

where P_j and V_j are the material properties and volume fraction of the constituent material *j*, and the sum of the volume fractions of all the constituent materials makes 1, i.e.,

$$\sum_{j=1} V_j = 1 \tag{4.15}$$

In orthotropic material, the effective mechanical properties of the fiber-reinforced composites is obtained based on a new form of rule of mixture as follows [166, 167]:

$$E_{11} = V_f E_{11}^f + V_m E_{11}^m \tag{4.16}$$

$$\frac{1}{E_{ii}} = \frac{V_f}{E_{ii}^f} + \frac{V_m}{E_{ii}^m} - V_f V_m \frac{{v_f}^2 E_{ii}^m \big/ E_{ii}^f + {v_m}^2 E_{ii}^f \big/ E_{ii}^m - 2 v^f v^m}{V_f E_{ii}^f + V_m E_{ii}^m} \quad (i = 2,3) \tag{4.17}$$

$$\frac{1}{G_{ij}} = \frac{V_f}{G_{ij}^f} + \frac{V_m}{G_{ij}^m} \qquad (\mathrm{ij} = 12, 13 \text{ and } 23) \tag{4.18}$$

$$v_{ij} = V_f v^f + V_m v^m \qquad (\mathrm{ij} = 12, 13 \text{ and } 23) \tag{4.19}$$

$$\rho = V_f \rho^f + V_m \rho^m \tag{4.20}$$

Where E_{ii}^f, G_{ij}^f, ν^f and ρ^f are elasticity modulus, shear modulus, Poisson's ratio and density, respectively, of the fiber, and E_{ii}^m, G_{ij}^m, ν^m and ρ^m are corresponding properties for the matrix. V_f and V_m are the fiber and matrix volume fractions and are related by $V_f + V_m = 1$.

4.3.2 Mori-Tanaka method

The Mori-Tanaka scheme [168,169] for estimating the effective moduli is applicable to regions of the graded microstructure, which have a well-defined continuous matrix and a discontinuous particulate phase. It takes into account the interaction of the elastic fields among neighbouring inclusions. It is assumed that the matrix phase, denoted by the subscript *m*, is reinforced by spherical particles of a particulate phase, denoted by the subscript *c*. In this notation, K_m and G_m are the bulk modulus and the shear modulus, respectively, and V_m is the volume fraction of the matrix phase. K_c, G_c and V_c are the corresponding material properties and the volume fraction of the particulate phase. Note that $V_m + V_c = 1$, that the Lame constant λ is related to the bulk and the shear moduli by $\lambda = K - 2G/3$, and that the stress-temperature modulus is related to the coefficient of thermal expansion by $\beta = (3\lambda + 2G)\alpha = 3K\alpha$. The following estimates for the effective local bulk modulus *K* and shear modulus *G* are useful for a random distribution of isotropic particles in an isotropic matrix:

$$\frac{K - K_m}{K_c - K_m} = \frac{V_c}{1 + (1 - V_c)(K_c - K_m)/(K_m + (4/3)K_m)} \tag{4.21}$$

$$\frac{G - G_m}{G_c - G_m} = \frac{V_c}{1 + (1 - V_c)(G_c - G_m)/(G_m + f_m)} \tag{4.22}$$

where $f_m = G_m(9K_m + 8G_m)/6(K_m + 2G_m)$. The effective values of Young's modulus, E, and Poisson's ratio, ν, are found from:

$$E = \frac{9KG}{3K + G}, \qquad \nu = \frac{3K - 2G}{2(3K + G)} \tag{4.23}$$

The effective thermal conductivity k is given by:

$$\frac{k-k_m}{k_c-k_m}=\frac{V_c}{1+(1-V_c)(k_c-k_m)/3k_m} \tag{4.24}$$

and the coefficient of thermal expansion α is determined from the correspondence relation:

$$\frac{\alpha-\alpha_m}{\alpha_c-\alpha_m}=\frac{1/K-1/K_m}{1/K_c-1/K_m} \tag{4.25}$$

4.3.3 Extended rule of mixture

To determine the effective material properties of CNT-reinforced composites, the rule of mixtures is the simplest and most intuitive approach. But direct application of rule of mixture to CNT-reinforced composites leads us to overestimate results comparing with results of long embedded CNT [170]. The load transfer between the CNT and polymeric phases is less than perfect (e.g. the surface effects, strain gradients effects, intermolecular coupled stress effects, etc.) [171,172]. Hence, Shen [141] introduced the CNT efficiency parameter η_i (i = 1, 2, 3) in the classic form of the rule of mixtures to consider the small scale effect and other effects on the material properties of CNT-reinforced composites. The values of η_i were determined later by matching the elastic moduli of CNT-reinforced composites predicted by molecular dynamics (MD) simulations with the prediction of the extended rule of mixture.

According to the extended rule of mixture, the effective Young's modulus and shear modulus of FG composites reinforced by aligned CNTs are expressed by the following relations [141]:

$$E_{11}=\eta_1 V_f E_{11}^f+V_m E^m \tag{4.26}$$

$$\frac{\eta_2}{E_{22}}=\frac{V_f}{E_{22}^f}+\frac{V_m}{E^m} \tag{4.27}$$

$$\frac{\eta_3}{G_{12}}=\frac{V_f}{G_{12}^f}+\frac{V_m}{G^m} \tag{4.28}$$

where E_{11}^f , E_{22}^f and G_{12}^f are the Young's and shear moduli of the CNTs, E^m and G^m are the corresponding properties for the matrix, and the η_i (i =1,2,3) are the

CNT efficiency parameters, respectively. V_f and V_m are the fiber and matrix volume fractions, respectively, and for FG CNT-reinforced composites, V_f and V_m vary through the thickness according to Eqs. (4.3) to (4.6). It is worth noting that in most available studies on the FG CNT-reinforced composites, the material properties are assumed to be graded in the thickness direction, and are estimated through the extended rule of mixture. However, the extended rule of mixture is not applicable when CNTs aggregates in the matrix or are dispersed in the matrix as randomly oriented dispersion.

4.3.4 Eshelby-Mori-Tanaka approach

The Eshelby-Mori-Tanaka approach, based on the equivalent elastic inclusion idea of Eshelby [173] and the concept of average stress in the matrix due to Mori and Tanaka [168], is also known as the equivalent inclusion-average stress method. The equivalent continuum model based on the Eshelby-Mori-Tanaka approach has been widely used in literature to predict effective material properties of CNT-reinforced composites [174-176]. In this thesis, Eshelby-Mori-Tanaka approach is also used to determine the effective material properties of CNT-reinforced composites. According to types of CNTs dispersion within the matrix phase, the following discussion is categorized as aligned CNTs, randomly oriented CNTs, and agglomerated CNTs.

4.3.4.1 Aligned carbon nanotubes

We consider first a polymer composite reinforced with aligned CNTs. The matrix is assumed to be elastic and isotropic, with Young's modulus E_m and Poisson's ratio ν_m . Each straight CNT is modeled as a long fiber with transversely isotropic elastic properties [147]. Therefore, the composite is also transversely isotropic, and its constitutive relation can be expressed as:

$$\begin{Bmatrix} \sigma_{11} \\ \sigma_{22} \\ \sigma_{33} \\ \sigma_{23} \\ \sigma_{13} \\ \sigma_{12} \end{Bmatrix} = \begin{bmatrix} k+m & l & k-m & 0 & 0 & 0 \\ l & n & l & 0 & 0 & 0 \\ k-m & l & k+m & 0 & 0 & 0 \\ 0 & 0 & 0 & p & 0 & 0 \\ 0 & 0 & 0 & 0 & m & 0 \\ 0 & 0 & 0 & 0 & 0 & p \end{bmatrix} \begin{Bmatrix} \varepsilon_{11} \\ \varepsilon_{22} \\ \varepsilon_{33} \\ \gamma_{23} \\ \gamma_{13} \\ \gamma_{12} \end{Bmatrix} \tag{4.29}$$

where *k*, *l*, *m*, *n*, and *p* are Hill's elastic moduli [177]. Using the Eshelby-Mori-Tanaka, the Hill's elastic moduli are found to be [174]:

$$k = \frac{E_m \left\{ E_m V_m + 2k_r \left(1+\nu_m\right) \left[1+V_f \left(1-2\nu_m\right) \right] \right\}}{2\left(1+\nu_m\right) \left[E_m \left(1+V_f-2\nu_m\right) + 2V_m k_r \left(1-\nu_m-2\nu_m^2\right) \right]} \tag{4.30}$$

$$n = \frac{E_m^2 V_m \left(1+V_f - V_m \nu_m\right) + 2V_m V_f \left(k_r n_r - l_r^2\right)\left(1+\nu_m\right)^2 \left(1-2\nu_m\right)}{\left(1+\nu_m\right)\left[E_m \left(1+V_f - 2\nu_m\right) + 2V_m k_r \left(1-\nu_m - 2\nu_m^2\right)\right]} +$$

$$\frac{E_m \left[2V_m^2 k_r \left(1-\nu_m\right) + V_f n_r \left(1+V_f - 2\nu_m\right) - 4V_m l_r \nu_m\right]}{E_m \left(1+V_f - 2\nu_m\right) + 2V_m k_r \left(1-\nu_m - 2\nu_m^2\right)} \tag{4.31}$$

$$p = \frac{E_m \left[E_m V_m + 2p_r \left(1+\nu_m\right)\left(1+V_f\right)\right]}{2\left(1+\nu_m\right)\left[E_m \left(1+V_f\right) + 2V_m p_r \left(1+\nu_m\right)\right]} \tag{4.32}$$

$$k = \frac{E_m \left[E_m V_m + 2m_r \left(1+\nu_m\right)\left(3+V_f - 4\nu_m\right)\right]}{2\left(1+\nu_m\right)\left\{E_m \left[V_m + 4V_f \left(1-\nu_m\right)\right] + 2V_m m_r \left(3-\nu_m - 4\nu_m^2\right)\right\}} \tag{4.33}$$

$$l = \frac{E_m \left\{\nu_m V_m \left[E_m + 2k_r \left(1+\nu_m\right)\right] + 2V_f k_r \left(1-\nu_m^2\right)\right\}}{\left(1+\nu_m\right)\left[E_m \left(1+V_f - 2\nu_m\right) + 2V_m k_r \left(1-\nu_m - 2\nu_m^2\right)\right]} \tag{4.34}$$

Where k_r , l_r , m_r , n_r , and p_r are the Hill's elastic moduli for the reinforcing phase (CNTs). V_f and V_m are the fiber and matrix volume fractions, respectively. The elastic moduli parallel and normal to CNTs are related to Hill's elastic moduli by:

$$E_{||} = n - \frac{l^2}{k} \quad , \quad E_{\perp} = \frac{4m\left(kn - l^2\right)}{kn - l^2 + mn} \tag{4.35}$$

4.3.4.2 Randomly oriented carbon nanotubes

The orientation distribution of CNT in the nanocomposite is characterized by a probability density function for randomly oriented CNT, in which case the composite is isotropic. Shi et al. [174] derived expressions for the bulk modulus *K* and shear modulus *G* of a composite reinforced with randomly oriented CNTs using Eshelby-Mori-Tanaka approach, which are given as:

$$K = K_m + \frac{V_f (\delta_r - 3K_m \alpha_r)}{3(V_m - V_f \alpha_r)} \tag{4.36}$$

$$G = G_m + \frac{V_f (\eta_r - 2G_m \beta_r)}{2(V_m - V_f \beta_r)} \tag{4.37}$$

where

$$\alpha_r = \frac{3(K_m + G_m) + k_r + l_r}{3(G_m + k_r)} \tag{4.38}$$

$$\beta_r = \frac{1}{5}\left[\frac{4G_m + 2k_r + l_r}{3(G_m + k_r)} + \frac{4G_m}{G_m + p_r} + \frac{2\left[G_m(3K_m + G_m) + G_m(3K_m + 7G_m)\right]}{G_m(3K_m + G_m) + m_r(3K_m + 7G_m)}\right] \tag{4.39}$$

$$\delta_r = \frac{1}{3}\left[n_r + 2l_r + \frac{(2k_r + l_r)(3K_m + 2G_m - l_r)}{G_m + k_r}\right] \tag{4.40}$$

$$\eta_r = \frac{1}{5}\left[\frac{2}{3}(n_r - l_r) + \frac{8G_m p_r}{G_m + p_r} + \frac{2(k_r - l_r)(2G_m + l_r)}{3(G_m + k_r)} + \frac{8m_r G_m(3K_m + 4G_m)}{3K_m(m_r + G_m) + G_m(7m_r + G_m)}\right] \tag{4.41}$$

where K_m and G_m are the bulk and shear moduli of the matrix, respectively, k_r, m_r, n_r and l_r are the Hill's elastic moduli for the reinforcing phase. The effective Young's modulus E and Poisson's ratio ν of the material are given by:

$$E = \frac{9KG}{3K + G} \tag{4.41}$$

$$\nu = \frac{3K - 2G}{6K + 2G} \tag{4.42}$$

4.3.4.3 Agglomerated carbon nanotubes

In this section, we aim to compute effective material properties of the composite reinforced by agglomerated CNTs making use of a two-parameter micromechanics model. Considering the micromechanics model, we use the stepping scheme [178] to analyze the effective properties of the composites. The stepping scheme predicts the effective properties of composites with high inclusion volume fraction and/or several kinds of inclusions. The method is relatively simple and the obtained results agree well with experimental data [178].

The regions with concentrated CNTs are assumed to be spherical in shape and are considered as inclusions with different elastic properties from the surrounding material, as shown in Figure 4.18. The volume fractions of CNTs inside the cluster are different from that in the matrix. The stepping scheme implies that there are two kinds of inclusion, CNTs and clusters, in the matrix. Thus, the stepping scheme can be implemented to analyze the effective properties. The procedure is as follows: Firstly, the cluster is homogenized to obtain an equivalent inclusion, and the same

homogenization for the medium containing CNTs outside the clusters forms an equivalent matrix. Secondly, based on by Eshelby-Mori-Tanaka approach, the effective properties of the composite can be calculated using these equivalent media of the matrix and inclusions. The total volume V_r of the CNTs in the representative volume element (RVE) can be divided into the following two parts [174]:

$$V_r = V_r^{inclusion} + V_r^{m} \tag{4.43}$$

where $V_r^{inclusion}$ and V_r^{m} denote the volumes of CNTs dispersed in the inclusions (concentrated regions) and in the matrix, respectively. Agglomeration of the CNTs

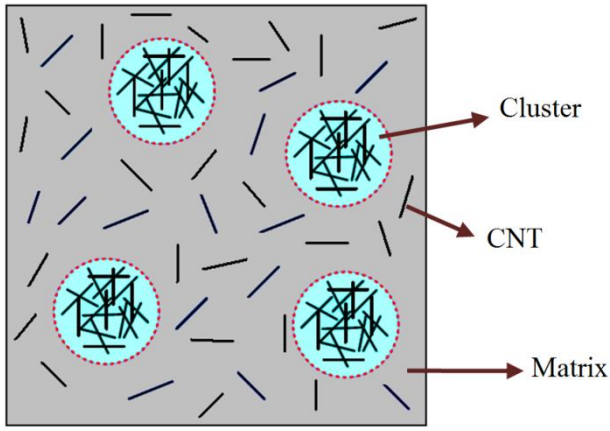

Figure 4.18. Representative Volume Element (RVE) with model of CNTs agglomeration.

within the matrix material causes the elastic properties to degrade as compared to a CNT reinforcement which is uniformly distributed. This aspect of the nanocomposites can be investigated qualitatively by using the agglomeration constants μ and ξ are defined as [174]:

$$\mu = \frac{V^{inclusion}}{V}, \quad \xi = \frac{V_r^{inclusion}}{V_r} \tag{4.44}$$

where $V^{inclusion}$ is the volume of the sphere inclusions in the RVE. The parameter μ denotes the volume fraction of inclusions with respect to the total volume *V* of the RVE. When μ=1, CNTs are uniformly dispersed in the matrix, and with the decrease of μ, the agglomeration degree of CNTs is more severe. The parameter ξ denotes the volume ratio of CNTs that are dispersed in inclusions to the total volume of the nanotubes. When $\xi = 1$, all the CNTs are concentrated in the inclusions with the concentration of CNTs in the inclusions decreasing with decreasing ξ. When $\mu = \xi$, the CNTs are uniformly distributed within the matrix and ξ must be greater than μ for agglomeration to be present. The effective elastic moduli of the hybrid inclusions and the matrix can be calculated by different micromechanics methods. We assume the CNTs are transversely isotropic. Furthermore, it is assumed that the CNTs are randomly oriented in the inclusions, and, therefore, the inclusions are isotropic. The effective bulk moduli K_{in} and K_{out} and the effective shear moduli G_{in} and G_{out} of the inclusions and the matrix are respectively given by [174]:

$$K_{in} = K_m + \frac{V_r \xi (\delta_r - 3K_m \alpha_r)}{3(\mu - V_r \xi + V_r \xi \alpha_r)} \tag{4.45}$$

$$K_{out} = K_m + \frac{V_r (1-\xi)(\delta_r - 3K_m \alpha_r)}{3(1-\mu - V_r (1-\xi) + V_r (1-\xi)\alpha_r)} \tag{4.46}$$

$$G_{in} = G_m + \frac{V_r \xi (\eta_r - 2G_m \beta_r)}{2(\mu - V_r \xi + V_r \xi \alpha_r)} \tag{4.47}$$

$$G_{out} = G_m + \frac{V_r (1-\xi)(\eta_r - 2G_m \beta_r)}{2(1-\mu - V_r (1-\xi) + V_r (1-\xi)\beta_r)} \tag{4.48}$$

Finally, the effective bulk modulus *K* and the effective shear modulus *G* of the composite are derived from the Eshelby-Mori-Tanaka method as:

$$K = K_{out}\left[1 + \frac{\mu\left(\frac{K_m}{K_{out}} - 1\right)}{1 + \alpha(1-\mu)\left(\frac{K_m}{K_{out}} - 1\right)}\right] \tag{4.49}$$

$$G=G_{out}\left[1+\frac{\mu\left(\frac{G_m}{G_{out}}-1\right)}{1+\beta(1-\mu)\left(\frac{G_m}{G_{out}}-1\right)}\right] \tag{4.50}$$

with

$$\alpha=\frac{1+\nu_{out}}{3(1-\nu_{out})} \tag{4.51}$$

$$\beta=\frac{2(4-5\nu_{out})}{3(1-\nu_{out})} \tag{4.52}$$

$$\nu_{out}=\frac{3K_{out}-2G_{out}}{2(3K_{out}+G_{out})} \tag{4.53}$$

where

$$\alpha_r=\frac{3(K_m+G_m)+k_r+l_r}{3(G_m+k_r)} \tag{4.54}$$

$$\beta_r=\frac{1}{5}\left[\frac{4G_m+2k_r+l_r}{3(G_m+k_r)}+\frac{4G_m}{G_m+p_r}+\frac{2\left[G_m(3K_m+G_m)+G_m(3K_m+7G_m)\right]}{G_m(3K_m+G_m)+m_r(3K_m+7G_m)}\right] \tag{4.55}$$

$$\delta_r=\frac{1}{3}\left[n_r+2l_r+\frac{(2k_r+l_r)(3K_m+2G_m-l_r)}{G_m+k_r}\right] \tag{4.56}$$

$$\eta_r=\frac{1}{5}\left[\frac{2}{3}(n_r-l_r)+\frac{8G_m p_r}{G_m+p_r}+\frac{2(k_r-l_r)(2G_m+l_r)}{3(G_m+k_r)}+\frac{8m_r G_m(3K_m+4G_m)}{3K_m(m_r+G_m)+G_m(7m_r+G_m)}\right] \tag{4.57}$$

The effective Young's modulus E and Poisson's ratio ν of the nanocomposite are derived by Eqs. (4.41) and (4.42).

4.4 Summary and conclusions

This chapter has devoted particulate attention to mathematical modeling of FGMs. For modelisation of volume fraction and fiber orientation, firstly, the classic form of power-law distribution was introduced. Furthermore, various profiles for volume fractions of CNT in FG CNT-reinforced composites based on classic form of power-law distribution were presented. Lack of available versatile power-law distribution motivated us to introduce a band-new generalized power-law distribution for defining variation of volume fraction or fiber orientation in FGMs composites. By using generalized power-law distribution, it was possible to study the effect of the different kinds of material profiles including symmetric, asymmetric and classic on mechanical behavior of a FGM structures. Another advantage of generalized power-law distribution was to have a desirable volume fraction of the material on the inner or outer surface while there was a smooth gradation of volume fraction through the required direction.

To compute effective material properties in FG composites and nanocomposites, commonly used homogenization methods were presented. In case of FG composites, rule of mixture and Mori-Tanaka method have been explained. Owing to shortcoming of rule of mixture in direct application into CNT-reinforced composites, the extended rule of mixture for nanocomposites reinforced by aligned CNTs has been explained. Besides, to study other form of CNTs dispersion, Eshelby-Mori-Tanaka approach was introduced for determining effective material properties of nanocomposites reinforced by either aligned, randomly oriented, or agglomerated CNTs.

Chapter 5

Solution procedure

5.1 Overview

This chapter is devoted to solution procedure for solving coupled governing differential equations with variable coefficients derived in the chapter 3. In the present methodology, generalized differential quadrature method (GDQM) as a semi-analytical approach is adopted to solve the governing equations. This chapter starts with an introduction to GDQM and a definition of the method will be presented. Afterwards, weighting coefficients for first order derivative and then extension to the two-dimensional case is discussed. Since the imperative point for successful application of GDQM is how to distribute the grid points in specified domain, grid point distribution in GDQM is explained. Eventfully, section 5.3 presents the application of GDQM in thermal, vibration, and static analyses of FGMs.

5.2 Differential quadrature method

Most engineering problems are governed by a set of partial differential equations (PDEs) with related boundary conditions. Generally, it is very difficult to gain the closed-form solution of these equations. On the other hand, the solution of these PDEs is always demanded owing to practical interests. In most cases, the approximate solution is constituted by functional values at certain discrete points (grid points or mesh points). At this stage, one may ask the relation between the derivatives in the partial differential equation and the functional values at the grid points. It sounds that there exists a bridge which links them. The numerical discretization technique is such a bridge, and the corresponding approximate solution is named the numerical solution. Currently there are many available numerical discretization techniques. Among all of them, the finite difference (FD), finite element (FE), and finite volume (FV) methods fall under the category of low order methods [42]. The FD method is based on the Taylor series expansion or the polynomial approximation while the FE method is based on variational principle or the principle of weighted residuals. The FV method applies the physical conservation law directly to a finite cell. Most numerical simulations of engineering problems can be carried out by the low order FD, FE, and FV methods using a large number of grid points. In some practical applications, nonetheless, the numerical solutions of PDEs are required at only a few specified points in the physical domains. To accomplish an acceptable degree of accuracy, low order methods still require the use of a large number of grid points to obtain accurate solutions at these specified points. An example can be found in the vibration analysis. Upon numerical discretization of the governing PDEs, the eigenvalues of the resultant algebraic equation system provide the vibrational frequencies of the problem. Usually, the number of interior grid points is equal to the dimension of the resultant algebraic equation system, thus giving the same number of eigenfrequencies. Among all the computed eigenfrequencies, only

the low frequencies are of practical interest. However, inasmuch as the computed eigenfrequencies have the same order of accuracy, a large number of grid points are still necessary in order to gain such low frequencies accurately. Accordingly, a lot of virtual storage and computational effort are needed. This drawback is much more profound when due to non-linear variation of material properties in FGMs, more computational effort is required. Thus, to accomplish the same order of accuracy, the mesh spacing used by high order methods can be much larger than that used by low order methods. Accordingly, high order methods are capable of yielding accurate numerical solutions using very few grid points.

In seeking an efficient discretization technique to obtain accurate numerical solution using a considerably small number of grid points, Bellman et al. [179,180] introduced the differential quadrature method (DQM), where a partial derivative of a function with respect to a coordinate direction is expressed as a linear weighted sum of all functional values at all mesh points along that direction. The DQM was initiated from the idea of integral quadrature. Its weighting coefficients are not related to any special problem and only depend on the grid points and the derivative order. The most imperative part of DQM is to determine the weighting coefficients for discretization of any order partial derivative. There exist some major drawbacks to the original differential quadrature method that restrict its wide applications. These drawbacks are related to the determination of the weighting coefficients for the partial derivative approximation. There are two methods in use, which were proposed by Bellman et al. [180] to obtain the weighting coefficients. The first method may encounter an ill-conditioning problem when the number of grid points becomes large. The second method imposes restriction on the choice of the grid points. This leads to a major restriction on this method to problems in structural analysis, since all sorts of boundary conditions could appear and different mesh grids may be needed for different boundary conditions and structure geometry. In order to overcome these drawbacks, Shu [181] presented generalized differential quadrature method (GDQM), in which the weighting coefficients of the first-order derivative were determined by a simple algebraic formulation without any restriction on choice of grid points, and the weighting coefficients of the second- and higher-order derivatives are determined by a recurrence relationship.

5.2.1 Definition

As shown in Figure 5.1, we consider a one-dimensional problem. It is assumed that a function $f(x)$ is sufficiently smooth over the whole domain. Following the main idea of DQM introduced by Bellman, the first order derivative of the function $f(x)$

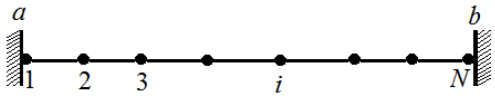

Figure 5.1. A one-dimensional problem.

with respect to x at a grid point x_i, is approximated by a linear sum of all the functional values in the whole domain, that is [42,43]:

$$f_x(x_i) = \left.\frac{df}{dx}\right|_{x_i} = \sum_{j=1}^{N} a_{ij} f(x_j), \qquad for\ i = 1,2,...,N \tag{5.1}$$

where a_{ij} represent the weighting coefficients, and N is the number of grid points in the whole domain. It should be noted that weighting coefficients a_{ij} are different at different locations of x_i.

5.2.2 Weighting coefficients for first order derivative

Consider the one-dimensional problem over a closed interval $[a,b]$ as shown in Figure 5.1. It is supposed that there are N grid points with coordinates as $x_1, x_2, ..., x_N$, which $a = x_1$ and $b = x_N$. Bellman et al. [180] assumed that a function $f(x)$ is sufficiently smooth over the interval $[a,b]$ so that its first order derivative $f^{(1)}(x)$ at any grid point can be approximated by Eq. (5.1). In the following, we shall show that weighting coefficients can be computed by employing some explicit formulations.

5.2.2.1 Bellman's Approach

Bellman et al. [180] proposed two approaches to compute the weighting coefficients in Eq. (5.1). The two approaches are based on the use of two different test functions.

5.2.2.1.1 Bellman's first approach

In this approach, the test functions are chosen as [42]:

$$g_k(x) = x^k, \qquad k = 0,1...N-1 \tag{5.2}$$

Obviously, Eq. (5.2) gives N test functions. For the weighting coefficients in Eq. (5.1), i and j are taken from 1 to N. Thus, the total number of weighting coefficients is $N \times N$. To obtain these $N \times N$ weighting coefficients, the N test functions should be applied to N grid points $x_1, x_2, .., x_N$. As a consequence, the following $N \times N$ algebraic equations for a_{ij} are obtained:

$$\begin{cases} \sum_{j=1}^{N} a_{ij} = 0 \\ \sum_{j=1}^{N} a_{ij} x_j = 1 \\ \sum_{j=1}^{N} a_{ij} x_j^k = k x_i^{k-1}, \qquad k = 2,3,...N-1 \end{cases} \tag{5.3}$$

for $i = 1,2,...,N$

Eq. (5.3) has a unique solution because its matrix is of Vandemonde form. Unfortunately, when *N* is large, the matrix is ill-conditioned. In practical application of this approach, *N* is usually chosen to be less than 13.

5.2.2.1.2 Bellman's second approach

This approach is similar to the first approach, but with different test functions

$$g_k(x) = \frac{L_N(x)}{(x - x_k) L_N^{(1)}(x_k)}, \qquad k = 1,2,....,N \tag{5.4}$$

where $L_N(x)$ is the Legendre polynomial of degree *N* and $L_N^{(1)}(x)$ is the first order derivative of $L_N(x)$. By choosing x_k to be the roots of the shifted Legendre polynomial and applying Eq. (5.4) at *N* grid points $x_1, x_2, .., x_N$. Belman et al. [180] presented a simple algebraic formulation to compute a_{ij}:

$$a_{ij} = \frac{L_N^{(1)}(x_i)}{(x_i - x_j) L_N^{(1)}(x_j)}, \qquad for \quad j \neq i \tag{5.5a}$$

$$a_{ii} = \frac{1 - 2x_i}{2x_i (x_i - 1)} \tag{5.5b}$$

Using Eq. (5.5), the computation of the weighting coefficients is a simple task. However, this approach is not flexible as the first approach because the coordinates of the grid points in this approach cannot be chosen arbitrarily. Instead, they should be chosen as the roots of the Legendre polynomial of degree *N*. So, Eq. (5.5) only reflects a special case. Due to the inflexibility associated with the second approach in selecting the grid points, the first approach is usually adopted in practical applications.

5.2.2.2 Shu's Approach

Shu's general approach [181] was inspired from Bellman's approaches. In order to find a simple algebraic expression for calculating the weighting coefficients without restricting the choice of grid meshes, Shu chose Lagrange interpolated polynomials

as the set of tests functions $g(x)$ instead of using power polynomials or Legendre polynomials:

$$g_i(x) = \frac{M(x)}{(x - x_k)M^{(1)}(x_k)}, \qquad k = 1, 2, ..., N, \tag{5.6}$$

here

$$M(x_i) = \prod_{j=1}^{N} (x - x_j) \tag{5.7}$$

$M^{(1)}(x)$ is the first derivative of $M(x)$,

$$M^{(1)}(x_i) = \prod_{j=1,\, j\neq i}^{N} (x_i - x_j) \tag{5.8}$$

and N is the number of grid points.

When Eq. (5.1) is satisfied for all the test functions $g_i(x)$, a simple algebraic expression can be obtained to determine the weighting coefficients

$$c_{ij}^{(1)} = \frac{M^{(1)}(x_i)}{(x_i - x_j)M^{(1)}(x_j)}, \qquad for\ i \neq j \tag{5.9a}$$

$$c_{ij}^{(1)} = \frac{M^{(2)}(x_i)}{2M^{(1)}(x_i)}, \qquad i, j = 1, 2, ..., N \tag{5.9b}$$

Eq. (5.9) provides simple expressions for computing $c_{ij}^{(1)}$ without any restriction in choice of the co-ordinates of the grid points x_i .It is obvious that once the grid points x_i are given, $M^{(1)}(x)$ is very easily obtained from Eq. (5.8). Hence, $c_{ij}^{(1)}$ can be easily calculated for $i \neq j$. The calculation of $c_{ij}^{(1)}$ is based on the calculation of the second derivative of $M(x)$ which is more difficult to obtain. Instead of using Eq. (5.9), a more convenient relationship can be obtained and used for calculating $c_{ij}^{(1)}$. It can be shown by using a Taylor series expansion that the following relationship exists for $c_{ij}^{(1)}$:

$$\sum_{j=1}^{N} c_{ij}^{(1)} = 0 \qquad for\ i = 1, 2, ..., N \tag{5.10}$$

Thus, from Eq. (5.10) the coefficient $c_{ij}^{(1)}$ can be calculated from $c_{ij}^{(1)}\ (i \neq j)$; that is:

$$c_{ii}^{(1)} = -\sum_{j=1,\, j\neq i}^{N} c_{ij}^{(1)} \qquad for\ i = 1, 2, ..., N \tag{5.11}$$

The weighting coefficients for second and higher order derivatives can be similarly obtained. A recurrence relationship has been found for the *m*th order weighting coefficients $c_{ij}^{(m)}$:

$$c_{ij}^{(m)} = m\left(c_{ii}^{(m-1)}c_{ij}^{(1)} - \frac{c_{ij}^{(m-1)}}{x_i - x_j}\right) \qquad for\ i \neq j,\ n = 2,3,...,N-1,\ \ i,j = 1,2,...N \quad (5.12)$$

Thus the $c_{ij}^{(m)}$ can be derived from the $(m-1)$ th order weighting coefficients $c_{ij}^{(m-1)}$. The $c_{ij}^{(m)}$ can be obtained from a relationship similar to Eq. (5.11):

$$c_{ii}^{(m)} = -\sum_{j=1,\, j\neq i}^{N} c_{ij}^{(m)} \qquad for\ i = 1,2,...,N \quad (5.13)$$

Thus, Eqs. (5.12) and (5.13) together with Eqs. (5.9) and (5.11) give a convenient and general form for determining the weighting coefficients for the derivatives of orders one through $N-1$.

5.2.3 Extension to the two-dimensional case

In practice, most problems are two-dimensional or three-dimensional. Thus, it is necessary to extend the GDQ approximation from the one-dimensional case to the multi-dimensional cases. In the following, we will only demonstrate the extension of the one-dimensional case to the two-dimensional case. Extension to the three-dimensional case can be carried out in the same manner as the extension to the two-dimensional case.

As shown by Shu [42], the one-dimensional GDQM can be directly extended to the multi-dimensional case if the discretization domain is regular. The regular domain could be a rectangle or other regular shapes such as a circle. Here, for simplicity, we

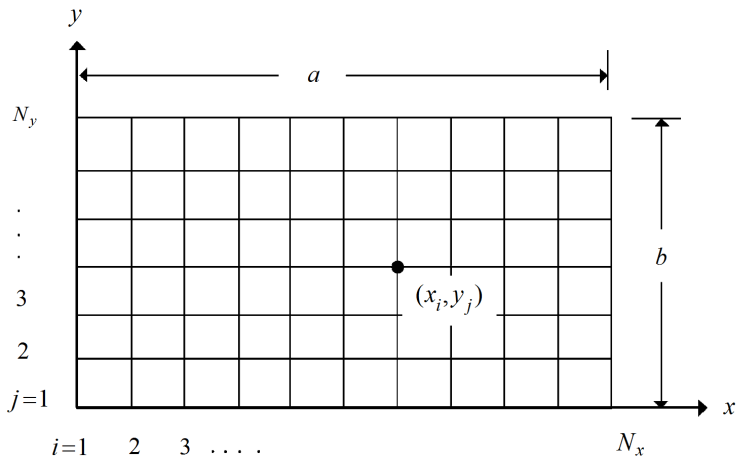

Figure 5.2. Rectangular domain and grid distribution.

only consider a rectangular domain for demonstration. Consider a two-dimensional function $f(x,y)$ defined on a rectangular domain, as depicted in Figure 5.2. It is clearly seen from the figure that along each horizontal line, the *x* interval is the same, and along each vertical line, the *y* interval is the same. Thus, we can use the same *x* coordinate distribution for each horizontal line and the same *y* coordinate distribution for each vertical line. The partial derivative at any grid point in a two-dimensional domain is approximated by a linear weighted sum of all the functional values in the whole two-dimensional domain. Let $\partial^n f/\partial x^n$ and $\partial^m f/\partial y^m$ be the *n*th and *m*th order derivatives of a function $f(x,y)$ with respect to *x* and *y*, respectively. At any grid point, the approximation gives:

$$\left.\frac{\partial^n f}{\partial x^n}\right|_i = \sum_{i=1}^{N_x} c_{ij}^{x,n} f_i \qquad for\ i = 1,2,...,N_x \tag{5.14a}$$

$$\left.\frac{\partial^m f}{\partial x^m}\right|_i = \sum_{j=1}^{N_y} c_{ij}^{y,m} f_j \qquad for\ i = 1,2,...,N_y \tag{5.14b}$$

where $c_{ij}^{x,n}$ and $c_{ij}^{y,m}$ are the weighting coefficients related to $\partial^n f/\partial x^n$ and $\partial^m f/\partial y^m$, and N_x and N_y are the number of grid points in *x* and *y* directions, respectively. It should be noted that the index *i* in Eq. (5.14) denotes the one-dimensional indexing of the two-dimensional grid points. So, before Eq. (5.14) is applied, one has to convert the two-dimensional grid point distribution into a one-dimensional array.

5.2.4 Grid point distribution

Another important point for successful application of the GDQM is how to distribute the grid points. In fact, the accuracy of this method is usually sensitive to the grid point distribution. The optimal grid point distribution depends on the order of derivatives in the boundary condition and the number of grid points used. The grid point distribution also plays a crucial role in determining the convergence speed and stability of the GDQM. The natural and simplest choice of the grid points through the computational domain is the one having equally spaced points in the coordinate direction of the computational domain. However, it is demonstrated that non-uniform grid distribution usually yields better results than equally spaced distribution. Quan and Chang [182] compared numerically the performances of the often-used non-uniform meshes and concluded that the grid points originating from the Chebyshev polynomials of the first kind are optimum in all the cases examined there. Bert and Malik [183] indicated that the preferred type of grid points changes with problems of interest and recommended the use of Chebyshev-Gauss-Lobatto grid for the structural mechanics computation. With Lagrange interpolating polynomials, it has

been proven that Chebysheve-Gausse-Lobatto sampling points rule guarantees convergence and efficiency to the GDQM [184]. Tornabene and Viola [44,185] compared the natural frequencies of non-FGM and FGM panels obtained by the GDQM with those by FEM commercial programs including Abaqus, Ansys, Straus, Femap/Nastran and Pro/Mechanica. It was found that the computational effort in terms of time and number of grid points was smaller and, at the same time, the accuracy is better for the GDQM results than for the FEM. In addition, the Chebyshev-Gauss-Lobatto grid performed the best among the other non-uniform typical grid distributions for all cases.

The Chebyshev-Gauss-Lobatto points for the two-dimensional domain are given by [184]:

$$x_i = \frac{a}{2}\left(1-\cos\left(\frac{(i-1)\pi}{N_x-1}\right)\right), \qquad i=1,2,...,N_x \tag{5.15a}$$

$$y_i = \frac{b}{2}\left(1-\cos\left(\frac{(j-1)\pi}{N_y-1}\right)\right), \qquad j=1,2,...,N_y \tag{5.15b}$$

5.3 Application of GDQM

In this section, GDQM is applied to discretize the governing equations and the boundary conditions of various problems in mechanical response of FGM. Firstly we apply GDQ solution to solve the governing equations in free vibration and static problems of FGMs. Later on, GDQM is employed in thermal stress analysis of FGMs.

5.3.1 Free vibration problems

Since in all cases defined in section 3.2.1 the methodology of the application of GDQM for discretization of governing eqations is the same, herein, we just apply GDQM to a 2-D domain (r_i, z_j) with $i=1,2,...,N$ and $j=1,2,...,M$. For a cylindrical panel with graded volume fractions of fibers, the 3-D governing equations were determined in Eqs. (3-2) to (3-4). In order to transfer the 3-D problem to the 2-D one, trigonometric functions expansion through the radial direction is used. For the cylindrical panel simply supported at one pair of opposite edges, the displacement components can be expanded in terms of trigonometric functions in the direction normal to these edges. In this work, it is assumed that the edges $\theta = 0$ and $\theta = \Phi$ are simply supported. Hence,

$$u_r(r,\theta,z,t)=\sum_{m=1}^{\infty}U_r(r,z)\sin(\beta_m\theta)e^{i\omega t}, \tag{5.16}$$

$$u_\theta(r,\theta,z,t)=\sum_{m=1}^{\infty}U_\theta(r,z)\cos(\beta_m\theta)e^{i\omega t}, \tag{5.17}$$

$$u_z(r,\theta,z,t)=\sum_{m=1}^{\infty}U_z(r,z)\sin(\beta_m\theta)e^{i\omega t}, \tag{5.18}$$

$\beta_m = m\pi/\Phi$, $(m=1,2,...)$

Where m and ω are circumferential wave number and the natural frequency of the vibration, respectively. It should be noted that for the case of closed cylindrical shells, β_m is assumed to be equal m. Upon substituting Eqs. (5.16) to (5.18) into the governing Eqs. (3.2) to (3.4), the coupled partial differential equations reduce to a set of coupled differential equations as follows:

$$\begin{bmatrix} A_{1r} & A_{1\theta} & A_{1z} \\ A_{2r} & A_{2\theta} & A_{2z} \\ A_{3r} & A_{3\theta} & A_{3z} \end{bmatrix} \begin{Bmatrix} U_r \\ U_\theta \\ U_z \end{Bmatrix} = -\rho\omega^2 \begin{Bmatrix} U_r \\ U_\theta \\ U_z \end{Bmatrix}, \tag{5.19}$$

At this stage, the GDQM, Eq. (5.14), can be applied to discretize the Eq. (5.19). As a result, the discretized equations take the following forms:

$$\left((C_{13})_{ij}\frac{1}{r} - (C_{12})_{ij}\frac{1}{r} + \left(\frac{\partial C_{13}}{\partial r}\right)_{ij} \right) \sum_{k=1}^{M} d_{jk} U_{zik}$$

$$+ \sum_{k=1}^{N} \left(\left(\left(\frac{\partial C_{33}}{\partial r}\right)_{ij} + (C_{33})_{ij}\frac{1}{r} \right) c_{ik} + (C_{33})_{ij}\, c_{ik}^{(2)} \right) U_{rkj}$$

$$+ \sum_{k=1}^{M} \left(\left(\frac{\partial C_{55}}{\partial z}\right)_{ij} d_{jk} + (C_{55})_{ij}\, d_{jk}^{(2)} \right) U_{rik}$$

$$+ \beta_m \left((C_{44})_{ij}\frac{1}{r^2} - \left(\frac{\partial C_{23}}{\partial r}\right)_{ij}\frac{1}{r} + (C_{22})_{ij}\frac{1}{r^2} \right) U_{\theta ij}$$

$$+ \left(\left(\frac{\partial C_{23}}{\partial r}\right)_{ij}\frac{1}{r} - (C_{44})_{ij}\frac{1}{r^2}\beta_m{}^2 - (C_{22})_{ij}\frac{1}{r^2} \right) U_{rij}$$

$$+\left(\left(C_{13}\right)_{ij}+\left(C_{55}\right)_{ij}\right)\sum_{k_1=1}^{N}\sum_{k_2=1}^{M}c_{ik_1}d_{jk_2}U_{zk_1k_2}$$

$$+\left(\frac{\partial C_{55}}{\partial z}\right)_{ij}\sum_{k=1}^{N}c_{ik}U_{zkj}-\frac{1}{r}\beta_m\left(\left(C_{44}\right)_{ij}+\left(C_{23}\right)_{ij}\right)\sum_{k=1}^{N}c_{ik}U_{\theta kj}=-\rho_{ij}\omega^2U_{rij}\ , \qquad (5.20)$$

$$\sum_{k=1}^{M}\left(\left(\frac{\partial C_{66}}{\partial z}\right)_{ij}d_{jk}+\left(C_{66}\right)_{ij}d_{jk}^{(2)}\right)U_{\theta ik}$$

$$+\sum_{k=1}^{N}\left(\left(\left(\frac{\partial C_{44}}{\partial r}\right)_{ij}+\left(C_{44}\right)_{ij}\frac{1}{r}\right)c_{ik}+\left(C_{44}\right)_{ij}c_{ik}^{(2)}\right)U_{\theta kj}$$

$$+\left(\left(C_{22}\right)_{ij}\frac{1}{r}+\left(\frac{\partial C_{44}}{\partial r}\right)_{ij}+\left(C_{44}\right)_{ij}\frac{1}{r}\right)\frac{1}{r}\beta_mU_{rij}+\left(\frac{\partial C_{66}}{\partial z}\right)_{ij}\frac{1}{r}\beta_mU_{zij}$$

$$+\frac{1}{r}\beta_m\sum_{k=1}^{M}\left(\left(C_{66}\right)_{ij}d_{jk}^{(2)}+\left(C_{12}\right)_{ij}d_{jk}\right)U_{zik}$$

$$-\left(\left(\overline{C}_{22}\right)_{ij}\frac{1}{r^2}{\beta_m}^2U_{\theta}+\left(\overline{C}_{44}\right)_{ij}\frac{1}{r^2}\right)U_{\theta ij}$$

$$\frac{1}{r}\beta_m\left(\left(\overline{C}_{23}\right)_{ij}+\left(\overline{C}_{44}\right)_{ij}\right)\sum_{k=1}^{N}c_{ik}U_{rkj}=-\rho_{ij}\omega^2U_{\theta ij}\ , \qquad (5.21)$$

$$\sum_{k=1}^{M}\left(\left(\frac{\partial C_{11}}{\partial z}\right)_{ij}d_{jk}+\left(C_{11}\right)_{ij}d_{jk}^{(2)}\right)U_{zik}+\left(\frac{\partial C_{12}}{\partial z}\right)_{ij}\frac{1}{r}U_{rij}$$

$$+\left(\left(C_{12}\right)_{ij}\frac{1}{r}+\left(C_{55}\right)_{ij}\frac{1}{r}+\left(\frac{\partial C_{55}}{\partial r}\right)_{ij}\right)\sum_{k=1}^{M}d_{jk}U_{rik}$$

$$+\left(\left(\frac{\partial C_{55}}{\partial r}\right)_{ij}+\left(C_{55}\right)_{ij}\frac{1}{r}\right)\sum_{k=1}^{N}c_{ik}U_{zkj}+\sum_{k=1}^{N}\left(\left(\frac{\partial C_{13}}{\partial z}\right)_{ij}c_{ik}+\left(C_{55}\right)_{ij}c_{ik}^{(2)}\right)U_{rkj}$$

$$-\frac{1}{r}\beta_m\left(\left(\overline{C}_{12}\right)_{ij}+\left(\overline{C}_{66}\right)_{ij}\right)\sum_{k=1}^{M}d_{jk}U_{\theta ik}$$

$$+\left(\left(\bar{C}_{55}\right)_{ij}+\left(\bar{C}_{13}\right)_{ij}\right)\sum_{k_1=1}^{N}\sum_{k_2=1}^{M}c_{ik_1}d_{jk_2}U_{rk_1k_2}=-\rho_{ij}\omega^2U_{zij}\,, \tag{5.22}$$

where $c_{ij}\,,d_{ij}$ and $c_{ij}^{(2)}\,,d_{ij}^{(2)}$ are the first and second order GDQM weighting coefficients in the *r*- and *z*-directions of the panel, respectively. In a similar manner the boundary conditions can be discretized. For this purpose, using Eq. (5.14) and GDQM discretization rule for special derivatives, the boundary conditions at $r=r_i$ and $r=r_o$, as stated in Eq. (3.6), become:

$$C_{13}\sum_{k=1}^{M}d_{jk}U_{zik}+C_{23}\frac{1}{r}U_{rij}-C_{23}\frac{1}{r}\beta_mU_{\theta ij}+C_{33}\sum_{k=1}^{N}c_{ik}U_{rkj}=0$$

$$-C_{44}\frac{1}{r}U_{\theta ij}+C_{44}\sum_{k=1}^{N}c_{ik}U_{\theta kj}+C_{44}\frac{1}{r}\beta_mU_{rij}=0$$

$$C_{55}\sum_{k=1}^{N}c_{ik}U_{zkj}+C_{55}\sum_{k=1}^{M}d_{jk}U_{rik}=0 \tag{5.23}$$

where $i=1$ at $r=r_i$ and $i=N$ at $r=r_o$, and $j=1,2,...,M$. The boundary conditions at $x=0$ and L stated in Eq. (3.8) become:
Simply supported (S):

$$U_{rij}=0,\qquad U_{\theta ij}=0,$$

$$C_{11}\sum_{k=1}^{M}d_{jk}U_{zik}+C_{12}\frac{1}{z}U_{rij}-C_{12}\frac{1}{z}\beta_mU_{\theta ij}+C_{13}\sum_{k=1}^{N}c_{ik}U_{rkj}=0,$$

for $j=1,M$ and $i=1,2,...,N$ (5.24)

Clamped (C):

$$U_{rij}=0,\qquad U_{\theta ij}=0,\qquad U_{zij}=0,$$

for $j=1,M$ and $i=1,2,...,N$ (5.25)

Free (F):

$$C_{11}\sum_{k=1}^{M} d_{jk}U_{zik} + C_{12}\frac{1}{r}U_{rij} - C_{12}\frac{1}{r}\beta_m U_{\theta ij} + C_{13}\sum_{k=1}^{N} c_{ik}U_{rkj} = 0,$$

$$C_{66}\sum_{k=1}^{M} d_{jk}U_{\theta ik} + C_{66}\frac{1}{r}\beta_m U_{zij} = 0,$$

$$C_{55}\sum_{k=1}^{N} c_{ik}U_{zkj} + C_{55}\sum_{k=1}^{M} d_{jk}U_{rik} = 0, \quad \text{for } j = 1, M \text{ and } i = 1, 2, ..., N \tag{5.26}$$

To perform the eigenvalue system of equations, the degrees of freedom are separated into the domain and the boundary degrees of freedom as:

$$\{U_d\} = \begin{Bmatrix} U_r \\ U_\theta \\ U_z \end{Bmatrix}_{domain}, \quad \{U_b\} = \begin{Bmatrix} U_r \\ U_\theta \\ U_z \end{Bmatrix}_{boundary} \tag{5.27}$$

Using Eq. (5.27), the discretized form of the equations of motion in the matrix form can be rearranged as:

$$[S_{db}]\{U_b\} + [S_{dd}]\{U_d\} = -\omega^2 [M]\{U_d\} \tag{5.28}$$

where $[S_{db}]$ and $[S_{dd}]$ are stiffness matrices and $[M]$ is the mass matrix. In a similar manner, the discretized form of the boundary conditions becomes:

$$[S_{bb}]\{U_b\} + [S_{bd}]\{U_d\} = 0 \tag{5.29}$$

where $[S_{bb}]$ and $[S_{bd}]$ are the stiffness matrices. In the above equations, the elements of stiffness matrices are obtained based on the definition of vectors of domain and boundary degrees of freedom from the generalized differential quadrature discretized form of the equations of motion and the boundary conditions. Using Eq. (5.29) to eliminate the boundary degrees of freedom **b** from Eq. (5.28), one obtains:

$$[S]\{U_d\} = -\omega^2 [M]\{U_d\} \tag{5.30}$$

where

$$[S] = [S_{dd}] - [S_{db}][S_{bb}]^{-1}[S_{bd}] \tag{5.31}$$

The natural frequencies of the FGM cylindrical panel can be determined by solving the standard eigenvalue problem using MATLAB software.

It is worth noting that in case of FGSW panel described in section 3.2.1.2, a set of coupled equations of motion governs each layer while the whole equations of motion (3×3 equations) should be solved together for the whole panel. To link equations of each layer to each other, the continuity conditions, stated in Eq. (3.10), are enforced at any arbitrary interior *k*th interface. By applying GDQM to the equations of motion in each layer, the discretized form of the equations of motion in the matrix form is arranged as:

$$\left[A_{db}\right]_{3(3N-6)\times6}\left\{U_b\right\}_{6\times1}+\left[A_{dd}\right]_{3(3N-6)\times3(3N-6)}\left\{U_d\right\}_{3(3N-6)\times1}=-\omega^2\left[M\right]\left\{U_d\right\}_{3(3N-6)\times1} \tag{5.31}$$

where $\left[A_{db}\right]$ and $\left[A_{dd}\right]$ are stiffness matrices and $\left[M\right]$ is the mass matrix. In a similar manner, the discretized form of the continuity conditions at the first and second interfaces becomes:

$$\left[A_b\right]^1_{3\times3}\left\{U_b\right\}_{3\times1}+\left[A_{bd}\right]^1_{3\times2(3N-6)}\left\{U_d\right\}_{2\times(3N-6)}+\left[A_{kk}\right]^1_{3\times3}\left\{U_k\right\}^1_{3\times1}=\left\{0\right\} \tag{5.32}$$

$$\left[A_b\right]^2_{3\times3}\left\{U_b\right\}_{3\times1}+\left[A_{bd}\right]^2_{3\times2*(3N-6)}\left\{U_d\right\}_{2*(3N-6)}+\left[A_{kk}\right]^2_{3\times3}\left\{U_k\right\}^2_{3\times1}=\left\{0\right\} \tag{5.33}$$

where $\left[A_b\right]$, $\left[A_{bd}\right]$, and $\left[A_{kk}\right]$ are the stiffness matrices. $\left\{U_k\right\}^i$ is the *i*th interface degrees of freedom vector. The discretized form of the boundary conditions Eq. (5.23) becomes:

$$\left[A_{bb}\right]_{6\times6}\left\{U_b\right\}_{6\times1}+\left[A_{bd}\right]_{6\times3(3N-6)}\left\{U_d\right\}_{3(3N-6)}=\left\{0\right\} \tag{5.34}$$

where $\left[A_{bb}\right]$ and $\left[A_{bd}\right]$ are the stiffness matrices. Analogous to method explained earlier, boundary degrees of freedom are eliminated and one finds:

$$\left(\left[A\right]+\omega^2\left[M\right]\right)\left\{U_d\right\}=\left\{0\right\} \tag{5.35}$$

where

$$\left[A\right]=\left[A_{dd}\right]-\left[A_{db}\right]\left[A_{bb}\right]^{-1}\left[A_{bd}\right] \tag{5.36}$$

The above eigenvalue equation can be solved to obtain the natural frequencies of FGSW panels.

5.3.2 Static problems

For the static analysis of FGM cylindrical panel, it is assumed that $\omega = 0$ in Eqs. (5.20) to (5.22). The discretized forms of the boundary conditions on the inner and outer surfaces of the cylindrical panel, mentioned in Eqs. (3.7) to (3.8), can be expressed as follows.

On the inner surface *($r = a$)*:

$$C_{13}\sum_{k=1}^{M} d_{jk}U_{zik} + C_{23}\frac{1}{r}U_{rij} - C_{23}\frac{1}{r}\beta_m U_{\theta ij} + \bar{C}_{33}\sum_{k=1}^{N} c_{ik}U_{rkj} = 0$$

$$-C_{44}\frac{1}{r}U_{\theta ij} + C_{44}\sum_{k=1}^{N} c_{ik}U_{\theta kj} + C_{44}\frac{1}{r}\beta_m U_{rij} = 0$$

$$C_{55}\sum_{k=1}^{N} c_{ik}U_{zkj} + C_{55}\sum_{k=1}^{M} d_{jk}U_{rik} = 0 \tag{5.37}$$

On the outer surface *($r = b$)*:

$$C_{13}\sum_{k=1}^{M} d_{jk}U_{zik} + C_{23}\frac{1}{r}U_{rij} - C_{23}\frac{1}{r}\beta_m U_{\theta ij} + C_{33}\sum_{k=1}^{N} c_{ik}U_{rkj} = q$$

$$-C_{44}\frac{1}{r}U_{\theta ij} + C_{44}\sum_{k=1}^{N} c_{ik}U_{\theta kj} + C_{44}\frac{1}{r}\beta_m U_{rij} = 0$$

$$C_{55}\sum_{k=1}^{N} c_{ik}U_{zkj} + C_{55}\sum_{k=1}^{M} d_{jk}U_{rik} = 0 \tag{5.38}$$

In the case of static analysis, and the global assembling leads to the following set of linear algebraic equations:

$$\begin{bmatrix} [S_{bb}] & [S_{bd}] \\ [S_{db}] & [S_{dd}] \end{bmatrix} \begin{Bmatrix} \{U_b\} \\ \{U_d\} \end{Bmatrix} = \begin{Bmatrix} \{q\} \\ 0 \end{Bmatrix} \tag{5.39}$$

where $\{q\}$ is mechanical load vector. Finally, displacement components are obtained from the following relation:

$$[S]\{U_d\} = [S_{db}][S_{bb}]^{-1}\{q\} \tag{5.40}$$

where

$$[S] = [S_{db}][S_{bb}]^{-1}[S_{bd}] - [S_{dd}] \tag{5.41}$$

The system of Eq. (5.40) can be solved by using MATLAB to find the displacement fields of the FGM cylindrical panel under mechanical load.

5.3.3 Thermal stress problems

In this section, we aim to use GDQ procedure to derive temperature distribution and thermal displacements of FGMs described in two different thermal problems based on elasticity theory (section 3.2.2) and TSDT (section 3.3.2.1).

The first case, explained in section 3.2.2, describes thermo-elastic analysis of 1-D FGM cylindrical panel based on 3-D elasticity theory. In this case, the Fourier expansion form of the temperature field in the θ- and z-direction can be represented as:

$$T(r,\theta,z)=\sum_{m=1}^{\infty}\sum_{n=1}^{\infty}\mathrm{T}(r)\sin(\beta_m\theta)\sin(\frac{n\pi}{L}z) \tag{5.42}$$

$\beta_m = m\pi/\Phi$, $(m=1,2,...)$

The above assumed form of the temperature field identically satisfies the homogeneous boundary conditions (3.37) to (3.40) for the temperature at the edges. In addition, the following solutions that satisfy the boundary conditions at the simply supported edges ($z=0,L$) is assumed:

$$u_r(r,\theta,z)=\sum_{m=1}^{\infty}\sum_{n=1}^{\infty}U_r(r)\sin(\beta_m\theta)\sin(\frac{n\pi}{L}z), \tag{5.43}$$

$$u_\theta(r,\theta,z)=\sum_{m=1}^{\infty}\sum_{n=1}^{\infty}U_\theta(r)\cos(\beta_m\theta)\sin(\frac{n\pi}{L}z), \tag{5.44}$$

$$u_z(r,\theta,z)=\sum_{m=1}^{\infty}\sum_{n=1}^{\infty}U_z(r)\sin(\beta_m\theta)\cos(\frac{n\pi}{L}z) \tag{5.45}$$

Upon substituting Eqs. (5.43) to (5.45) into the governing Eq. (3.23), the coupled partial differential equations are reduced to a set of 1-D ordinary differential equations (ODE) as follows

$$\begin{bmatrix} J_{1r} & J_{1\theta} & J_{1z} & J_{1T} \\ J_{2r} & J_{2\theta} & J_{2z} & J_{2T} \\ J_{3r} & J_{3\theta} & J_{3z} & J_{3T} \\ 0 & 0 & 0 & J_{4T} \end{bmatrix} \begin{Bmatrix} U_r \\ U_\theta \\ U_z \\ \mathrm{T} \end{Bmatrix} = \{0\} \tag{5.46}$$

At this stage, by applying Eq. (5.1) to Eq. (5.46), and also boundary conditions on the inner and outer surfaces Eqs. (3.39) and (3.40), governing equations including heat conduction equation and related boundary conditions are discritized. Similar to the procedure explained in section 5.3.2, domain and boundary degrees of freedom are separated and in vector forms they are denoted as (*d*) and (*b*), respectively. Based on this definition, the matrix form of the equilibrium equations and the related boundary conditions take the following form:

$$\begin{bmatrix} [A_{bb}] & [A_{bd}] \\ [A_{db}] & [A_{dd}] \end{bmatrix} \begin{Bmatrix} \{U_b\} \\ \{U_d\} \end{Bmatrix} = \begin{Bmatrix} \{\hat{T}\} \\ \{0\} \end{Bmatrix} \tag{5.47}$$

where $\{\hat{T}\}$ is thermal load vector and $\{U_d\}$, $\{U_b\}$ are as follows:

$$\{U_d\} = \{\{U_{rd}\}, \{U_{\theta d}\}, \{U_{zd}\}, \{\mathrm{T}_d\}\}^T \tag{5.48}$$

$$\{U_b\} = \{\{U_{rb}\}, \{U_{\theta b}\}, \{U_{zb}\}, \{\mathrm{T}_b\}\}^T \tag{5.49}$$

Displacement components and temperature are obtained from the following relations:

$$[A]\{U_d\} = [A_{db}][A_{bb}]^{-1}\{\hat{T}\} \tag{5.50}$$

where

$$[A] = [A_{db}][A_{bb}]^{-1}[A_{bd}] - [A_{dd}] \tag{5.51}$$

By solving Eq. (5.50) displacement and temperature fields of the FGM cylindrical panel are determined.

Now, we turn our attention to the second case introduced in section 3.3.2.1, which is related to thermal stress analysis of 2-D FGM cylindrical panel based on TSDT. In order to determine displacements and thermal stresses, the temperature distribution in the 2-D FGM should be obtained firstly. The 2-D FGM panel shown in Figure 3.7 is assumed to be exposed to ambient air T_∞ with a heat-transfer coefficient h_a at lower and upper edges. The inner surface of the panel experiences a high heat flux while the outer surface is subjected to temperature load. The thermal boundary conditions are as follow:

Heat flux at the inner radius $z = -h/2 :\ q = q_0$ (5.52)

Heat convection at the lower edge $x = 0:\ k\dfrac{\partial T}{\partial x} + h_a(T - T_\infty) = 0$ (5.53)

Heat convection at the upper edge $x = L:\ k\dfrac{\partial T}{\partial x} + h_a(T - T_\infty) = 0$ (5.54)

Temperature at the outer radius $z = h/2:\ T = T_0$ (5.55)

The assumed form of the temperature field which satisfies the boundary conditions mentioned in Eq. (3.80) and Eqs. (5.52) to (5.55) for the temperature at the edges is considered by assuming the following form:

$$T(x,\theta,z) = \sum_{m=1}^{\infty} \mathrm{T}(x,z)\sin(\beta_m\theta), \tag{5.56}$$

where $\beta_m = m\pi/\Theta$, $(m = 1, 2, ...)$

Upon substituting Eq. (5.56) into the equation of steady-state heat transfer (3.81), the partial differential equations reduce to an ordinary differential relation as follows:

$$\left(\frac{\partial k}{\partial z} + k\frac{1}{Z_m + z}\right)\frac{\partial \mathrm{T}}{\partial z} + k\frac{\partial^2 \mathrm{T}}{\partial z^2} - k\left(\frac{Z_m}{Z_m + z}\right)^2 \beta_m{}^2\mathrm{T} + \frac{\partial k}{\partial x}\frac{\partial \mathrm{T}}{\partial x} + k\frac{\partial^2 \mathrm{T}}{\partial x^2} = 0 \tag{5.57}$$

At this stage, the GDQM, Eq. (5.1), can be applied to discretize the 1-D equation of steady-state heat transfer (5.57) and the boundary conditions stated in Eqs. (5.52) to (5.55). As a result, at each domain grid point (z_i, x_j) with $z_i = 2, ..., N_z - 1$ and $x_j = 2, ..., N_x - 1$, the discretized equation takes the following forms:

$$\left(\frac{\partial k}{\partial z} + k\frac{1}{Z_m + z}\right)\sum_{k=1}^{N_z} c_{ik}\mathrm{T}_{kj} + k\sum_{k=1}^{N_z} c_{ik}^{(2)}\mathrm{T}_{kj} - k\left(\frac{Z_m}{Z_m + z}\right)^2 \beta_m{}^2\mathrm{T}_{ij} + \frac{\partial k}{\partial x}\sum_{k=1}^{N_x} d_{jk}\mathrm{T}_{ik}$$

$$+k\sum_{k=1}^{N_x} d_{jk}^{(2)}\mathrm{T}_{ik} = 0 \tag{5.58}$$

where c_{ij}, d_{ij} and $c_{ij}^{(2)}, d_{ij}^{(2)}$ are the first and second order GDQM weighting coefficients in the *z*- and *x*-directions, respectively. After employing the aforementioned solution procedure, one obtains the discretized form of the equation of heat transfer and the related boundary conditions which in matrix form can be written as,

$$\begin{bmatrix} [A_{bb}] & [A_{bd}] \\ [A_{db}] & [A_{dd}] \end{bmatrix} \begin{Bmatrix} \mathrm{T}_b \\ \mathrm{T}_d \end{Bmatrix} = \begin{Bmatrix} \{f_{conv}\} \\ \{0\} \end{Bmatrix} \tag{5.59}$$

where subscripts '*d*' and '*b*' refer to domain and boundary, respectively. $\{f_{conv}\}$ is convection vector related to heat convection boundary conditions at upper and lower edges. Then temperature field is obtained from the following relations

$$\mathrm{T}_d = [B]^{-1}[A_{db}][A_{bb}]^{-1}\{f_{conv}\} \tag{5.60}$$

where

$$[B] = [A_{db}][A_{bb}]^{-1}[A_{bd}] - [A_{dd}] \tag{5.61}$$

Due to temperature-dependent thermal conductivity, i.e. $k(z,x,T)$, a nonlinear ordinary differential equation (ODE) of the form (5-58) is obtained for the temperature field. Therefore, an iterative method should be used to solve the system of nonlinear equation (5-58). To begin the iterations, the spatially varying thermal conductivity is evaluated at a constant reference temperature T_{ref} and the GDQM solution for the temperature field is obtained by solving a linear ODE with prescribed thermal conductivity. In the next iteration, the thermal conductivity is updated based on the temperature field from the previous iteration and the heat conduction problem solved again to obtain an updated temperature field. This process is repeated until the change in peak temperature between two consecutive iterations falls below an absolute tolerance. The description of the procedure is well understood through the flow chart shown in Figure 5.3.

In the mechanical analysis, the temperature field obtained from the thermal analysis is entered into the governing equations of the 2-D FGM as a thermal loading. The Fourier expansion form of the displacement components in the θ-direction can be represented as:

$$\overline{u} = \sum_{m=1}^{\infty} \underline{u} \cos(\beta_m \theta), \tag{5.62}$$

$$\overline{v} = \sum_{m=1}^{\infty} \underline{v} \sin(\beta_m \theta), \tag{5.63}$$

$$\overline{w} = \sum_{m=1}^{\infty} \underline{w} \cos(\beta_m \theta), \tag{5.64}$$

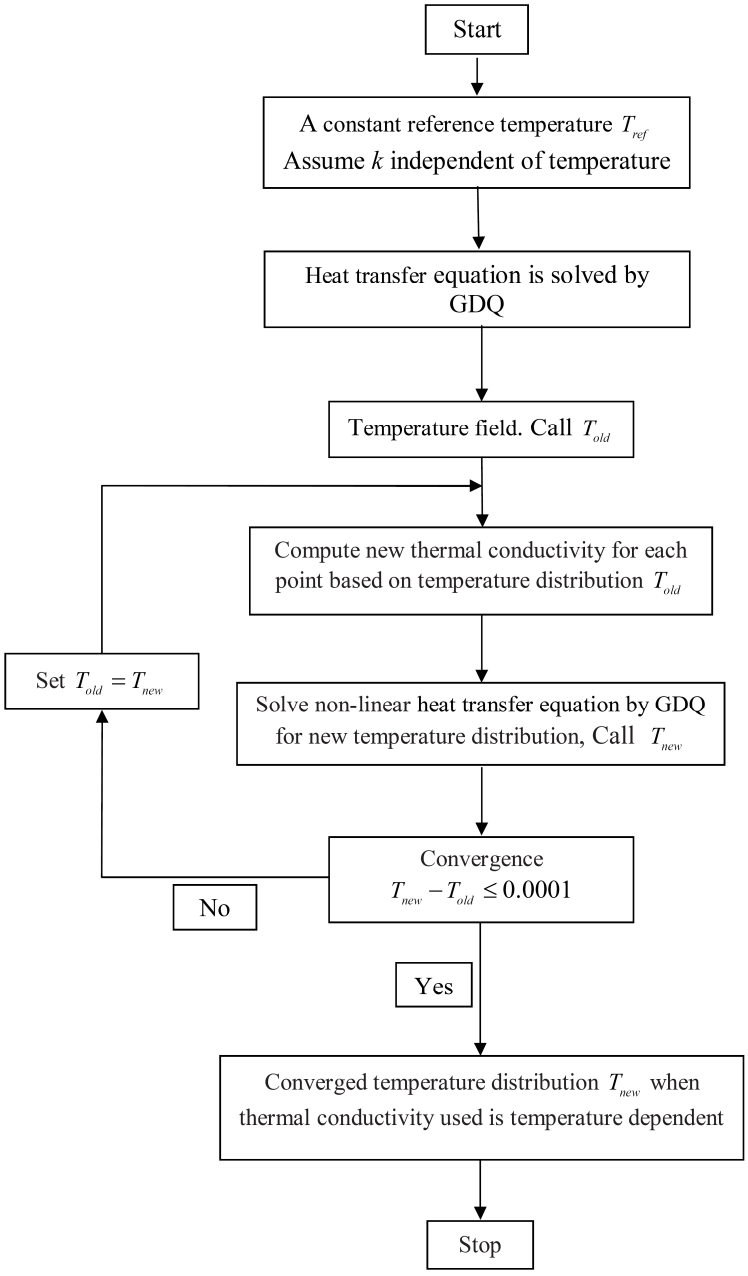

Figure 5.3. Flow chart for computation of temperature distribution based on temperature-dependent material properties.

$$\overline{\psi}_1 = \sum_{m=1}^{\infty} \underline{\psi}_1 \cos(\beta_m \theta), \tag{5.65}$$

$$\overline{\psi}_2 = \sum_{m=1}^{\infty} \underline{\psi}_2 \sin(\beta_m \theta), \tag{5.66}$$

where $\beta_m = m\pi/\Theta$, $(m = 1, 2, ...)$.

After substituting Eqs. (5.62) to (5.66) into Eq. (3.77), the partial differential equations in terms of the variables x and θ reduce to ordinary differential equations in terms of the variable x and by application GDQ discretization rules for spatial derivatives, the discretized form of the differential equations of motion are obtained. Rearranging the GDQ analogs of field equations and boundary conditions within the framework of a generalized problem yields:

$$\begin{bmatrix} [A_{bb}] & [A_{bd}] \\ [A_{db}] & [A_{dd}] \end{bmatrix} \begin{Bmatrix} \delta_b \\ \delta_d \end{Bmatrix} = \begin{Bmatrix} \{F_{Tb}\} \\ \{F_{Td}\} \end{Bmatrix} \tag{5.67}$$

in which the subscripts *b* and *d* refer to the boundary and domain grid points, respectively. $\{F_{Tb}\}$ and $\{F_{Td}\}$ are thermal vectors related to thermal boundary conditions and temperature field obtained from the thermal analysis, respectively. The displacement vectors δ_d and δ_b are defined by:

$$\{\delta_d\} = \left[\{\Gamma_d^{(1)}\} \quad \{\Gamma_d^{(2)}\} \quad ... \quad \{\Gamma_d^{(N)}\} \right]^T$$

$$\{\Gamma_d^{(i)}\} = \left[\underline{u}_d^{(i)} \quad \underline{v}_d^{(i)} \quad \underline{w}_d^{(i)} \quad \underline{\psi}_{1d}^{(i)} \quad \underline{\psi}_{2d}^{(i)} \right]^T, \qquad (i = 1, 2, ...N_x) \tag{5.68}$$

and

$$\{\delta_b\} = \left[\{\Gamma_b^{(1)}\} \quad \{\Gamma_b^{(2)}\} \quad ... \quad \{\Gamma_b^{(N)}\} \right]^T$$

$$\{\Gamma_b^{(i)}\} = \left[\underline{u}_b^{(i)} \quad \underline{v}_b^{(i)} \quad \underline{w}_b^{(i)} \quad \underline{\psi}_{1b}^{(i)} \quad \underline{\psi}_{2b}^{(i)} \right]^T, \qquad (i = 1, 2, ...N_x) \tag{5.69}$$

Finally thermal displacement components of the 2-D FGM cylindrical panel are obtained from the following relations:

$$\{\delta_d\} = [L]^{-1}\left[\{F_{Td}\} - [A_{db}][A_{bb}]^{-1}\{F_{Tb}\}\right] \tag{5.70}$$

where

$$[L] = [A_{dd}] - [A_{db}][A_{bb}]^{-1}[A_{bd}] \tag{5.71}$$

5.4 Summary and conclusions

In this chapter, GDQM has been adopted for solving coupled governing differential equations with variable coefficients derived in chapter 3. Starting with an introduction on GDQM, weighting coefficients for first order derivative and then extension to the two-dimensional case have been discussed. The Chebyshev-Gauss-Lobatto points, which performed the best among the other non-uniform typical grid distributions as reported in literature, was selected for distribution of grid points.

Eventually, GDQM was applied to discretize the governing equations and boundary conditions of various problems in free vibration, static, thermal analyses of structures composed of FGMs. In this case, the solution procedure for free vibration analysis of cylindrical panels has been explained in detail. Afterwards, discussion has been focused on the application of GDQM in static analysis. At the end, GDQM has been employed to derive temperature distribution and thermal displacements of FGMs described in two different thermal problems based on elasticity theory and then TSDT. It can be inferred that GDQM was a simple and powerful numerical technique for various structural analysis of FGMs. In the next chapter, efficiency and accuracy of GDQM in several FGM problems will be examined and fast rate of convergence of the method will be shown.

Chapter 6

Numerical results and discussion

6.1 Overview

This chapter deals with numerical results and discussion for various analyses of FGMs categorized into three sections namely 1-D FG fiber-reinforced composites, 2-D FGM composites, and FG CNT-reinforced composites. Section 6.2 allocated to 1-D FG fiber-reinforced composites is divided into two subsections named as “free vibration and static analyses” and “thermal stress analysis”. In section 6.2.1, firstly, numerical results for free vibration and static analyses of cylindrical panels with graded fiber orientation and also graded fiber volume fractions are presented. Then, in section 6.2.2 new and interesting results for FG Sandwich (FGSW) panel are elaborated and discussed. After that in the next section, a parametric study for rectangular plate resting on elastic foundation with graded fiber volume fraction is carried out. Regarding thermal stress analysis, section 6.2.2.1 compares results of thermal behavior of FG fiber-reinforced cylindrical panels with discretely laminated ones. On the other hand, in section 6.2.2.2 novel results for the thermal stress analysis of a closed cylindrical resting on elastic foundations are presented. Section 6.2 is allocated to 2-D FGM composites. Firstly, new results for free vibration and static analyses of 2-D FGM cylindrical panel is presented followed by a comparison study with classic 1-D FGMs. Then, results of thermal behavior of 2-D FGM cylindrical panel with temperature-dependent materials are studied and interesting results are elaborated. In the following, brand-new results for FG CNT-reinforced composites are given in section 6.4. Firstly a parametric study for free vibration of annular sectorial plates resting on elastic foundation reinforced by graded agglomerated CNTs is presented in section 6.4.1. Afterwards, free vibration characteristics of rectangular plate reinforced by graded aligned CNTs are studied. Eventually, in section 6.4.2 new and interesting results for mechanical buckling of FG CNT-reinforced rectangular plates reinforced by CNTs subjected to uniaxial and biaxial in-plane loadings are presented and discussed.

6.2 1-D FG fiber-reinforced composites

In this section, new and interesting numerical results specialized in 1-D FG fiber-reinforced composites are presented. According to different types of analysis, this section is separated into “free vibration and static analyses” and “thermal stress analysis”. In each section, detailed parametric studies are carried out to highlight the influences of different parameters encompassing material profiles and geometrical parameters on the mechanical behavior of plates and shells composed of 1-D FG fiber-reinforced composites. Furthermore, the fast rate of convergence of the semi-analytical method, GDQM, is demonstrated and comparison studies are carried out to establish its very high accuracy and versatility. The effective mechanical properties

of the fiber-reinforced composites are obtained based on a micromechanical model as mentioned in section 4.3.1.

6.2.1 Free vibration and static analyses

In this section we will focus on useful results of free vibration and static problems. Depending on the geometry of the structure, this section is divided into three subsections. Section 6.2.1.1 discusses cylindrical panels, Section 6.2.1.2 discusses Sandwich panels, and Section 6.2.1.3 discusses rectangular plates. It should be noted that each subsection deals with distinct FGM mathematical modeling and material properties.

6.2.1.1 Cylindrical panels

Herein free vibration and static analyses of cylindrical panels with graded fiber orientation and also graded fiber volume fractions are presented. In order to validate the analysis, results for an FGM isotropic cylindrical shell ($\Phi = 2\pi$) are compared with Shakeri et al. [186], as shown in Table 6.1. The mechanical properties are as follows:

r_i =0.25 m., r_o =0.5 m.,

on inner surface E_c = 380 Gpa, ρ_c =3800 kg/m^3,

on outer surface E_m =70 Gpa., ρ_m =2707 kg/m^3,

The comparison shows that the present results agree well with those reported in the literature.

Table 6.1. Comparison of first natural frequency for various *p*.

p	Present (HZ.)	Shakeri [186] (HZ.)
0.01	2356.1	2441.5
0.5	2916.2	3006.2
5	4147.7	4394.5
20	4150.8	4394.5

Further validation of the present results for isotropic FGM cylindrical panel are shown in Table 6.2. In this Table, comparison is made for different *L/R* and *L/h* ratios and as it is observed there is good agreement between the results.

Now, we characterize the response of orthotropic cylindrical panel with graded fiber volume fractions or fiber orientation through the thickness of the panel. The orthotropic panel consists of continuous tungsten reinforcement fibers in a copper

Table 6.2. Comparison of the normalized natural frequency for various *L/R* and *L/h* ratios

		p			
		0	**0.5**	**1**	**4**
***L/h* =2**	***L/R*=0.5**				
Ref.[67]		0.9334	0.8213	0.7483	0.6011
Ref. [138]		0.9187	0.8013	0.7263	0.5267
Present Results		0.9249	0.8018	0.7253	0.5790
***L/h* =2**	***L/R* =1**				
Ref.[67]		0.9163	0.8105	0.7411	0.5967
Ref. [138]		0.8675	0.7578	0.6875	0.5475
Present Results		0.8857	0.7667	0.6935	0.5531
***L/h* =5**	***L/R* =0.5**				
Ref.[67]		0.2153	0.1855	0.1678	0.1413
Ref. [138]		0.2113	0.1814	0.1639	0.1367
Present Results		0.2129	0.1817	0.1638	0.1374
***L/h* =5**	***L/R* =1**				
Ref.[67]		0.2239	0.1945	0.1769	0.1483
Ref. [138]		0.2164	0.1879	0.1676	0.1394
Present Results		0.2154	0.1848	0.1671	0.1391

matrix (W/Cu). These material combinations have found widespread use in high performance application [187]. The relevant material properties for the constituent materials are listed in Table 6.3. The equations of motion of the panel were derived in section 3.2.1.1, and solved by using GDQM explained in section 5.3.1. Mathematical modeling of the FG fiber-reinforced panel is according to classic power-law distribution (section 4.2.1). In other words, fiber volume fraction follows classic power-law distribution, Eq. (4.1), and fiber orientation ϕ with respect to the z-axis in the $z-\theta$ surface varies through the thickness by Eq. (4.2).

At this stage, a convergence study of the non-dimensional natural frequency $\Omega = \omega r_i \sqrt{\rho / E_T}$ is shown in Figure 6.1 for a graded panel with a linear variation of fiber orientation from $\phi_i = 0^0$ to $\phi_o = 90^0$, as shown in Figure 4.3. As noticed, fast rate of convergence of the method is evident at different $S = R/h$ ratios and it is found that only seven GDQ grid in the thickness direction can yield accurate results. It can also be seen for the considered system the formulation is stable while increasing the number of points and that the use of 50 points guarantees convergence of the procedure.

Now we compare a graded panel with a linear variation of fiber orientation from

Table 6.3. Mechanical properties of the orthotropic material.

	Cu	W
E (GPa)	115.0	400.0
ν	0.31	0.28
ρ (kg/m^3)	8960	19,300

$\phi_i = 0^0$ to $\phi_o = 90^0$ with 2-layer $[0^0/90^0]$, 3-layer $[0^0/45^0/90^0]$ and 4-layer $[0^0/30^0/60^0/90^0]$ discrete laminates.

The effect of S ratio on the normalized natural frequency is shown in Figure 6.2. As observed the non-dimensional natural frequency decreases sharply with increasing the S ratio for thick panels and remains almost unaltered for thin ones (S>150). As can be seen from this figure the normalized natural frequency of a graded fiber orientation is lower than that of a similar discrete laminated and closer to 4-layer laminated one. Similar results can be obtained from Figure 6.3. In this figure, comparison is made between graded fiber volume fractions and discrete laminated panels for various values of circumferential wave numbers.

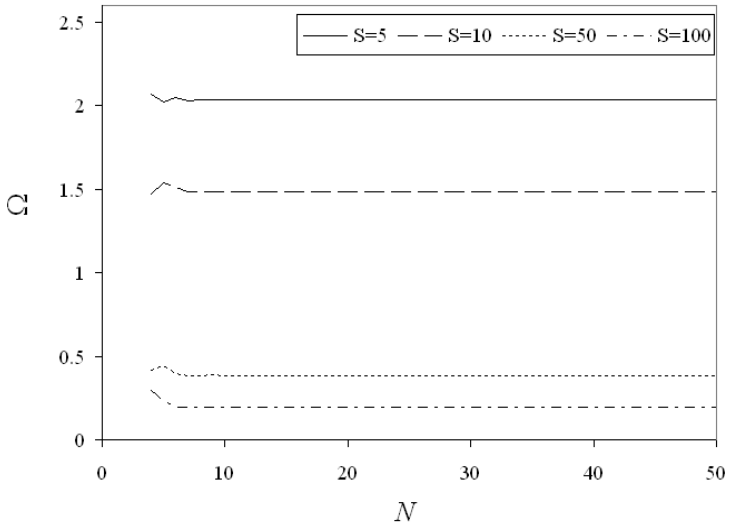

Figure 6.1. Convergency of the non-dimensional natural frequency of the panel ($\Phi = \pi/6,\ p = 1, m = 1$)

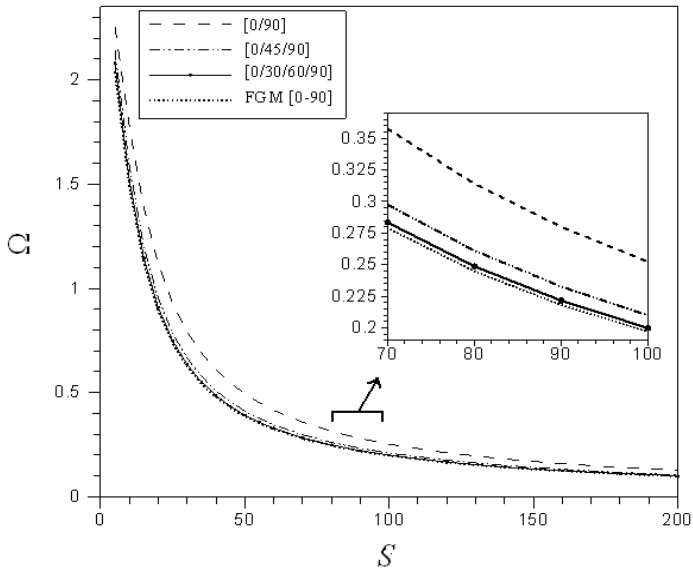

Figure 6.2. Effect of S ratio on the non-dimensional natural frequency for FGM, 2-layer, 3-layer and 4-layer ($\Phi = \pi / 6,\ p = 1, m = 1$)

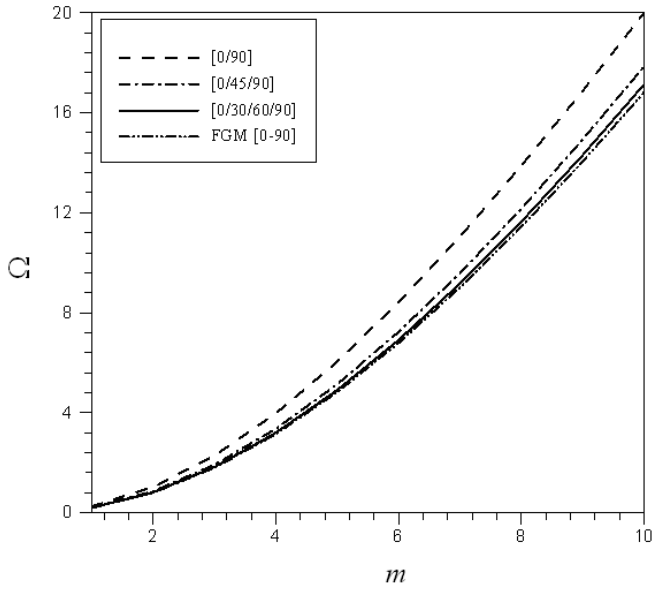

Figure 6.3. Variation of the non-dimensional natural frequency versus circumferential wave m ($\Phi = \pi / 6,\ p = 1, S = 100$)

Herein, we assume that the FG panel has a linear variation of fiber volume fraction according to Eq. (4.1) starting at V_i =1 (0% Tungsten, 100% Copper) on the inner surface of the shell to V_o = 0.25 (75% Tungsten, 25% Copper) on the outer surface. For this case, fibers are oriented at $\phi = 0$, with respect to the axial direction of the panel shell. The normalized natural frequency is, $\Omega = \omega r_i \sqrt{\rho^i / E_2^i}$ (ρ^i, E_2^i are mechanical properties of copper). The effect of *S* ratio on the normalized natural frequency of panel with graded fiber volume fractions is shown in Figure 6.4. As it is observed that unlike the FG fiber orientation panel, normalized natural frequency of graded fiber volume fractions is larger than that of a discrete laminated and close to that of the 2-layer. Similar observations can be seen from Figure 6.5. Also according to Figure 6.5 the non-dimensional natural frequency increases with the increase of the circumferential wave number.

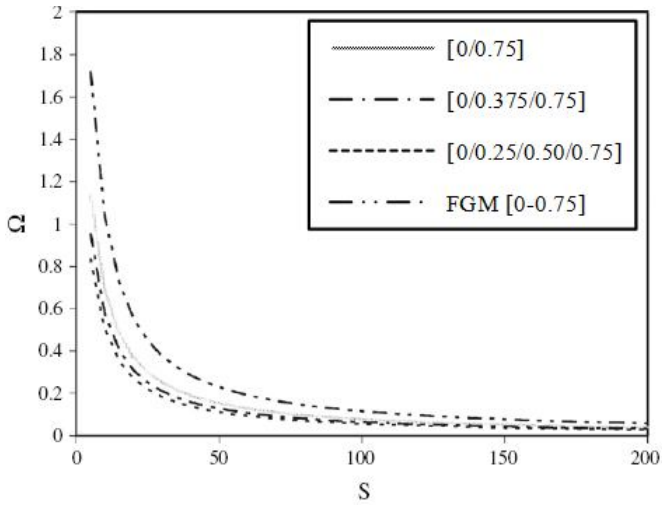

Figure 6.4. Effect of *S* ratio on the normalized natural frequency for graded fiber volume fractions, FGM, 2-layer, 3-layer, 4-layer ($\Phi = \pi / 6, p = 1, m = 1$)

In Figure 6.6, effect of various volume fraction profiles on the non-dimensional natural frequency of FG fiber-reinforced panel is studied. To this end, fiber volume fraction follows a smooth variation according to 1-D generalized power-law distribution indicated in Eq. (4.9). As demonstrated in Figure 4.5, by setting *a*=1,

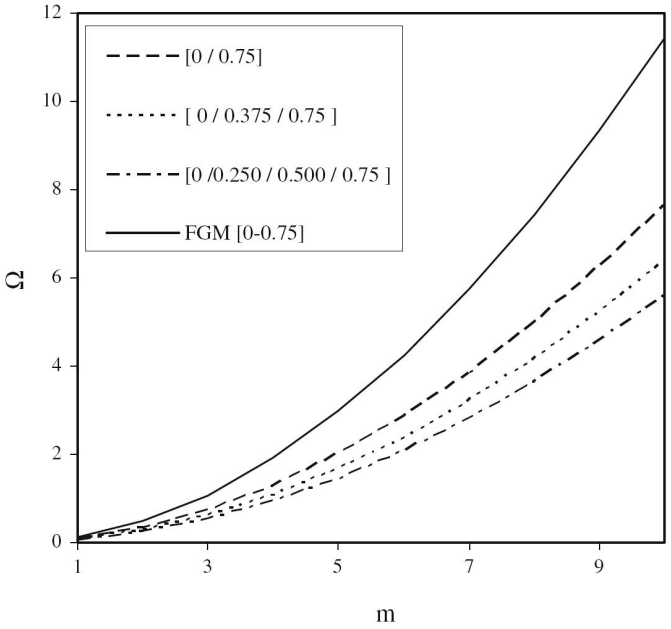

Figure 6.5. Variation of the normalized natural frequency against m ($\Phi = \pi / 6$, S=100)

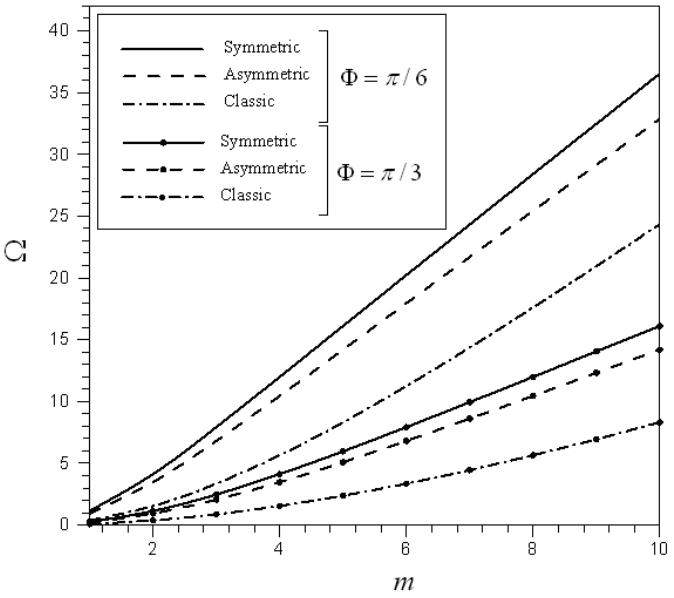

Figure 6.6. Variation of the first non-dimensional natural frequency vs. circumferential wave numbers for three different fiber orientation profiles

b=1, and *c*=2 in Eq. (4.9) symmetric volume fraction is obtained. Also, asymmetric profiles is derived by setting *a*=1, *b*=1 and *c*=4. As observed in Figure 6.6 the maximum non-dimensional natural frequency can be obtained through using symmetric fiber orientation profile. This interesting result can be used as a strategy for the design of FG fiber orientation cylindrical panels.

Now we turn our attention to static analysis of cylindrical panels with graded fiber volume fractions. To validate the static analysis, the present results are obtained for one- layer orthotropic cylindrical shell under internal static load and compared with similar results by Varadan [188]. The non- dimensional parameters are:

$$(\overline{\sigma}_z, \overline{\sigma}_\theta) = \frac{10(\sigma_z, \sigma_\theta)}{qS^2}, \overline{\sigma}_r = \frac{\sigma_r}{q}, \ \overline{\tau}_{r\theta} = \frac{10\tau_{r\theta}}{qS} \tag{6.1}$$

As it is observed from Table 6.3 there is good agreement between the results.

The displacement and stress components are non-dimensionalized as follows:

$$(\overline{\sigma}_z, \overline{\sigma}_\theta) = \frac{(\sigma_z, \sigma_\theta)}{qS^4}, \overline{\sigma}_r = \frac{\sigma_r}{q}, \overline{U}_r = \frac{100E_iU_r}{qhS^4}, \ \overline{\tau}_{rz} = \frac{\tau_{rz}}{qS} \tag{6.2}$$

where E_i is Young's modulus of 100% copper (inner surface).

Table 6.3. Comparison of the maximum stresses for one-layer orthotropic cylindrical shell (*N*=13, *L*/*R*=4)

S		$U_r(\frac{L}{2},\frac{\phi}{2},0)$	$\sigma_z(\frac{L}{2},\frac{\phi}{2},\frac{h}{2})$	$\sigma_\theta(\frac{L}{2},\frac{\phi}{2},\frac{h}{2})$	$\tau_{rz}(0,\frac{\phi}{2},0)$
5	Present	2.2717	0.02579	0.960813	0.00946
	[188]	2.272	0.02579	0.9608	0.00946
10	Present	1.1430	0.01545	0.80325	0.006344
	[188]	1.143	0.01545	0.8033	0.00634
50	Present	0.7560	0.01941	0.73874	0.00506
	[188]	0.756	0.01941	0.7387	0.00506
100	Present	0.7078	0.02837	0.7035	0.00477
	[188]	0.708	0.02838	0.7035	0.00478

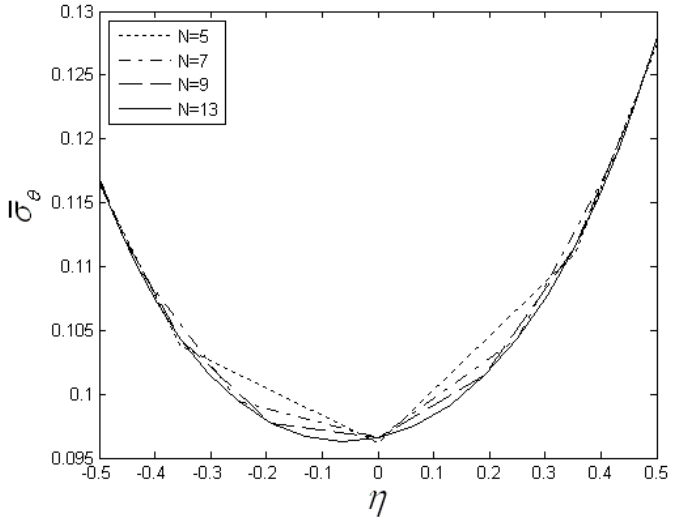

Figure 6.7. Convergency of the non-dimensional circumferential stress through the thickness panel with continuous grading reinforcement (p=1, S=10, L/R=1, a=1, b=1, c=2)

The cylindrical panel has geometrical parameters as: $L = 2\text{m}, R = 0.5\text{m}$. A convergence study of the non-dimensional circumferential stress through the thickness are shown in Figure 6.7, by considering a=1, b=1, c=2 in Eq. (4.9). As it

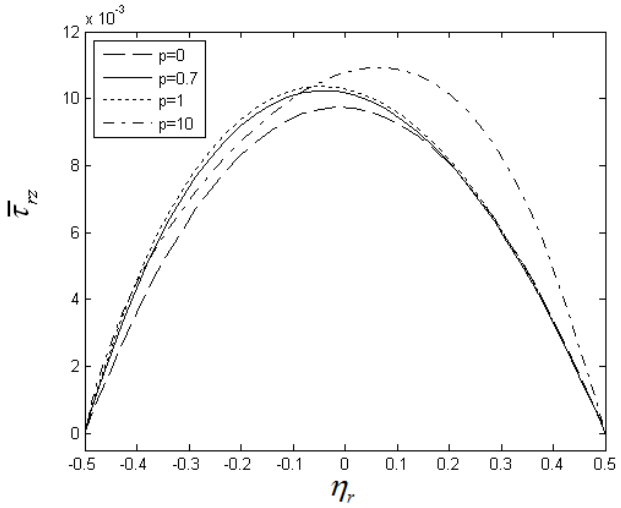

Figure 6.8. Through-the-thickness variation of the non-dimensional transverse shear for different values of parameter p (S=10, L/R=1, a=1, b=1, c=2)

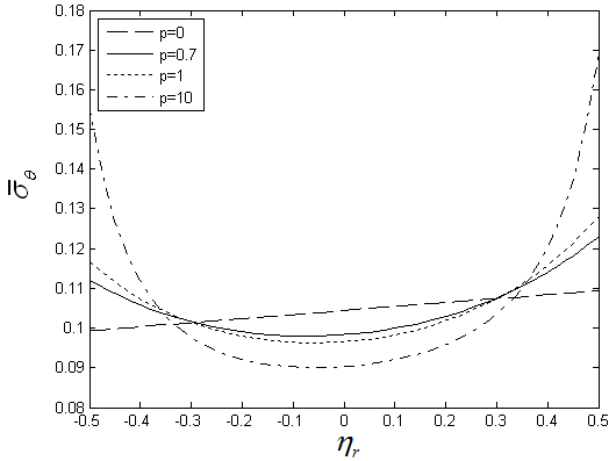

Figure 6.9. Through-the-thickness variation of the circumferential stress for different values of parameter p (S=10, L/R=1, a=1, b=1, c=2)

can be seen that fast rate of convergence of the method is evident and for the considered system, the formulation is stable while increasing the number of points.

The influence of the parameter index p on the non-dimensional transverse shear and circumferential stresses along the thickness of cylindrical panel are presented in Figures 6.8 and 6.9, by considering a=1, b=1, c=2 in Eq. (4.9). The circumferential stress is linear for $p = 0$. Figure 6.8 shows the peak of transverse shear stress increases by increasing copper matrix phase (with increasing parameter p). It is worth noting that Figure 6.8 shows distribution of transverse shear stress in cylindrical shell in contrast with the orthotropic (p=0) cylindrical panel is not symmetric with respect to the mid-surface. In Figure 6.9, it is seen that the non-dimensionalized circumferential stress on the inner and outer surfaces increases with increasing the volume fraction of matrix phase.

Now we compare static behaviour of the FGM orthotropic cylindrical panel with discretely laminated 2-layer, 3-layer shell containing [1/0.25], [1/0.625/0.25] volume fractions of matrix phase, respectively. Figure 6.10 demonstrates how the non-dimensional axial and transverse shear stress components benefit from a gradual change in volume fraction from the shell's inner surface to its outer surface.

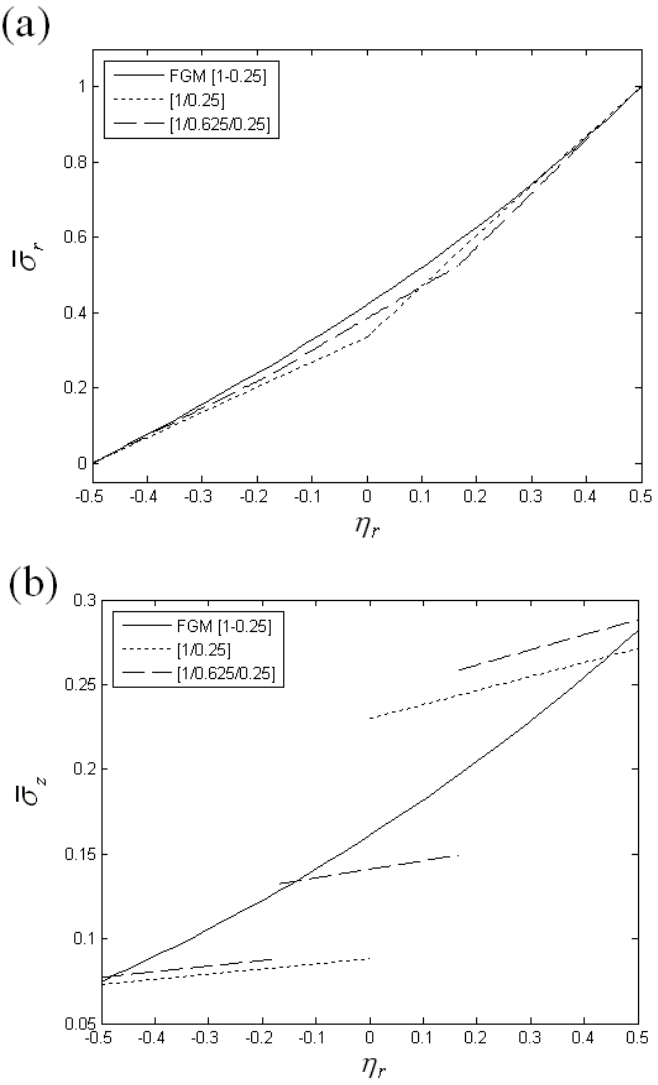

Figure 6.10. Through-the-thickness variation of the mechanical entities for FGM orthotropic, discretely laminated 2-layer and 3-layer cylindrical shells (S=10, L/R=1)

6.2.1.2 Sandwich Panel

In this section, the free vibration of FGSW panels with graded fiber orientation and fiber volume fraction is considered. The composite material consists of unidirectional silicon-carbide fibers in a titanium matrix. The fiber orientation of each layer follows

generalized power-law distribution according to Eq. (4.10). Also, the fiber volume fraction of FGSW panel is assumed to have a variation through the thickness of the panel, as defined in Eq. (4-11). The material properties of titanium and silicon carbide are listed in Table 6.4. The faces have variation of the fiber orientation, while the core has variation of fiber volume fraction. The non-dimensional natural frequencies are defined as: $\Omega_m = \omega_m h^2 \sqrt{\rho_i (1+\nu_i^2)/E_i}$ where ρ^i, E^i and ν_i are mechanical properties of fiber phase.

Table 6.4. Mechanical properties of titanium and silicon carbide.

	Young's modulus, E [GPa]	**Poisson's ratio, ν**	**mass density, $\rho\,(Kg/m^3)$**
Titanium (Ti-6Al-4V)	105.75	0.298	4420
Silicon Carbide (SiC)	410	0.170	3100

To show the accuracy of the analysis, two examples are presented. As a first example, a comparative study for evaluation of non-dimensional frequency parameter between the present semi-analytical solution technique and the exact

Table 6.5. Comparison studies of non-dimensional frequency parameter with those of Messina and Soldatos [189] for the three-layered orthotropic plate with different lamination angle (pattern $[+\theta/-\theta/+\theta]$).

$\phi\,(^0)$	**Methods**	
	Exact elasticity solution [189]	**Present**
0	0.16489	0.16412
15	0.11541	0.11505
30	0.088013	0.087999
45	0.065634	0.065489
60	0.048226	0.048201
75	0.040409	0.040387
90	0.03925	0.03911

elasticity solution published by Messina et al. [189] is carried out in Table 6.5 for a three-layer orthotropic infinite plate with different lamination angle. It can be observed from Table 6.5 that there is a very good agreement between the results confirming the accuracy of the current approach. In the second example, the results

of a FG Al/ZrO_2 thick plate with simply supported edges for different values of circumferential mode shape parameter m are compared with those of Vel [73] in Table 6.6. The volume fraction of the zirconia varies linearly through the thickness

Table 6.6. Comparison of the non-dimensional natural frequencies for a FG Al/ZrO_2 flat plate with different values of circumferential mode shape m ($p=1$).

m	Methods	$\bar{\omega}_m^{(1)}$	$\bar{\omega}_m^{(2)}$	$\bar{\omega}_m^{(3)}$	$\bar{\omega}_m^{(4)}$
1	Present	2.8115	8.3357	13.972	34.309
	Exact elasticity solution [73]	2.8236	8.3388	13.985	34.357
2	Present	9.3010	16.659	27.421	37.199
	Exact elasticity solution [73]	9.3200	16.663	27.442	37.211
3	Present	17.115	24.952	39.179	41.530
	Exact elasticity solution [73]	17.162	24.957	39.194	41.548
4	Present	25.389	33.201	46.901	47.089
	Exact elasticity solution [73]	25.416	33.206	46.982	47.156
5	Present	33.759	41.378	52.100	53.189
	Exact elasticity solution [73]	33.772	41.397	52.161	53.201
6	Present	42.105	49.505	56.714	59.932
	Exact elasticity solution [73]	42.128	49.519	56.796	59.987

of the plate going from aluminum on the bottom surface to zirconia on the top surface. For this material the fibers are oriented at $\phi = 0^{\circ}$, with respect to the axial direction of the panel. In Table 6.6, the accuracy of the presented formulations and the method of solution are compared with those of exact elasticity solution, by setting the mid-surface radius $R \to \infty$, and as observed there is excellent agreement between the results.

The effects of the different distributions of the fiber orientation through the thickness are studied by considering the fundamental normalized frequencies of different types of FGSW panels. Fiber orientation profiles along the thickness of the different types of FGSW panels are illustrated in Figures 4.8 to 4.10. Figure 6.11 shows, influence of the power-law index p on the fundamental normalized frequencies of the different types of FGSW panels with $h_f/h = 0.1$ and S=100. It can be noted that in Figure 6.11 the natural frequencies of classic profile exhibits a fast descending behaviour

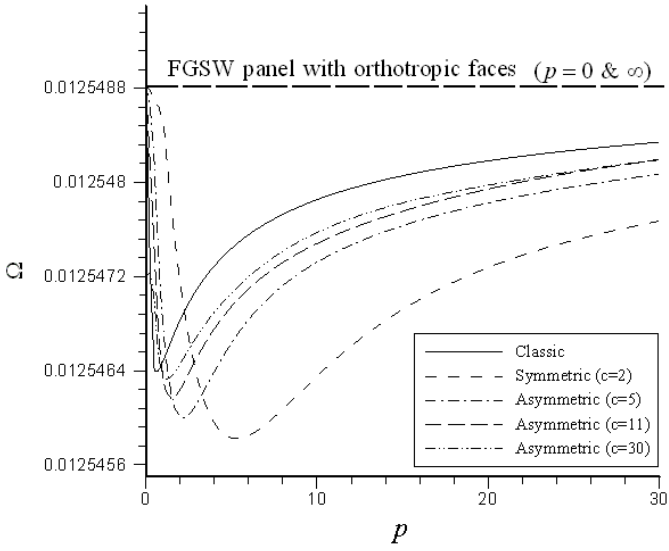

Figure 6.11. Influence of the power-law index p on the fundamental normalized frequencies of the different types of FGSW panels ($h_f/h = 0.1$, $\Phi = \pi/2$, S=100, q=1)

Table 6.7. Influence of the parameter c on the fundamental normalized frequencies of FGSW panel for different values of S ratio and h_f/h ratio ($\Phi = \pi/2$, a=1, b=1, p=1, q=1, m=1).

		c			
h_f/h	S	**2**	**5**	**7**	**11**
0.1	10	0.12537560	0.12529958	0.12528068	0.12526882
	20	0.06269119	0.06265696	0.06265059	0.06264686
	50	0.02509032	0.02508283	0.02508171	0.02508107
	70	0.01792432	0.01792049	0.01791992	0.01791959
	100	0.01254862	0.01254679	0.01254651	0.01254635
0.2	10	0.12400170	0.12389270	0.12386664	0.12385058
	20	0.06196463	0.06191933	0.06191122	0.06190657
	50	0.02479070	0.02478136	0.02477997	0.02477917
	70	0.01770917	0.01770435	0.01770364	0.01770323
	100	0.01239741	0.01239508	0.01239472	0.01239452
0.3	10	0.12072586	0.12066545	0.12064731	0.12063513
	20	0.06027847	0.06025039	0.06024444	0.06024094
	50	0.02410525	0.02409871	0.02409762	0.02409700
	70	0.01721808	0.01721452	0.01721395	0.01721363
	100	0.01205281	0.01205100	0.01205072	0.01205055

from the FGSW panels with orthotropic faces ($p = 0$), varying the power-law index from $p = 0$ to $p = 1$, while for values of *p* greater than unity frequencies increase by increasing the power-law exponent *p* and tend to the FGSW panels with orthotropic faces ($p = \infty$). It is shown that with increasing parameter *c*, the minimum value of natural frequency of FGSW panel increases and is close to that of classic fiber orientation profile. In Table 6.7, the fiber orientation profile of faces through the radial direction becomes asymmetric with increasing parameter *c* (*c* > 2), also fiber orientation on the inner and outer surfaces of faces is the same ($\phi = 0^0$). Table 6.7 shows the influence of the parameter *c* on the fundamental normalized frequencies for different values of *S* ratio and h_f / h ratio. As parameters *c* and *S* ratio increase, the fundamental normalized frequency decreases.

The fundamental normalized frequencies of FGSW panel are tabulated in Table 6.8 for different values of the fiber volume fraction on the outer surfaces of core, h_f / h ratio and *S* ratio. It is interesting to note that frequencies increase with the increase of volume fraction of silicon carbide fibers due to the fact that titanium has a much smaller Young's modulus than silicon carbide.

Table 6.8. The fundamental normalized frequencies of FGSW panel for different values of the fiber volume fraction on the outer surfaces of core, h_f / h ratio and S ratio ($\Phi = \pi / 2$, *a*=1, *b*=0, *p*=1, *q*=1, *m*=1).

		V_o			
h_f / h	***S***	**0.8**	**0.7**	**0.6**	**0.5**
0.1	10	0.12527698	0.11852101	0.11265539	0.10744143
	20	0.06264994	0.05924848	0.05629551	0.05367097
	50	0.02508159	0.02371450	0.02252732	0.02147191
	70	0.01791985	0.01694241	0.01609353	0.01533880
	100	0.01254647	0.01186176	0.01126706	0.01073828
0.2	10	0.12385897	0.11766195	0.11214782	0.10715933
	20	0.06190958	0.05879977	0.05602980	0.05352206
	50	0.02477964	0.02353236	0.02242023	0.02141247
	70	0.01770346	0.01681205	0.01601704	0.01529648
	100	0.01239463	0.01177038	0.01121353	0.01070875
0.3	10	0.12063519	0.11553966	0.11077049	0.10630155
	20	0.06024193	0.05769933	0.05531478	0.05307655
	50	0.02409716	0.02308146	0.02212720	0.02123005
	70	0.01721370	0.01648842	0.01580673	0.01516560
	100	0.01205059	0.01154300	0.01106579	0.01061682

6.2.1.3 Rectangular plates

In this section, the new results for three-dimensional natural frequencies of FG fiber-reinforced rectangular plates resting on two-parameter elastic foundation are presented. The orthotropic plate consists of continuous tungsten reinforcement fibers in a copper matrix (W/Cu), as listed in Table 6.3. The foundation is described by the Pasternak or two-parameter model. The equations of motion of the plate and related boundary conditions for elastic foundations were derived in section 3.2.1.3. The FG plate is assumed to have an arbitrary variation of fiber volume fraction in the thickness direction according to classic power-law distribution, Eq. (4.1).

First of all, convergence and validation study of the normalized natural frequency is considered for an isotropic plate on elastic foundation in Table 6.9. The comparison shows that the present results agreed well with those in the literature.
Figure 6.12 shows the effect of Winkler elastic coefficient on the first three non-dimensional natural frequencies for different values of shearing layer elastic

Table 6.9. Comparison of the first three normalized natural frequency of an isotropic on the elastic foundation (N=13, $K_g = 10$)

		$b/h=5$		$b/h=2$	
	K_w	Ω_{11}	Ω_{12}	Ω_{11}	Ω_{12}
PRESENT	0	1.646182	2.685124	2.233409	4.405606
[190]		1.6462	2.6851	2.2334	4.4056
[191]		1.6462	2.6851	2.2334	4.4056
[192]		1.6462	2.6851	2.2334	4.4056
PRESENT	10	1.657742	2.687861	2.253924	4.415035
[190]		1.6577	2.6879	2.2539	4.415
[191]		1.6577	2.6879	2.2539	4.415
[192]		1.6577	2.6879	2.2539	4.415
PRESENT	100	1.743700	2.70962	2.429988	4.498601
[190]		1.7437	2.7096	2.43	4.4986
[191]		1.7437	2.7096	2.43	4.4986
[192]		1.7437	2.7096	2.43	4.4986
PRESENT	1000	1.845099	2.803268	3.711146	5.228465
[190]		1.8451	2.8033	3.7111	5.2285
[191]		1.8451	2.8033	3.7111	5.2285
[192]		1.8451	2.8033	3.7112	5.2285

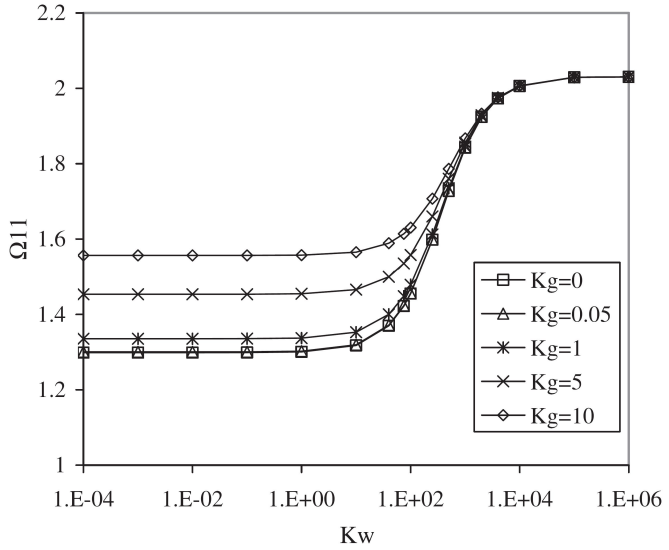

Figure 6.12. Variation of the first non-dimensional natural frequency vs. Winkler elastic coefficient for different shearing layer elastic coefficients (*h/b*=0.5, *a/b*=1)

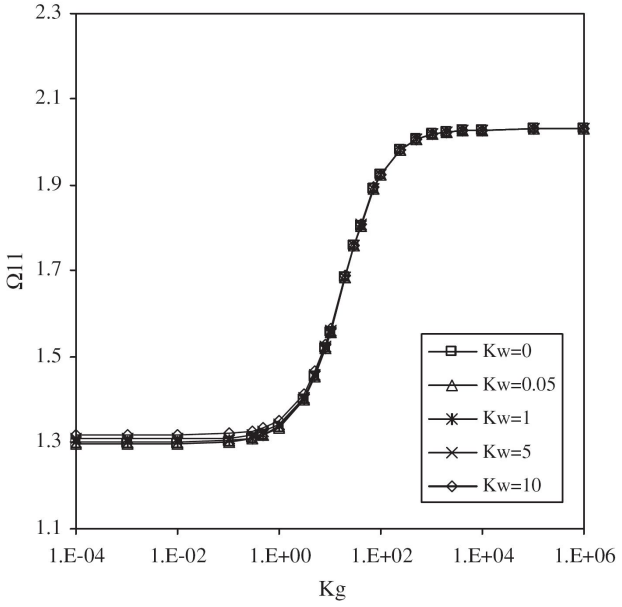

Figure 6.13.Variation of the first non-dimensional natural frequency vs. shearing layer elastic coefficients for different Winkler elastic coefficient (*h/b*=0.5, *a/b*=1)

coefficients. The most effective range of Winkler foundation stiffness in increasing the non-dimensional natural frequencies is from 10^2 to 10^4. It is also observed for the large values of Winkler elastic coefficient, the shearing layer elastic coefficient has less effect and the results become independent of it, in other words, the non-dimensional natural frequencies converge with increasing Winkler foundation stiffness.

The influence of shearing layer elastic coefficient on the first non-dimensional natural frequency is shown in Figure 6.13. It can be seen that the variations of Winkler elastic coefficient has little effect on the non-dimensional natural frequencies at different values of shearing layer elastic coefficient.

Table 6.10. the first three non-dimensional natural frequencies of a fiber reinforced square plate on the elastic foundation (a/b=1)

	K_w	$K_g = 0$			$K_g = 10$		
		Ω_{11}	Ω_{22}	Ω_{33}	Ω_{11}	Ω_{22}	Ω_{33}
$h/b = 0.01$	0	101.833	203.665	305.497	101.833	203.665	305.497
	10	101.833	203.665	305.497	101.833	203.665	305.497
	10^2	101.833	203.665	305.497	101.833	203.665	305.497
	10^3	101.833	203.665	305.497	101.833	203.665	305.497
$h/b = 0.1$	0	1.514	6.986	14.533	1.913	7.338	14.885
	10	1.537	6.991	14.535	1.931	7.342	14.887
	10^2	1.728	7.032	14.553	2.087	7.381	14.904
	10^3	3.0360	7.429	14.733	3.252	7.759	15.075
$h/b = 0.5$	0	1.298	3.225	5.134	1.556	3.415	5.258
	10	1.317	3.232	5.139	1.565	3.416	5.259
	10^2	1.455	3.282	5.171	1.630	3.422	5.259
	10^3	1.842	3.429	5.247	1.867	3.456	5.265

In Table 6.10 the effects of the elastic foundation coefficients and plate's thickness on the first three-non-dimensional natural frequencies of an orthotropic FG square plates is shown. It is observed that both Winkler and shearing layer elastic coefficients have significant effects on the non-dimensional natural frequency. The non-dimensional frequency increases for thin plates. It is also observed for lower ratio of thickness to length (h/b = 0.01), Winkler and shearing layer elastic coefficients do not have any effect on the non-dimensional natural frequencies. However, for larger values of h/b ratio, both Winkler and shearing layer elastic coefficients have significant effects on the non-dimensional natural frequencies.

6.2.2 Thermal stress analysis

In order to draw a distinction between results of thermal stress analysis provided here, this section is separated into two subsections; section 6.2.2.1 deals with novel results for thermal behavior of 1-D FG fiber-reinforced cylindrical panels compared with discretely laminated ones, and section 6.2.2.2 discusses new results for the thermal stress analysis of a 1-D FG fiber-reinforced closed cylindrical shells resting on elastic foundations.

6.2.2.1 Cylindrical panels

Steady-state response of a FG fiber reinforced cylindrical panel is studied and new results are presented in this section. The material properties of the panel vary continuously and smoothly in the radial direction of the panel according to classic power-law distribution, Eq. (4.1). Here, we assume that the FG shell has a continuous variation starting at 0% Tungsten and 100% Copper on the inner surface of the shell to 75% Tungsten and 25% Copper on the outer surface. Figure 6.14 shows distribution of the non-dimensional radial stress through the thickness at different *S* ratios. It is noticed that the peak of the non-dimensionalized radial stress decreases with increasing the *S* ratio. As expected, the radial stress is on zero the

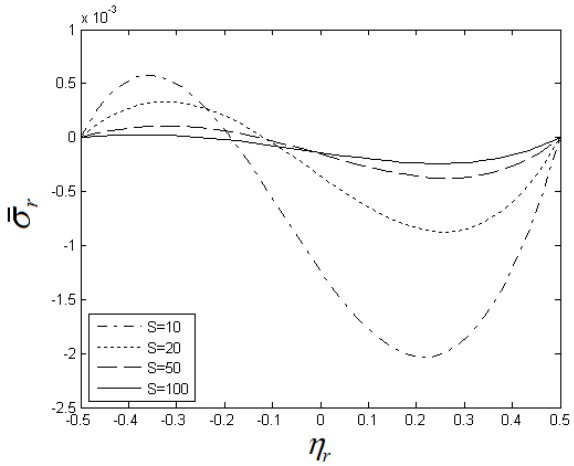

Figure 6.14. Variation of the non-dimensional radial stress through the thickness at different *S* ratios

inner and outer surfaces and its direction changes from tension to compression. The through-the-thickness plot of the non-dimensional circumferential stress is presented in Figure 6.15 at different *S* ratios. The maximum value of the circumferential stress is on the outer surface. This stress is of tension on the inner and outer surfaces.

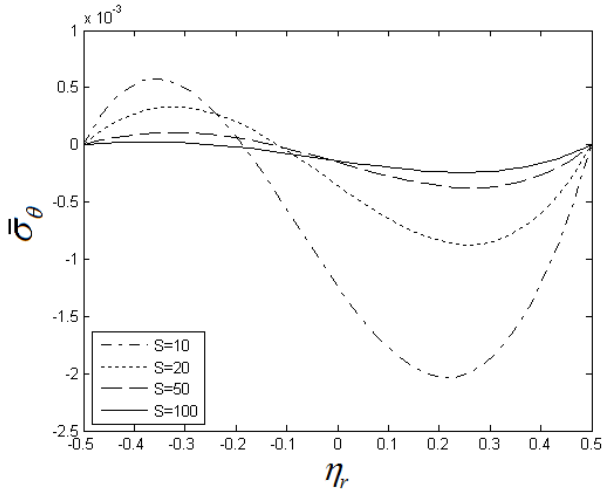

Figure 6.15. Variation of the non-dimensional circumferential stress through the thickness at different *S* ratios.

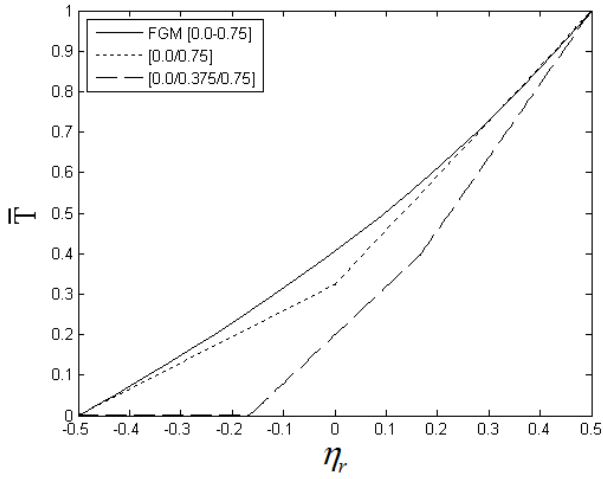

Figure 6.16.The temperature distribution across the thickness for orthotropic FGM, 2-layer and 3-layer.

The temperature distribution is studied across the thickness of the orthotropic FGM, two-layer and three-layer panel, as shown in Figure 6.16. It is noticed that contrary to two- and three-layer, the heat flux for FGM is continuous. It is interesting to note that the temperature distribution of the orthotropic FGM is close to that of the two-layer panel and the temperature distribution of the three-layer is completely different. This

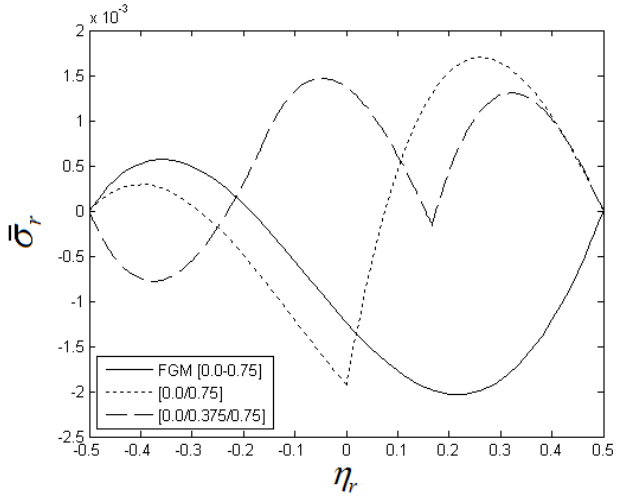

Figure 6.17. Comparison of the non-dimensional radial stress between orthotropic FGM, 2-layer and 3-layer.

is due to the lower conductivity (higher temperature gradient) of continuous fiber-reinforced compared to that of 2 and 3 layers. Because unlike 2 and 3 layers cylindrical panel where the 1st-layer consists of 100% copper with high thermal conductivity, for FG volume fraction, the amount of copper (higher thermal conductivity constituent) decreases from inner surface towards outer surface and at the same time the amount of tungsten (lower thermal conductivity constituent) increases. Moreover, because of higher thermal resistance of 2 layers, arising from thicker layers, in comparison with 3 layers, the temperature gradient for 2 layers will be higher than 3 layers. Therefore the temperature gradient increases from 3 layers to 2 layers and then FG fiber reinforced respectively. It is also observed that the temperature distribution is almost constant along the entire 1st-layer for three-layer model. It is because the 1st-layer consists of 100% copper which has high thermal conductivity, besides 1st-layer for three-layer model is thinner than 1st-layer of two-layer one. Therefore thermal resistance in 1st-layer of three-layer is smaller than 1st

layer of two-layer one. The same distinct behavior is seen for the stress field distributions in Figures 6.17 to 6.19. According to these figures the stress field distributions of the FG fiber reinforced panel is closer to that of the two-layer one. These figures also demonstrate how the non-dimensional radial, circumferential, axial and transverse shear stress components benefit from a gradual change in volume fraction from the shell's inner surface to its outer surface.

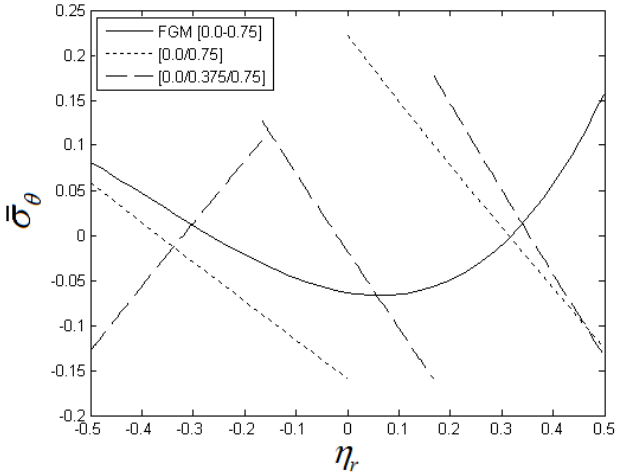

Figure 6.18. Comparison of the non-dimensional circumferential stress between orthotropic FGM, 2-layer and 3-layer.

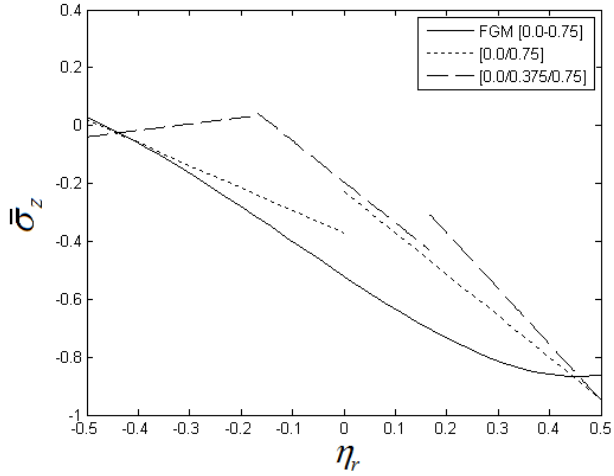

Figure 6.19. Comparison of the non-dimensional axial stress between orthotropic FGM, 2-layer and 3-layer.

6.2.2.2 Closed cylindrical shells

In this section, a parametric study is presented for 1-D FG fiber-reinforced closed cylindrical shells resting on elastic foundation with respect to different foundation stiffnesses and parameters of generalized power-law distribution. The elastic foundation is embedded into inner surface ($r = r_i$). The orthotropic cylindrical shell consists of continuous tungsten reinforcement fibers in a copper matrix (*W/Cu*).

Non-dimensional temperature, displacements and stresses are defined as follows:

$$\overline{\mathrm{T}} = \frac{\mathrm{T}}{\mathrm{T}_o}, U = \frac{10U}{\alpha^i \mathrm{T}_o}, \overline{\sigma} = \frac{\sigma}{\alpha^i E^i \mathrm{T}_o} \tag{6.3}$$

Where α^i and E^i are material properties of matrix phase. The non-dimensional forms of the elastic foundation coefficients are defined as $K_w = k_w E^i H \big/ [R^2(1-\nu^i)]$ and $K_g = k_g E^i H \big/ (1-\nu^i)$ in which ν^i is the Poisson's ratio of matrix phase. The cylindrical shell has geometrical parameters as: $L = 2\mathrm{m}, R = 0.5\mathrm{m}$.

Distribution of non-dimensional radial stress and temperature field through the thickness of FG fiber-reinforced cylindrical shell resting on elastic foundation for various parameter $c\,(1 \le c \le 11)$ are presented in Figures 6.20 and 6.21, by setting *a*=1, *b*=1, *p*=1 in Eq. (4.9). For *c*=1, the cylindrical shell is composed of 25% copper

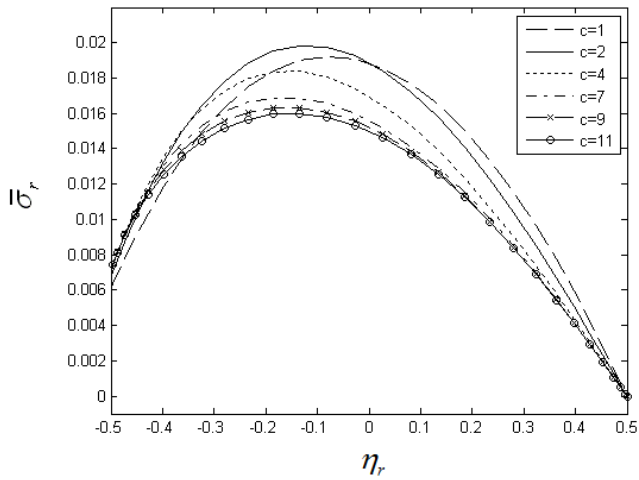

Figure 6.20.Through-the-thickness variation of radial stress along the thickness for various values of the parameter *c* (*p*=1, *a*=1, *b*=1, *S*=10, $K_w = 1e2$, $K_g = 1e-1$)

and 75% tungsten and for c=2, the shape of the profile volume fraction of matrix phase along radial direction is symmetric. The matrix phase volume fraction profile along radial direction becomes asymmetric with increasing parameter c $(c > 2)$. Also, matrix phase volume fraction on the inner and outer surface of cylindrical shell

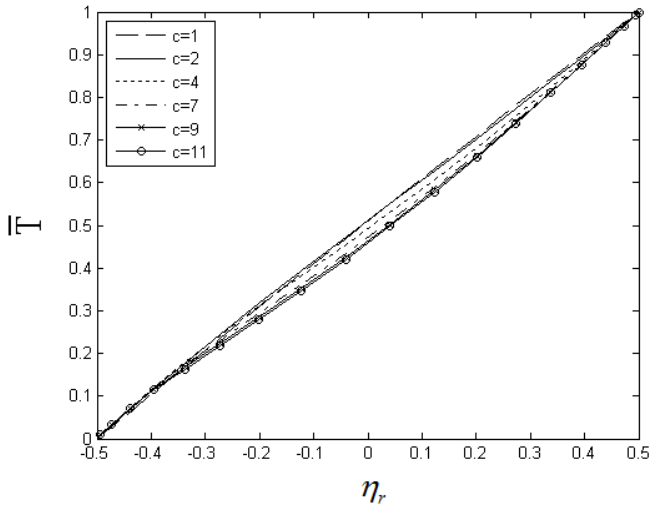

Figure 6.21.Through-the-thickness variation of temperature field along the thickness for various values of the parameter c (p=1, a=1, b=1, S=10, $K_w = 1e2$, $K_g = 1e-1$)

for the different values of parameter c is the same $(V_m = 0.25)$. The distribution of the temperature field is almost linear for $c = 1$ and becomes nonlinear with increasing parameter c. As shown in Figure 6.20, the peak of the non-dimensional radial stress for symmetric profile is larger than for asymmetric profile. Also, the peaks of the non-dimensional radial stress decrease and tend to the inner surface with increasing parameter c.

Distribution of the radial, axial and transverse shear stresses through the thickness of FG fiber-reinforced cylindrical shell for different Winkler elastic coefficient are presented in Figures 6.22 to 6.24, by setting a=1, b=1, c=2 (symmetric profile). Figures 6.22 and 6.23 show that the non-dimensional radial and transverse shear

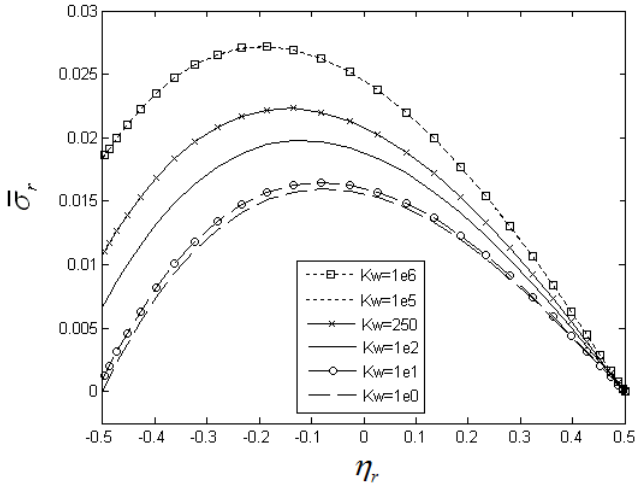

Figure 6.22. Distribution of the non-dimensional radial stress through the thickness of FG fiber-reinforced cylindrical shell with respect to different Winkler elastic coefficients (p=1, a=1, b=1, c=2, S=10, $K_g = 1e-2$)

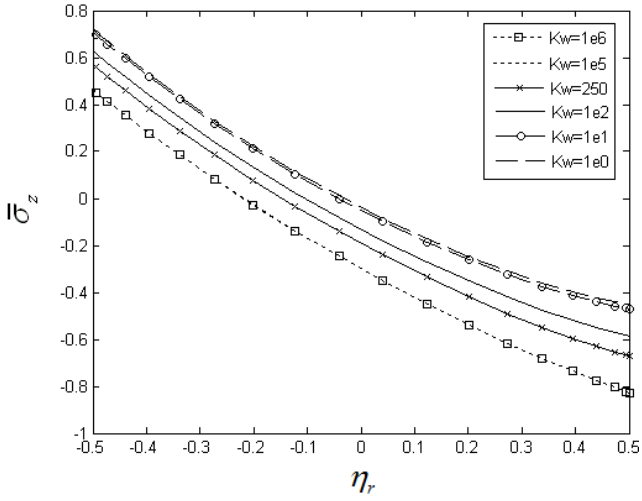

Figure 6.23. Distribution of the non-dimensional axial stress through the thickness with respect to different Winkler elastic coefficients (p=1, a=1, b=1, c=2, S=10, $K_g = 1e-2$)

stresses increase with increasing Winkler elastic coefficient. On the contrary, the axial stress through the thickness decreases with increasing Winkler elastic coefficient. As observed in Figures 6.22-6.24, the mechanical entities of FGM fiber-reinforced cylindrical shell converge with increasing Winkler foundation stiffness.

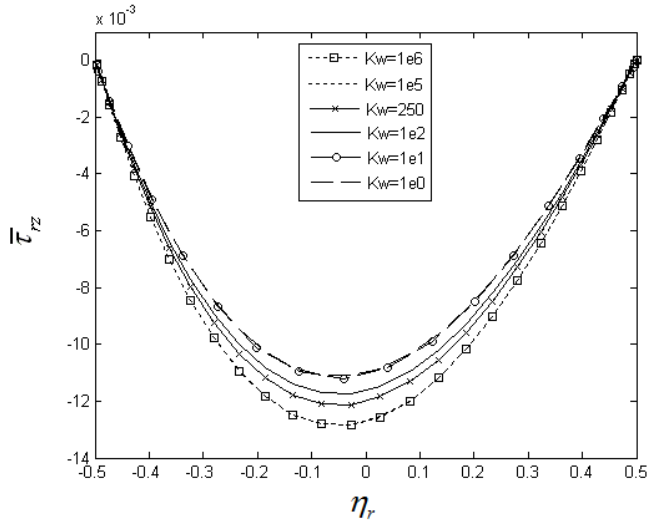

Figure 6.24. Distribution of the non-dimensional transverse shear stress through the thickness with respect to different Winkler elastic coefficients (p=1, a=1, b=1, c=2, S=10, $K_g = 1e-2$)

6.3 2-D FGM composites

One of the main contributions of this thesis is to provide novel results for mechanical responses of 2-D FGM composites. To this end, section 6.3.1 is allocated to presenting new results for free vibration and static analyses of 2-D FGM cylindrical panels followed by a comparison study with classic 1-D FGMs. After that, thermal behaviour of 2-D FGM cylindrical panels with temperature-dependent materials is studied and interesting results is elaborated in section 6.3.2. In this section, Mori-Tanaka method introduced in section 4.3.2 is used to determine the effective mechanical properties of 2-D FGM composites.

6.3.1 Free vibration and static analyses

Taking variation of material properties in two directions into account, the natural frequencies and mode shapes of radial, axial and circumferential displacement components of a cylindrical panel are determined in this section. The equations of motion of the cylindrical panel were derived in section 3.2.1.1, and solved by using 2-D GDQM. The panel is made of continuous silicon-carbide reinforcement fibers in a titanium matrix, listed in Table 6.4. For all results presented here, the vibration frequency is expressed in terms of a non-dimensional frequency parameter $\Omega_{ms} = \omega_{ms} h\pi^2 \sqrt{\rho_T / E_T}$ (ρ_T, E_T are mechanical properties of Titanium (Ti-6Al-4V)). In this section, C-C, C-S, S-S, F-C, S-F and F-F denote clamped–clamped, clamped–simply supported, simply supported–simply supported, free–clamped, simply supported–free and free–free conditions at circumferential edges and simply supported axial pair of edges. In the following, we compared the several different volume fraction profiles of conventional 1-D and 2-D FGM with appropriate choice of the radial and axial parameters of the 2-D six-parameter power-law distribution defined in Eq. (4.12), as shown in Table 6.11. It should be noted that for 2-D FGM notation *Classical-Symmetric* indicates that 2-D FGM panel has classical and symmetric volume fraction profiles through the radial and axial directions, respectively.

Table 6.11. Various volume fraction profiles, different parameters and volume fraction indices of 2-D power-law distributions.

Volume fraction profile	Radial volume fraction index and parameters	Axial volume fraction index and parameters
Classical-Classical	$\alpha_r = 0$	$\alpha_z = 0$
Symmetric-Symmetric	$\alpha_r = 1, \beta_r = 2$	$\alpha_z = 1, \beta_z = 2$
Classical- Symmetric	$\alpha_r = 0$	$\alpha_z = 1, \beta_z = 2$
Classical radially	$\alpha_r = 0$	$\gamma_z = 0$
Symmetric radially	$\alpha_r = 1, \beta_r = 2$	$\gamma_z = 0$

To verify the presented formulation, in Table 6.12 the fundamental frequencies of the classical radially FGM cylindrical panel with four edges simply supported obtained by the present analysis are compared with those presented by Pradyumna and Bandyopadhyay [193], based on the higher order shear deformation theory. The

results of present analysis are obtained using 9×9 grid points. An excellent agreement of the two methods is obvious.

The effect of different types of fiber volume fraction profiles on the frequency parameters of C-S 2-D FGM panels for different values of circumferential wave numbers *m* are compared in Figure 6.25. According to Figure 6.25, the lowest frequency parameter is obtained by using *Classical-Classical* volume fractions profile. On the contrary, 1-D FGM panel with *Symmetric* volume fraction profile has the maximum value of the frequency parameter. Therefore, graded fiber volume show that, with increasing values of the circumferential wave number *m* $(m>2)$, fraction in two directions has high capabilities to reduce the frequency parameter

Table 6.12. Comparison of the normalized natural frequency of classical radially FGM cylindrical panel with four edges simply supported for various γ_r and R/L ratios.

		R/L			
γ_r		**0.5**	**1**	**5**	**10**
0	Ref. [193]	68.8645	51.5216	42.2543	41.908
	$M=N=5$	69.97756	52.10533	42.72019	42.37183
	$M=N=9$	69.97003	52.10028	42.716036	42.36770
	$M=N=11$	69.97003	52.10028	42.716036	42.36770
0.2	Ref. [193]	64.4001	47.5968	40.1621	39.8472
	$M=N=5$	65.14701	47.93925	39.12822	38.80092
	$M=N=9$	65.45263	48.13411	39.08355	38.75680
	$M=N=11$	65.43035	48.13411	39.08355	38.75680
0.5	Ref. [193]	59.4396	43.3019	37.287	36.9995
	$M=N=5$	60.11963	43.55386	36.12641	35.82024
	$M=N=9$	60.35742	43.76887	36.09438	35.78910
	$M=N=11$	60.35742	43.76887	36.09438	35.78910
1	Ref. [193]	53.9296	38.7715	33.2268	32.9585
	$M=N=5$	54.10335	38.51794	31.98603	30.70648
	$M=N=9$	54.71405	39.16213	32.04008	31.76079
	$M=N=11$	54.71405	39.16213	32.04008	31.76079
2	Ref. [193]	47.8259	34.3338	27.4449	27.1789
	$M=N=5$	46.90162	34.77015	27.66574	27.42946
	$M=N=9$	48.52503	34.68517	27.56144	27.32382
	$M=N=11$	48.52503	34.68517	27.56144	27.32382

than conventional 1-D FGM. Moreover in Figure 6.25, the interesting and new results frequency parameter of the *Classical* FGM cylindrical panel is close to that of a *Symmetric-Symmetric*. Therefore, it can be concluded that by using 2-D six-parameter power-law distributions leads to a more flexible design so that maximum or minimum value of natural frequency can be obtained to a required manner. It is worth noting that the effect of the circumferential wave number *m* on the growth rate of the frequency parameter is more tangible for the *Symmetric and Symmetric-Symmetric* volume fraction profiles.

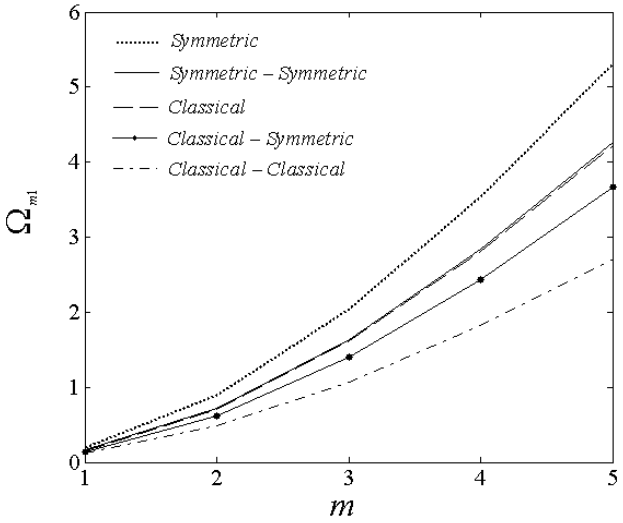

Figure 6.25. Variation of the frequency parameters verses circumferential wave numbers *m* with different volume fraction profiles for C-S cylindrical panel $(L/R = 10, S = 5, \Phi = \pi/2)$

In Figure 6.26, the effects of variation of circumferential wave numbers *m* on the frequency parameters of 2-D FGM panel for different values of L/R ratios and various boundary conditions are demonstrated. According to Figures 6.26a to 6.26b, the general behavior of the frequency parameters of 2-D FGM panel for all boundary conditions is that the frequency parameters converge only in the range beyond that of the fundamental frequency parameters. This means that the effects of the boundary conditions are more prominent at low circumferential wave numbers, particularly those in the range before that of the fundamental frequency parameters, than at high circumferential wave numbers. It is also seen that when the L/R ratios become

smaller the discrepancies between the frequency parameters for the different boundary conditions become larger. To conclude these observations, it can be said that for all the five boundary conditions (C-C, C-F, S-S, S-F, C-S) the effects of the

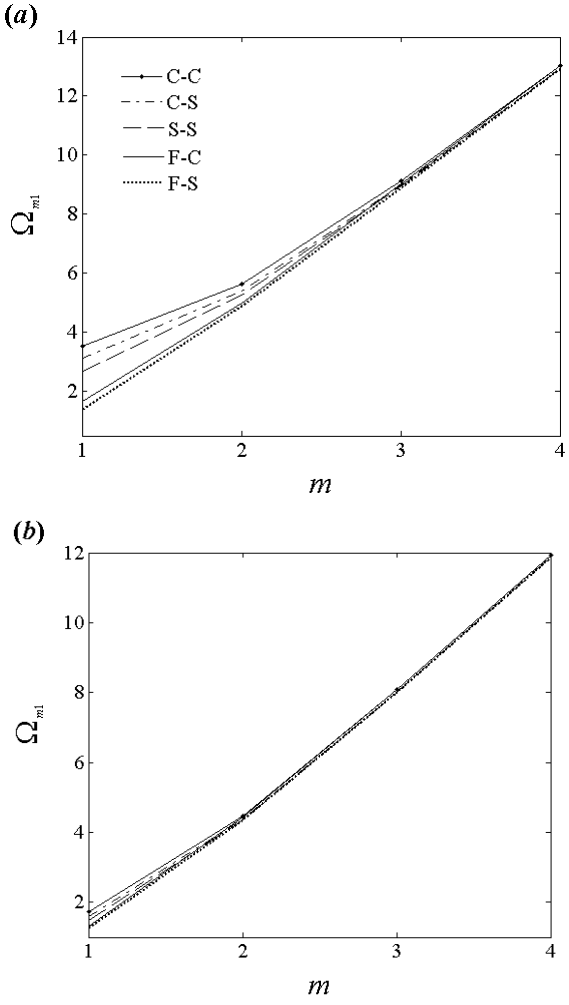

Figure 6.26. Variation of circumferential wave numbers *m* on the frequency parameters of 2-D FGM for different values of L/R ratios and various boundary conditions ((**a**): $L/R = 1$; (**b**): $L/R = 2$) ($S = 5,\ \Phi = \pi/3, \alpha_r = \alpha_z = 0, \gamma_r, \gamma_z = 1$)

boundary conditions are found to be prominent for small L/R ratios and for low circumferential wave numbers *m.* Figure 6.26 shows that the C-C 2-D FGM panel has the highest, whereas the F-S one has the lowest frequency parameter values,

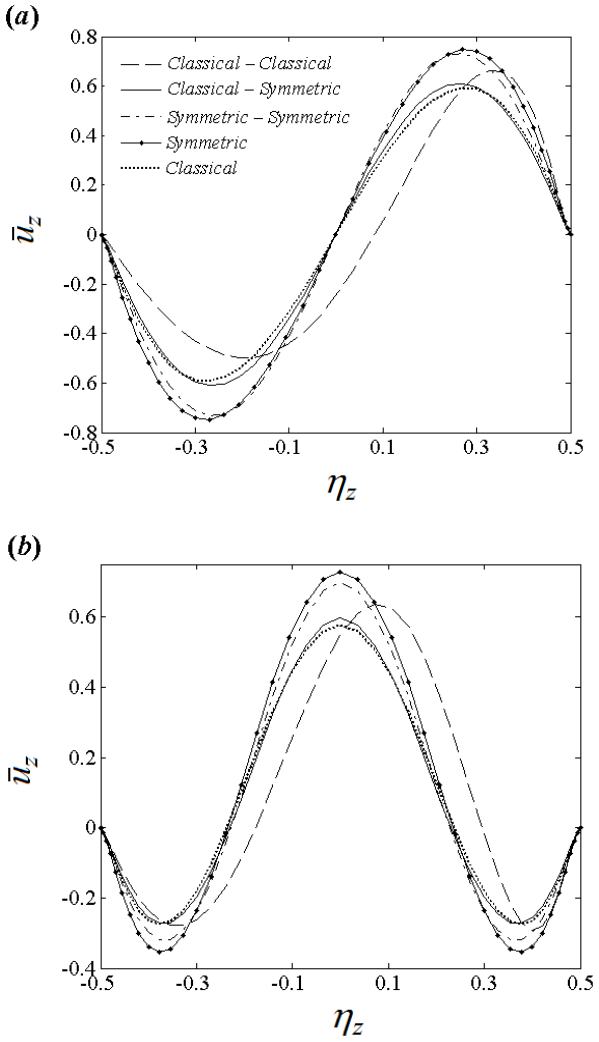

Figure 6.27. The influences of the various different of fiber volume fraction profiles on the mode shape of the axial displacement of C-C 2-D FGM corresponding to the first two vibrating modes ((**a**): (*m*,*s*)=(1,1), (**b**): (*m*,*s*)=(1,2)) ($\Phi = \pi/2$, $L/R = 10$, $S = 10$, $\theta = \pi/4$)

implying that an 2-D FGM cylindrical panel with greater supporting rigidity will have higher vibrating frequencies. The influences of the different fiber volume fraction profiles on the mode shape of the axial displacement of C-C 2-D FGM corresponding to the first three vibrating modes are shown in Figure 6.27. In this

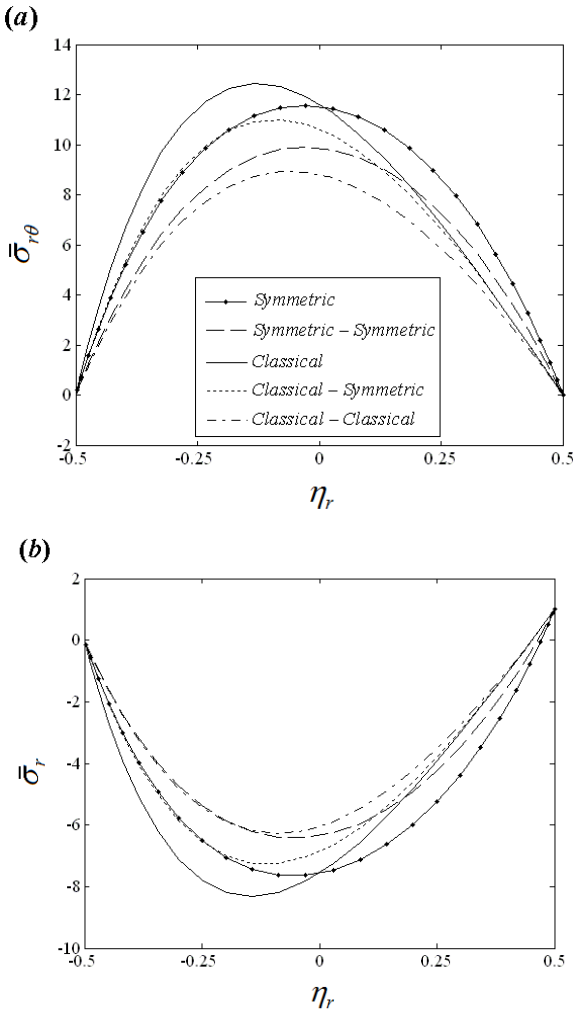

Figure 6.28. The influence of the various ceramic volume fraction profiles on the mechanical entities of F-S 2-D FGM cylindrical panel ($\Phi = 2\pi/3, , S = 10, \theta = \pi/3$)

figure, the modal displacement (u_j) of FGM panels in vibration is normalized by dividing its maximum absolute value, denoted by $\overline{u}_j$. As it is depicted, except for *Classical-Classical* profile, distributions of the axial displacement along the length of 2-D FGM are symmetric with respect to the reference surface in axial direction due to symmetric volume fraction profile with respect to such direction. It can be observed from Figure 6.27 that the non-dimensional axial displacement of 2-D FGM panel with graded *Classical-Classical* profile are lower than that of the other profiles.

In the following discussion, the benefit of gradation of material properties in two directions over classical one-dimensional FGM cylindrical panel subjected to static load on the outer surface, similar to the case in section 6.2.1.1, is illustrated. The effect of different types of ceramic volume fraction profiles on the mechanical entities of F-S 2-D FGM cylindrical panel is compared in Figure 6.28. In this figure, the stress components are non-dimensionalized as follows:

$$\overline{\sigma}_r, \overline{\sigma}_{r\theta} = \frac{\sigma_r, \sigma_{r\theta}}{q} \tag{6.5}$$

where q is the static load on the outer surface. According to Figure 6.28, the lowest magnitude of mechanical entities is obtained by using *Classical-Classical* volume fractions profile. On the contrary, 1-D FGM cylindrical panel with *Classical* volume fraction profile has the maximum magnitude of mechanical entities. Therefore, graded ceramic volume fraction in two directions has high capabilities to reduce the mechanical stresses than conventional 1-D FGM. Moreover, in Figure 6.28, it is interesting to note that distribution of the mechanical entities in FGM cylindrical panel with *Symmetric* and *Symmetric-Symmetric* profiles is symmetric with respect to the mid-surface of the cylindrical panel. It can be inferred from these figures that the 2-D power-law distribution for ceramic volume fraction of 2-D FGM gives designers a powerful tool for flexible design of structures under multi-functional requirements.

6.3.2 Thermal stress analysis

In the subsequent discussion, for the first time, detailed parametric studies is done to study the influences of both various volume fraction profiles and variation of the material properties with temperature on temperature field and thermal stresses of 2-D FGM cylindrical panel. The governing equations based on TSDT and heat conduction equation were derived and presented in section 3.3.2.1. The material properties of 2-D FGM are assumed to be graded in radial and axial directions simultaneously according to a brand-new 2-D power-law distribution mentioned in Eq. (4.13). In order to take temperature-dependent properties into account, the

material properties are expressed as non-linear functions of environment temperature stated in Eq. (3.74). The solution procedure of the analysis was fully explained in section 5.3.3.
Firstly, to validate our analysis, the accuracy and effectiveness of the present method for a one-dimensional FGM cylindrical shell under uniform thermal load were examined by comparison study given in Ref. [194]. Figure 6.29 shows the variation of the radial stress through the thickness at the middle length of the cylinder due to the uniform thermal loading. It is noticed that the present results agree well with the literature.

After validation of the analysis, the new and interesting results are presented and discussed in the following. We compare the various volume fraction profiles of conventional 1-D and 2-D FGMs with appropriate choice of the sigmoidal and axial parameters of the 2-D power-law distribution, as shown in Table 6.13. It should be noted that the notation *Sigmoidal–Symmetrical* indicates that the 2-D FGM panel has sigmoidal and symmetrical volume fraction profiles in the radial and axial directions, respectively. Non-dimensional thernal stresses are as follows:

$$\overline{\sigma}_i = \frac{\sigma_i}{\alpha E q_o} \tag{6.4}$$

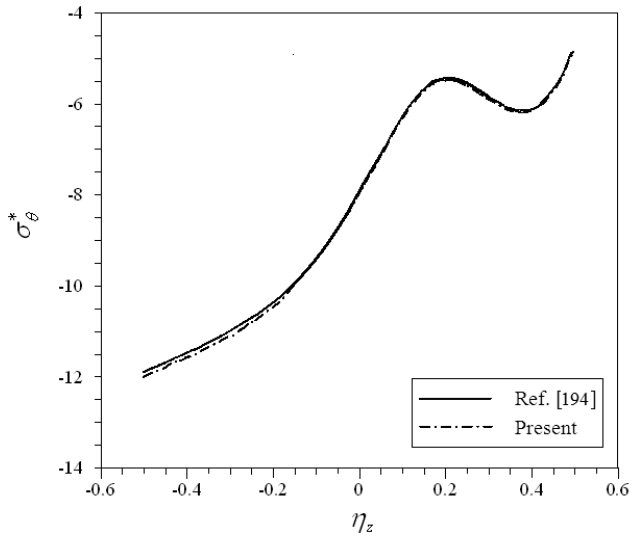

Figure 6.29. Variation of circumferential stress through the thickness of FGM cylindrical shell under uniform thermal load.

where α and E are mechanical properties of titanium and q_o is heat flux at the inner surface. The panel has geometrical parameters as: $L = 0.8\text{m}, Z_m = 0.25\text{m}$.

Table 6.13. Different ceramic volume fraction profiles, different parameters and volume fraction indices of 2-D power-law distributions.

Volume fraction profile	Sigmoidal parameters	Axial volume fraction index and parameters
Sigmoidal-Symmetrical	$\gamma_z = 1$	$\alpha_x = 1, \beta_x = 2$
Sigmoidal- Classical	$\gamma_z = 1$	$\alpha_x = 0$
Symmetrical axially	$\gamma_z = 0$	$\alpha_x = 1, \beta_x = 2$
Classical axially	$\gamma_z = 0$	$\alpha_x = 0$
Sigmoidal radially	$\gamma_z = 1$	$\gamma_x = 0$

Since the thermal conductivity of 2-D FGM panel is a function of temperature, the nonlinear equation of heat transfer is solved using an iterative procedure until the change in peak temperature between two consecutive iterations falls below an

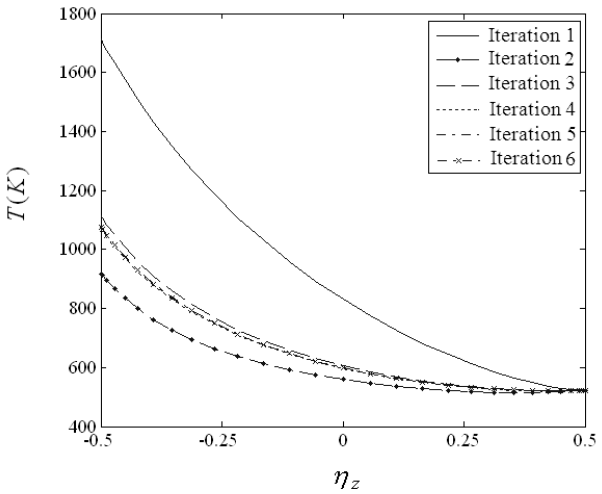

Figure 6.30. Convergence of temperature field for a *Sigmoidal-Symetrical* 2-D FGM with temperature-dependent material properties $(Z_m/h = 10, \Theta = 2\pi/3, z = L/2, \theta = \pi/6)$

absolute tolerance of 10^{-4}. The iterative procedure was explained in section 5.3.3. The procedure is illustrated for a 2-D FGM panel with *Sigmoidal-Symetrical* volume fraction profile, i.e. $\alpha_x = 1,\ \beta_x = 2,\ \gamma_x = 1,\ \gamma_z = 1,\ s = 1$. It can be seen that the

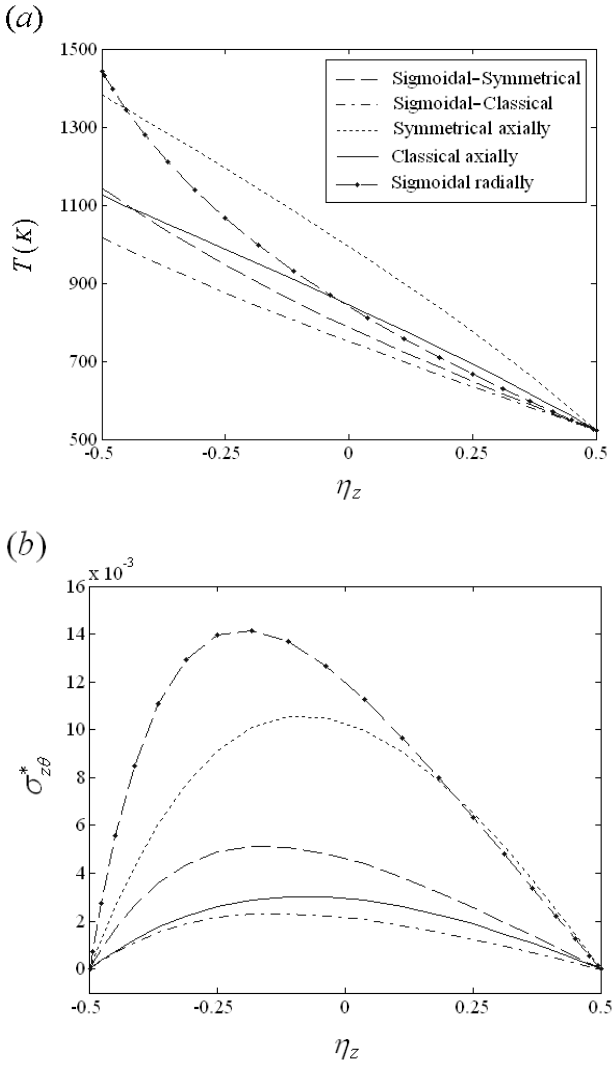

Figure 6.32. Through-thickness variation of temperature field and transverse shear stress of 2-D FGM with temperature-dependent materials for various volume fraction profiles $(Z_m/h = 10, \Theta = 3\pi/4, \gamma_z = 1)$

temperature field converges rapidly to the specified tolerance in 4 iterations. The variation of the temperature through radial direction is demonstrated in Figure 6.30 corresponding to iterations 1 to 6. There is a noticeable decline in the temperature between iterations 1 and 2. Subsequent iterations serve to refine the temperature field until it has converged to the specified tolerance.

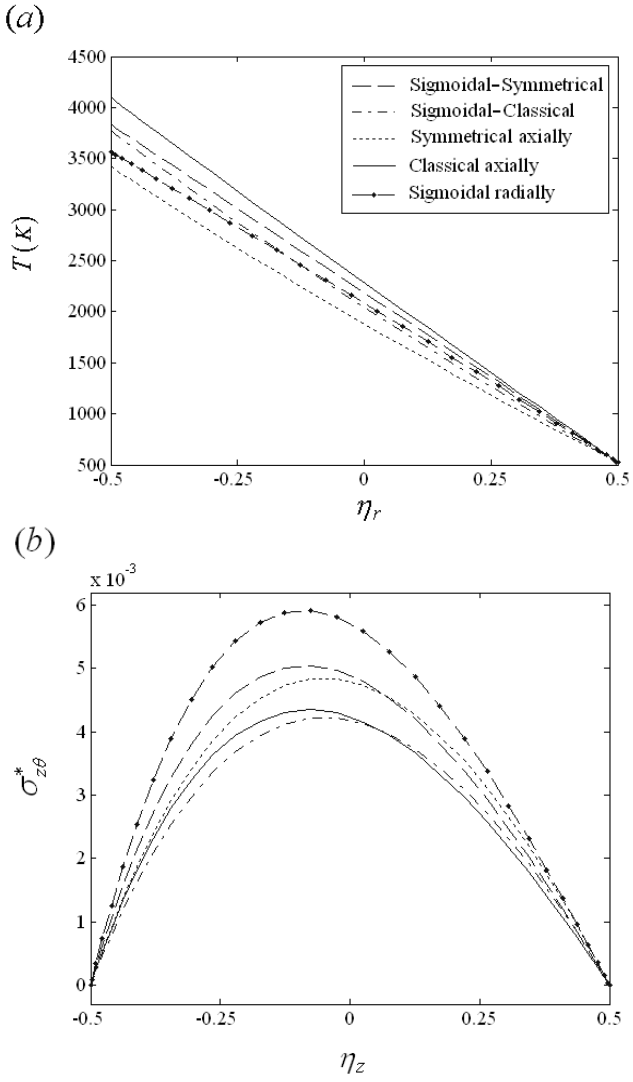

Figure 6.31. Variation of temperature field and transverse shear stress of 2-D FGM through the thickness various volume fraction profiles with temperature-independent materials $(Z_m/h = 10, \Theta = 3\pi/4, \gamma_z = 1)$

In order to show the importance of considering the variation of material properties with temperature, distribution of temperature field and transverse shear stress of 2-D FGM with C-C boundary conditions through the thickness for the case of temperature-independent and temperature-dependent material properties are presented in Figures 6.31 and 6.32, respectively. The material properties for the case temperature-independent are calculated at the reference temperature, 300K. The magnitude of the maximum thermal stresses shown in Figure 6.31 is found to be reduced by grading volume fractions in two directions, for the case where the material properties are assumed to be temperature-independent. Comparing Figures 6.31 and 6.32, it can be observed that the temperature field for the case of temperature-independent is found to be greater than that computed with temperature-dependent properties. The temperature-dependency of the material properties reduces peak of the non-dimensional transverse shear stress by 45 % for *Sigmoidal- Classical* profile. Thus, calculations and design based on temperature-independent properties yield conservative estimates. It can also be inferred from Figures 6.31 and 6.32 that the discrepancy between value of thermal stresses with different volume fractions for the case of temperature-dependent material properties is higher than that of temperature-independent properties.

Impacts of considering temperature-dependent material properties on distribution of temperature field of 2-D FGM in two directions are shown in Figure 6.33. It can be inferred from Figure 6.33 that considering temperature-dependent material properties results in more gradual distribution of temperature in two directions than that of temperature-independent materials. In Figure 6.33, it is interesting to note that the peak of the temperature field for *Sigmoidal-Classical* profile with temperature-dependent materials tends to the lower edge of the shell with higher amount of ceramic phase, while maximum values of the temperature field with temperature-independent materials take place at position closer to the upper edge with higher amount of metal phase.

In the following, we turn our attention to the effect of sigmoid exponent S on the variation of temperature field, axial, circumferential and out-of-plane transverse shear stresses through the thickness of 1-D panel with sigmoidal radial variation of volume fraction, as shown in Figure 6.34. In this figure, the temperature gradient at the inner surface is increased as the sigmoid exponent $\boldsymbol{S}$ is increased. This trend is opposite to that observed at the outer surface. This is because as the sigmoid exponent is increased, the contained quantity of ceramic phase at the inner surface increases, and volume fraction of ceramic at the outer surface is reduced. By considering Eq. (4.13), when sigmoid exponent $\boldsymbol{S}$ increases considerably, the thermal behavior of the panel with radial variation of volume fraction approaches a

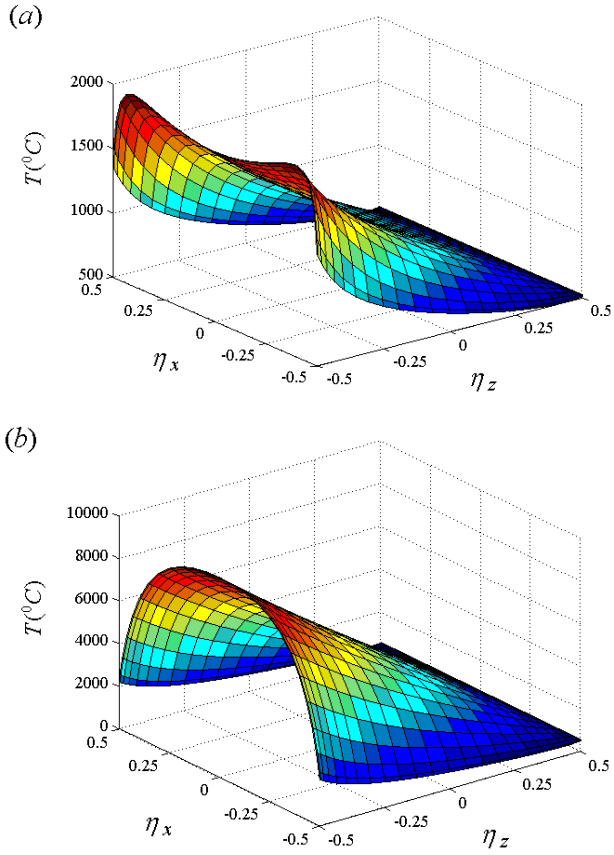

Figure 6.33. Temperature field for *Sigmoidal- Symetrical* 2-D FGM with C-C boundary conditions $(Z_m/h = 10, \Theta = \pi/3, \gamma_z = 1)$ **a**) temperature-dependent materials, **b)** temperature-independent materials.

discrete [1/0.3] laminate with a sharp transition in ceramic volume fraction from the 1 to 0.3 at the midsurface. It is found from Figure 6.34, there is a steep variation in temperature field and circumferential stress at the midsurface for significantly higher sigmoid exponent ($S = 50$) due to a sharp transition in contained quantity of ceramic. From Figure 6.34, it is observed that the impact of the sigmoid exponent on the circumferential stress at the inner surface is more pronounced than that at outer surface. It can be concluded from Figure 6.34 that 1-D cylindrical panel with sigmoidal radial variation of volume fraction exhibits smooth variations of the in-plane stress, thereby minimizing the magnitude of thermal stresses and the likelihood

of premature failure at an interface between adjoining lamina as in the case of discretely laminated composite.

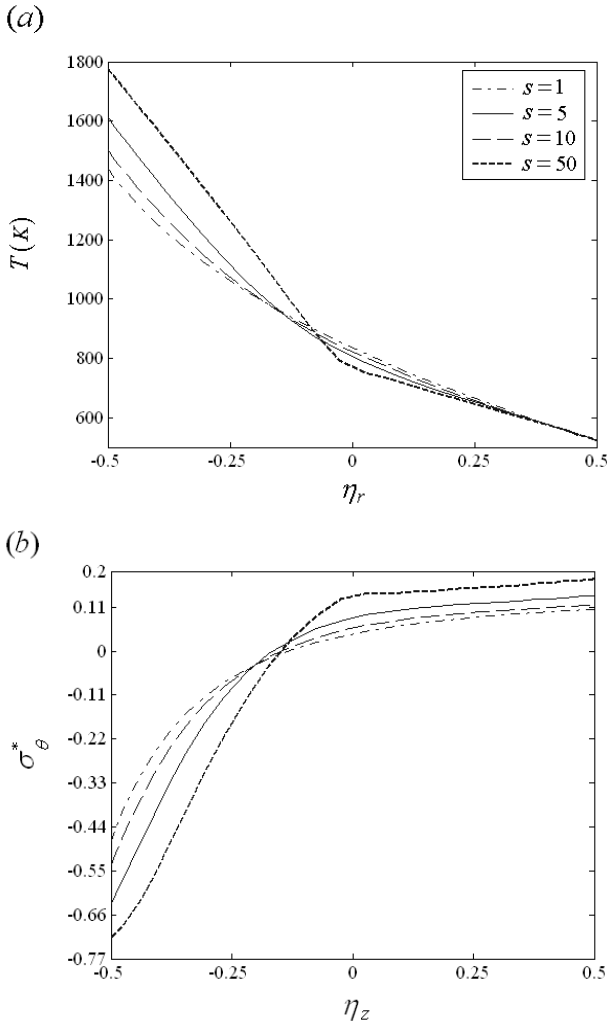

Figure 6.34. The effect of sigmoid exponent *s* on the temperature field and circumferential stress through the thickness of FGM with S-S boundary conditions $(Z_m/h = 10, \Theta = 2\pi/3)$

6.4 FG CNT-reinforced composites

One of the primary objectives of the present thesis is to applying the concept of FGM into CNT-reinforced composites and presenting state-of-the-art and outstanding results for FG CNT-reinforced composites. In order to achieve the objective, this section presents and discusses effects of different CNTs distributions, various types of CNT dispersion within the matrix phase, geometrical parameters, and boundary conditions on the free vibration characteristics and mechanical buckling of FG CNT-reinforced composites.

6.4.1 Free vibration

This section deals with new results for free vibration of FG CNT-reinforced composites. To better handle the discussion, the section is divided into two subsections based on type of the structure. In the first part, annular sectorial plates reinforced by graded agglomerated CNTs resting on elastic foundations is studied and numerical results are presented. Then, the attention will be paid to rectangular plates reinforced by graded aligned CNTs.

6.4.1.1 Annular sectorial plates

In this part, we aim to study impacts of CNT agglomeration, various graded CNTs volume fractions, elastic foundation stiffness parameters, and geometrical parameters on the vibration characteristics of the annular sectorial plates resting on Pasternak elastic foundation. The material properties of the plate are assumed to be graded in the thickness direction. It is assumed that CNTs agglomerates within the matrix phase. As explained in section 4.3.4.3, the effective material properties of CNT-reinforced composite were estimated through an equivalent continuum model based on the Eshelby-Mori-Tanaka approach in which a two-parameter micromechanics model of agglomeration was employed. Different profiles of CNTs volume fraction through the thickness have been proposed in Eqs. (4.3)-(4.6).

First of all, to demonstrate the convergence and accuracy of the solution, an illustrative example is solved and the results are compared with the existing available data in the literature. In Table 6.14, the results for the FGM annular plate with outer-inner radius ratio $r_o / r_i = 2.5$ for various circumferential wave numbers are compared with those obtained using the Chebyshev-Ritz by Dong [195]. It can be observed from Table 6.14 that there is a very good agreement between the results confirming the accuracy of the current approach.

Note that for all results presented, the non-dimensional natural frequency parameter and the elastic foundation coefficients are defined as:

$$\lambda_{mn} = \omega_{mn}\left(r_o^2/\pi^2\right)\sqrt{\rho_m h/D_m}\,,\quad K_w = k_w D_m/r_o^4\,,\quad K_S = k_s D_m/r_o^2 \tag{6.4}$$

where $D_m = E_m h^3/12(1-\nu_m^2)$ is the flexural rigidity (ρ_m, E_m and ν_m are mechanical properties of matrix). The material properties of CNTs are selected from [196]. Also, the material properties of polymer matrix are assumed to be E_m=10 GPa , ν_m=0.3 and ρ_m=1.15 g/cm^3 at T = 300 K [196].

In order to obtain accurate frequency parameters of FG CNT-reinforced annular sectorial plates resting on Pasternak elastic foundation, a set of calculations is first undertaken in Table 6.15 to determine the requisite number of grid points in the radial N_r and thickness N_z directions. The effect of the inner-to-outer radius ratio (r_i/r_o) and the elastic foundation coefficients (K_w, K_S) on the convergence rate of the frequency parameters of FG CNT-reinforced annular sectorial plates is investigated in Table 6.15, respectively. It is seen from Table 6.15 that insignificant effect of the foundation stiffness parameters on the rate of convergence of frequency parameters for FG CNT-reinforced annular sectorial plate is found. It is evident from Table 6.15 that the present 2-D GDQM converges very fast as the number of grid

Table 6.14. Comparison of frequency parameter of a clamped-clamped FGM annular plate for various circumferential wave numbers ($r_o/r_i = 2.5, h/r_o = 0.5$).

m	Methods	Ω_{m1}	Ω_{m2}	Ω_{m3}	Ω_{m4}	Ω_{m5}
The gradient index $p = 1$						
0	Present	8.2102	13.869	15.510	19.485	20.165
	Chebyshev–Ritz [195]	8.214	13.872	15.514	19.486	20.168
1	Present	8.330	9.688	13.763	14.849	15.533
	Chebyshev–Ritz [195]	8.333	9.689	13.766	14.85	15.535
2	Present	8.866	11.144	13.809	15.613	16.549
	Chebyshev–Ritz [195]	8.869	11.145	13.81	15.615	16.55
3	Present	9.922	12.671	14.406	16.453	17.721
	Chebyshev–Ritz [195]	9.924	12.672	14.407	16.455	17.721
The gradient index $p = 5$						
0	Present	10.09	18.337	19.719	24.424	25.798
	Chebyshev–Ritz [195]	10.099	18.338	19.724	24.426	25.794
1	Present	10.262	12.335	18.191	18.578	19.648
	Chebyshev–Ritz [195]	10.266	12.336	18.192	18.578	19.651
2	Present	10.933	14.391	18.447	19.489	20.703
	Chebyshev–Ritz [195]	10.937	14.392	18.448	19.49	20.704
3	Present	12.243	16.662	19.310	20.694	22.421
	Chebyshev–Ritz [195]	12.246	16.664	19.31	20.695	22.421

Table 6.15. Convergence test of fundamental frequency parameters of C-F annular sectorial plate resting on Pasternak elastic foundation $(h/r_o = 0.5,\ \Theta = 90^0)$.

		$N_r \times N_z$				
(K_w, K_s)	r_i/r_o	7×7	9×9	11×11	13×13	17×17
Profile– V $(\xi = 1, \mu = 0.5)$						
$(0,0)$	0.1	2.3901	2.3753	2.3653	2.3626	2.3626
	0.4	2.2020	2.1928	2.1842	2.1821	2.1821
	0.7	3.1101	3.0577	3.0247	3.0205	3.0205
$(10,10)$	0.1	2.6739	2.6645	2.6562	2.6551	2.6551
	0.4	2.5500	2.5309	2.5195	2.5186	2.5186
	0.7	3.3521	3.3472	3.3479	3.3458	3.3458
$(100,10)$	0.1	2.7119	2.7098	2.6999	2.6992	2.6992
	0.4	2.6187	2.6004	2.5899	2.5898	2.5898
	0.7	3.4521	3.4521	3.4555	3.4534	3.4534
$(1000,100)$	0.1	2.8509	2.8338	2.8270	2.8268	2.8268
	0.4	2.7314	2.7229	2.7199	2.7191	2.7191
	0.7	4.0391	4.0674	4.1779	4.1771	4.1771
Profile– X $(\xi = 0.8, \mu = 0.6)$						
$(0,0)$	0.1	5.3129	5.2726	5.0431	5.0422	5.0422
	0.4	5.7610	5.7469	5.7183	5.7177	5.7177
	0.7	9.6990	9.6468	9.5629	9.5621	9.5621
$(10,10)$	0.1	5.4516	5.3928	5.2899	5.2894	5.2894
	0.4	6.2549	6.1086	6.0815	6.0809	6.0809
	0.7	9.7809	9.7809	9.7001	9.6994	9.6994
$(100,10)$	0.1	5.6009	5.5015	5.3971	5.3967	5.3967
	0.4	6.2993	6.2657	6.2403	6.2399	6.2399
	0.7	9.9551	9.8439	9.7641	9.7637	9.7637
$(1000,100)$	0.1	6.9253	6.8051	6.6823	6.6819	6.6819
	0.4	7.7909	7.7877	7.7930	7.7923	7.7923
	0.7	11.2119	11.0356	10.9863	10.9856	10.9856

points $N_r \times N_z$ increases. It can also be concluded that using 13×13 grid points can produce accurate frequency parameters for FG CNT-reinforced composite annular

sectorial plates resting on Pasternak elastic foundation up to at least five significant digits. The variation of inner-outer radius ratio with the frequency parameters of C-C Profile– X annular sectorial plate resting on Pasternak elastic foundation for different values of h/r_o ratios is shown in Figure 6.35. According to Figure 6.35, the general behavior of the frequency parameters of annular sectorial plate resting on Pasternak elastic foundation for all r_i/r_o ratios is that the effects of the h/r_o ratios are more prominent at high inner-to-outer radius ratios. As it is observed, the frequency parameter decreases rapidly with the decrease of the r_i/r_o ratio and then remains almost unaltered for the $r_i/r_o < 0.4$.

Figure 6.36 shows the variation of the frequency parameter of the C-C annular sectorial plate with different values of agglomeration parameter μ and plate angle Θ. The frequency parameters of the annular sectorial plate resting on Pasternak elastic foundation decrease rapidly with the increase of the plate angle for various agglomeration parameter μ and then approach a constant value for higher plate angle ($\Theta > 90^0$).

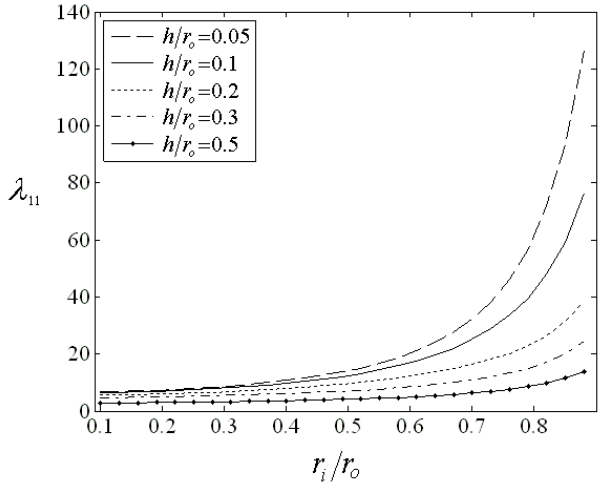

Figure 6.35. Variation of inner-to-outer radius ratio with the frequency parameters of C-C annular sectorial plate resting on Pasternak elastic foundation with Profile– V for different values of h/r_o ratios ($\Theta = 120^0$, $K_w = 200, K_S = 100, \xi = 1, \mu = 0.5$)

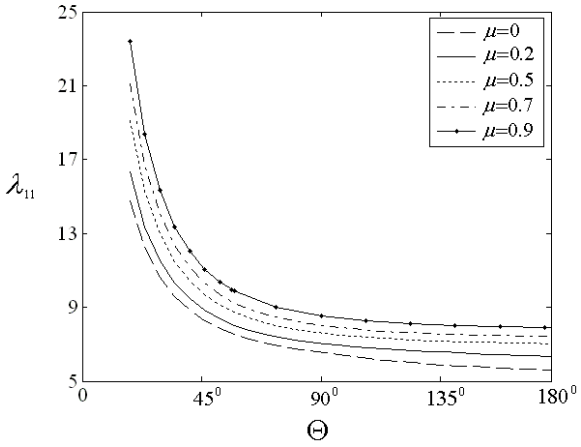

Figure 6.36. Effect of plate angle Θ on the frequency parameter of the C-C annular sectorial plate resting on elastic foundation with different values of agglomeration parameter μ

($K_w = 1000, K_S = 100, \xi = 1, h/r_o = 0.2, r_i/r_o = 0.3$)

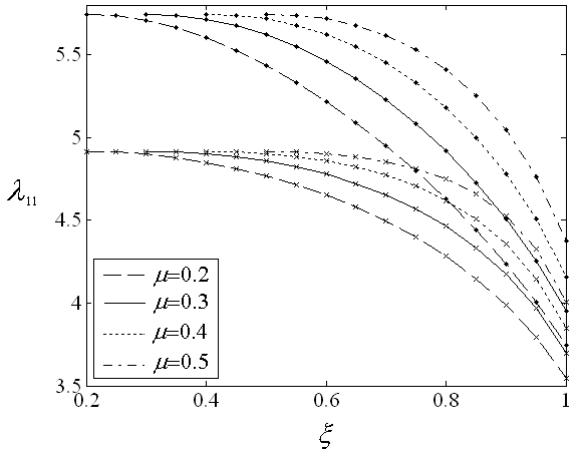

Figure 6.37. Variation of the frequency parameters versus agglomeration parameter ξ with different types of agglomerated CNTs distributions and agglomeration parameter μ

(Profile– V , Profile– X) ($K_w = 100, K_S = 10, h/r_o = 0.3, r_i/r_o = 0.5, \Theta = 60^0$)

Figure 6.37 shows variation of the frequency parameter of the Profile–V and Profile–X annular sectorial plates resting on Pasternak elastic foundation with agglomeration parameters μ and ξ. It can also be inferred from Figure 6.37 that the fundamental frequency parameter decreases with increasing agglomeration parameter ξ. It should be noted at this point that this natural frequency behavior contrasts with the natural frequency behavior of the annular sectorial plate with increasing

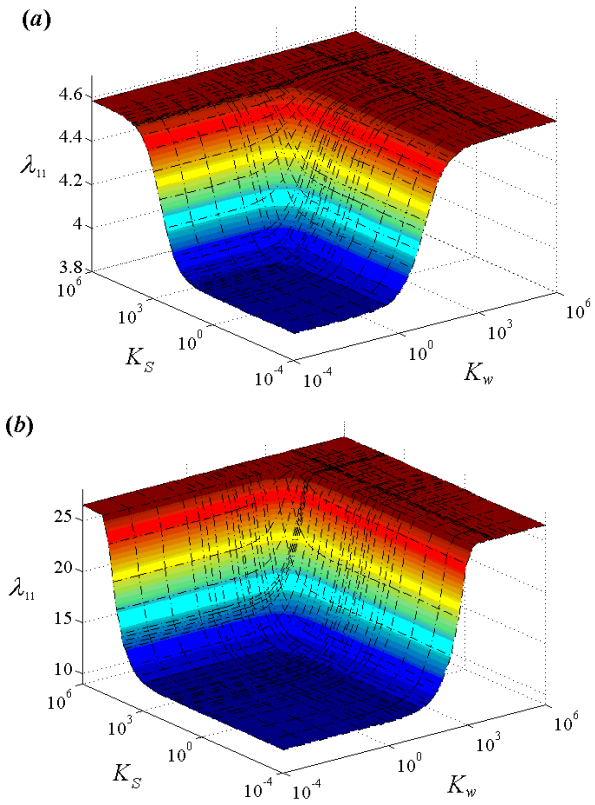

Figure 6.38. Variation of the frequency parameter versus Winkler and shearing layer elastic coefficients for various h/r_o ratio (**a:** $h/r_o = 0.5$, **b:** $h/r_o = 0.1$)

($\mu = 0.5, \xi = 1, r_i/r_o = 0.5, \Theta = 60^0$)

agglomeration parameter μ. Moreover, Figure 6.37 reveals that, with increasing values of agglomeration parameter ξ, the agglomerated CNTs with Profile–V has notably higher decreasing rate of frequency parameter than Profile–X profile.

In Figures 6.38a and 6.38b, comparisons are made among the frequency parameters of annular sectorial plates resting on elastic foundation with various h/r_o ratios. According to this figure, it is interesting to note that the range of variation of the frequency parameter with increasing Winkler and shearing layer elastic coefficients increases with the increase of the h/r_o ratio.

6.4.1.2 Rectangular plates

In this section, numerical results for the free vibration analysis of rectangular nanocomposite plates reinforced by aligned CNTs are presented. The effective material properties at a point were estimated by either the Eshelby-Mori-Tanaka (section 4.3.4.1) approach or the extended rule of mixture (section 4.3.3.). Poly methyl methacrylate, referred to as PMMA, is selected for the matrix, and the material properties of which are assumed to be $\rho^m = 1.15\,\mathrm{g/cm^3}$, $\nu^m = 0.34$, $E^m = 2.5\,\mathrm{GPa}$ at room temperature (300 K) [114]. The (10,10) SWCNTs are

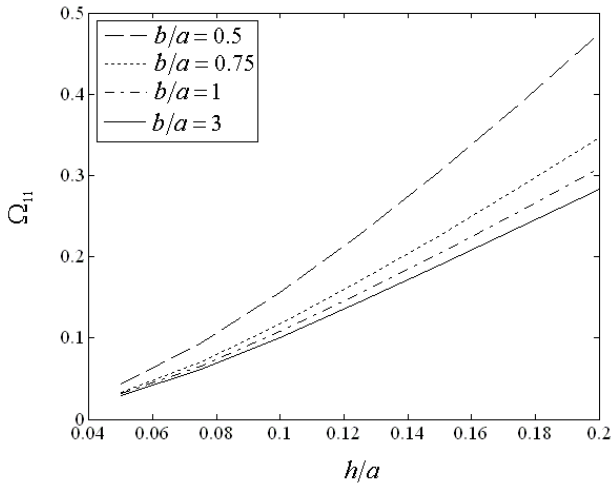

Figure 6.39. Effect of thickness to length on the fundamental frequency parameter of the plate for different values of b/a ratio.

selected as reinforcements. The key issue for successful application of the extended rule of mixture to CNTRCs is to determine the CNT efficiency parameter η_i. There are no experiments conducted to determine the value of η_i for CNTRCs. Shen [114] determined the CNT efficiency parameters η_1, η_2 and η_3 by matching the Young's moduli E_{11} and E_{22} and shear modulus G_{12} of CNTRCs predicted from the extended rule of mixture to those from the MD simulations given by Han and Elliott [196]. For example, $\eta_1 = 0.137$, $\eta_2 = 1.022$ and $\eta_3 = 0.715$ for the case of $V_{CN}^* = 0.12$ and $\eta_1 = 0.142$, $\eta_2 = 1.626$ and $\eta_3 = 1.138$ for the case of $V_{CN}^* = 0.17$ and $\eta_1 = 0.141$, $\eta_2 = 1.585$ and $\eta_3 = 1.109$ for the case of $V_{CN}^* = 0.28$. These values will be used in all following examples, in which taking $\eta_3/\eta_2 = 0.7/1$ and $G_{13} = G_{12}$ and $G_{23} = 1.2G_{12}$ [114]. Herein, natural frequencies of the plate are obtained and

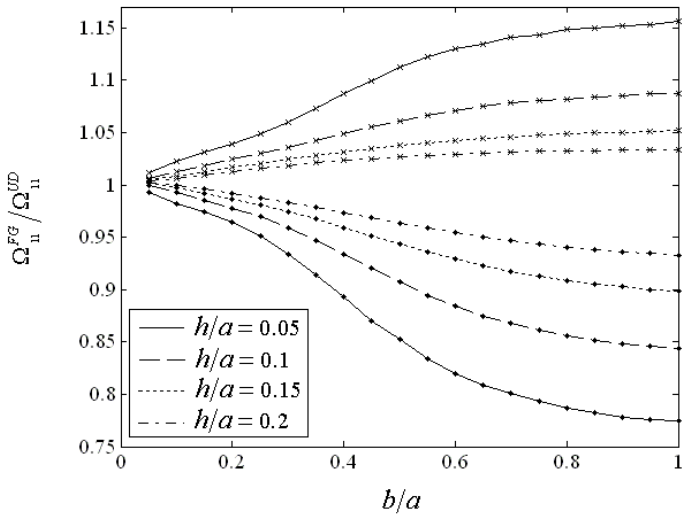

Figure 6.40. Variation of the $\Omega_{11}^{FG}/\Omega_{11}^{UD}$ ratio versus width to length ratio with for various h/a ratio (Profile– X to Profile−UD frequency parameter ratio, Profile – ◊ to Profile−UD frequency parameter ratio).

considered to be dimensionless as $\Omega_{nl} = \omega_{nl} h\sqrt{\rho^m / E^m}$ (called the frequency parameter).

Figure 6.39 depicts the effect of thickness to length ratio on the fundamental frequency parameter of the plate for different values of b/a ratio with $V^*_{CN} = 0.12$. The results in Figure 6.39 indicate that the fundamental frequency parameter increases with the increasing values of the h/a ratio. Fundamental frequency parameter ratio of the nanocomposite plate for various h/a and b/a ratio is calculated and plotted in Figure 6.40. It is worthy to mention that frequency parameter ratio decreases rapidly with the increase of the b/a ratio for different values of the h/a ratio and then approach a constant value for higher b/a ratio. It is interesting to note that the effect of the h/a ratio on the Profile$-\Diamond$ to Profile$-$UD frequency parameter ratio is more significant than that of the Profile$-$X to Profile$-$UD frequency parameter ratio $(\Omega_{11}^{FG}/\Omega_{11}^{UD})$. Also it is seen that discrepancies between frequency parameters of the Profile$-$X and Profile$-$UD

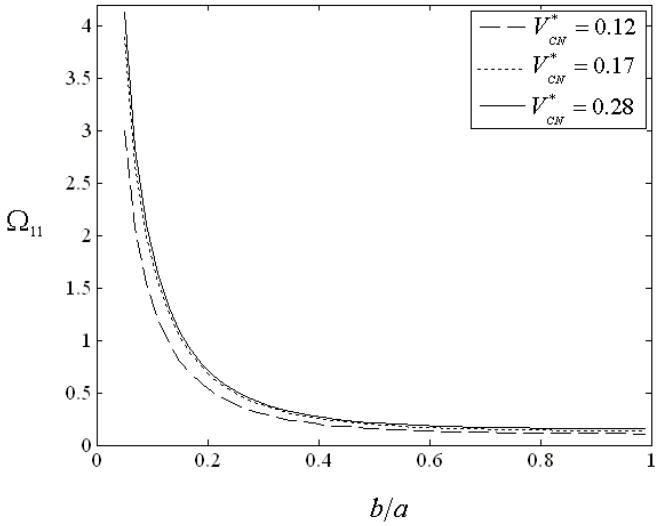

Figure 6.41. Effect of CNTs volume fraction on the frequency parameter of the plate for various b/a ratio $(h/a = 0.1)$

are lower than those of Profile$-\Diamond$ and Profile$-$UD .

The effect of the CNTs volume fraction V_{CN}^{*} on the frequency parameter of the plate for various b/a ratio is shown in Figure 6.41. It is found that the frequency parameter of the plate is increased with increase in CNTs volume fraction. It should be noted that the frequency parameter decreases rapidly with the increase of the b/a ratio and then remains almost unaltered for $b/a > 0.5$.

In order to study the prediction methods of the mechanical properties of nanocomposites, the frequency parameters obtained from extended rule of mixture are compared in Table 6.16 with those of Eshelby-Mori-Tanaka method for various types of CNT volume fraction profiles and different values of h/a and b/a ratio. It can be concluded from Table 6.16 that prediction methods of effective material properties have an insignificant influence on the variation of the frequency parameters with h/a and b/a ratio. It should be noted that the extended rule of mixture has higher frequency parameter than that of the Eshelby-Mori-Tanaka approach. It is worth mentioning that the same achievement has been recently determined again by Lei et al. [120] confirming our results.

Table 6.16. Non-dimensional natural frequency parameters of nanocomposite square plate with prediction methods of the mechanical properties of nanocomposites.

		Extended rule of mixture			Eshelby–Mori–Tanaka approach		
V_{CN}^{*}	h/a	Type I	UD	Type II	Type I	UD	Type II
0.12							
	0.01	0.002168	0.001797	0.001321	0.002157	0.001770	0.001304
	0.05	0.046574	0.040326	0.031155	0.046316	0.040160	0.030945
	0.1	0.138998	0.127824	0.107776	0.138154	0.124965	0.106101
	0.15	0.239550	0.227818	0.204612	0.237812	0.224701	0.202019
	0.2	0.342507	0.331268	0.309019	0.340802	0.330018	0.307549
0.17							
	0.01	0.002536	0.002095	0.001526	0.002522	0.002073	0.001507
	0.05	0.052363	0.045605	0.035409	0.052259	0.045468	0.035198
	0.1	0.149456	0.138447	0.118676	0.147904	0.136195	0.115931
	0.15	0.252229	0.240654	0.219649	0.250821	0.389605	0.218164
	0.2	0.357232	0.345423	0.326300	0.355096	0.342901	0.325134
0.28							
	0.01	0.003179	0.002616	0.001890	0.003155	0.002601	0.001838
	0.05	0.062227	0.054321	0.042818	0.062079	0.054134	0.042256
	0.1	0.168995	0.155834	0.137657	0.166601	0.153361	0.133259
	0.15	0.279679	0.263376	0.247275	0.277491	0.261496	0.243801
	0.2	0.393079	0.373005	0.360713	0.391132	0.369814	0.358924

6.4.2 Mechanical Buckling

Novel results for mechanical buckling of FG CNT-reinforced rectangular plates reinforced by SWCNTs subjected to uniaxial and biaxial in-plane loadings are presented here. A numerical study is performed to study the influences of the different types of compressive in-plane loadings, CNTs volume fractions, various types of CNTs volume fraction profiles, geometrical parameters, and different types of estimation of effective material properties on the critical mechanical buckling load of FG nanocomposite plates. For more explanation we choose the loading of plate as follows:

- Plane loading in the *x* direction.
- Plane loading in the *y* direction.
- Plane loading in the *x* and *y* directions.

For uniaxially compressed nanocomposite plate (sections 6-1 and 6-2), the extended rule of mixture explained in section 4.3.3 is used for predicting the overall material properties and responses of the plate, while for the case of biaxial in-plane loadings (section 6-3), effective elastic moduli are computed by using Eshelby-Mori-Tanaka approach introduced in section 4.3.4.1. PMMA is selected for the matrix, and the material properties of which are assumed to be $\nu^m = 0.34$, $E^m = 2.5\,\text{GPa}$ at room temperature (300 K) [116]. The (10,10) SWCNTs are selected as reinforcements.

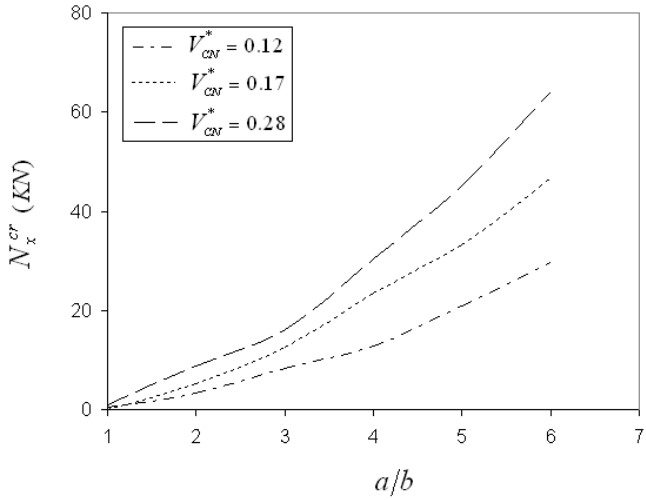

Figure 6.42. Critical buckling load $(N_x)_{cr}$ nanocomposite rectangular plate for various values of *a/b* and CNTs volume fraction (*t/b* =0.1, N_y=0).

All material properties and effective thickness of SWCNTs used for the present analysis are properly selected according to the MD simulation results of Shen [114]. It is noted that the effective wall thickness obtained for (10, 10)-tube is 0.067 nm, which satisfies the Vodenitcharova-Zhang criterion [197], and the wide used value of 0.34 nm for tube wall thickness is thoroughly inappropriate for SWCNTs.

6.4.2.1 Loading of plate only in *x* direction

In this section, nanocomposite rectangular plate is subjected to a uniform compressive load on edges x=0 and x=a. Figure 6.42 shows the critical load versus the aspect ratio of a/b with different CNTs volume fractions and various types of CNTs volume fraction profiles. From Figure 6.42, it is concluded that the critical buckling load of various types of CNTs volume fraction profiles become larger when the CNTs volume fraction increases. Another important result in Figure 6.42 is that the influence of the CNTs volume fraction on the critical buckling load for different types of CNTs profiles is generally significant at high aspect ratio of a/b. To assess the effects of various types of volume fraction profiles and aspect ratio of t/b, critical load for different values of CNTs volume fraction are presented in Table 6.17. It is observed from Table 6.17 that nanocomposite plates with Profile– X and Profile – ◊ have highest and lowest critical load, respectively. This means that the FG nanocomposite plates with symmetric profiles of the CNTs volume fraction can likely be designed according to the actual requirement and it is a potential alternative to the plates with uniformly distributed CNTs.

Table 6.17. Comparison between critical buckling load versus a/b $(N_x)_{cr}$ (KN) in various types of CNTs volume fraction profiles (t/b =0.1).

	Profile–X			Profile–UD			Profile – ◊		
a/b	$V_{CN}^{*}=0.12$	$V_{CN}^{*}=0.17$	$V_{CN}^{*}=0.28$	$V_{CN}^{*}=0.12$	$V_{CN}^{*}=0.17$	$V_{CN}^{*}=0.28$	$V_{CN}^{*}=0.12$	$V_{CN}^{*}=0.17$	$V_{CN}^{*}=0.28$
1	0.8514	1.1959	1.4426	0.6219	1.1721	1.3265	0.5587	1.1665	1.2256
2	5.1456	8.6542	10.549	4.0212	5.5487	9.2018	3.3214	5.2135	8.7521
3	11.054	18.562	22.853	9.0954	15.156	18.201	8.2487	12.598	16.258
4	18.789	32.325	39.564	14.029	27.298	33.235	12.897	23.520	30.298
5	30.055	50.054	61.593	23.548	38.129	50.129	20.784	33.351	45.098
6	42.035	71.519	88.324	33.521	52.529	70.219	29.587	46.651	64.032

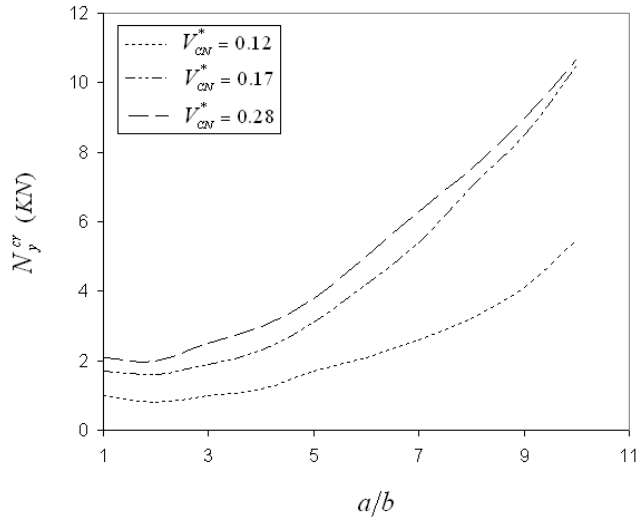

Figure 6.43. Variation of the critical buckling in-plane load $(N_y)_{cr}$ against the aspect ratio a/*b* (*t*/*b*=0.1, N_x=0).

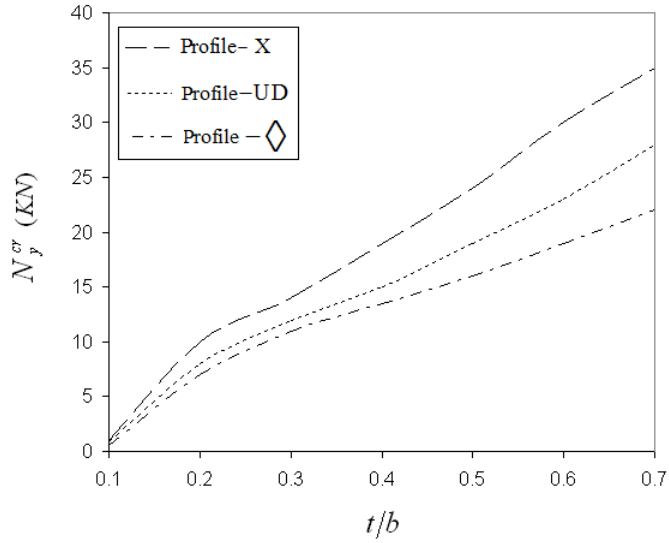

Figure 6.44. Critical load $(N_y)_{cr}$ against the aspect ratio *t*/*b* for various types of CNTs volume fraction profiles (*a*/*b*=1, N_x=0, V^*_{CN} = 0.12).

6.4.2.2 Loading of plate only in the *y* direction

In this section for more attention to the effect of CNTs, we assume that loading of plate is only in the *y* direction. Variation of the critical buckling in-plane load N_y^{cr} against the aspect ratio *t/b* for Profile– X nanocomposite plate is plotted in Figure 6.43. It can be inferred from Figure 6.43 that with increasing the CNTs volume fractions, influence of the aspect ratio *a/b* on the critical buckling loads is more significant. The variation of the critical buckling load versus the aspect ratio of *t/b* for various types of CNTs volume fraction profiles is shown in Figure 6.44 for $V_{CN}^{*} = 0.12$. The results in Figure 6.44 indicate that discrepancy among the various types of CNTs profiles increases with the increasing values of the aspect ratio of *t/b*.

6.4.2.3 Loading of plate in *x* and *y* directions

In this section we consider two axial loading of plate (N_x and N_y) and their relation is $N_x=\gamma N_y$. Also, the material properties of the FGM nanocomposite plate are assumed to be graded in the thickness direction and estimated through the Eshelby-Mori-Tanaka approach. Influence of different types of CNTs volume fraction profiles on critical biaxial buckling load against aspect ratio *t/b* is presented in Figure 6.45 for $V_{CN}^{*} = 0.12$. It is worthy of mention that critical biaxial buckling load of the

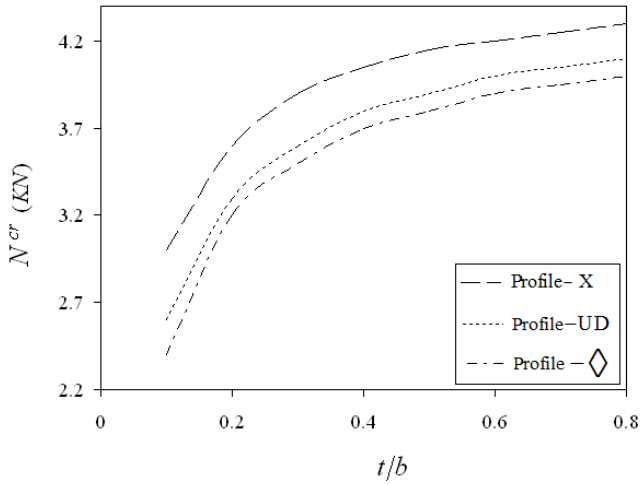

Figure 6.45. Influence of different types of CNTs volume fraction profiles on critical buckling load against aspect ratio *t/b* (*a/b* =1, γ=1, $V_{CN}^{*} = 0.12$)

$\text{Profile}-\Diamond$ nanocomposite plate is lower than that of one with $\text{Profile}-\text{X}$ and close to that of the uniformly distributed CNTs. Moreover, it can be concluded that for various types of estimation of effective material properties (extended rule of mixture and Mori-Tanaka method) and different loading of plate, nanocomposite plates with $\text{Profile}-\text{X}$ and $\text{Profile}-\Diamond$ have highest and lowest critical load, respectively. In addition, it is found that the critical biaxial buckling load increases rapidly with increasing the aspect ratio *t/b* and then remains almost unaltered for $t/b > 0.5$.

6.5 Summary and conclusions

In this chapter, numerical results and discussion for several problems of FGMs summarized into three parts comprising 1-D FG fiber-reinforced composites, 2-D FGM composites, and FG CNT-reinforced composites, have been presented.

Firstly, interesting and new results for free vibration, static, and thermal analyses 1-D FG fiber-reinforced composites were elaborated. We compared structural responses of continuously graded fiber-reinforced composites with those of traditionally laminated ones. The new results have been revealed that natural frequency of the FG fiber orientation panels was smaller than that of a discrete laminated composite and close to that of a 4-layer one. In contrast, the normalized natural frequency of a FG fiber volume fractions was larger than that of a discrete laminated composite and close to that of a 2-layer. Furthermore, obtained results showed that FG orthotropic composites exhibited continuously variations of both the in-plane and transverse static and thermal stress components, thereby reducing the likelihood of failure at interfaces between adjoining lamina as in the case of discretely laminated composites.

Secondly, results for free vibration and static analyses of 2-D FGM cylindrical panels followed by a comparison study with classic 1-D FGMs were presented. It has been shown that the lowest frequency parameter can be obtained by using *Classical-Classical* volume fractions profile. On the contrary, 1-D FGM panels with *Symmetric* volume fraction profile leads to the maximum value of the frequency parameter. Therefore, graded volume fraction in two directions has high capabilities to reduce the frequency parameter than conventional 1-D FGM. Afterwards, thermal behaviour of 2-D FGM cylindrical panels with temperature-dependent materials was studied. It has been deduced that the discrepancy between values of thermal stresses with different volume fractions for the case of temperature-dependent material properties was higher than that of with temperature-independent properties. From obtained results, it was concluded that calculations and design based on temperature-independent properties lead to conservative estimates.

Thirdly, numerical results for the cases of free vibration and mechanical buckling of FG CNT-reinforced composites have been presented and discussed. Influences of CNT agglomeration and various graded CNTs volume fractions on the free vibration characteristics of CNT-reinforced composites have been studied. The obtained results have revealed that the agglomeration parameters μ and ξ have completely different effects on the natural frequency of the FG CNT-reinforced composites. By increasing agglomeration degree of CNTs (or in other words by decreasing parameter μ) natural frequency increased. While this trend was reversed for parameter ξ. In case of buckling analysis, results revealed that the critical buckling load for $\text{Profile}-\text{V}$ was lower than that of one with $\text{Profile}-\text{X}$ and was close to that of the uniformly distributed CNTs. This was because the distribution pattern of CNTs can have an effect on the stiffness of the plate and it was thus expected that the desired stiffness can be achieved by adjusting the CNTs distribution through the thickness of plates. It was concluded that CNTs distributed close to top and bottom are more efficient than those distributed nearby the mid-plane of the plate.

Chapter 7

Conclusions and outlook for future research

7.1 Overview

The main objective of the research presented in this thesis was to study mechanical responses of FGM composites. The study has been organized into seven parts so far: (1) In the first chapter, an introduction to FGMs was given and various objectives of the thesis have been explained in details. (2) The aim of chapter 2 was to provide a short description on some basic concepts, including composite materials and their macro-mechanical analysis, 3-D elasticity, and 2-D plate theories, followed by a critical overview on the state-of-the-art literature on FGMs. (3) In chapter 3, theoretical formulations of various problems in the mechanics of FGMs were presented. (4) Chapter 4 elaborated mathematical modelling of FGMs along with homogenization methods to compute effective material properties. (5) In chapter 5, the solution procedure, known as GDQM, for solving coupled governing differential equations with variable coefficients has been stated. (6) Finally, chapter 6 was dedicated to numerical results and discussion for various analyses of FGMs categorized into three sections including 1-D FG fiber-reinforced composites, 2-D FGM composites, and FG CNT-reinforced composites. In the final chapter, the methodologies used in the present thesis and main conclusions are presented. Then, the suggestions for further extension of this research are elaborated.

7.2 Methodology used in the thesis

7.2.1 Theoretical formulations

In this thesis, not only based on 3-D elasticity theory governing equations of free vibration, static, and thermal stress analyses of FGMs have been derived, but also 2-D plate theories also have been used to formulate various problems. The basic approach in formulations based on 3-D elasticity theory was to derive Navier equations. In this case, first, 3-D elasticity equations of motion for cylindrical panels composed of FG monoclinic materials, in a general form, have been derived. Then, formulations for sandwich panels have been discussed. After that, the attention has been paid to formulations of FG rectangular plates and annular sectorial plates resting on elastic foundations based on 3-D elasticity theory. In the next part, thermo-elastic governing equations for FG orthotropic cylindrical panels based on 3-D elasticity have been derived. In case of formulations based on 2-D theories, the displacements were expanded in terms of thickness and transverse displacement was independent of the transverse coordinate. Based on FSDT, theoretical formulations for free vibration and mechanical buckling of CNT-reinforced plates have been perfomed. In this thesis, for the first time, governing equations for a 2-D FGM panel based on TSDT of Reddy have been derived.

7.2.2 Mathematical modelling of FGMs

For mathematical modelling of variation of volume fraction or fiber orientation, firstly, the classic form of power-law distribution was introduced. Furthermore, for modelling of gradation in volume fractions of CNT, various profiles for FG CNT-reinforced composites were presented. As one of the contributions of the present thesis, 1-D and 2-D generalized power-law distribution were presented. To compute effective material properties of composites, rule of mixture and Mori-Tanaka method has been used. In case of nanocomposites, for the first time, Eshelby-Mori-Tanaka method has been employed to determine the effective material properties of nanocomposites reinforced by various type of CNTs dispersion.

7.2.3 Solution procedure

Due to the complexity of the governing equations caused by variable coefficients initiated from non-homogeneity, it was very difficult to obtain the exact solutions. Owing to non-linear variation of material properties, seeking a powerful numerical method was highly desirable. In present thesis, GDQM as a semi-analytical approach was adopted to solve coupled governing differential equations. The 1-D and 2-D GDQM was applied in various problems consisting of thermal, vibration, and static analyses of FGMs. By solving free vibration, static, and thermal equations and by comparing the results with those of other methodologies, accuracy, convergency and efficiency of the methodology was asserted. In the present methodology, by using maximum 13 grid points, accurate and converged results for various FGM problems were obtained. Also, it was found that less computational efforts with respect to other available methods have been found.

7.3 Main conclusions

The significant findings of the work presented in this thesis can be summarized into three rudimentary categories as follows:

7.3.1 1-D FG fiber-reinforced composites

- ✓ For the first time, natural frequencies, static, and thermal stresses of FG fiber orientation and volume fraction fiber-reinforced composites panels have been compared with discretely laminated composites and new and interesting results have been presented. In case of free vibration analysis, the new results have been revealed that normalized natural frequency of the FG fiber orientation cylindrical panels was smaller than that of a discrete laminated composites and close to that of a 4-layer. In contrast, the

normalized natural frequency of a FG fiber volume fraction was larger than that of a discrete laminated composite and close to that of a 2-layer. On the other hand, in thermal analysis, it is interesting to note that the temperature distribution and thermal stress field distributions of a FG fiber-reinforced composite was closer to that of 2-layer one, and the 3-layer composite presented a set of results drastically distinct from the two other models. This was due to the lower conductivity (higher temperature gradient) of FG fiber-reinforced composite compared to that of 2- and 3-layer ones. Besides, because of higher thermal resistance of 2-layer, arising from thicker layers in comparison with 3-layer, the temperature gradient for 2-layer was higher than that of 3layer. Therefore, the temperature gradient increased from the 3-layer composite to the 2-layer one and then FG fiber-reinforced composite, respectively. Furthermore, obtained results showed that FG orthotropic panels exhibited continuously variations of both the in-plane and transverse static and thermal stress components, thereby reducing the likelihood of failure at interfaces between adjoining lamina as in the case of discretely laminated composites. This trend was much more appreciable in the thermal analysis.

- ✓ It has been shown the normalized natural frequencies of the FG fiber-reinforced panels decrease rapidly with the increase of the mid-radius to thickness S ratio and then approach a constant value for thin cylindrical panels. This behavior is the same as that of a discrete laminate composite panel.
- ✓ In this thesis, as the first endeavor, brand-new generalized power-law distributions for defining variation of volume fraction or fiber orientation in 1-D and 2-D FGMs composites have been intorduced. By using generalized power-law distribution, it was possible to study the effect of the different kinds of material profiles including symmetric, asymmetric, sigmoidal, and classic on mechanical behavior of a FGM structures. Furthermore, distribution and magnitude of thermal stresses/frequency characteristics or modal displacements can be reduced/increased to a required manner by selecting appropriate different parameters of power-law distribution and volume fractions profiles in the required direction(s). Another advantage of generalized power-law distribution was to have a desirable volume fraction of the material on the inner or outer surface, while there was a smooth gradation of volume fraction through the required direction. In case of FG fiber-reinforced composite, it was shown that maximum natural frequency of the can be obtained through using symmetric profile of fiber orientation.
- ✓ In this research work, for the first time a detailed parametric study was carried out to highlight the influences of continuously grading fiber

orientation face sheets and different profile of fiber volume fraction and fiber orientation on the vibration characteristics of the FGSW panels. It has been found that the fundamental normalized frequencies increase with the increase of volume fraction of silicon carbide fibers on the outer surfaces of core. It was also shown that with increasing the thickness of face sheet-to-panel ratio h_f / h, the fundamental normalized frequencies decrease. The results showed that for $p = 1$ the fundamental normalized frequencies of classic profile is smaller than that of other types of FGSW panels. In contrast, for $p > 10$ the fundamental normalized frequencies increase with increasing parameter *c* and close to that of classic fiber orientation profile.

- ✓ As an interesting and new finding, it has been found that for the large values of Winkler elastic coefficient, the shearing layer elastic coefficient has less effect and the results become independent of it, in other words, the non-dimensional natural frequencies converge with increasing Winkler foundation stiffness. Furthermore, it has resulted that the variations of Winkler elastic coefficient has little effect on the non-dimensional natural frequencies at different values of shearing layer elastic coefficient. In case of closed cylindrical shells resting on elastic foundations, the results revealed that non-dimensional radial and transverse shear stresses increase with increasing Winkler elastic coefficient. On the contrary, the axial stress through the thickness decreases with increasing Winkler elastic coefficient. The mechanical entities of FGM fiber-reinforced cylindrical shell converged with increasing Winkler foundation stiffness.

7.3.2 2-D FGM composites

- ✓ Based on the achieved results, it has been inferred that the 2-D generalized power-law distribution proposed for volume fractions of 2-D FGM composites gives designers a powerful tool for flexible design of structures under multi-functional requirements. Results indicated the advantages of using panels with graded volume fractions in two directions to a more flexible design than the conventional 1-D FGM.
- ✓ It has been shown that the lowest frequency parameter can be obtained by using *Classical-Classical* volume fractions profile. On the contrary, 1-D FGM panels with *Symmetric* volume fraction profile leads to the maximum value of the frequency parameter. Therefore, graded volume fraction in two directions has high capabilities to reduce the frequency parameter than conventional 1-D FGM.

- ✓ The new results demonstrated that with increasing values of the circumferential wave number, frequency parameter of the *Classical* panel is close to that of *Symmetric-Symmetric*. Also, it was found that the effect of the circumferential wave number on the growth rate of the frequency parameter is more tangible for the *Symmetric and Symmetric-Symmetric* volume fraction profiles.
- ✓ The general behavior of the frequency parameters of 2-D FGM panels for all boundary conditions was that the frequency parameters converged only in the range beyond that of the fundamental frequency parameters.
- ✓ In this thesis, new theoretical formulations for 2-D FGM composites based on TSDT of Reddy have been formulated and governing equations for thermal analysis have been derived. For a realistic investigation of 2-D FGMs, temperature-dependent properties were taken into account. It has been deduced that the discrepancy between values of thermal stresses with different volume fractions for the case of temperature-dependent material properties was higher than that those of with temperature-independent properties.
- ✓ It is found that calculations and design based on temperature-independent properties yield conservative estimates.

7.3.3 FG CNT-reinforced composites

- ✓ In the present thesis, for the first time, effects of CNT agglomeration and various graded CNTs volume fractions on the free vibration characteristics of CNT-reinforced composites have been studied. Results showed that the frequency parameters of the annular sectorial plate resting on Pasternak elastic foundation decrease rapidly with the increase of the plate angle and then approach a constant value for higher plate angle. The obtained results have revealed that the agglomeration parameters μ and ξ have completely different effects on the natural frequency of the FG CNT-reinforced composites. By increasing agglomeration degree of CNTs or in other words by decreasing parameter μ, natural frequency increased. While this trend was reversed for parameter ξ. The higher volume fraction of CNT in inclusions was, the higher natural frequency was.
- ✓ The results showed that the prediction methods of effective material properties have an insignificant influence on the variation of the frequency parameters with the plate aspect ratio and the CNTs volume fraction. It should be noted that the extended rule of mixture has higher frequency parameter than that of the Eshelby-Mori-Tanaka approach. It is worth

mentioning that the same achievement has been recently determined again by Lei et al. [120] confirming our results.

- ✓ In this thesis, a new numerical study was performed to investigate the influences of the different types of compressive in-plane loadings, different types of CNTs volume fraction profiles, and geometrical parameters on the critical mechanical buckling load of FG CNT-reinforced plates. The results showed that in the case of uniaxial loading, the impact of the CNTs volume fraction on the critical buckling load for different types of CNTs profiles was generally significant at high aspect ratio. Moreover, the critical buckling load for $Profile-V$ was lower than that of one with $Profile-X$ and was close to that of the uniformly distributed CNTs. This was because the distribution pattern of CNTs can have an effect on the stiffness of the plate and it was thus expected that the desired stiffness can be achieved by adjusting the CNTs distribution through the thickness of plates. It was inferred that CNTs distributed close to top and bottom are more efficient than those distributed nearby the mid-plane of the plate.

7.3 Suggestions for future works

This work presented in this thesis opens new opportunities for further research. As a direct result of the work presented in this thesis the following suggestions can be made.

- With astonishing advances in the development of material science and technology, FGMs have been employed in micro-electro-mechanical systems (MEMS) to nanoelectro-mechanical systems (NEMS) to reach the high sensitivity and desired performance [198-200]. It is highly important to consider the size effect initiating from the underling microstructures in the theoretic and experimental investigations of the microscale or nanoscale FGMs. Accordingly, future works can be considering size effects on the microscale or nanoscale FGMs for their potential application in MEMS and NEMS. To this end, nonlocal continuum mechanics modeling is required to be properly developed. Although classical or local continuum mechanics modeling is effective in studying large-scale FGM nanostructures, its applicability to capture the small-scale effect on nano-material mechanical behaviors is limited. The limited applicability is due to the fact that at small size the lattice spacing between individual atoms becomes increasingly important and the discrete structure of the material can no longer be homogenized into a continuum [201,202]. Therefore, cautious employment of classical continuum models has been proclaimed when directly applying to nanostructure analysis. In order to incorporate the small length scale

effect, continuum mechanics models need to be refined. This may be accomplished by using the nonlocal continuum theory.

- In the design of FG fiber-reinforced plates and shells, it is of technical importance to study their resistance to buckling under loading conditions. For this purpose, the determination of the buckling load alone is not sufficient in general, but it is further needed to study the postbuckling behavior, that is, the behavior of the shell after passing through the buckling load. One of the reasons is to estimate the influence of practically unavoidable imperfections on the buckling load and the second is to evaluate the ultimate strength to exploit the load-carrying capacity of the FG fiber-reinforced plates and shells. Due to lack of study on the postbuckling behavior of FG fiber-reinforced plates and shells, the postbuckling analysis of 1-D and 2-D FGM composites will be also future extension of the current work. In addition, using generalized power law distribution the effect of the different kinds of material profiles including symmetric, asymmetric, and sigmoidal on postbuckling behaviour of a FGM structures can be studied.
- The FGMs composites can be integrated with piezoelectric materials so as to improve their dynamical behaviours. The piezoelectric materials are well-known for their sensing and actuating capabilities [203]. Such structures have the great ability to control the size, shape, vibration and stability of the structural components due to their direct and converse piezoelectric impacts. As an illustration, a piezoelectric sensor patch can monitor the deformation of a structure while a piezoelectric actuator patch can control the deformation of the structure through the converse piezoelectric effect. Therefore, the piezoelectric materials have been acquired many applications in vibration control and monitoring. Therefore, it is of great importance to analyze the behavior of FGMs composites integrated with piezoelectric materials. To sum up, the future extension of this thesis can be studying FG fiber-reinforced or 2-D FGM composites integrated with sensors and actuators.
- In most conditions of severe environments, when plate deflection-to thickness ratio is greater than 0.4 [154], the nonlinearity is very important and the nonlinear dynamic equations of plates are needed to perform the analysis. As a result, other extension of the present work is to investigate non-linear vibration analysis of 2-D FGM plates by considering non-linear geometrical effects. It is interesting to note that GDQM along with a direct iterative method [204] can be used for solving the non-linear governing equations.

References

[1] S. Suresh, A. Mortensen: Fundamentals of functionally graded materials. IOM Communications Ltd, London, 1998.

[2] K. Ichikawa: Functionally graded materials in the 21st century: a workshop on trends and forecasts. Kluwer Academic Publishers, 2000.

[3] E.C.N. Silva, M.C. Walters, G.H. Paulino: Modeling bamboo as a functionally graded material: lessons for the analysis of affordable materials. Journal of Materials Science, 41, 6991–7004, 2006.

[4] M. Koizumi: The Concept of FGM, Ceramic Trans., Functionally Gradient Materials, 34, 3-10, 1993.

[5] H. M.Yin, L.Z. Sun, G.H.Paulino: Micromechanics-Based Elastic Model for Functionally Graded Materials with Particle Interactions. Acta Mater. 52, 3535–3543, 2004.

[6] A.J. Goupee: Multiscale Investigation of Random Heterogenous Media in Materials and Earth Sciences. PhD thesis, University of Maine, Mechanical Engineereing Department. 2010.

[7] A.W. Leissa, A.F. Martin: Some exact plane elasticity solutions for nonhomogeneous, orthotropic sheets. J Elast, 23, 97–112, 1990.

[8] A.F. Martin, A.W. Leissa: Application of the Ritz method to plane elasticity problems for composite sheets with variable fibre spacing. Int J Numer Methods Eng, 28, 1813–25, 1989.

[9] A.W. Leissa, A.F. Martin: Vibration and buckling of rectangular composite plates with variable fiber spacing. Compos Struct, 14, 339–57, 1990.

[10] O. Joergensen, A.E. Giannakopoulos, S. Suresh: Spherical indentation of composite laminates with controlled gradients in elastic anisotropy. Int. J. Solids Struct. 35, 50-97, 1998.

[11] M.A. Steinberg: Materials for Aerospace, U.S. goals for subsonic, supersonic and hypersonic flight and for space exploration call for alloys

and composites notable for strength, light weight and resistance to heat. Sci. Am. 244, 59–64, 1986.

[12] Columbia Accident Investigation Board: Report of Columbia accident investigation board, vol. I, chap 6 (PDF). p. 173, 2003.

[13] Columbia Accident Investigation Board: In-flight options assessment, vol. II, appendix D.12 (PDF). 30 January 2006 (2003).

[14] S. Iijima: Helical microtubes of graphitic carbon. Nature, 354, 56–8, 1991.

[15] D. Salvetat, A. Rubio: Mechanical properties of carbon nanotubes: a fiber digest for beginners. Carbon, 40, 1729–1734, 2002.

[16] M. Endo, T. Hayashi, Y.A. Kim, et al.: Applications of carbon nanotubes in the twenty-first century. Phil Trans R Soc Lond A, 362, 2223–2238, 2004.

[17] J.M. Wernik, S.A. Meguid: Multiscale modeling of the nonlinear response of nano-reinforced polymers. Acta Mech, 217, 1–16, 2011.

[18] E.T. Thostenson, ZF Ren, T-W Chou: Advances in the science and technology of carbon nanotubes and their composites: a review. Compos Sci Technol, 61, 1899–1912, 2001.

[19] M. Moniruzzaman, K.I. Winey: Polymer nanocomposites containing carbon nanotubes. Macromolecules, 39, 5194–5205, 2006.

[20] B. Valter, M.K. Ram, C. Nicolini: Synthesis of multiwalled carbon nanotubes and poly (o-anisidine) nanocomposite material: fabrication and characterization of its Langmuir-Schaefer films. Langmuir, 18, 1535–1541, 2002.

[21] S.A. Meguid, Y. Sun: On the tensile and shear strength of nano-reinforced composite interfaces. Mater Des, 25, 289–96, 2004.

[22] M. Koizumi: FGM activities in Japan. Compos Part B-Eng., 28, 1–4, 1997.

[23] M. Finot, S. Suresh, C. Bull, S. Sampath: Curvature changes during thermal cycling of a compositionally graded Ni–Al2O3 multi-layered material. Mater. Sci. Engrg. A, 205, 59–71, 1996.

[24] M. Finot, S. Suresh: Small and large deformation of thick and thin-film multi-layers: effect of layer geometry, plasticity and compositional gradients, J. Mech. Phys. Solids, 44, 683–721, 1996.

[25] Y. Fukui: Fundamental Investigation of Functionally Gradient Material Manufacturing System Using Centrifugal Force. Int. J. Japan Soc. Mech. Engrs. Set, III, 34, 144-148, 1991.

[26] H. Yamaoka, M. Yuki, K. Tahara, T. Irisawa, R. Watanabe, A. Kawasaki: Fabrication of Functionally Gradient Material by Slurry Stacking and Sintering Process. Ceramic Trans., Functionally Gradient Materials, 34, 165-172, 1993.

[27] S. Elam, J. Lee, R. Holmes, F. Zimmerman, M. Effinger: Lightweight Chambers for Thrust Assemblies. For presentation at the 52d International Astronautics Conference, Toulouse, France, October 1-5, 2001.

[28] W.A. Gooch, B.H.C. Chen, M.S. Burkins, R. Palicka, J. Rubin, R. Rayichandran: Development and ballistic testing of a functionally gradient ceramic/metal appliqué. Mater. Sci. Forum, Switzerland, Trans Tech Publications, Dresden, Germany, pp 614-21, 1999.

[29] E.S.C. Chin: Army focused research team on functionally graded armor composites. Mater. Sci. Eng. A, Struct. Mater., Prop. Microstruct. Process. Elsevier, San Antonio, TX, USA, 155-61, 1999.

[30] K. Yamada, J. Sakamura, K. Nakamura: Broadband ultrasound transducers using piezoelectrically graded materials, Mater. Sci. Forum, Trans Tech Publications, Dresden, Germany, 527-32, 1999.

[31] J. Zhao, X. Ai, X.P. Huang: Relationship between the thermal shock behavior and the cutting performance of a functionally gradient ceramic tool. Journal of Materials Processing Technology 129, 161-166, 2002.

[32] M.M. Gasik, S. Ueda: Micromechanical modelling of functionally graded W-Cu materials for divertor plate components in a fusion reactor, Mater. Sci. Forum, Trans Tech Publications, Dresden, Germany, 603-7, 1999.

[33] F. Watari, A. Yokoyama, H. Matsuno, F. Saso, M. Uo, T. Kawasaki: Biocompatibility of titanium/hydroxyapatite and titanium/cobalt functionally graded implants. Materials Science Forum 308-311: 356-361, 1999.

[34] F. Wang, H.P. Lee, C. Lu: Thermal-mechanical study of functionally graded dental implants with the finite element method. Journal of Biomedical Materials Research- Part A, 146-158, 2007.

[35] F. Watari, A. Yokoyama, M. Omori, T. Hirai, H. Kondo, M. Uo, T. Kawasaki: Biocompatibility of materials and development to functionally graded implant for bio-medical application. Composites Science and Technology, 64, 893-908, 2004.

[36] I.P. Borovinskaya, A.G. Merzhanov, V.I. Uvarov: SHS materials of graded porosity. Materials Science Forum 308-311: 151-156, 1999.

[37] G.H. Paulino, Z-H Jin, RHJ Dodds: Failure of functionally graded materials. In: Karihaloo B and Knauss WG (Eds) Encyclopedia of Comprehensive Structural Integrity, Vol. 2, Chapter 13, Elsevier, Amsterdam, 2003.

[38] M. Jabbari, S. Sohrabpour, M.R. Eslami: General solution for mechanical and thermal stresses in a functionally graded hollow cylinder due to nonaxisymmetric steady-state loads. J. Appl. Mech. 70: 111-118, 2003.

[39] M. Jabbari, A. Bahtui, M.R. Eslami: Axisymmetric mechanical and thermal stresses in thick long FGM cylinders. J. Therm. Stresses 29:643-663, 2006.

[40] Y. Ootao, Y. Tanigawa: Transient thermoelastic analysis for a functionally graded hollow cylinder. J. Therm. Stresses 29:1031-1046, 2006.

[41] N. Noda, Thermal Stress in Materials with Temperature-Dependent Properties, Appl. Mech. Rev. 44: 383–397, 1991.

[42] C. Shu: Differential Quadrature and Its Application in Engineering. Springer, Berlin, 2000.

[43] C. Shu, B.E. Richards: Application of generalized differential quadrature to solve two-dimensional incompressible Navier Stockes equations. Int. J. Numer. Meth. Fluid 15:791-798, 1992.

[44] F. Tornabene, E. Viola: 2-D solution for free vibrations of parabolic shells using generalized differential quadrature method. European Journal of Mechanics A/Solids, 27: 1001–1025, 2008.

[45] B. Boresi, A. Peter, P. Ken: Elasticity in Engineering Mechanics, second ed. Wiley, New York, 1999.

[46] R.M. Jones, Mechanics Of Composite Materials, Taylor & Francis, Philadelphia, 1998.

[47] J. N. Reddy, Mechanics of Laminated Composite Plates and Shells: Theory and Analysis, Second Edition, CRC Pr N. Noda: Transient thermal stresses problem in a transversely isotropic finite circular cylinder under three-dimensional temperature field. J Therm Stresses, 6, 57–71, 1983.

[48] T. Gomshima, K. Miyao: Transient thermal stresses in a plate with a hole due to rotating heat source. J Therm Stresses, 13, 43–56, 1990.

[49] S.P. Jeon, Y. Tanigawa, D. Sone: Analytical treatment of axisymmetrical thermoelastic field with Kassir's nonhomogeneous material properties and its adaptation to boundary value problem of slab under steady temperature field. J Therm Stresses, 20, 325–43, 1997.

[50] Y. Tanigawa, H Morishita, S. Ogaki: Derivation of systems of fundamental equations for a three-dimensional thermoelastic field with nonhomogeneous material properties and its application to a semi-infinite body. J Therm Stresses, 22, 689–711, 1999.

[51] W.M. Lai, D. Rubin: Introduction to Continuum Mechanics. 3rd ed. Elsevier Science & Technology, San Diego, CA, 1997.

[52] J.N. Reddy: Theory and analysis of elastic plates and shells, CRC Press, 2007.

[53] J.M. Whitney, CT Sun: A higher order theory for extensional motion of laminated composites. J Sound Vib, 30, 85–97, 1973.

[54] K.H. Lo, R.M. Christensen, E.M. Wu: A high-order theory of plate deformation part 1: homogeneous plates. J Appl Mech. 44, 663–8, 1977.

[55] T. Kant: Numerical analysis of thick plates. Comput Methods Appl Mech. 31, 1–18, 1982.

[56] A. Bhimaraddi: Stevens LK. A higher order theory for free vibration of orthotropic, homogeneous, and laminated rectangular plates. J Appl Mech. 51, 195–8, 1994.

[57] N.F. Hanna, AW Leissa: A higher order shear deformation theory for the vibration of thick plates. J Sound Vib, 170, 545–55, 1994.

[58] J.N. Reddy, CD Chin: Thermoelastical analysis of functionally graded cylinders and plates. J Therm Stress, 21, 593–626, 1998.

[59] W.Q. Chen, X. Wang, H.J. Ding: Free vibration of a fluid-filled hollow sphere of a functionally graded material with spherical isotropy. J. Acoust. Soc. Am., 106: 2588–2594, 1999.

[60] A. Alibeiglooa, K.M. Liew: Free vibration analysis of sandwich cylindrical panel with functionally graded core using three-dimensional theory of elasticity. Composite Structures 113:23–30, 2014.

[61] P. Malekzadeh, A.R. Fiouz, M. Sobhrouyan: Three-dimensional free vibration of functionally graded truncated conical shells subjected to thermal environment. Int. J. Press. Vessels Pip., 89:210–221, 2012.

[62] H. Santos, C.M. Mota Soares, C.A. Mota Soares, J.N. Reddy: A semi-analytical finite element model for the analysis of cylindrical shells made of functionally graded materials. Compos. Struct., 91: 427–432, 2009.

[63] Y. Qu, Guang Meng: Three-dimensional elasticity solution for vibration analysis of functionally graded hollow and solid bodies of revolution. Part I: Theory. European Journal of Mechanics A/Solids 44:222-233, 2014.

[64] Y.Qu, Guang Meng: Three-dimensional elasticity solution for vibration analysis of functionally graded hollow and solid bodies of revolution. Part II: Application. European Journal of Mechanics A/Solids 44:) 234-248, 2014.

[65] Sh. Hosseini-Hashemi, M. Azimzadeh-Monfared, H. Rokni Damavandi Taher: A 3-D Ritz solution for free vibration of circular/annular functionally graded plates integrated with piezoelectric layers. International Journal of Engineering Science 48:1971–1984, 2010.

[66] H-S Shen, H. Wang: Nonlinear vibration of shear deformable FGM cylindrical panels resting on elastic foundations in thermal environments. Composites: Part B 60:167–177, 2014.

[67] H. Matsunaga: Free vibration and stability of functionally graded shallow shells according to a 2D higher-order deformation theory. Composite Structures 84: 132–146, 2008.

[68] X. Zhao, Y.Y. Lee, K.M. Liew: Thermoelastic and vibration analysis of functionally graded cylindrical shells. International Journal of Mechanical Sciences 51:694–707, 2009.

[69] F. Tornabene, E. Violaa, Daniel J. Inman: 2-D differential quadrature solution for vibration analysis of functionally graded conical, cylindrical shell and annular plate structures. Journal of Sound and Vibration 328:259–290, 2009.

[70] R.C. Batra, J. Jin: Natural frequencies of a functionally graded anisotropic rectangular plate. J. Sound. Vib. 282: 509-516, 2005.

[71] G.J. Nie, R.C. Batra: Static deformations of functionally graded polar-orthotropic cylinders with elliptical inner and circular outer surfaces. Composites Science and Technology 70: 450–457, 2010.

[72] Y. Fu, P. Zhang, F. Yang: Interlaminar stress distribution of composite laminated plates with functionally graded fiber volume fraction. Materials and Design 31: 2904–2915, 2010.

[73] S.S. Vel: Exact elasticity solution for the vibration of functionally graded anisotropic cylindrical shells. Composite Structures 92: 2712–2727, 2010.

[74] H-S Shen, C-L Zhang: Non-linear analysis of functionally graded fiber reinforced composite laminated plates, Part I: Theory and solutions. International Journal of Non-Linear Mechanics 47:1045–1054,2012.

[75] H-S Shen, C-L Zhang: Non-linear analysis of functionally graded fiber reinforced composite laminated plates, Part II: Numerical results. International Journal of Non-Linear Mechanics 47: 1055–1064,2012.

[76] X. Li, J. Zhang, Y. Zheng: Static and Free Vibration Analysis of Laminated Composite Plates Using Isogeometric Approach Based on the Third Order Shear Deformation Theory. Advances in Mechanical Engineering 2014: 1-16, 2013.

[77] H-S Shen: Boundary layer theory for the nonlinear vibration of anisotropic laminated cylindrical shells. Composite Structures 97:338–352, 2013.

[78] A. Naderi · A. R. Saidi: Bending–stretching analysis of moderately thick functionally graded anisotropic wide beams. Arch Appl Mech 83:1359–1370, 2013.

[79] Y. Obata, N. Noda: Steady thermal stresses in a hollow circular cylinder and a hollow sphere of a functionally gradient material. J Therm Stresses;17:471–87, 1994.

[80] S. Takezono, K. Tao, E. Inamura, M. Inoue: Thermal stress and deformation in functionally graded material shells of revolution under thermal loading due to fluid. JSME Int J Ser A: Mech Mater Eng, 39: 573–581, 1996.

[81] N. Tutuncu, M. Ozturk: Exact solutions for stresses in functionally graded pressure vessels. Compos Part B: Eng, 32: 683–686, 2001.

[82] Z.Q. Cheng, R.C. Batra: Three-dimensional thermoelastic deformations of a functionally graded elliptic plate Composites: Part B, 31: 97–106, 2000.

[83] J.N. Reddy, Z.Q. Cheng: Three-dimensional thermomechanical deformations of functionally graded rectangular plates. European Journal of Mechanics A/Solids, 20:841–855, 2001.

[84] S.S. Vel, R.C. Batra: Exact thermoelasticity solution for functionally graded thick rectangular plates. AIAA Journal, 40: 1421–1433, 2002.

[85] S.S. Vel, R.C. Batra: Three-dimensional analysis of transient thermal stresses in functionally graded plates. International Journal of Solids and Structures, 40: 7181–7196, 2003.

[86] L.F. Qian, R.C. Batra: Transient thermoelastic deformations of a thick functionally graded plate Journal of Thermal Stresses, 27: 705–740, 2004.

[87] T. Darabseh, N. Yilmaz, M. Bataineh : Transient thermoelasticity analysis of functionally graded thick hollow cylinder based on Green–Lindsay model. International Journal of Mechanics and Materials in Design 8, Issue 3, pp 247-255. 2012.

[88] M. K. Ghosh, M. Kanoria: Analysis of thermoelastic response in a functionally graded spherically isotropic hollow sphere based on Green–Lindsay theory. Acta Mechanica 207, Issue 1-2:51-67, 2009.

[89] Y. Ootao, Y. Tanigawa: Three-dimensional solution for transient thermal stresses of an orthotropic functionally graded rectangular plate. Composite Structures 80:10–20, 2007.

[90] P. Malekzadeh, M. Ghaedsharaf: Three-dimensional thermoelastic analysis of finite length laminated cylindrical panels with functionally graded layers. 49, Issue 4, pp 887-906. 2014.

[91] J. Ying, Chao-feng Lü, C. W. Lim: 3D thermoelasticity solutions for functionally graded thick plates. Journal of Zhejiang University SCIENCE A 10, Issue 3: 327-336, 2009.

[92] J. Go, A. M. Afsar, J. I. Song: Analysis of Thermoelastic Characteristics of a Rotating FGM Circular Disk by Finite Element Method. Advanced Composite Materials 19, Issue 2:197-213, 2010.

[93] X. Wang, L.J. Sudak: Three-dimensional analysis of multi-layered functionally graded anisotropic cylindrical panel under thermomechanical loading. Mechanics of Materials 40:235–254, 2008.

[94] M. Bouremana, A. Tounsi, A. Kaci, I. Mecha, Controlling thermal deformation by using composite materials having variable fiber volume fraction. Materials and Design 30: 2532–2537, 2009.

[95] J.L. Pelletier, S.S. Vel: An exact solution for the steady-state thermoelastic response of functionally graded orthotropic cylindrical shells. International Journal of Solids and Structures 43 :1131–1158, 2006.

[96] M. Nemat-Alla: Reduction of thermal stresses by developing two-dimensional functionally graded materials. International Journal of Solids and Structures 40(26):7339–7356, 2003.

[97] H.S. Hedia: Comparison of one-dimensional and two-dimensional functionally graded materials for the backing shell of the cemented acetabular cup. Journal of Biomedical Materials Research Part B—Applied Biomaterials 74B(2):732–739, 2005.

[98] H.S. Hedia, M.A.N. Shabara, T.T. El-Midany et al.: Improved design of cementless hip stems using two-dimensional functionally graded materials. Journal of Biomedical Materials Research Part B—Applied Biomaterials 79B(1):42–49, 2006.

[99] A. Sutradhar, GH Paulino: The simple boundary element method for transient heat conduction in functionally graded materials. Computer Methods in Applied Mechanics and Engineering 193(42–44):4511–4539, 2004.

[100] Y.S. Chan, L.J. Gray, T. Kaplan et al.: Green's function for a two-dimensional exponentially graded elastic medium. Proceedings of Royal Society of London—Series A 460(2046):1689–1706, 2004.

[101] L.F. Qian, R.C. Batra: Design of bidirectional functionally graded plate for optimal natural frequencies. Journal of Sound and Vibration 280(1–2):415–424, 2005.

[102] M. Nemat-Alla, A.I.E. Ahmed, I. Hassab-Allah:, Elastic–plastic analysis of two-dimensional functionally graded materials under thermal loading, Int. J. Solids Struct. 46, 2774–2786, 2009.

[103] D.L. Clements, J. Kusuma, W.T. Ang, A note on antiplane deformations of inhomogeneous materials. Int. J. Eng. Sci, 35 (1997) 593–601.

[104] M. Nemat-Alla, N. Noda, Thermal stress intensity factor for functionally gradient half space with an edge crack under thermal load. Arch. Appl. Mech. 66 (8) (1996) 569–580.

[105] M. Nemat-Alla, N. Noda, Study of an edge crack problem in a semi-infinite functionally graded medium with two dimensionally non-homogenous coefficient of thermal expansion under thermal load, J. Therm. Stresses. 19 (1996) 863–888.

[106] M. Nemat-Alla, N. Noda, Edge crack problem in a semi-infinite FGM plate with a bi-directional coefficient of thermal expansion under two-dimensional thermal loading, Acta Mech. 144 (2–3) (2000) 211–229.

[107] M. Nemat-Alla, N. Noda, I. Hassab-Allah, Analysis and investigation of thermal stress intensity factor for edge cracked FGM plates. In: Bulletin of the Faculty of Engineering, 29 (2001). Assiut University, 89–102.

[108] M. Marin, Numerical solution of the Cauchy problem for steady-state heat transfer in two-dimensional functionally graded materials. Int. J. Solids Struct. 42 (2005) 4338–4351.

[109] J. Aboudi, M. Pindera, S. Arnold, Thermoplasticity theory for bidirectionally functionally graded materials, J. Therm. Stresses. 19 (1996) 809–861.

[110] J. R. Cho, D. Y. Ha, Optimal tailoring of 2D volume-fraction distributions for heat-resisting functionally graded materials using FDM, Comput. Methods Appl. Mech. Eng. 191, (2002) 3195–3211.

[111] M. Nemat-Alla, Reduction of thermal stresses by developing twodimensional functionally graded materials, Int. J. Solids Struct. 40: 7339–7356, 2003.

[112] M. Asgari, M. Akhlaghi, Transient thermal stresses in two-dimensional functionally graded thick hollow cylinder with finite length, Arch. Appl. Mech. 80:353-376, 2010.

[113] M. Asgari, M. Akhlaghi, Transient heat conduction in two-dimensional functionally graded hollow cylinder with finite length, Heat Mass Transfer. 45(11):1383–1392, 2009.

[114] H-S Shen: Nonlinear bending of functionally graded carbon nanotube-reinforced composite plates in thermal environments. Compos Struct. 91, 9–19, 2009.

[115] H-S Shen, Z.H. Zhu: Buckling and postbuckling behavior of functionally graded nanotube-reinforced composite plates in thermal environments. Comput Mater Continua, 18, 155–82, 2010.

[116] H-S Shen, C-L Zhang: Thermal buckling and postbuckling behavior of functionally graded carbon nanotube-reinforced composite plates. Mater Des, 31, 3403–11, 2010.

[117] P. Zhu, Z.X. Lei, K.M. Liew: Static and free vibration analyses of carbon nanotube-reinforced composite plates using finite element method with first order shear deformation plate theory, Compos. Struct. 94, 1450–1460, 2012.

[118] Z.X. Wang, H-S Shen: Nonlinear vibration of nanotube-reinforced composite plates in thermal environments. Comput Mater Sci, 50, 2319–2330, 2011.

[119] A. Alibeigloo: Static analysis of functionally graded carbon nanotube-reinforced composite plate embedded in piezoelectric layers by using theory of elasticity, Compos. Struct. 95, 612–622, 2013.

[120] Z.X. Lei, K.M. Liew, J.L. Yu: Free vibration analysis of functionally graded carbon nanotube-reinforced composite plates using the element-free kp-Ritz method in thermal environment. Composite Structures 106: 128–138, 2013.

[121] R. Moradi-Dastjerdi, A. Pourasghar, M. Foroutan:The effects of carbon nanotube orientation and aggregation on vibrational behavior of functionally graded nanocomposite cylinders by a mesh-free method. Acta Mech 22:, 2817–2832, 2013.

[122] M.H. Yas, M. Heshmati: Dynamic analysis of functionally graded nanocomposite beams reinforced by randomly oriented carbon nanotube under the action of moving load. Appl. Math. Model. 36: 1371–1394, 2012.

[123] J.E. Jam, A. Pourasghar, S. Kamarian: The effect of the aspect ratio and waviness of CNTs on the vibrational behavior of functionally graded nanocomposite cylindrical panels. Polym. Compos. 33: 2036–2044, 2012.

[124] PL. Pasternak, On a new method of analysis of an elastic foundation by means of two foundation constants. Cosudarstrennoe Izdatelstvo Literaturi po Stroitelstvu i Arkhitekture, Moscow, USSR, (1954) 1–56 [in Russian].

[125] Z.Y. Huang, C.F. Lu, W.Q. Chen, Benchmark solutions for functionally graded thick plates resting on Winkler–Pasternak elastic foundations, Compos. Struct. 85 (2008) 95–104.

[126] Z.Q. Cheng, R.C. Batra, Exact correspondence between eigenvalues of membranes and functionally graded simply supported polygonal plates, J. Sound Vib. 229 (2000) 879–895.

[127] Sh. Hosseini-Hashemi, H. Rokni Damavandi Taher, H. Akhavan, M. Omidi, Free vibration of functionally graded rectangular plates using first-order shear deformation plate theory, Appl. Math. Modell. 34 (2010) 1276–1291.

[128] A.M. Zenkour, M.N.M. Allam, M. Sobhy: Bending analysis of FG visco-elastic sandwich beams with elastic cores resting on Pasternak's elastic foundations. Acta Mech., 212: 233–252, 2010.

[129] A.M. Zenkour, M.N.M. Allam, M. Sobhy: Bending of a fiber-reinforced viscoelastic composite plate resting on elastic foundations. Arch. Appl. Mech., 81: 77–96, 2011.

[130] Sh. Hosseini Hashemi, H. Rokni Damavandi Taher, M. Omidi: 3-D free vibration analysis of annular plates on Pasternak elastic foundation via p-Ritz method. Journal of Sound and Vibration 311:1114–1140, 2008.

[131] S.A. Sheikholeslami, A.R. Saidi: Vibration analysis of functionally graded rectangular plates resting on elastic foundation using higher-order shear and normal deformable plate theory. Composite Structures 106: 350–361, 2013.

[132] Z.Y. Huang, C.F. Lü, W.Q. Chen: Benchmark solutions for functionally graded thick plates resting on Winkler–Pasternak elastic foundations. Compos. Struct., 85: 95–104, 2008.

[133] D.N. Paliwal, H. Kanagasabapathy, K.M. Gupta: The large deflection of an orthotropic cylindrical shell on a Pasternak foundation, Composite Structures 31, 1995, 31–37.

[134] D.N. Paliwal, R.K. Pandey, T. Nath: Free vibration of circular cylindrical shell on Winkler and Pasternak foundation, International Journal of Pressure Vessels and Piping 69, 1996, 79–89.

[135] R. Yang, H. Kameda, S. Takada: Shell model FEM analysis of buried pipelines under seismic loading, Bulletin of the Disaster Prevention Research Institute, Kyoto University 38, 1998, 115–146.

[136] J.B. Cai, W.Q. Chen, G.R. Ye, H.J. Ding: On natural frequencies of a transversely isotropic cylindrical panel on a kerr foundation. Journal of Sound and vibration, 2000, 232(5), 997-1004.

[137] H.T. Gunawan, T. Mikami, S. Kanie, M. Sato: Free vibration characteristics of cylindrical shells partially buried in elastic foundations, Journal of Sound and Vibration 290, 2006, 785–793.

[138] M. Farid, P. Zahedinejad, P. Malekzadeh: Three dimensional temperature dependent free vibration analysis of functionally graded material curved panels resting on two parameter elastic foundation using a hybrid semi-analytic, differential quadrature method, Materials and Design 31, 2010, 2–13.

[139] Hui-Shen Shen: Nonlinear thermal bending of FGM cylindrical panels resting on elastic foundations under heat conduction. Composite Structures 113:216–224, 2014.

[140] A.G. Shah, T. Mahmood, Naeem, N.N., Iqbal, Z., Arshad, A.H., Vibrations of functionally graded cylindrical shells based on elastic foundations, Acta Mech, 2009.

[141] D. Zenkert: The handbook of sandwich construction. Engineering Materials Advisory Services Ltd. (EMAS); 1997.

[142] S. Abrate: Impact on composite structures. Cambridge UK: Cambridge University Press; 1998.

[143] A. Subramanian, V. Dayal, D. J. Barnard: Damage characterization of carbon/epoxy laminates using compression-after-impact (CAI) and ultrasonic NDE. AIP Conf. Proc. 1511, 987, 2013.

[144] Q. Li, V.P. Iu, K.P. Kou: Three-dimensional vibration analysis of functionally graded material sandwich plates, J Sound Vib 2008; 311 (1–2):498–515.

[145] T.A. Anderson: 3D elasticity solution for a sandwich composite with functionally graded core subjected to transverse loading by a rigid sphere. Compos Struct 2003; 60:265–74.

[146] H.J. Xiang, Y. Yang: Free and forced vibration of a laminated FGM Timoshenko beam of variable thickness under heat conduction. Compos Part B/Eng 2008; 39:292–303.

[147] A.M. Zenkour. A comprehensive analysis of functionally graded sandwich plates. Part 1 – deflection and stresses. Int J Solids Struct 2005; 42:5224–42.

[148] A.M. Zenkour. A comprehensive analysis of functionally graded sandwich plates. Part 2 – buckling and free vibration deflection and stresses. Int J Solids Struct 2005; 42: 5243–58.

[149] M. Kashtalyan, Menshykova M. Three-dimensional elasticity solution for sandwich panels with a functionally graded core. Compos Struct. 2009; 87: 36–43.

[150] RK Bhangale, N. Ganesan: Thermoelastic buckling and vibration behavior of a functionally graded sandwich beam with constrained viscoelastic core. J Sound Vib 2006; 295: 294–316.

[151] F.P. Incropera: Fundamentals of Heat and Mass Transfer. John Wiley & Sons. 2012.

[152] S. Jafari Mehrabadi, B.Sobhani Aragh: Stress analysis of functionally graded open cylindrical shell reinforced by agglomerated carbon nanotubes. Thin-Walled Structures 80:130–141, 2014.

[153] DO Brush, BO Almroth: Buckling of bars, plates, and shells. McGraw-Hill; 1975.

[154] H-S Shen: Functionally graded materials, nonlinear analysis of plates and shells. Florida: CRC Press, 2009.

[155] G.N. Praveen, JN Reddy: Nonlinear Transient Thermoelastic Analysis of Functionally Graded Ceramic-Metal Plates, Int. J. Solids Struct., 35:4457–4476, 1998.

[156] JN Reddy, CD Chen: Thermomechanical Analysis of Functionally Graded Cylinders and Plates. J. Therm. Stresses, 21:593–626 1998.

[157] JN Reddy, Z-Q Cheng: Three-Dimensional Thermomechanical Deformations of Functionally Graded Rectangular Plates. Eur. J. Mech. A/Solids, 20: 841–855, 2011.

[158] L. Della Croce, P. Venini: Finite elements for functionally graded Reissnere Mindlin plates. Comput. Methods Appl. Mech. Eng. 193:705-725, 2004.

[159] A.M. Zenkour: Generalized shear deformation theory for bending analysis of functionally graded plates. Appl. Math. Model. 30, 67-84, 2006.

[160] Fidelus JD, Wiesel E, Gojny FH, Schulte K, Wagner HD. Thermo-mechanical properties of randomly oriented carbon/epoxy nanocomposites. Composites Part A 2005;36:1555–61.

[161] A. Shah, T. Mahmood, M. Naeem, Vibrations of FGM thin cylindrical shells with exponential volume fraction law. Appl. Math. Mech. Eng., 30 (2009) 607–615.

[162] S.H. Arshad, MN Naeem, and N Sultan, Frequency analysis of functionally graded material cylindrical shells with various volume fraction laws. Part C: Journal of Mechanical Engineering Science (2007) 221: 1483.

[163] E. Viola, F. Tornabene, Free vibrations of three-parameter functionally graded parabolic panels of revolution. Mech Res Commun, 36 (2009), 587–594.

[164] F. Tornabene, E. Viola, Free vibrations of four-parameter functionally graded parabolic panels and shells of revolution. European Journal of Mechanics - A/Solids 28, Issue 5 (2009) 991-1013.

[165] F. Tornabene, Free vibration analysis of functionally graded conical, cylindrical shell and annular plate structures with a four-parameter power-law distribution. Computer Methods in Applied Mechanics and Engineering, 198 (2009) 2911–2935.

[166] H-S Shen: A comparison of buckling and postbuckling behavior of FGM plates with piezoelectric fiber reinforced composite actuators. Compos Struct 91:375–84, 2009.

[167] V.V. Vasiliev, E.V. Morozov: Mechanics and analysis of composite materials. 1st ed. Elsevier Science Ltd.; 2001.

[168] T. Mori, K. Tanaka: Average stress in matrix and average elastic energy of materials with misfitting Inclusions. Acta Metall. 21, 571-574, 1973.

[169] Y. Benveniste: A new approach to the application of Mori–Tanaka's theory of composite materials, Mechanics of Materials 6:147–157, 1987.

[170] M.M. Shokrieh, R. Rafiee: Prediction of mechanical properties of an embedded carbon nanotube in polymer matrix based on developing an equivalent long fiber, Mechanics Research Communications;37:235–240, 2010.

[171] G.D. Seidel, D.C. Lagoudas: Micromechanical analysis of the effective elastic properties of carbon nanotube reinforced composites. Mech Mater 38:884–907, 2006.

[172] D Qian, EC Dickey, R Andrews, T. Rantell: Load transfer and deformation mechanisms in carbon nanotube–polystyrene composites. Appl Phys Lett 76:2868–70, 2000.

[173] J.D. Eshelby: The determination of the elastic field of an ellipsoidal inclusion and related problems. Proc R Soc London Ser A 241:376–96, 1957.

[174] D.L. Shi, X.Q. Feng, Y.Y. Huang, K.C. Hwang, H.J. Gao: The effect of nanotube waviness and agglomeration on the elastic property of carbon nanotubereinforced composites. J Eng Mater Technol 126:250–7, 2004.

[175] G. Formica, W. Lacarbonara, R. Alessi: Vibrations of carbon nanotube-reinforced composites. J Sound Vib 329:1875–89, 2010.

[176] G.M. Odegard, T.S. Gates, K.E .Wise, C. Park, E.J. Siochi: Constitutive modelling of nanotube reinforced polymer composites. Compos Sci Technol 63: 1671–87, 2003.

[177] R. Hill: A Self-Consistent Mechanics of Composite Materials. J. Mech. Phys. Solids, 13: 213–222, 1965.

[178] Q.S. Yang, X. Tao, H. Yang: A stepping scheme for predicting effective properties of the multi-inclusion composites. Int J Eng Sci 45:997–1006, 2007.

[179] R.E. Bellman, J. Casti: Differential quadrature and longtem integration. J. Math. Anal. and Applications, 34, 235-238, 1971.

[180] R.E. Bellman, B.G. Kashef, J. Casti: Differential quadrature: a technique for the rapid solution of nonlinear partial differential equations. J. Computational Phys., 10, 40-52, 1972.

[181] C. Shu: Generalized differential-integral quadrature and application to the simulation of incompressible viscous flows including parallel computation. Ph.D. Thesis, University of Glasgow, July 1991.

[182] J.R. Quan, C.T. Chang: New insights in solving distributed system equations by the quadrature method – I. Analysis. Comput. Chem. Eng. 13:779–788, 1989.

[183] C.W. Bert, M. Malik: Differential quadrature method in computational mechanics: a review. ASME Appl. Mech. Rev. 49, 1-28, 1996.

[184] C. Shu, W. Chen, H. Xue, H. Du: Numerical study of grid distribution effect on accuracy of DQ analysis of beams and plates by error estimation of derivative approximation. Int. J. Numer. Meth. Eng. 51:159–179, 2001.

[185] F. Tornabene, E. Viola: Free vibration analysis of functionally graded panels and shells of revolution. Meccanica 44: 255–281, 2009.

[186] M. Shakeri, M. Akhlaghi, S.M. Hosseini: Vibration and radial wave propagation velocity in functionally graded thick hollow cylinder. Compos Struct 76:174–81, 2006.

[187] DB Miracle. Aeronautical applications of metal–matrix composites, vol. 21. Material Park (OH): Compos ASM Int; 1043–9, 2001.

[188] T.K.Varadan, K. Bhaskar: Bending of laminated orthotropic cylindrical shells-an elasticity approach. J. Compos. Struct. 17:141–156,1991.

[189] A. Messina, K.P. Soldatos: A general vibration model of angle-ply laminated plates that accounts for the continuity of interlaminar stresses. Int J Solids Struct 39:617–35, 2002.

[190] P. Malekzadeh: Three-dimensional free vibrations analysis of thick functionally graded plates on elastic foundations. Composite Structures 89;367–373, 2009.

[191] D. Zhou, Y.K. Cheung, S.H. Lo, F.T.K. Au: Three-dimensional vibration analysis of rectangular thick plates on Pasternak foundation, Int. J. Numer. Meth. Eng. 59: 1313–34, 2004.

[192] H. Matsunaga: Vibration and stability of, thick plates on elastic foundations. J. Eng. Mech. (ASCE) 126:27–34, 2000.

[193] S. Pradyumna, J.N. Bandyopadhyay: Free vibration analysis of functionally graded panels using higher-order finite-element formulation. J. Sound Vib. 318:176-192, 2008.

[194] M. Ruhi, A. Angoshtari, R. Naghdabadi: Thermoelastic analysis of thick-walled finite-length cylinders of functionally graded materials, Journal of Thermal Stresses 28: 391–408, 2005.

[195] C.Y. Dong: Three-dimensional free vibration analysis of functionally graded annular plates using the Chebyshev–Ritz method, Mater. Des. 29:1518–1525, 2008.

[196] Y. Han, J. Elliott: Molecular dynamics simulations of the elastic properties of poly-mer/carbon nanotube composites, Comput. Mater. Sci., 39: 315–323, 2007.

[197] C.Y. Wang, L.C. Zhang: A critical assessment of the elastic properties and effective wall thickness of single-walled carbon nanotubes. Nanotechnology 19: 075705, 2008.

[198] A.S. Mahmud, Y. Liu, T.H. Nam: Gradient anneal of functionally graded NiTi. Smart Mater Struct 17:015031, 2008.

[199] D.J. Hasanyan, R.C. Batra, R.C. Harutyunyan: Pull-in instabilities in functionally graded micro-thermo-electromechanical systems. J Therm Stress 31:1006–21, 2008.

[200] A. Witvrouw, A. Mehta: The use of functionally graded poly-SiGe layers for MEMS applications. Mater Sci Forum 492–493:255–60, 2005.

[201] J. Peddieson, G.R. Buchanan, R.P. McNitt: Application of nonlocal continuum models to nanotechnology. Int J Eng Sci 41(3–5):305–312, 2003.

[202] R.F. Gibson, E.O. Ayorinde, Y-F Wen: Vibrations of carbon nanotubes and their composites: A review. Compos Sci Technol 67(1):1–28, 2007.

[203] M. Schwartz, Encyclopaedia of Smart Materials, Wiley & Sons, New York, 2002.

[204] J. Yang, L.L. Ke, S. Kitipornchai: Nonlinear free vibration of single-walled carbon nanotubes using nonlocal Timoshenko beam theory. Physica E 42:1727–1735, 2010.

Publications

A1- Peer reviewed journal publications included in Science Citation Index

a) Related to the present thesis:

[1] **B. Sobhani Aragh**, M.H. Yas: Three dimensional free vibration of functionally graded fiber orientation and volume fraction of cylindrical panels. *Materials and Design* 31, 4543–4552, 2010.

[2] **B. Sobhani Aragh**, M.H. Yas: Static and free vibration analyses of continuously graded fiber-reinforced cylindrical shells using generalized power-law distribution. *Acta Mechanica* 215, 155–173, 2010.

[3] **B. Sobhani Aragh**, M.H. Yas: Effect of continuously grading fiber orientation face sheets on vibration of sandwich panels with functionally graded core, *International Journal of Mechanical Sciences* 53, 628–638, 2011.

[4] M.H. Yas, **B. Sobhani Aragh**: Elasticity solution for free vibration analysis of four-parameter functionally graded fiber orientation cylindrical panels using differential quadrature method. *European Journal of Mechanics A/Solids* 30, 631-638, 2011.

[5] M.H. Yas, **B. Sobhani Aragh**: Free vibration analysis of continuous grading fiber reinforced plates on elastic foundation. *International Journal of Engineering Science* 48, 1881–1895, 2010.

[6] M.H. Yas, **B. Sobhani Aragh**: Three-Dimensional analysis for thermo elastic response of functionally graded fiber reinforced cylindrical panel. *Composite Structures* 92, 2391–2399, 2010.

[7] **B. Sobhani Aragh**, M.H. Yas: Three-dimensional analysis of thermal stresses in four-parameter continuous grading fiber reinforced of cylindrical panels. *International Journal of Mechanical Sciences* 52, 1047–1063, 2010.

[8] **B. Sobhani Aragh**, A. Zeighami, M. Rafiee, M.H. Yas, M. Abdel Wahab: 3-D thermo-elastic solution for continuously graded isotropic and fiber-reinforced cylindrical shells resting on elastic foundations. *Applied Mathematical Modelling* 37, 6556–6576, 2013.

[9] **B. Sobhani Aragh**, H. Hedayati: Static response and free vibration of two-dimensional functionally graded metal/ceramic open cylindrical shells under various boundary conditions. *Acta Mechanica*, 223, 309–330, 2012.

[10] S. Jafari Mehrabadi, **B. Sobhani Aragh**: On the thermal analysis of 2-D temperature-dependent functionally graded open cylindrical shells. *Composite Structures* 96, 773–785, 2013.

[11] **B. Sobhani Aragh**, H. Hedayati, E. Borzabadi Farahani, M. Hedayati: A novel 2-D six-parameter power-law distribution for free vibration and vibrational displacements of two-dimensional functionally graded fiber-reinforced curved panels, European Journal of Mechanics A/Solids 30, 865-883, 2011.

[12] **B. Sobhani Aragh**, A.H. Nasrollah Barati, H. Hedayati: Eshelby-Mori-Tanaka approach for vibrational behavior of continuously graded carbon nanotube-reinforced cylindrical panels, *Composites Part B: Engineering* 43, 1943–1954, 2012.

[13] H. Hedayati, **B. Sobhani Aragh**: Influence of graded agglomerated CNTs on vibration of CNT-reinforced annular sectorial plates resting on Pasternak foundation. *Applied Mathematics and Computation* 218, 8715–8735, 2012.

[14] S. Jafari Mehrabadi, **B. Sobhani Aragh**, V. Pourdonya: Free Vibration Analysis of Nanocomposite Plates Reinforced by Graded Carbon Nanotubes Based on First-Order Shear Deformation Plate Theory, Advances in Applied Mathematics and Mechanics, 5, No. 1, 90-112, 2013.

[15] S. Jafari Mehrabadi, **B. Sobhani Aragh**, V. Khoshkhahesh, A. Taherpour: Mechanical buckling of nanocomposite rectangular plate reinforced by aligned and straight single-walled carbon nanotubes. *Composites Part B: Engineering* 43, 2031–2040, 2012.

[16] **B. Sobhani Aragh**, E. Borzabadi Farahani, A.H. Nasrollah Barati: Natural frequency analysis of continuously graded carbon nanotube-reinforced cylindrical shells based on third-order shear deformation theory. *Mathematics and Mechanics of Solids* 18, No. 3, 264–284, 2012.

b) Other publications:

[1] Jafari Mehrabadi S., **Sobhani Aragh B.**, Stress analysis of functionally graded open cylindrical shell reinforced by gglomerated carbon nanotubes. *Thin-Walled Structures* 80 (2014) 130–141.

[2] Hedayati H., Hedayati M., **Sobhani Aragh B.** Borzabadi Farahani E., 2-D differential quadrature solution for vibration characteristics of two-dimensional functionally graded metal/ceramic open cylindrical shells. *Mechanics of Advanced Materials and Structures*. Volume 21, Issue 4, (2014), 305-320.

[3] Yas, M.H. **Sobhani Aragh, B.**, Heshmati, M., Three-dimensional free vibration analysis of functionally graded fiber reinforced cylindrical panels using differential quadrature method. Structural Engineering and Mechanics, Vol. 37, No. 5 (2011).

[4] **Sobhani Aragh B.**, Yas M.H., Three-dimensional free vibration analysis of four-parameter continuous grading fiber reinforced cylindrical panels resting on Pasternak foundations. *Archive of Applied Mechanics* 81 (2011) 1759–1779.

[5] Rafiee M., Mohammadi M., **Sobhani Aragh B.**, Yaghoobi H., Nonlinear free and forced thermoelectro-aero-elastic vibration and dynamic response of piezoelectric functionally graded laminated composite shells, Part I: Theory and analytical solutions. *Composite Structures* 103 (2013) 179–187.

[6] Rafiee M., Mohammadi M., **Sobhani Aragh B.**, Yaghoobi H., Nonlinear free and forced thermoelectro-aero-elastic vibration and dynamic response of piezoelectric functionally graded laminated composite shells, Part II: Numerical results. *Composite Structures* 103 (2013) 188–196.